Acta Pharmacologica Sinica (2012) 33: 429–430
 1671-4083/12 $32.00
www.nature.com/aps

Research Highlight

A new antihypertensive drug ameliorate insulin resistance

Yan-xia LIU

Acta Pharmacologica Sinica (2012) 33: 429–430; doi: 10.1038/aps.2012.31

Insulin resistance (IR) is defined as decreased sensitivity and/or responsiveness to insulin that promote glucose disposal. A growing body of clinical and epidemiologic evidence indicates that essential hypertension and IR often coexist[1]. Approximately 50 percent of patients with hypertension can be considered to have IR and hyperinsulinemia[1]. This inextricable linkage between hypertension and IR has been identified to increase the prevalence of cardiovascular disease (CVD) and new onset of type II diabetes that is the major cause of morbidity and mortality in this clinical syndrome[2]. However, the driving force linking IR and hypertension remains to be fully elucidated.

In the current first-line antihypertensive agents, various drugs have been shown to have different glycometabolic effects. Diuretics or beta blockers have been proved to decrease insulin sensitivity and subsequently deteriorate IR states, whereas calcium channel blockers have been investigated to be neutral[3]. Only angiotensin-converting enzyme (ACE) inhibitors and angiotensin II (Ang II) type 1 (AT1) receptor antagonists have been reported to enhance insulin sensitivity and reduce new onset of type II diabetes in hypertensive individuals as highlighted in a recent meta-analysis[4]. Indeed, there is not even consensus as to whether or not there are pronounced benefits on IR after ARBs treatments. Bahadir *et al* reported that the effects of telmisartan on IR were neutral in hypertensive patients with the metabolic syndrome[5]. Despite intense research, drugs able to ameliorate hypertension and, at the same time, improve IR and/or hyperinsulinemia are still lacking. It is a great value to develop a new generation of antihypertensive drugs with advantages in improving metabolic disorders.

Endothelial dysfunction, characterized by impaired endothelium-independent vascular relaxation and an imbalance between decreased nitric oxide (NO) release and enhanced ET-1 production, is commonly observed in patients with hypertension, diabetes, hyperlipidemia and other cardiovascular diseases, and has been considered to be an underlying pathophysiological mechanism that served as the link between IR and hypertension[6, 7]. On one hand, endothelial dysfunction associated with IR states is featured by injured insulin-stimulated NO release from endothelium with decreased blood flow and reduced delivery of substrates and hormones to insulin target tissues[8]. On the other hand, the imbalance between endothelial-derived relaxing and contracting factors is a potential contributor to the abnormal modulation of vascular tone and the pathogenesis of high blood pressure[6]. Thus, the pharmacological approach to restoring endothelial function is expected to be a feasible way to ameliorate IR associated with hypertension. Actually, results of the current basic research strongly support that the improvements of IR states in hypertension after ACEIs or ARBs medications are mainly due to their protection against endothelial dysfunction[7].

Endothelial cells express a diverse array of ion channels which play important roles in modulating cell functions. It has been recognized that activation of endothelial ATP-sensitive potassium channels (K_{ATP}) can modulate the progression of endothelial dysfunction. Opening of endothelial K_{ATP} channels can regulate intracellular Ca^{2+} levels that affect the production and release of endothelial autacoids, *eg*, NO, ET-1, and prostaglandins[6]. Theoretically, endothelial K_{ATP} channel openers are predicted to be able to inhibit the development of IR in hypertensive patients.

An article by WANG *et al*[9] in recent issue of *Acta Pharmacologica Sinica* demonstrates for the first time that iptakalim, a novel selective K_{ATP} channel opener, could prevent the establishment and progression of IR with hypertension in animal models via keeping the balance between NO and ET-1 signaling in endothelial cells. WANG *et al* show that treating the fructose-fed rats (FFRs) with iptakalim for 4 weeks lowered

Department of Pharmacology, School of Basic Medical Sciences, Tianjin Medical University, Tianjin 300070, China
(liuyanxia@tmu.edu.cn)

blood pressure and restored the balance between the production of NO and secretion of ET-1. Furthermore, the impaired ACh-induced endothelium-dependent relaxation of aortic tissue derived from the FFRs was improved significantly after iptakalim administration. Of note, using the euglycemic-hyperinsulinemia clamp analysis, they confirmed that iptakalim can improve insulin sensitive index (ISI), normalize the glucose infusion rate (GIR), and decrease plasma insulin levels in FFRs. In spontaneously hypertensive rats (SHRs), besides effectively lowering blood pressure, they also found that iptakalim treatment ameliorated IR states. These pharmacological characteristics implicates that iptakalim is suitable for the treatment of hypertension associated with IR. Interestingly, iptakalim could significantly increase the release of NO and expression of eNOS protein and inhibit the production of ET-1 in PI3-kinase inhibitor wortmannin and hyperinsulinemia stimulated human umbilical vein endothelial cells (HUVECs). These *in vitro* results indicate that iptakalim could protect against IR-induced endothelial dysfunction. Based on these observations, they conclude that activation of K_{ATP} channel by iptakalm ameliorate IR associated with hypertension via restoring the balance between NO and ET-1 signaling in endothelial cells.

Abundant previous pharmacological studies have demonstrated that iptakalim is a highly selective K_{ATP} channel opener, which can preferentially relax small arteries and effectively reduce blood pressure[10, 11]. Another article published in Acta Pharmacologica Sinica suggested that iptakalim, via activating K_{ATP} channels, enhances the endothelial chemerin/ChemR23 axis and NO production and thus improves endothelial function[12]. They also claim that there is a casual relationship between the antihypertensive response of iptakalim and KCNJ11 polymorphisms in Chinese Han hypertensive patients[13]. The study around of iptakalim has attracted widespread concern in the field of cardiovascular research[6, 14, 15].

Notably, Wang *et al* provided the experimental evidence that iptakalim was able to ameliorate IR states with hypertension though restoring endothelial function in animals[9]. Because metabolic disorders such as IR and/or hyperinsulinemia and type II diabetes are often observed in hypertensive individuals, it is possible that iptakalm may exhibit additional benefits in these patients. Their most interesting finding uncovers the advanced property of iptakalim and is a valuable contribution in the field of hypertension and IR therapy.

1 Reaven GM. Insulin resistance/compensatory hyperinsulinemia, essential hypertension, and cardiovascular disease. J Clin Endocrinol Metab 2003; 88: 2399–403.
2 Sowers JR. Insulin resistance and hypertension. Am J Physiol Heart Circ Physiol 2004; 286: H1597–602.
3 Taylor EN, Hu FB, Curhan GC. Antihypertensive medications and the risk of incident type 2 diabetes. Diabetes Care 2006; 29: 1065–70.
4 Garcia-Puig J, Ruilope LM, Luque M, Fernandez J, Ortega R, Dal-Re R. AVANT Study Group Investigators. Glucose metabolism in patients with essential hypertension. Am J Med 2006; 119: 318–26.
5 Bahadir O, Uzunlulu M, Oguz A, Bahadir MA. Effects of telmisartan and losartan on insulin resistance in hypertensive patients with metabolic syndrome. Hypertens Res 2007; 30: 49–53.
6 Minamino T, Hori M. Protecting endothelial function: A novel therapeutic target of ATP-sensitive potassium channel openers. Cardiovasc Res 2007; 73: 448–9.
7 Kim JA, Montagnani M, Koh KK, Quon MJ. Reciprocal relationships between insulin resistance and endothelial dysfunction: molecular and pathophysiological mechanisms. Circulation 2006; 113: 1888–904.
8 Vincent MA, Montagnani M, Quon MJ. Molecular and physiologic actions of insulin related to production of nitric oxide in vascular endothelium. Curr Diab Rep 2003; 3: 279–88.
9 Wang Y, Zeng FH, Long CL, Pan ZY, Cui WY, Wang RH, *et al*. The novel ATP-sensitive potassium channel opener iptakalim prevents insulin resistance associated with hypertension via restoring endothelial function. Acta Pharmacol Sin 2011; 32: 1466–74.
10 Wang H. Cardiovascular ATP-sensitive potassium channel as a new molecular target for development of antihypertensive drugs. Acta Pharmacol Sin 1998; 19: 397–402.
11 Pan Z, Huang J, Cui W, Long C, Zhang Y, Wang H. Targeting hypertension with a new adenosine triphosphate-sensitive potassium channel opener iptakalim. J Cardiovasc Pharmacol 2010; 56: 215–28.
12 Duan RF, Cui WY, Wang H. Association of the antihypertensive response of iptakalim with KCNJ11 (Kir6.2 gene) polymorphisms in Chinese Han hypertensive patients. Acta Pharmacol Sin 2011; 32: 1078–84.
13 Zhao RJ, Wang H. Chemerin/ChemR23 signaling axis is involved in the endothelial protection by K_{ATP} channel opener iptakalim. Acta Pharmacol Sin 2011; 32: 573–80.
14 Costa AD. Iptakalim: a new or just another KCO? Cardiovasc Res 2009; 83: 417–8.
15 Sikka P, Kapoor S, Bindra VK, Saini M, Saxena KK. Iptakalim: A novel multi-utility potassium channel opener. J Pharmacol Pharmacother 2012; 3: 12–4.

Acta Pharmacologica Sinica (2012) 33: 431–437
 1671-4083/12 $32.00
www.nature.com/aps

Original Article

Polygalasaponin F induces long-term potentiation in adult rat hippocampus via NMDA receptor activation

Feng SUN, Jian-dong SUN, Ning HAN, Chuang-jun LI, Yu-he YUAN, Dong-ming ZHANG, Nai-hong CHEN*

State Key Laboratory of Bioactive Substances and Functions of Natural Medicines, Institute of Materia Medica, Chinese Academy of Medical Sciences and Peking Union Medical College, Beijing 100050, China

Aim: To investigate the effect and underlying mechanisms of polygalasaponin F (PGSF), a triterpenoid saponin isolated from *Polygala japonica*, on long-term potentiation (LTP) in hippocampus dentate gyrus (DG) of anesthetized rats.
Methods: Population spike (PS) of hippocampal DG was recorded in anesthetized male Wistar rats. PGSF, the NMDAR inhibitor MK801 and the CaMKII inhibitor KN93 were intracerebroventricularly administered. Western blotting analysis was used to examine the phosphorylation expressions of NMDA receptor subunit 2B (NR2B), Ca^{2+}/calmodulin-dependent kinase II (CaMKII), extracellular signal-regulated kinase (ERK), and cAMP response element-binding protein (CREB).
Results: Intracerebroventricular administration of PGSF (1 and 10 μmol/L) produced long-lasting increase of PS amplitude in hippocampal DG in a dose-dependent manner. Pre-injection of MK801 (100 μmol/L) or KN93 (100 μmol/L) completely blocked PGSF-induced LTP. Furthermore, the phosphorylation of NR2B, CaMKII, ERK, and CREB in hippocampus was significantly increased 5–60 min after LTP induction. The up-regulation of p-CaMKII expression could be completely abolished by pre-injection of MK801. The up-regulation of p-ERK and p-CREB expressions could be partially blocked by pre-injection of KN93.
Conclusion: PGSF could induce LTP in hippocampal DG in anesthetized rats via NMDAR activation mediated by CaMKII, ERK and CREB signaling pathway.

Keywords: polygalasaponin F; hippocampus; long-term potentiation; NMDA receptor (NMDAR); Ca^{2+}/calmodulin-dependent kinase II (CaMKII); extracellular signal-regulated kinase (ERK); cAMP response element binding protein (CREB)

Acta Pharmacologica Sinica (2012) 33: 431–437; doi: 10.1038/aps.2011.199; published online 30 Jan 2012

Introduction

Polygala japonica HOUTT (*P japonica*), a folk medicine herb used as expectorant, anti-inflammatory, antibacterial, ataractic, and antidepressant agents in the south of China. These activities may be due to the presence of various saponins in *P japonica*, since studies have indicated that the saponins found in Polygala have antipsychotic and expectorant effects[1, 2]. Polygalasaponin F (PGSF), a triterpenoid saponin, was first isolated from *P japonica* by Zhang *et al* in 1995[3]. Previous studies indicate that PGSF possesses evident anxiolytic and sedative-hypnotic activities, and has cognition improving and cerebral protective effects[4]. A structural analogues of PGSF, polygalasaponin XXXII (PGS32) has been found to improve the hippocampus-dependent learning and memory and induce Long-term potentiation (LTP) in adult rats[5].

LTP of synaptic transmission is currently the best available cellular model for learning and memory in the mammalian brain[6]. LTP has also been proposed as a tool for screening nootropic drug candidates. Although LTP can be induced in a variety of brain regions, hippocampal LTP is the most investigated form of synaptic plasticity, because the hippocampus is involved essentially in learning and memory processes[7, 8]. In particular we chose dentate gyrus (DG) of the hippocampus, which is critically involved in hippocampus dependent memory formation[9].

Accumulating evidence indicates that the NMDA receptor (NMDAR) plays an essential role in the induction of LTP in the hippocampal DG area[10]. Evidence indicates that NMDARs are regulated by tyrosine phosphorylation and that LTP in DG is correlated specifically with tyrosine phosphorylation of the NMDAR subunit 2B (NR2B), which is a major functional component of the hippocampal NMDAR[11, 12].

One effect of NMDAR activation is the influx of calcium (Ca^{2+}), which can bind to calmodulin (CaM)[13]. The Ca^{2+}/CaM complex activates many downstream signaling molecules. Ca^{2+}/CaM-dependent protein kinase II (CaMKII) is one of its target proteins to be implicated in synaptic plasticity[14]. CaMKII is present in high concentrations in the postsynaptic density, a cytoskeletal structure beneath the postsynaptic membrane in hippocampus[15]. Activation of CaMKII by Ca^{2+}/CaM

* To whom correspondence should be addressed.
E-mail chennh@imm.ac.cn
Received 2011-10-25 Accepted 2011-12-09

initiates its autophosphorylation on threonine residue 286, which makes it independent of Ca^{2+} and renders it constitutively active[16, 17]. CaMKII is essential for the induction of LTP in the hippocampus. The hippocampal LTP is blocked by CaMKII inhibitors[18]. In addition, Lledo PM *et al* reported that postsynaptic application of CaMKII produces an increase in synaptic efficacy that mimics LTP[19].

Increasing evidence indicates that the long-lasting potentiation of synaptic efficacy requires an activation of MAPK/ERK in mammals. ERK phosphorylation has been shown to occur in a variety of memory models and following different LTP paradigms in the hippocampus[20, 21]. It is now well established that ERK activation is via multiple upstream kinases, among which CaMKII is the major one[22].

One transcription factor, cAMP response element binding protein (CREB), is a nuclear target of many kinases[23]. Once phosphorylated, CREB appears to mediate the transduction of neuronal stimulation into gene expression, which is also a necessary component for hippocampus-dependent memory formation in mammals[24, 25].

Based on the above ideas, the present study was aimed to examine whether PGSF plays its cognition-enhancing effect through improvements of basic synaptic transmission in the DG and explore the underlying mechanisms.

Materials and methods

Materials

Anti-phospho-CaMKII antibody, anti-CaMKII antibody, anti-phospho-ERK antibody, anti-ERK antibody, and anti-rabbit IgG secondary antibody, anti-mouse IgG secondary antibody were purchased from Santa Cruz Biotechnology (Santa Cruz, CA, USA). Anti-phospho-CREB antibody, anti-CREB antibody, anti-phospho-NR2B antibody, and anti-NR2B antibody were obtained from Cell Signaling Biotechnology (Hertfordshire, UK). MK801 (a high-affinity NMDAR antagonist) and KN93 (an inhibitor of CaMKII) were obtained from Sigma. Enhanced chemiluminescent (ECL) substrate was from Pierce (Rockford, IL, USA). PGSF with purity greater than 98% was obtained from phytochemistry department in Institute of Materia Medica, Chinese Academy of Medical Sciences and Peking Union Medical College, Beijing, China, and dissolved in dimethyl sulfoxide (DMSO) to make stock solution at 0.1 mol/L and diluted with physiological saline before use.

Animals

Male Wistar rats (230–260 g) in this study were provided by the Experimental Animal Center of the Chinese Academy of Medical Sciences, Beijing, China. Rats were housed in a temperature- and light-control room (23±1 °C, 12 h light cycle) and had free access to food and water. All animals were handled in accordance with the standards established in the Guide for the Care and Use of Laboratory Animals published by the Institute of Laboratory Animal Resources of the National Research Council (United States) and approved by the Animal Care Committee of the Peking Union Medical College and the Chinese Academy of Medical Sciences (Beijing, China).

Electrophysiological assays

Surgical preparation

The animals were prepared as previously described[26, 27]. Briefly, rats were anesthetized with urethane carbamate (1.5 g/kg, ip) before being fixed on an SR-6N stereotaxic apparatus (Narishige Science Instrument, Japan). Three holes were sequentially drilled at 0.8 mm, 3.8 mm, and 7.5 mm posterior to the bregma and 1.8 mm, 2.5 mm, and 4.2 mm lateral to the mid-line for an outer guide cannula, a monopolar recording electrode, and a bipolar stimulating electrode, respectively. The cannula was placed into the lateral cerebral ventricle at a depth of 2.5–3.0 mm, the recording electrode was placed in the granular cell layer of DG at a depth of 3.0–3.5 mm, and the stimulating electrode was lowered into the perforant path (PP) to a depth of 3.0–3.5 mm. The synaptic responses were monitored by a VC-11 memory oscilloscope (Nihon Kohden, Japan). Once the locations of the cannula and electrodes were verified, they were kept in place for the whole experimental duration.

Measurement of evoked potentials

The population spike (PS) amplitude was employed to assess the excitation level of the granular cell population in the DG. An evoked response was generated in the DG granular cell layer by stimulating the PP at low frequency (0.033 Hz) with single constant current pulses (150 μs in duration) triggered by an SEN-7203 electrical stimulator (Nihon Kohden, Japan) through a SS-202J isolator (Nihon Kohden, Japan). After input/output curve determination, the baseline responses were evoked by a stimulus with an intensity to produce 20% of the maximal PS amplitude.

Intracerebroventricular (icv) drug delivery

Drugs or vehicle injections were delivered via a cannula in the lateral cerebral ventricle after 30 min of electrophysiological baseline measurement from the DG of the contralateral hemisphere. Injections were performed using a 5 μL volume over a 5 min period via a Hamilton syringe. The dose of PGSF was calculated based on the theoretical concentration that the drug would have in the brain (assuming a brain volume of approximately 2 mL). Thus, for an estimated brain concentration of PGSF at 1 μmol/L (equivalent to the dose of 2×10^{-3} μmol per rat), 5 μL of 0.4 mmol/L PGSF was injected and for the brain concentration of PGSF at 10 μmol/L (equivalent to the dose of 2×10^{-2} μmol per rat), 5 μL of 4 mmol/L PGSF was injected. Control rats were injected with 0.4% DMSO. For inhibitor experiments, MK801 and KN93 were dissolved in DMSO and diluted with physiological saline to give the desired final concentration (100 μmol/L). The final concentration of DMSO was 0.4%.

Western blotting analysis

After electrophysiological recording, hippocampus from the experimental rats was removed immediately and stored at -70 °C until use. Western blotting analysis was employed to detect p-NR2B, p-CaMKII, p-ERK, and p-CREB protein

levels in the hippocampus after LTP induction by 1 μmol/L PGSF and to examine the effect of MK801 on the change of p-CaMKII, and the effects of KN93 on p-ERK and p-CREB protein levels. Tissues of hippocampus were homogenized in a buffer of 150 mmol/L NaCl, 25 mmol/L Tris-HCl, 1 mmol/L EGTA, 1 mmol/L EDTA, pH 7.4, 1% Triton X-100, 1 mmol/L PMSF. Protein concentrations were measured with a BCA protein assay kit (Pierce). Samples were separated by a SDS-polyacrylamide gel electrophoresis (SDS-PAGE) and then transferred onto PVDF membranes (Millipore). The membranes were blocked with 3% BSA in Tris-buffered saline with 0.1% Tween 20 (TBS-T) for 2 h at room temperature, and then incubated at 4 °C overnight with primary antibodies (1:1000 dilutions) followed by species-appropriate horseradish peroxidase (HRP)-conjugated secondary antibody (1:5000 dilutions) for 2 h at room temperature. The immunoreactive bands were visualized using enhanced chemiluminescence (ECL) system (FUJIFILM, Tokyo, Japan). The density of each band was quantified by Gelpro 32 software.

Statistical analysis

All data were shown as the mean±SEM. Group differences of PS amplitude in the electrophysiological assays were evaluated using two-way analysis of variance (ANOVA). Group differences in the Western blotting assays were performed by one-way ANOVA. *P*-values of <0.05 were regarded as statistically significant.

Results

Effects of PGSF on basic synaptic transmission in the hippocampal DG of anesthetized rats

We examined the effects of PGSF (1 μmol/L and 10 μmol/L) on synaptic transmission in the hippocampal DG area of anesthetized rats. We stimulated the PP coming from entorhinal area and recorded the evoked PS in DG region of rat hippocampus. As shown in Figure 1, the baseline amplitude of the PS stabilized within the first 30 min in both the control and the PGSF groups; two-way ANOVA showed no significant difference between the control and PGSF groups [$F(2, 90)=0.03$, $P=0.971$], as well as the six time points [$F(5, 90)=1.999$, $P=0.086$]. Moreover, the PS amplitude did not fluctuate significantly for 60 min after vehicle (0.4% DMSO) administration. In contrast, after the injection of 1 μmol/L PGSF, the PS amplitude increased to 170%±15% of baseline within 5 min. At 15, 30, and 60 min, the PS amplitude increased to 180%±17%, 210%±22%, and 227%±27% of baseline, respectively. Furthermore, PS amplitude increased to 276%±30% of baseline within 5 min after 10 μmol/L PGSF application and at 15, 30, and 60 min, the PS amplitude increased to 312%±31%, 332%±43%, and 401%±36% of baseline, respectively. There was a significant main effect of the control and PGSF groups [$F(2, 180)=269.956$, $P<0.001$] (1 μmol/L PGSF group *vs* control, $P<0.001$; 10 μmol/L PGSF group *vs* control, $P<0.001$). The more than 200% increase of PS amplitude over baseline for longer than 30 min indicated the formation of PGSF-induced LTP in the hippocampal DG area *in vivo*.

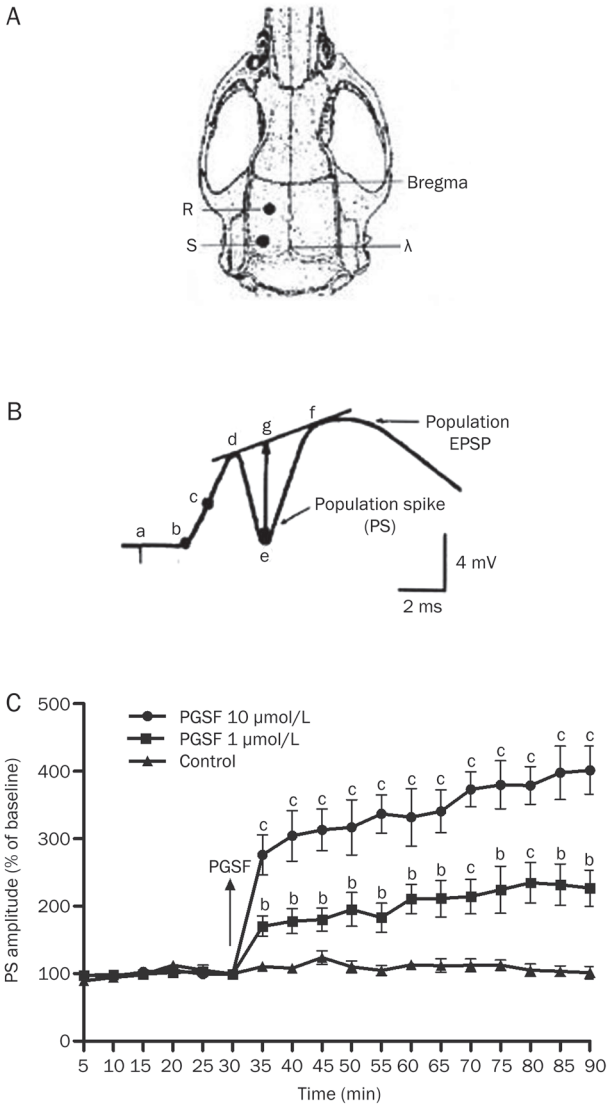

Figure 1. Effects of PGSF on basic synaptic transmission in the hippocampal DG of anesthetized rats. (A) Anatomical diagram of a rat skull. The points R and S represent the approximate locations of the recording electrode and the stimulating electrode, respectively. (B) Measurement of PS amplitude. a, stimulus artifact; b, initial point of excitatory postsynaptic potential (EPSP); c, middle point of bd; d–f, end points of the peaks; length of g-e, amplitude of PS. (C) Time-course plots of perforant path-evoked PS of the control group and PGSF groups. The baseline was recorded from 30 min before administration. At 30 min, 5 μL 0.4 mmol/L PGSF or 5 μL 4 mmol/L PGSF (icv, final concentration was 1 μmol/L or 10 μmol/L) was injected in the test subjects, whereas 0.4% DMSO was injected in control animals. The arrow shows the time point of icv injection. All values are presented as the mean±SEM of 6 rats. $^bP<0.05$, $^cP<0.01$ *vs* control group, two-way ANOVA.

Effects of PGSF on the phosphorylation of NR2B, CaMKII, ERK, and CREB in hippocampus of rats after PGSF-induced LTP

In order to elucidate the molecular mechanisms underlying the apparent facilitation of long-term potentiation induced by PGSF in hippocampus of adult rats, we detected the phosphorylation changes of several proteins which are related

closely to LTP. First, the level of p-NR2B was evaluated with Western blotting at different time points after LTP induction by 1 μmol/L PGSF. Results showed that p-NR2B increased at 5 min (1.59-fold increase, n=6, P<0.05) peaked at 15min (2.65-fold increase, n=6, P<0.01) and maintained for 60 min (1.62-fold increase, n=6, P<0.05) after LTP induction (Figure 2A, 2B). Next, we analysed the phosphorylation state of CaMKII at distinct time points. We found that p-CaMKII strongly increased at 5 min (2.89-fold increase, n=6, P<0.01). The increased phosphorylation peaked at 15 min (3.78-fold increase, n=6, P<0.01) and was sustained for at least 60 min (2.56-fold increase, n=6, P<0.01) after LTP induction (Figure 2C, 2D). Similar to the expression of p-CaMKII, the increased p-ERK was observed at 5 min after LTP induction (1.78-fold increase, n=6, P<0.01), peaked at 30min (2.43-fold increase, n=6, P<0.01) and persisted for at least 60 min (1.79-fold increase, n=6, P<0.01) (Figure 2E, 2F). Finally, CREB phosphorylation level was detected. Results identified a strong increment at 30 min (1.83-fold increase, n=6, P<0.01) and remained to 60 min (1.59-fold increase, n=6, P<0.01) after LTP induction (Figure 2G, 2H).

Effects of MK801 and KN93 on LTP induced by PGSF

Because the above studies have found that the NR2B and CaMKII were activated after induction of the hippocampal LTP by PGSF, we next evaluated the role of NMDAR and CaMKII in the induction of PGSF-induced LTP. After establishing a stable baseline for 30 min, MK801 was applied 30 min before PGSF injection, two-way ANOVA showed no significant difference between the control and MK801 groups [F(2, 90)=2.158, P=0.121], as well as the six time points [F(5, 90)=0.330, P=0.894] (Figure 3A). The PS amplitude of MK801-treated group decreased to 96%±9% of baseline from 177%±16% in the PGSF group at 5 min after PGSF delivering. The PS amplitude also remained near baseline levels at the other time points. There was a significant main effect of the three groups [F(2, 360)=209.617, P<0.001] (MK801-treated group *vs* PGSF group, P<0.001; *vs* control, P>0.05), indicating that the induction of PGSF-induced LTP was completely blocked by pre-treatment with MK801.

In the same way, KN93 was applied 30 min before PGSF injection, two-way ANOVA showed no significant difference between the control and the KN93 groups [F(2, 90)=1.83, P=0.166], as well as the six time points [F(5, 90)=0.36, P=0.961] (Figure 3B). The PS amplitude decreased to 112%±8% of baseline from 177%±16% in the PGSF group at 5 min after PGSF delivering. The PS amplitude also remained near baseline levels at the other time points. There was a significant main effect of the three groups [F(2, 360)=174.773, P<0.001] (KN93-treated group *vs* PGSF group, P<0.001; *vs* control, P>0.05), indicating that the induction of PGSF-induced LTP was completely blocked by pre-treatment with KN93.

Effect of MK801 on phosphorylation of CaMKII induced by PGSF

It is well-known that NMDAR is a key receptor for CaMKII activation, and based on the results we have found that activations of the NMDAR and CaMKII are required for PGSF-

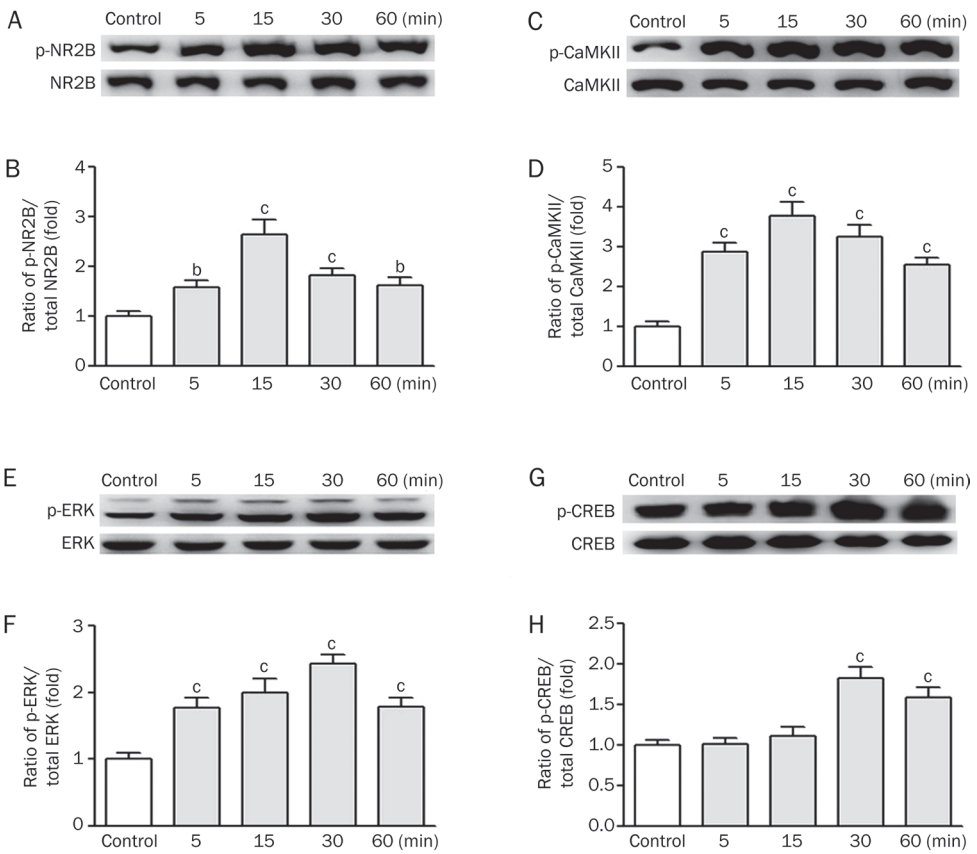

Figure 2. Effects of PGSF on the phosphorylation of NR2B, CaMKII, ERK, and CREB in hippocampus of rats after LTP induction. Representative Western blotting of phosphorylated and total forms of NR2B, CaMKII, ERK, and CREB (A, C, E, and G). The histogram showed the densitometric quantitation of the immunoreactive bands at different times after LTP induction (B, D, F, and H). The phosphorylation levels of NR2B, CaMKII, ERK, and CREB were normalized by total NR2B, CaMKII, ERK, and CREB and expressed as fold changes of their respective controls (mean±SEM; n=6). ^{b}P<0.05, ^{c}P<0.01 *vs* control value, one-way ANOVA.

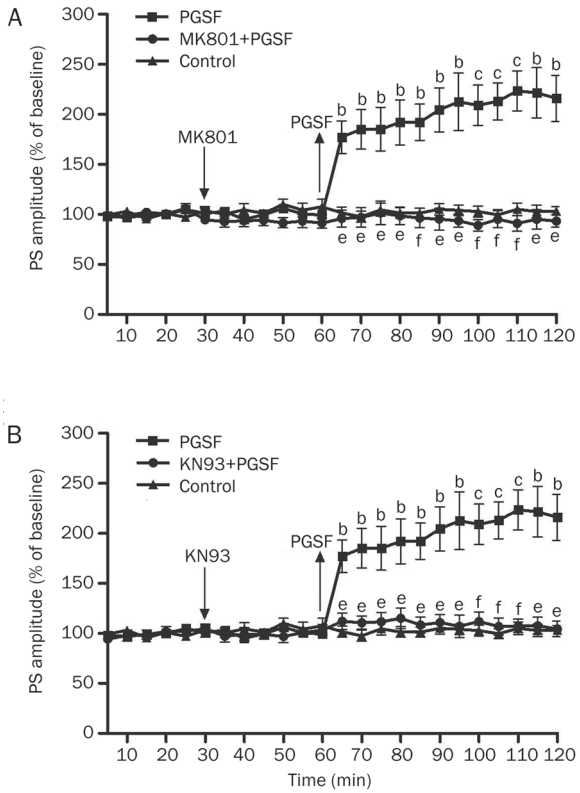

Figure 3. Effects of MK-801 and KN93 on LTP induced by PGSF. MK-801(A) or KN93 (B) was applied at 30 min prior to PGSF application. Downward arrows indicate time points at which MK-801 or KN93 was applied and upward arrows indicate time points when PGSF was delivered. MK-801 or KN93 completely abolished the induction of LTP induced by PGSF. All values are expressed as the mean±SEM of 6 rats, $^{b}P<0.05$, $^{c}P<0.01$ *vs* control. $^{e}P<0.05$, $^{f}P<0.01$ *vs* PGSF group, two-way ANOVA.

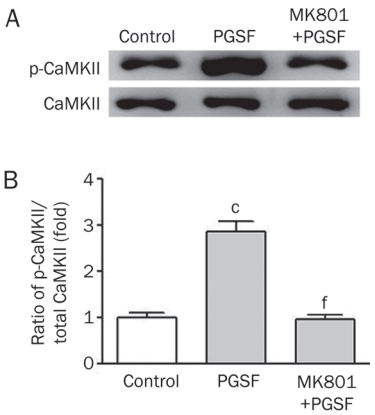

Figure 4. Effects of MK-801 on phosphorylation of CaMKII induced by PGSF. Representative Western blotting of phosphorylated and total forms of CaMKII (A). The histogram showed the densitometric quantitation of the immunoreactive bands (B). P-CaMKII levels were normalized by total CaMKII levels and expressed as fold changes of the control (mean±SEM; $n=6$). $^{c}P<0.01$ *vs* control, $^{f}P<0.01$ *vs* PGSF group, one-way ANOVA.

induced potentiation. Therefore, we investigated whether the enhancement of phosphorylation of CaMKII induced by PGSF was dependent on the NMDAR.

The above results indicated that p-CaMKII was upregulated significantly 5 min after PGSF application, so we observed the effect of MK801 on p-CaMKII at this time point. The result showed that the phosphorylation of CaMKII was decreased from 2.86 fold to 0.96 fold in the presence of MK801, compared with the PGSF-treated group (Figure 4A, 4B), indicating that CaMKII activation induced by PGSF was totally dependent upon the NMDAR.

Effects of KN93 on phosphorylation of ERK and CREB induced by PGSF

Given that the ERK and CREB were also activated after PGSF-induced potentiation, we next evaluated the signaling pathway for ERK and CREB activation induced by PGSF. It is well-known that CaMKII is located upstream of ERK. Therefore, we explored whether the enhancement of p-ERK induced by PGSF was dependent on CaMKII. In the above results, p-ERK was upregulated significantly 5 min after PGSF application, so we observed the effect of KN93 on p-ERK at this time point. The result showed that the phosphorylation of ERK was decreased from 1.68 fold to 1.20 fold in the presence of KN93, compared with the PGSF-treated group (Figure 5A, 5B). The phosphorylation level of ERK was partly, but significantly reduced by pretreatment of KN93, indicating that the activation of ERK is partially dependent on CaMKII.

In the meanwhile, we tested whether CREB was also CaMKII dependent. As p-CREB was upregulated significantly 30 min after PGSF application, we observed the effect of KN93 on p-CREB at this time point. The result showed that pretreatment of KN93 attenuated the phosphorylation of CREB from 1.77 fold to 1.28 fold, compared with the PGSF-treated group (Figure 5C, 5D), suggesting that the activation of CREB is also partially dependent on CaMKII.

Discussion

In the present study, we present the first evidence that PGSF could facilitate LTP in the hippocampal DG. We found that basic synaptic transmission was potentiated within 5 min and LTP could be induced by icv injection of PGSF at the concentration of 1 μmol/L and 10 μmol/L. LTP induced by PGSF lasted for at least 60 min. This action was totally dependent on NMDAR and CaMKII. MAPK/ERK and CREB were the downstream pathway of CaMKII activation. PGSF-induced potentiation might be modulated via enhanced tyrosine phosphorylation of NR2B subunit of NMDAR.

As described in Results, MK801 strongly abolished the effect of PGSF on the induction of LTP[28]. This is in agreement with previous studies that activation of the NMDAR was essential for the expression of LTP in the DG[29]. Thus, particular attention has been paid to NMDAR and its downstream factors.

First, we found that PGSF time-dependently increased the tyrosine phosphorylation of NR2B subunit after LTP induction, which is consistent with the reports that phosphorylation of NR2B subunit was increased with LTP induction[30, 31]. It is

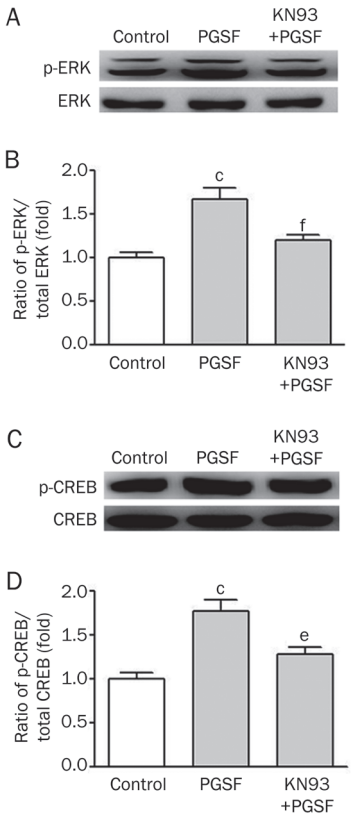

Figure 5. Effects of KN93 on phosphorylation of ERK and CREB induced by PGSF. Representative Western blotting of phosphorylated and total forms of ERK and CREB (A, C). The histogram showed the densitometric quantitation of the immunoreactive bands (B, D). P-ERK and p-CREB levels were normalized by total ERK and CREB levels and expressed as fold changes of their respective controls. Means±SEM. n=6. ^{c}P<0.01 *vs* control, ^{e}P<0.05, ^{f}P<0.01 *vs* PGSF group, one-way ANOVA.

well documented that tyrosine phosphorylation of NR2B is crucial for the induction of LTP in various types of synapses[32]. Tyrosine phosphorylation of NR2B can stabilize NMDAR on the cell surface and thereby increases the NMDAR responses. It can upregulate NMDAR current and prevent the removal of signaling molecules from the NMDAR complex[33–35]. Therefore, the action of NMDAR could be facilitated via the enhanced phosphorylation of NR2B induced by PGSF.

A great deal of evidence has led to the hypotheses that CaMKII is a mnemonic molecule. It has been obtained that the CaMKII plays an important role in LTP[36, 37]. In this study, we found that the phosphorylation of CaMKII strongly increased at 5 min after potentiation, peaked at 15 min, and was sustained for at least 60 min after LTP induced by PGSF. In addition, as described in Results, the facilitating effect of PGSF on the NMDAR-mediated LTP induction disappeared after pretreatment with CaMKII blocker KN93, thus indicating that the action of CaMKII was indispensible for PGSF-induced LTP. This strengthens our confidence that CaMKII plays a key role in PGSF-induced LTP. Furthermore, the NMDAR inhibitor MK801 perfectly prevented the upregulation of CaMKII phosphorylation induced by PGSF *in vivo*, suggesting that CaMKII phosphorylation was mediated through NMDAR activation. These results indicated that PGSF induces the long-lasting potentiation of synaptic efficacy, which may exert a cognitive effect in the adult rat brain, through the NMDAR followed by CaMKII activation.

It is well established that MAPK/ERK pathway is an essential component of NMDAR signal transduction controlling the neuronal synaptic plasticity[38]. In our experimental conditions, we found a rapid and strong increment in ERK phosphorylation after LTP induction, which lasted for at least 60 min. The time course was parallel with that of CaMKII activation. According to the time of reaching the maximum activation of CaMKII and ERK, we speculated that CaMKII was one of the upstream kinases of ERK activated by PGSF. Therefore, KN93 was pretreated before PGSF was applied. The results demonstrated that the activation of ERK was partially inhibited by KN93, suggesting that ERK was the downstream signaling molecule of CaMKII activation, which was consistent with other reports[39].

CREB is a key molecular involved in synaptic plasticity and memory[40]. CRE-mediated transcription is stimulated in the hippocampus during hippocampus dependent memory formation[41]. In the current study, CREB phosphorylation was increased 30 min after LTP induction. Moreover, we found that CREB phosphorylation was partially blocked with KN93 *in vivo*, suggesting that the CaMKII pathway at least in part mediated the activation of CREB induced by PGSF. The striking effect of CaMKII on the activation of ERK and CREB strongly supports that CaMKII is a critical molecule of the signal cascade responsible for synaptic potentiation induced by PGSF.

In addition, a close association between facilitated hippocampal LTP and enhanced learning and memory has been demonstrated[42, 43]. Therefore, PGSF probably enhanced learning and memory function through improvements of basic synaptic transmission in hippocampal DG. PGSF has tremendous potential for the development of therapeutic drugs that can be used to treat cognitive deficit diseases.

Acknowledgements

This work was supported by the National Natural Science Foundation of China (No 30973887, 81073078, 81102831, and Key Program No U832008), and Major Projects of National Science and Technology of China (No 2012ZX09301002-004).

Author contribution

Feng SUN designed the study, performed the research and wrote the paper; Jian-dong SUN provided assistance in experiment design and revised the paper; Ning HAN performed partial research; Yu-he YUAN assisted in experiment design; Dong-ming ZHANG and Chuang-jun LI extracted the PGSF; and Nai-hong CHEN designed the research and revised the paper.

References

1 Chung IW, Moore NA, Oh WK, O'Neill MF, Ahn JS, Park JB, *et al*. Behavioural pharmacology of polygalasaponins indicates potential antipsychotic efficacy. Pharmacol Biochem Behav 2002; 71: 191–5.
2 Peng W, Xu S. Antitussive and expectorant effects of four saponins isolated from *Polygala tenuifolia* wild. Chin Pharm J 1998; 3: 491.
3 Zhang D, Miyase T, Kuroyanagi M, Umehara K, Ueno A. Studies on the constituents of *Polygala japonica* Houtt I. Structures of polygalasaponins I–X. Chem Pharm Bull 1995; 43: 115–20.
4 Wei-dong ZHANG, Ting-zhao-LI, Chuan ZHANG, inventors; Zheng Dan Corporation, assignee. Polygalasaponin compounds and aglycones, total saponins and total aglycones and their application in medicine. China patent CN1651453A. 2005 Aug 10.
5 Xue W, Hu JF, Yuan YH, Sun JD, Li BY, Zhang DM, *et al*. Polygalasaponin XXXII from Polygala tenuifolia root improves hippocampal-dependent learning and memory. Acta Pharmacol Sin 2009, 30: 1211–9.
6 Citri A, Malenka RC. Synaptic plasticity: multiple forms, functions, and mechanisms. Neuropsychopharmacology 2008, 33: 18–41.
7 Morris RG. Elements of a neurobiological theory of hippocampal function: the role of synaptic plasticity, synaptic tagging and schemas. Eur J Neurosci 2006, 23: 2829–46.
8 Kesner RP, Hopkins RO. Mnemonic functions of the hippocampus: a comparison between animals and humans. Biol Psychol 2006; 73: 3–18.
9 Kesner RP. A behavioral analysis of dentate gyrus function. Prog Brain Res 2007; 163: 567–76.
10 Trommer BL, Kennelly JJ, Colley PA, Overstreet LS, Slater NT, Pasternak JF. AP5 blocks LTP in developing rat dentate gyrus and unmasks LTD. Exp Neurol 1995; 131: 83–92.
11 Lau LF, Huganir RL. Differential tyrosine phosphorylation of N-methyl-D-aspartate receptor subunits. J Biol Chem 1995; 270: 20036–41.
12 Rosenblum K, Berman DE, Hazvi S, Lamprecht R, Dudai Y. NMDA receptor and the tyrosine phosphorylation of its 2B subunit in taste learning in the rat insular cortex. J Neurosci 1997; 17: 5129–35.
13 Chin D, Means AR. Calmodulin: a prototypical calcium sensor. Trends Cell Biol 2000; 10: 322–8.
14 Hudmon A, Schulman H. Structure-function of the multifunctional Ca^{2+}/calmodulin-dependent protein kinase II. Biochem J 2002; 364: 593–611.
15 Suzuki S, Okumura-Noji K, Tanaka R, Tana T. Rapid translocation of cytosolic Ca^{2+}/Calmodulin-dependent protein kinase II into postsynaptic density after decapitation. J Neurochem 1994; 63: 1529–37.
16 Giese KP, Fedorov NB, Filipkowski RK, Silva AJ. Autophosphorylation at thr286 of the alpha calcium-calmodulin kinaseII in LTP and learning. Science 1998; 279: 870–3.
17 Coultrap SJ, Vest RS, Ashpole NM, Hudmon A, Bayer KU. CaMKII in cerebral ischemia. Acta Pharmacol Sin 2011; 32: 861–72.
18 Sanhueza M, McIntyre CC, Lisman JE. Reversal of synaptic memory by Ca^{2+}/calmodulin-dependent protein kinase II inhibitor. J Neurosci 2007; 27: 5190–9.
19 Lledo PM, Hjelmstad GO, Mukherji S, Soderling TR, Malenka RC, Nicoll RA. Calcium/calmodulin-dependent kinase II and long-term potentiation enhance synaptic transmission by the same mechanism. Proc Natl Acad Sci U S A 1995; 92: 11175–9.
20 Kelleher RJ 3rd, Govindarajan A, Jung HY, Kang H, Tonegawa S. Translational control by MAPK signaling in long-term synaptic plasticity and memory. Cell 2004; 116: 467–79.
21 Lynch MA. Long-term potentiation and memory. Physiol Rev 2004; 84: 87–136.
22 Girault JA, Valjent E, Caboche J, Hervé D. ERK2: a logical AND gate critical for drug-induced plasticity? Curr Opin Pharmacol 2007; 7: 77–85.
23 Wu GY, Deisseroth K, Tsien RW. Activity-dependent CREB phosphorylation: convergence of a fast, sensitive calmodulin kinase pathway and a slow, less-sensitive mitogen-activated protein kinase pathway. Proc Natl Acad Sci U S A 2001; 98: 2808–13.
24 Pittenger C, Huang YY, Paletzki RF, Bourtchouladze R, Scanlin H, Vronskaya S, *et al*. Reversible inhibition of CREB/ATF transcription factors in region CA1 of the dorsal hippocampus disrupts hippocampus-dependent spatial memory. Neuron 2002; 34: 447–62.
25 Bourtchuladze R, Frenguelli B, Blendy J, Cioffi D, Schutz G, Silva AJ. Deficient long-term memory in mice with a targeted mutation of the cAMP-responsive element-binding protein. Cell 1994; 79: 59–68.
26 Liu SL, Zhang JT. Effects of naloxone on l-clausenamide-induced long-term potentiation in dentate gyrus of anesthetized rats. Zhongguo Yao Li Xue Bao 1999; 20: 112–6.
27 Wang XY, Zhang JT. NO mediates ginsenoside Rg1-induced long-term potentiation in anesthetized rats. Acta Pharmacol Sin 2001; 22: 1099–102.
28 Lu W. Blocking NMDA receptor at rest: a possible alleviation of depression. Acta Pharmacol Sin 2011; 32: 1087–8.
29 Davis S, Butcher SP, Morris RG. The NMDA receptor antagonist D-2-amino-5-phosphonopentanoate (D-AP5) impairs spatial learning and LTP *in vivo* at intracerebral concentrations comparable to those that block LTP *in vitro*. J Neurosci 1992; 12: 21–34.
30 Rostas JA, Brent VA, Voss K, Errington ML, Bliss TV, Gurd JW. Enhanced tyrosine phosphorylation of the 2B subunit of the N-methyl-Daspartate receptor in long-term potentiation. Proc Natl Acad Sci U S A 1996; 93: 10452–6.
31 Grosshans DR, Clayton DA, Coultrap SJ, Browning MD. Proteomic analysis of NMDA receptor-adhesion protein signaling complexes. Nat Neurosci 2000; 3: 661–9.
32 O'Dell TJ, Kandel ER, Grant SG. Long-term potentiation in the hippocampus is blocked by tyrosine kinase inhibitors. Nature 1991; 353: 558–60.
33 Grosshans DR, Clayton DA, Coultrap SJ, Browning MD. LTP leads to rapid surface expression of NMDA but not AMPA receptors in adult rat CA1. Nat Neurosci 2002; 5: 27–33.
34 Salter MW, Kalia LV. Src kinases: a hub for NMDA receptor regulation. Nat Rev Neurosci 2004; 5: 317–28.
35 Yu XM, Salter MW. Src, a molecular switch governing gain control of synaptic transmission mediated by N-methyl-D-aspartate receptors. Proc Natl Acad Sci U S A 1999; 96: 7697–704.
36 Lisman J. The CaM kinase II hypothesis for the storage of synaptic memory. Trends Neurosci 1994; 17: 406–12.
37 Wang JH, Kelly PT. Postsynaptic injection of Ca^{2+}/CaM induces synaptic potentiation requiring CaMKII and PKC activity. Neuron 1995; 15: 443–52.
38 Thomas GM, Huganir RL. MAPK cascade signalling and synaptic plasticity. Nat Rev Neurosci 2004; 5: 173–83.
39 Hu JF, Xue W, Ning N, Yuan YH, Zhang JT, Chen NH. Ginsenoside Rg1 activated CaMKIIalpha mediated extracellular signal-regulated kinase/mitogen activated protein kinase signaling pathway. Acta Pharmacol Sin 2008; 29: 1119–26.
40 Sekeres MJ, Neve RL, Frankland PW, Josselyn SA. Dorsal hippocampal CREB is both necessary and sufficient for spatial memory. Learn Mem 2010; 17: 280–3.
41 Impey S, Mark M, Villacres EC, Poser S, Chavkin C, Storm DR. Induction of CRE-mediated gene expression by stimuli that generate long-lasting LTP in area CA1 of the hippocampus. Neuron 1996; 16: 973–82.
42 Silva AJ, Paylor R, Wehner JM, Tonegawa S. Impaired spatial learning in alpha-calcium-calmodulin kinase II mutant mice. Science 1992; 257: 206–11.
43 Tsien JZ, Huerta PT, Tonegawa S. The essential role of hippocampal CA1 NMDA receptor-dependent synaptic plastisty in spatial memory. Cell 1996; 87: 1327–38.

Acta Pharmacologica Sinica (2012) 33: 438–444
 1671-4083/12 $32.00
www.nature.com/aps

Original Article

Ginsenoside Rb1 selectively inhibits the activity of L-type voltage-gated calcium channels in cultured rat hippocampal neurons

Zhi-ying LIN[1, #], Li-min CHEN[1, #], Jing ZHANG[1], Xiao-dong PAN[1, 2], Yuan-gui ZHU[1], Qin-yong YE[1, 2], Hua-pin HUANG[1, 2], Xiao-chun CHEN[1, 2, *]

[1]*Fujian Institute of Geriatrics,* [2]*Department of Neurology, the Affiliated Union Hospital of Fujian Medical University, Fuzhou 350001, China*

Aim: To investigate the effect of ginsenoside Rb1 on voltage-gated calcium currents in cultured rat hippocampal neurons and the modulatory mechanism.
Methods: Cultured hippocampal neurons were prepared from Sprague Dawley rat embryos. Whole-cell configuration of the patch-clamp technique was used to record the voltage-gated calcium currents (VGCCs) from the hippocampal neurons, and the effect of Rb1 was examined.
Results: Rb1 (2–100 μmol/L) inhibited VGCCs in a concentration-dependent manner, and the current was mostly recovered upon wash-out. The specific L-type Ca^{2+} channel inhibitor nifedipine (10 μmol/L) occluded Rb1-induced inhibition on VGCCs. Neither the selective N-type Ca^{2+} channel blocker ω-conotoxin-GVIA (1 μmol/L), nor the selective P/Q-type Ca^{2+} channel blocker ω-agatoxin IVA (30 nmol/L) diminished Rb1-sensitive VGCCs. Rb1 induced a leftward shift of the steady-state inactivation curve of I_{Ca} to a negative potential without affecting its activation kinetics or reversal potential in the *I–V* curve. The inhibitory effect of Rb1 was neither abolished by the adenylyl cyclase activator forskolin (10 μmol/L), nor by the PKA inhibitor H-89 (10 μmol/L).
Conclusion: Ginsenoside Rb1 selectively inhibits the activity of L-type voltage-gated calcium channels, without affecting the N-type or P/Q-type Ca^{2+} channels in hippocampal neurons. cAMP-PKA signaling pathway is not involved in this effect.

Keywords: ginsenoside Rb1; L-type Ca^{2+} channel; nifedipine; ω-conotoxin-GVIA; ω-agatoxin IVA; patch-clamp technique; hippocampus; cAMP-PKA signaling pathway

Acta Pharmacologica Sinica (2012) 33: 438–444; doi: 10.1038/aps.2011.181; published online 12 Mar 2012

Introduction

Ca^{2+}, an important regulator of neuronal activity, controls membrane excitability, triggers the release of neurotransmitters and mediates activity-dependent changes in gene expression. Voltage-gated Ca^{2+} channels play a key role in the control of free cytosolic Ca^{2+} [1]. According to their pharmacological and electrophysiological properties, at least 5 distinct types of voltage-gated Ca^{2+} channels have been identified and designated as L, N, P/Q, R, and T[2, 3]. L-, N-, and P/Q-type Ca^{2+} channels are pharmacologically identified and characterized by their specific blockers. Nifedipine is an L-type Ca^{2+} channel inhibitor, ω-conotoxin GVIA is an N-type Ca^{2+} channel inhibitor, and ω-agatoxin IVA is a P/Q-type Ca^{2+} channel inhibitor[4–9]. Because the elevation of intracellular Ca^{2+} levels ($[Ca^{2+}]_i$) caused by the excessive stimulation of Ca^{2+} channels plays a key role in the excitotoxic damage of neurons, agents blocking the elevation of $[Ca^{2+}]_i$ by regulating Ca^{2+} channels might have neuroprotective effects[10–12].

Ginseng, the root of *Panax ginseng* CA Meyer, has been used worldwide as an herbal medicine for the alleviation of many ailments, particularly those associated with aging and memory deterioration. Ginsenoside Rb1, a protopanaxadiol type saponin, is one of the most important active compounds of ginseng. Recently, ginsenoside Rb1 has been reported to effectively protect neurons from glutamate-induced toxicity and β-amyloid (Aβ)-induced toxicity by reducing intracellular Ca^{2+} levels[13–18]. However, how Rb1 decreases $[Ca^{2+}]_i$ by regulating Ca^{2+} channels remains unclear. Although studies have found that Rb1 inhibits voltage-gated Ca^{2+} channels in other cell types and that its mechanisms of action vary by cell type, there have been no research studies to date that have inves-

# These authors contributed equally to this paper.
* To whom correspondence should be addressed.
E-mail chenxiaochun998@gmail.com
Received 2011-09-27 Accepted 2011-11-28

tigated the action of ginsenoside Rb1 on voltage-gated Ca^{2+} channels in hippocampal neurons. In this paper, we analyzed the effect of ginsenoside Rb1 on voltage-gated Ca^{2+} channels in hippocampal neurons and the possible mechanism for this modulation.

Materials and methods

Materials

Ginsenoside Rb1 was obtained from the Department of Organic Chemistry at Jilin University (Changchun, China) with a purity >98%. Stock solutions of the Ca^{2+} channel antagonists, ω-conotoxin GVIA (Alomone Labs, UK), nifedipine (Sigma, UK) ω-agatoxin IVA (Alomone Labs, UK) and adenylyl cyclase agonist Forskolin (Sigma, UK), were prepared with the appropriate amounts of deionized water or dimethyl sulfoxide (DMSO) and frozen at -20 °C before appropriate dilution in the recording medium. H-89 was dissolved in the pipette solution (described below) and stored at -20 °C. After the whole-cell configuration was obtained, H-89 was dialyzed into the cell through the pipette.

Hippocampal neuron cultures

Chemical media and culture media were obtained from Sigma unless otherwise noted. The care and use of animals followed the guidelines of the Shanghai Institutes for Biological Sciences Animal Research Advisory Committee. The hippocampal neuron cultures were prepared as described previously[19] with some modifications. Briefly, whole brains were isolated from 18-day-old SD rat embryos, and the hippocampi were dissected and treated with 0.125% trypsin at 37 °C for 12 min. The cells were suspended with Dulbecco's Modified Eagle's Medium (DMEM) (GIBCO) containing 10% fetal bovine serum (HyClone, Logan, UT, USA) and 10% F-12 (GIBCO) and were plated at a density of 60 000 cells/mL on poly *D*-lysine-coated 35 mm dishes (Costar). Twenty-four hours after plating, half of the medium was changed to serum-free Neurobasal (NB) medium with 2% B27 supplement (GIBCO) and 1% glutamine. Thereafter, half of the changed medium was replaced twice a week with NB medium containing 2% B27 supplement and 0.25% glutamine. After 7 d *in vitro*, glial cell proliferation was inhibited by exposure to 2–4 mmol/L cytosine arabinoside. All the recordings were made with cells between d 6 and 8.

Electrophysiological recordings

Single patch recordings of Ca^{2+} channels from cultured hippocampal neurons at 6–8 d *in vitro* were made at room temperature using an EPC-9 patch-clamp amplifier and its corresponding Patchmaster software (Heka Electroniks, Germany) or an Axopatch-200B amplifier (Axon Instruments) with pCLAMP acquisition software. The gain was set to 1, filtered at 1 kHz, stored on videotape after digitization with a PCM processor, and displayed with a thermal pen recorder. The membrane capacitance and series resistance compensation were optimized.

Patch pipettes were fabricated from borosilicate glass capillaries (outer diameter 1.2 mm, inner diameter 0.69 mm, length 7.5 cm; B-120-69-15, Sutter Instruments) on a horizontal puller (Sutter Instruments). The microelectrodes had tip diameters of 2–3 μm and resistances of 3–6 MΩ. The pipettes were filled with an intracellular solution containing 80 mmol/L Cs-methanesulfonate, 20 mmol/L tetraethylammonium chloride (TEA-Cl), 1 mmol/L $CaCl_2$, 5 mmol/L $MgCl_2$, 11 mmol/L ethylene glycole-bis-(2-aminoethyl)-tetraacetic acid (EGTA), 10 mmol/L N-2-hydroxyethylpiperazine-N-2-ethanesulfonic acid (HEPES), and 10 mmol/L Na_2ATP. The chemicals were obtained from Sigma. CsOH was used to adjust the pH to 7.2–7.3. The osmolarity of the pipette solution was adjusted to 300 mOsm with sucrose. As suggested by Smirnov[20], the replacement of 1.5 mmol/L Ca^{2+} with 5 mmol/L Ba^{2+} was used to augment the amplitude of the inward current through Ca^{2+} channels. The potential dependency of activation and inactivation with 5 mmol/L Ba^{2+} was very similar to the results observed in 1.5 mmol/L Ca^{2+}. To isolate the Ba^{2+} current (I_{Ba}), the following reagents were used for the external solution: 115 mmol/L choline-Cl, 25 mmol/L TEA-Cl, 5 mmol/L 4-aminopyridine (4-AP), 5 mmol/L $BaCl_2$, 10 mmol/L glucose, 10 mmol/L HEPES, and 0.0005 mmol/L tetrodotoxin (TTX). Tris was used to adjust the pH to 7.4. The osmolarity of the extracellular solution was adjusted to 300 mOsm with sucrose. 4-AP and TEA were used to eliminate outward K^+ currents. TTX was used to eliminate inward Na^+ currents.

We recorded the voltage-gated calcium channel Ba^{2+} current (I_{Ba}) and used the following stimulating programs: an activation procedure and a drug application program. For the activation procedure, the cells were held at a potential of -60 mV and depolarized to potentials ranging from -70 mV to +70 mV with 10 mV as a step for a duration of 150 ms, and the steps were repeated every 10 s. For the drug application program, the cells were held at a potential of -60 mV and depolarized to 0 mV (0–+20 mV) for a duration of 200 ms, and the steps were repeated every 10 s.

Experimental drug application and treatment

The "U-tube" solution exchange method[21, 22] was used to apply the drugs. The whole cell measurements were initiated 5 min after break-in. Little run-down was observed during the 15 min necessary to collect the data. The current amplitudes of the cell before and after the experiment and the current densities of the cells of the different groups were compared.

Analysis of the electrophysiological recordings

The current recordings were analyzed using Clampfit 8.0 software (Axon, USA). Further analyses were performed using Microsoft Excel 2003 and Microcal Origin 8.0. All the data were described as the mean±the standard error of the mean. All the current recordings were normalized according to the whole cell capacitance to give the current density. A repeated measures ANOVA with Tukey-Kramer's post-test was used to compare the differences among entire current-voltage (I–V) relationships, and an unpaired Student's *t*-test was used to compare points on different curves that were activated by stepping to the same potential. *P* values less than 0.05 were

considered significant. The peak current was measured as the maximal current observed during the depolarizing step.

The calcium current steady-state activation curve was fitted to a Boltzmann equation of the following form:

$$I/I_{max}=1/\{1+\exp[(V-V_{1/2})/k]\}$$

where I is the voltage-dependent current amplitude, V is the membrane potential for activation, $V_{1/2}$ is the voltage at which activation is half maximal, and k is the slope factor.

Results

Voltage-gated calcium channel currents in hippocampal neurons

We recorded the whole-cell membrane currents from the somatic region of the neurons (Figure 1A) and identified a potent Ca^{2+} channel antagonist by its sensitivity to cadmium. We successively discriminated N-, P/Q-, and L-type Ca^{2+} channels by their specific blockers. ω-conotoxin GVIA and ω-agatoxin IVA showed irreversible blocking effects, while nifedipine exerted a partially reversible blocking effect (Figure 1B).

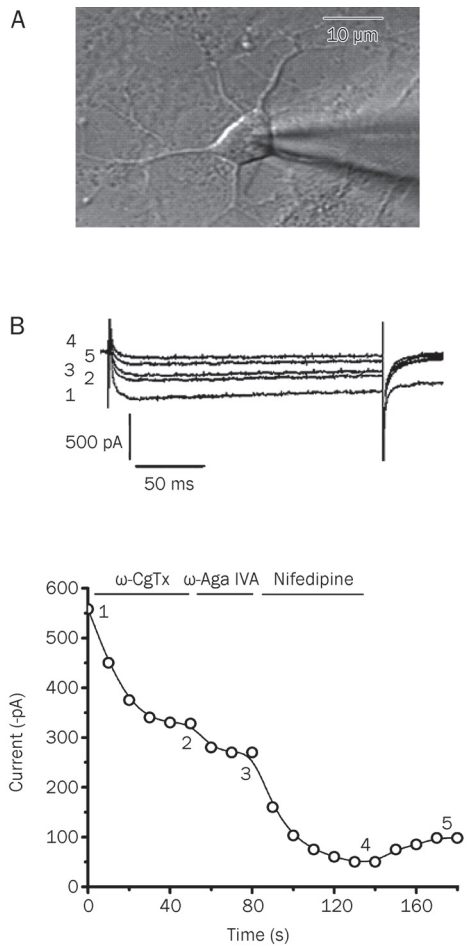

Figure 1. (A) Phase-contrast image showing a single patch recording from 7-d cultured hippocampal neurons for the recording of the VGCCs. Scale bar, 10 μm. (B) Pharmacological separation of the VGCC subtypes in hippocampal neurons. Upper panel, inward Ca^{2+} channel Ba^{2+} currents evoked by pulses from -60 mV to 0 mV at the times indicated in the lower panel. Lower panel, time course of effects of ω-conotoxin GVIA (1 μmol/L), ω-agatoxin IVA (30 nmol/L) and nifedipine (10 μmol/L) on the Ba^{2+} current amplitude.

Effect of ginsenoside Rb1 on VGCCs in hippocampal neurons

The method of extracellular micro-perfusion was used to study the effects of Rb1 on VGCCs. In these experiments with Rb1 treatment, only the peak currents were selected for comparison, and the current was evoked by a pulse of 200 ms duration from -60 mV to 0 mV (0–+20 mV). The inhibition rate of the I_{Ba} peak current was calculated as follows: [(maximum current value before administration – maximum current value after administration)/maximum current value before administration×100%]. The control group was treated with the extracellular solution, and the experimental groups were treated with 1, 2, 5, 10, and 100 μmol/L Rb1. Both the control group and the 1 μmol/L Rb1 group showed no inhibitory effects on the I_{Ba} (Figure 2A, 2B). However, the other experimental groups with 2, 5, 10, and 100 μmol/L Rb1 demonstrated inhibitory effects on the $I_{Ba.}$ The inhibition rates were 2%±0.87% (n=6), 5%±1.78% (n=4), 20%±3.96% (n=9), and 40%±6.71% (n=5), respectively. The I_{Ba} peak current inhibition rate of each group was significantly higher than that of the previous dose group (P<0.01) (Table 1). The effects of Rb1 on the I_{Ba} were partially reversible after wash-out with the bathing solution (Figure 2C, 2D).

Table 1. Effects of Ginsenoside Rb1 at different concentrations (1, 2, 5, 10, and 100 μmol/L) on the amplitude of I_{Ba}. Mean±SD. ^cP<0.01 compared with the previous group.

Groups	I_{Ba} inhibition (%)
Control	0±0.74
1 μmol/L Rb1	0±1.12
2 μmol/L Rb1	2±0.87^c
5 μmol/L Rb1	5±1.78^c
10 μmol/L Rb1	20±3.96^c
100 μmol/L Rb1	40±6.71^c

Mechanism of action of ginsenoside Rb1 on the VGCCs in hippocampal neurons

The I_{Ba} was still elicited by depolarizing from -60 mV to 0 mV (0–+20 mV) and recorded continuously every 10 s. Under the maximum activated voltage, the currents achieved stability after recording 5 to 6 times. As shown in Figure 3A, 10 μmol/L ginsenoside Rb1 inhibited the I_{Ba} by 21.53%±2.81% (n=5). The inhibitory effect was eliminated after the application of nifedipine, a selective blocker of L-type Ca^{2+} channels.

As shown in Figure 3B, 10 μmol/L Rb1 inhibited the I_{Ba} by 20.19%±2.98% (n=5) before ω-conotoxin-GVIA treatment and inhibited the I_{Ba} by 20.51%±3.15% (n=5) in the presence of ω-conotoxin-GVIA (P>0.05 compared to Rb1 treatment alone). As shown in Figure 3C, 10 μmol/L Rb1 inhibited the I_{Ba} by 19.80%±3.21% (n=5) before ω-agatoxin IVA treatment and inhibited the I_{Ba} by 20.34%±2.58% (n=5) in the presence

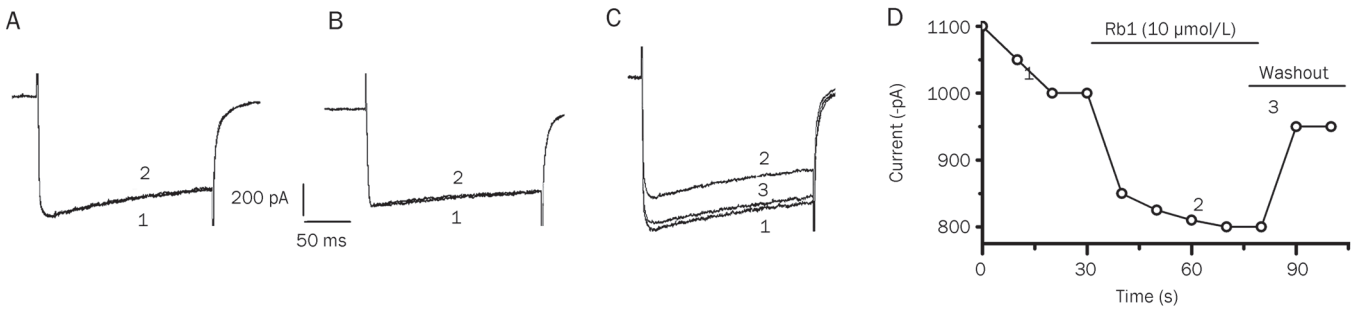

Figure 2. Effect of the extracellular solution, Rb1 (1 μmol/L) and Rb1 (10 μmol/L), on the I_{Ba} (A, B, and C, respectively). (1) Before drug application; (2) drug application; (3) washout. (D) represents the time course of the experiment corresponding to (C).

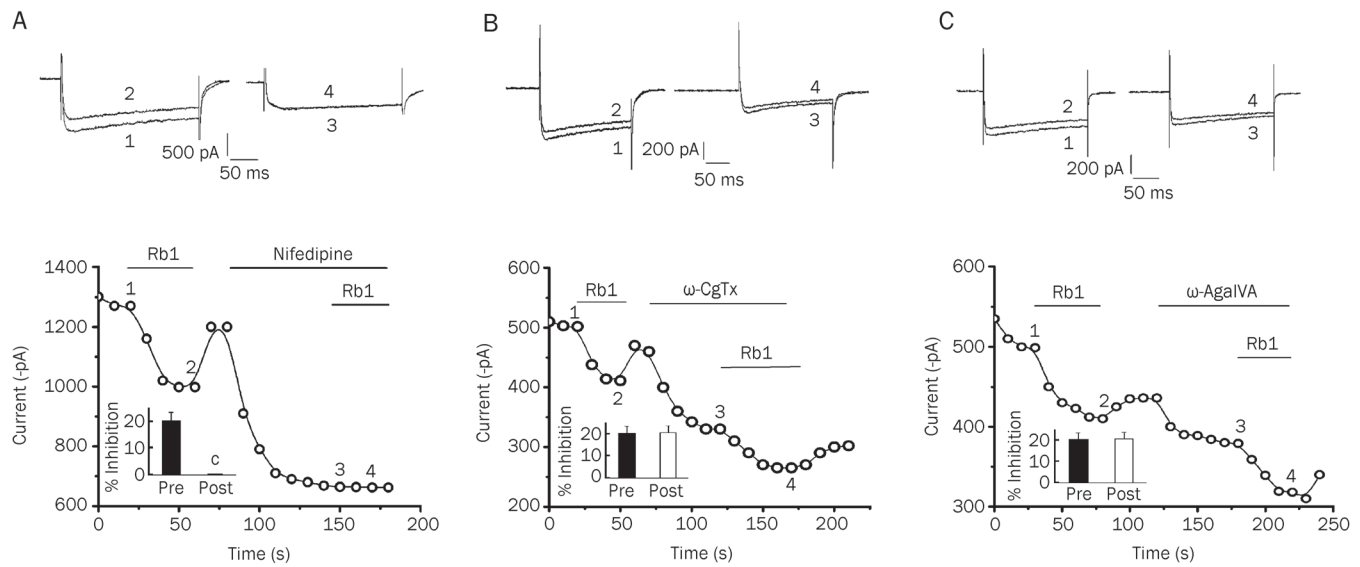

Figure 3. Rb1 inhibited the I_{Ba} in hippocampal neurons, and this inhibitory effect was eliminated after the application of nifedipine (A). Neither ω-conotoxin-GVIA nor ω-agatoxin IVA diminished the Rb1-sensitive I_{Ba} (B and C, respectively). Upper panel, pairs of the inward currents evoked by pulses from -60 to +0 mV (0–+20 mV) at the times indicated in the lower panel. Lower panel, time course of the effects of 10 μmol/L Rb1 on the I_{Ba} amplitude before and after application of the Ca^{2+} channel antagonists (10 μmol/L nifedipine, 1 μmol/L ω-conotoxin GVIA and 30 nmol/L ω-agatoxin IVA). The bar graphs for Rb1 inhibition (mean±SEM, n=5 for Rb1) on the I_{Ba} in cells untreated or treated with Ca^{2+} channel antagonists. ^cP<0.01 compared with Rb1 treatment alone.

of ω-agatoxin IVA (P>0.05 compared to Rb1 treatment alone). Thus, neither ω-conotoxin-GVIA nor ω-agatoxin IVA could diminish the Rb1-sensitive VGCCs.

To gain a better understanding of the action of Rb1 on the I_{Ba}, we explored its action on the I–V curve and the steady-state inactivation curve of the I_{Ba}. A dose of 10 μmol/L ginsenoside Rb1 inhibited the I_{Ba} at the maximum amplitude (control: I_{Ba}=752.56±48.42 pA, Rb1: I_{Ba}=600±40.70 pA, P<0.01, n=6), but had no effect on the activation threshold potential or the reversal potential of the I_{Ba} in the I–V relationship (Figure 4). Furthermore, 10 μmol/L Rb1 shifted the steady-state inactivation curve of the I_{Ba} to a hyperpolarizing voltage (Figure 5) (control: $V_{1/2}$=-17.70±0.40 mV, k=6.26±0.41; Rb1:$V_{1/2}$=-25.53±0.53 mV, k=8.24±0.47; P<0.05, n=6).

A continuous recording with 10 s intervals was used after the application of Rb1, and the inhibitory effects of Rb1 on the I_{Ba} were observed during the first 10 s interval in hippocampal neurons. The results indicated that Rb1 inhibited the I_{Ba} within 10 s. To determine if phosphorylation was involved in the inhibition of the I_{Ba} by ginsenoside Rb1, the adenylyl cyclase (AC) agonist forskolin and the protein kinase A (PKA) antagonist H-89 were used. The percentage of I_{Ba} inhibitory action by Rb1 was 20.15%±3.96% (n=9), while that with the bath application of forskolin (10 μmol/L) and Rb1 was 22.5%±2.95% (n=11). Forskolin did not offset the inhibitory effect of Rb1. In the presence of H-89 (10 μmol/L), the percent inhibitory action by Rb1 was reduced to 20.85%±3.78% (n=12), a value with no statistical significance compared with that of Rb1 alone (P>0.05), demonstrating that H-89 did not affect the inhibition of the I_{Ba} caused by Rb1 (Figure 6).

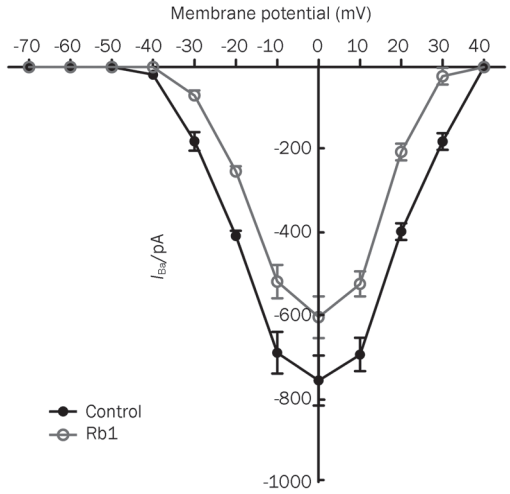

Figure 4. The I-V relationships of the I_{Ba} showed the inhibitory effects of 10 μmol/L Rb1 on the VGCCs (n=6). The holding potential was -60 mV, and the test potentials ranged from -70 mV to +70 mV in 10 mV increments.

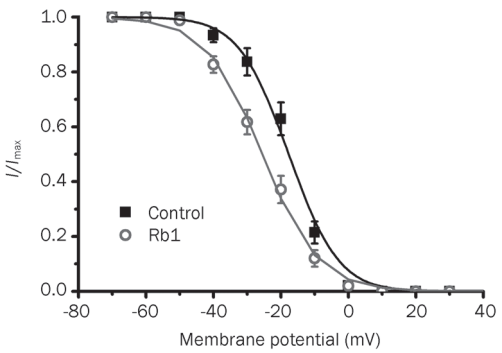

Figure 5. The effects of 10 μmol/L Rb1 on the voltage-dependence of the steady-state of I_{Ba} inactivation (n=6). The data were fitted to the Boltzmann equation.

Discussion

Ginsenosides, which are the pharmacologically active ingredients of *Panax ginseng*, produce reversible and selective inhibitory effects on voltage-dependent and ligand-gated ion channels[23–26]. Studies have also found that the mechanisms of action of saponins vary due to their types or the cell types they act on. For example, ginsenosides activate $G\alpha_{q/11}$, a protein coupled to PLC, leading to IP_3-dependent endoplasmic reticulum calcium release in *Xenopus oocytes*. However, this effect does not occur in neurons[27]. Although previous studies have reported the diversity of voltage-dependent Ca^{2+} channels in hippocampal neurons, and this diversity was also confirmed in the present experiment, none of the research literature mentions the action of the ginsenoside Rb1 on VGCCs in hippocampal neurons. We found that Rb1 at a concentration range of 1 to 100 μmol/L inhibited the calcium channel currents of hippocampal neurons in a dose-dependent manner.

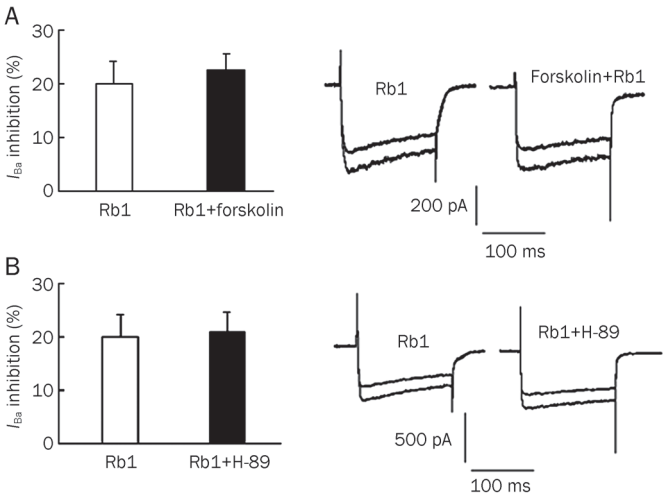

Figure 6. (A) The percentage of inhibitory action by 10 μmol/L Rb1 and Rb1 co-administered with forskolin. (B) The percentage of inhibitory action by 10 μmol/L Rb1 in the presence and absence of H-89.

The I_{Ca} peak current inhibition rate paralleled the increase of Rb1 concentration, and the inhibitory effect was mostly reversible.

Most studies support the effect of Rb1 in preventing neuronal death linked to neurodegenerative diseases[13, 15, 28, 29]. Its perturbed neuronal Ca^{2+} homeostasis is implicated in aging and age-related cognitive impairments[12]. Chen also showed that it could decrease the Aβ-induced elevation of intracellular calcium and stabilize microtubule integrity[18]. It is widely known that postsynaptic $[Ca^{2+}]_i$ and L-type voltage-gated calcium channel currents are upregulated in the hippocampus during aging, despite a significant decrease of cell density[30]. Elevated postsynaptic $[Ca^{2+}]_i$ and L-type voltage-gated calcium channel activity contribute to impaired synaptic plasticity[31] and working memory[32] in aged hippocampal neurons. The increase of L-type voltage-gated calcium channel currents also enhances the susceptibility of aging neurons for apoptosis. Fu has shown that the cholinesterase inhibitor tacrine can reduce Aβ-induced neuronal apoptosis by regulating L-type voltage-gated calcium channel activity[33]. Our results show that the ginsenoside Rb1 selectively targets L-type calcium channels by inhibiting voltage-gated calcium channels. Different calcium channels have distinct electrophysiological characteristics and are closely related to different cell functions. For example, ginsenoside selectively acts on the non-L-type calcium channels of chromaffin cells, which are related to the regulation of the secretion of catecholamines[34]. Additionally, ginsenoside Rf selectively acts on the N-type calcium channels of sensory neurons, which are related to the inhibition of neurotransmitter release following painful stimuli[35]. Therefore, we infer that the selective action of Rb1 on the L-type calcium channels of hippocampal neurons may be the cellular basis of its pharmacological effects in preventing neuronal death linked to neurodegenerative diseases.

In this study, Rb1 induced a leftward shift of the steady-

state inactivation curves of the I_{Ba} to a negative potential without affecting its activation kinetics or reversal potential in the I–V curve, indicating that Rb1 may alter the biophysical nature of the calcium channel and inhibit channel activity by accelerating channel activity access to the inactivation state without affecting its activation characteristics. These results suggest that Rb1 regulates the activity of calcium channels by altering their time dependence.

Protein phosphorylation modulates the function of VGCCs, and the AC-cAMP-PKA system plays a key role in this phosphorylation[36, 37]. Therefore, we used forskolin and H-89 to investigate whether the action of Rb1 on the I_{Ca} is involved in this mechanism. We found that co-application of forskolin and Rb1 did not affect the reduction caused by Rb1. Additionally, the action of Rb1 was not affected by H-89, indicating that the cAMP-PKA system might not be involved in the mechanism by which Rb1 reduces the I_{Ca}. These results confirmed our previous speculation that it is difficult to achieve Ca^{2+} channels phosphorylation within 10 s.

In summary, this study provides electrophysiological evidence that Rb1 induces calcium current inhibition by inhibiting the activity of the L-type Ca^{2+} channels in hippocampal neurons. This finding raises the possibilities that Rb1 may be useful and potentially therapentic choices in the treatment of neurological disorders.

Acknowledgements

We thank Prof Shu-min DUAN (Shanghai Institute of Neuroscience, Shanghai Institute of Biological Sciences, Chinese Academy of Sciences, Shanghai, China) for technical support. This work was supported by grants from the National Natural Science Foundation of China (No 30772555).

Author contribution

Xiao-chun CHEN designed the research; Zhi-ying LIN, Li-min CHEN, Jing ZHANG, and Xiao-dong PAN performed the experiments; Yuan-gui ZHU, Qin-yong YE, and Hua-pin HUANG contributed new analytical tools and performed the data analysis; Zhi-ying LIN wrote the paper.

References

1 Rosenthal W, Hescheler J, Trautwein W, Schultz G. Control of voltage-dependent Ca^{2+} channels by G protein-coupled receptors. FASEB J 1988; 2: 2784–90.
2 Miller RJ. Multiple calcium channels and neuronal function. Science 1987; 235: 46–52.
3 Patil PG, Brody DL, Yue DT. Preferential closed-state inactivation of neuronal calcium channels. Neuron 1998; 20: 1027–38.
4 Ahlijanian MK, Westenbroek RE, Catterall WA. Subunit structure and localization of dihydropyridine-sensitive calcium channels in mammalian brain, spinal cord, and retina. Neuron 1990; 4: 819–32.
5 Chin H, Smith MA, Kim HL, Kim H. Expression of dihydropyridine-sensitive brain calcium channels in the rat central nervous system. FEBS Lett 1992; 299: 69–74.
6 Feng ZP, Arnot MI, Doering CJ, Zamponi GW. Calcium channel beta subunits differentially regulate the inhibition of N-type channels by individual Gbeta isoforms. J Biol Chem 2001; 276: 45051–8.
7 Ohno-Shosaku T, Hashimotodani Y, Ano M, Takeda S, Tsubokawa H, Kano M. Endocannabinoid signalling triggered by NMDA receptor-mediated calcium entry into rat hippocampal neurons. J Physiol 2007; 584: 407–18.
8 Stephens GJ, Morris NP, Fyffe RE, Robertson B. The Cav2.1/alpha1A (P/Q-type) voltage-dependent calcium channel mediates inhibitory neurotransmission onto mouse cerebellar Purkinje cells. Eur J Neurosci 2001; 13: 1902–12.
9 Yarotskyy V, Elmslie KS. Omega-conotoxin GVIA alters gating charge movement of N-type (CaV2.2) calcium channels. J Neurophysiol 2009; 101: 332–40.
10 Menne J, Park JK, Agrawal R, Lindschau C, Kielstein JT, Kirsch T. Cellular and molecular mechanisms of tissue protection by lipophilic calcium channel blockers. FASEB J 2006; 20: 994–6.
11 Nikonenko I, Bancila M, Bloc A, Muller D, Bijlenga P. Inhibition of T-type calcium channels protects neurons from delayed ischemia-induced damage. Mol Pharmacol 2005; 68: 84–9.
12 Nah SY, Kim DH, Rhim H. Ginsenosides: are any of them candidates for drugs acting on the central nervous system? CNS Drug Rev 2007; 13: 381–404.
13 Fujita K, Hakuba N, Hata R, Morizane I, Yoshida T, Shudou M. Ginsenoside Rb1 protects against damage to the spiral ganglion cells after cochlear ischemia. Neurosci Lett 2007; 415: 113–17.
14 Liu M, Zhang J. Effects of ginsenoside Rb1 and Rg1 on synaptosomal free calcium level, ATPase and calmodulin in rat hippocampus. Chin Med J 1995; 108: 544–7.
15 Radad K, Gille G, Moldzio R, Saito H, Rausch WD. Ginsenosides Rb1 and Rg1 effects on mesencephalic dopaminergic cells stressed with glutamate. Brain Res 2004; 1021: 41–53.
16 Sakanaka M, Zhu P, Zhang B, Wen TC, Cao F, Ma YJ. Intravenous infusion of dihydroginsenoside Rb1 prevents compressive spinal cord injury and ischemic brain damage through upregulation of VEGF and Bcl-XL. J Neurotrauma 2007; 24: 1037–54.
17 Yuan QL, Yang CX, Xu P, Gao XQ, Deng L, Chen P. Neuroprotective effects of ginsenoside Rb1 on transient cerebral ischemia in rats. Brain Res 2007; 1167: 1–12.
18 Chen X, Huang T, Zhang J, Song J, Chen L, Zhu Y. Involvement of calpain and p25 of CDK5 pathway in ginsenoside Rb1's attenuation of beta-amyloid peptide25–35-induced tau hyperphosphorylation in cortical neurons. Brain Res 2008; 1200: 99–106.
19 Zhang JM, Wang HK, Ye CQ, Ge W, Chen Y, Jiang ZL. ATP released by astrocytes mediates glutamatergic activity-dependent heterosynaptic suppression. Neuron 2003; 40: 971–82.
20 Smirnov SV, Aaronson PI. Ca^{2+} currents in single myocytes from human mesenteric arteries: evidence for a physiological role of L-type channels. J Physiol 1992; 457: 455–75.
21 Bretschneider F, Markwardt F. Drug-dependent ion channel gating by application of concentration jumps using U-tube technique. Methods Enzymol 1999; 294: 180–9.
22 Duan S, Cooke IM. Selective inhibition of transient K^+ current by La^{3+} in crab peptide-secretory neurons. J Neurophysiol 1999; 81: 1848–55.
23 Choi S, Jung SY, Lee JH, Sala F, Criado M, Mulet J. Effects of ginsenosides, active components of ginseng, on nicotinic acetylcholine receptors expressed in *Xenopus oocytes*. Eur J Pharmacol 2002; 442: 37–45.
24 Choi S, Lee JH, Oh S, Rhim H, Lee SM, Nah SY. Effects of ginsenoside Rg2 on the 5-HT3A receptor-mediated ion current in *Xenopus oocytes*. Mol Cells 2003; 15: 108–13.
25 Sala F, Mulet J, Choi S, Jung SY, Nah SY, Rhim H. Effects of ginsenoside Rg2 on human neuronal nicotinic acetylcholine receptors.

J Pharmacol Exp Ther 2002; 301: 1052–9.

26 Bezprozvanny I, Mattson MP. Neuronal calcium mishandling and the pathogenesis of Alzheimer's disease. Trends Neurosci 2008; 31: 454–63.

27 Jeong SM, Lee JH, Kim S, Rhim H, Lee BH, Kim JH. Ginseng saponins induce store-operated calcium entry in *Xenopus oocytes*. Br J Pharmacol 2004; 142: 585–93.

28 Mook-Jung I, Hong HS, Boo JH, Lee KH, Yun SH, Cheong MY. Ginsenoside Rb1 and Rg1 improve spatial learning and increase hippocampal synaptophysin level in mice. J Neurosci Res 2001; 63: 509–15.

29 Liao B, Newmark H, Zhou R. Neuroprotective effects of ginseng total saponin and insenosides Rb1 and Rg1 on spinal cord neurons *in vitro*. Exp Neurol 2002; 173: 224–34.

30 Coon AL, Wallace DR, Mactutus CF, Booze RM. L-type calcium channels in the hippocampus and cerebellum of Alzheimer's disease brain tissue. Neurobiol Aging 1999; 20: 597–603.

31 Veng LM, Mesches MH, Browning MD. Age-related working memory impairment is correlated with increases in the L-type calcium channel protein alpha1D (Cav1.3) in area CA1 of the hippocampus and both are ameliorated by chronic nimodipine treatment. Brain Res Mol Brain Res 2003; 110: 193–202.

32 Thibault O, Hadley R, Landfield PW. Elevated postsynaptic $[Ca^{2+}]_i$ and L-type calcium channel activity in aged hippocampal neurons: relationship to impaired synaptic plasticity. J Neurosci 2001; 21: 9744–56.

33 Fu H, Li W, Lao Y, Luo J, Lee NT, Kan KK. Bis(7)-tacrine attenuates beta amyloid-induced neuronal apoptosis by regulating L-type calcium channels. J Neurochem 2006; 98: 1400–10.

34 Choi S, Jung S, Kim C, Kim H, Rhim H, Kim S. Effect of ginsenosides on voltage-dependent $Ca^{(2+)}$ channel subtypes in bovine chromaffin cells. J Ethnopharmacol 2001; 74: 75–81.

35 Nah SY, Park HJ, McCleskey EW. A trace component of ginseng that inhibits Ca^{2+} channels through a pertussis toxin-sensitive G protein. Proc Natl Acad Sci U S A 1995; 92: 8739–43.

36 Kavalali ET, Hwang KS, Plummer MR. cAMP-dependent enhancement of dihydropyridine-sensitive calcium channel availability in hippocampal neurons. J Neurosci 1997; 17: 5334–48.

37 Sanchez-Munoz I, Sanchez-Franco F, Vallejo M, Fernández A, Palacios N, Fernández M. Activity-dependent somatostatin gene expression is regulated by cAMP-dependent protein kinase and Ca^{2+}-calmodulin kinase pathways. J Neurosci Res 2010; 88: 825–36.

Acta Pharmacologica Sinica (2012) 33: 445–451

www.nature.com/aps

Original Article

Inhalation of hydrogen gas attenuates ouabain-induced auditory neuropathy in gerbils

Juan QU[1, #], Yun-na GAN[2, #], Ke-liang XIE[3, #], Wen-bo LIU[4], Ya-fei WANG[1], Ren-yi HEI[1], Wen-juan MI[1], Jian-hua QIU[1, *]

[1]Department of Otolaryngology, Xijing Hospital, Fourth Military Medical University, Xi'an 710032, China; [2]Department of Prosthondontics, College of Stomatology, Fourth Military Medical University, Xi'an 710032, China; [3]Department of Anesthesiology, General Hospital of Tianjin Medical University, Tianjin 300052, China; [4]Department of Neurosurgery, Xijing Institute of Clinical Neuroscience, Xijing Hospital, Fourth Military Medical University, Xi'an 710032, China

Aim: Auditory neuropathy (AN) is a hearing disorder characterized by abnormal auditory nerve function with preservation of normal cochlear hair cells. This study was designed to investigate whether treatment with molecular hydrogen (H_2), which can remedy damage in various organs via reducing oxidative stress, inflammation and apoptosis, is beneficial to ouabain-induced AN in gerbils.
Methods: AN model was made by local application of ouabain (1 mmol/L, 20 mL) to the round window membrane in male Mongolian gerbils. H_2 treatment was given twice by exposing the animals to H_2 (1%, 2%, and 4%) for 60 min at 1 h and 6 h after ouabain application. Before and 7 d after ouabain application, the hearing status of the animals was evaluated using the auditory brainstem response (ABR) approach, the hear cell function was evaluated with distortion product otoacoustic emissions (DPOAE). Seven days after ouabain application, the changes in the cochleae, especially the spiral ganglion neurons (SGNs), were morphologically studied. TUNEL staining and immunofluorescent staining for activated caspase-3 were used to assess the apoptosis of SGNs.
Results: Treatment with H_2 (2% and 4%) markedly attenuated the click and tone burst-evoked ABR threshold shift at 4, 8, and 16 kHz in ouabain-exposed animals. Neither local ouabain application, nor H_2 treatment changed the amplitude of DPOAE at 4, 8, and 16 kHz. Morphological study showed that treatment with H_2 (2%) significantly alleviated SGN damage and attenuated the loss of SGN density for each turn of cochlea in ouabain-exposed animals. Furthermore, ouabain caused significantly higher numbers of apoptotic SGNs in the cochlea, which was significantly attenuated by the H_2 treatment. However, ouabain did not change the morphology of cochlear hair cells.
Conclusion: The results demonstrate that H_2 treatment is beneficial to ouabain-induced AN via reducing apoptosis. Thus, H_2 might be a potential agent for treating hearing impairment in AN patients.

Keywords: auditory neuropathy (AN); ouabain; hearing loss; hydrogen gas (H_2); cochlea; spiral ganglion neuron; hair cell; auditory brainstem response; distortion product otoacoustic emissions; apoptosis

Acta Pharmacologica Sinica (2012) 33: 445–451; doi: 10.1038/aps.2011.190; published online 5 Mar 2012

Introduction

Auditory neuropathy (AN), also known as auditory dys-synchrony (AD), is a sensorineural hearing disorder and accounts for 7%–10% of all permanent childhood hearing impairment[1]. It was recently identified to define a specific type of hearing deficit resulting from the impairment of auditory nerve function[2]. Two hallmark features of AN are normal outer hair cell function and the presence of absent/abnormal auditory brainstem responses (ABR)[3]. Unfortunately, there is no effective treatment for AN mainly because its mechanism is unclear[3].

In 2007, Ohsawa *et al* found that hydrogen gas (H_2) demonstrated an antioxidant effect by selectively reducing hydroxyl radicals [·OH, the most cytotoxic reactive oxygen species (ROS)] without interfering with other physiological ROS[4]. Recently, many studies, including ours, have found that H_2 has therapeutic roles in many diseases via its ability to reduce oxidative stress, inflammation and apoptosis; these diseases include cerebral damage, spinal cord injury, sepsis, multiple organ dysfunction, chronic allograft nephropathy, tumors and type 2 diabetes[4–14]. Furthermore, H_2 can effectively protect against the morphological and functional cochlear hair cell damage induced by ROS[15]. In addition, a more recent study has reported that pretreatment with H_2 in drinking water can facilitate the recovery of hair cell function and attenuate noise-induced temporary hearing loss[16]. These findings strongly

# These three authors contributed equally to this work.
* To whom correspondence should be addressed.
E-mail qiujh@fmmu.edu.cn
Received 2011-08-19 Accepted 2011-12-09

indicate that H_2 treatment may be beneficial in cases of AN.

Ouabain is a cardiac glycoside that can specifically bind to Na^+/K^+-ATPase and block its activity. Following application of ouabain into the round window (RW) niche of gerbil, the animals showed relatively normal otoacoustic emissions and cochlear microphonics in conjunction with increased thresholds for cochlear whole-nerve action potentials (CAPs) and ABRs[17–19]. The ouabain-induced AN model has been shown to selectively and permanently destroy most spiral ganglion neurons (SGNs) with little effect on the morphology and function of the sensory hair cells and the cells in the cochlear lateral wall[17–19]. Thus, the ouabain-exposed gerbil is believed to be a reliable model of human AN[17]. In the present study, we tested the hypothesis that H_2 could attenuate ouabain-induced AN in gerbils by reducing apoptosis.

Materials and methods

Animals

Male Mongolian gerbils aged 4–8 months with healthy external ears were used in this study. The animals, which had normal Preyer's reflexes, were provided by the animal center of the Capital Medical University in China. The animals were housed at 20–22 °C with a 12-h light/dark cycle. Standard animal chow and water were freely available. All experimental procedures were approved by the Institutional Animal Care and Use Committee of Fourth Military Medical University and performed in accordance with the National Institutes of Health (NIH, USA) guidelines for the use of experimental animals.

The animals were randomly divided into four groups: Saline, Saline+H_2, Ouabain and Ouabain+H_2. The animals in the Ouabain and Ouabain+H_2 groups were subjected to the ouabain-induced AN model. The H_2 treatment was administered at 1 h and 6 h after ouabain or saline administration.

Ouabain-induced AN model

The ouabain-induced AN model was executed as described previously[17]. Briefly, the animals were anesthetized with sodium pentobarbital (40 mg/kg). Their body temperatures were measured and maintained at 37.5±0.5 °C using a heating pad. Sterile procedures were used to apply ouabain to the RW, wherein 20 μL of a 1 mmol/L ouabain (Sigma-Aldrich Chemical Co, St Louis, MO, USA) solution in normal saline was placed in the RW niche for 1 h. Then, the ouabain was removed with a small piece of filter paper. Finally, the surface of the bulla was fully closed with dental cement, and the incisions were closed with sutures. The control animals received normal saline injections in equal volumes.

H_2 treatment

Based on our previous studies[9, 12, 13], H_2 treatment was given via 1%, 2%, or 4% H_2 inhalation for 60 min at 1 h and again at 6 h after ouabain or saline injection. The animals assigned to the H_2 treatment were put in a sealed Plexiglas chamber with inflow and outflow outlets. H_2 was supplied through a TF-I gas flowmeter (YUTAKA Engineering Corp, Tokyo, Japan) and delivered by air into the chamber at a rate of 4 L/min. The concentration of H_2 in the chamber was continuously monitored with a commercially available detector (Hy-Alerta Handheld Detector Model 500, H_2 Scan, Valencia, CA, USA). The concentration of oxygen in the chamber was maintained at 21% with supplemental oxygen and continuously monitored with a gas analyzer (Medical Gas Analyzer LB-2, Model 40 mol/L, Beckman, USA). Carbon dioxide was removed from the chamber with Baralyme. The animals that were not assigned to receive the H_2 treatment were exposed to room air in this chamber.

Auditory brainstem response (ABR)

The hearing status of all animals was evaluated at baseline just before and 7 d after ouabain or saline administration using the ABR approach as previously described[16]. Elevations of the ABR threshold have been shown to provide an excellent, reliable indicator of the degree of cochlear hearing loss for experimental animals[20]. The animals were anesthetized with an intraperitoneal injection of 40 mg/kg pentobarbital sodium, and needle electrodes were placed subcutaneously beneath the pinna of the measured ear (reference electrode), beneath the apex of the nose (ground) and at the vertex (active electrode). The stimulus signal was generated with an Intelligent Hearing Systems device (Bio-Logic Systems, USA). Click sounds were produced at a rate of 57.7/s to evoke the ABRs. Tone burst sounds at 4, 8, and 16 kHz (0.2-ms rise/fall time and 1-ms flat segment) were generated to estimate the frequency-specific thresholds. The responses of 1024 sweeps were averaged at each intensity level step. The intensity of the stimulus was varied at stepwise increments of 5 dB sound pressure levels (SPL), and the threshold was defined as the lowest intensity level at which a response was still observed. Rectal temperatures of the animals were monitored and maintained by a warming pad throughout the recordings.

Distortion product otoacoustic emissions (DPOAE)

As described previously[16], the animals underwent DPOAE measurement at baseline just before and 7 d after ouabain or saline administration with an acoustic probe using the DP2000 DPOAE measurement system, version 3.0 (Starkey Laboratory, Eden Prairie, MN, USA). The DP-grams comprised 2f1–f2 DPOAE amplitudes as a function of f2. The stimulus parameters used for the DPOAE input/output (I/O) growth function were constructed as follows: a frequency ratio of 1.2 (f_2/f_1) and f2 in one-sixth-octave steps from 1 to 16 kHz. DPOAE was defined as being present when its level exceeded that of the noise floor by 3 dB.

Histological assessment

The animals were euthanized by decapitation under deep anesthesia after the ABR test at 7 d. The cochleae were quickly removed and fixed with 4% paraformaldehyde in 0.1 mol/L phosphate-buffered saline (PBS, pH 7.4) for 24 h at room temperature. After fixation, the cochleae were dissected and decalcified in 2% ethylenediaminetetraacetic acid (EDTA) and 0.25% glutaraldehyde for 3 weeks. Then, they were sectioned

at 6 μm thickness and stained with hematoxylin and eosin. The sections were digitized using an Olympus BX51 microscope (Olympus Optical, Hamburg, Germany). To determine the spiral ganglion neuronal density for each turn in the cochlea, the area of each spiral ganglion was measured with a MetaMorph imaging system (Universal Imaging Corporation, Downingtown, PA, USA), and morphologically intact SGNs (criterion: round cell body containing a nucleus and homogenous cytoplasm) were counted within this area[17].

TUNEL staining

To detect DNA fragmentation in the nuclei of cells, we used a TUNEL kit (Roche Diagnostics GmbH, Mannheim, Germany) to quantify the occurrence of apoptosis 24 h after ouabain or saline administration[9]. To determine the number of SGNs that underwent apoptosis, two independent and blinded pathologists counted the SGNs that were positive or negative in the TUNEL staining.

Immunofluorescent staining for activated caspase-3

The cochleae were harvested, fixed, and decalcified in 2% ETDA for 3 weeks. Then, the samples were sectioned at 6 μm thickness and stained with cleaved caspase-3 (Asp175) antibody (Cell Signaling Technology, Danvers, MA, USA) as previously described[17]. Photomicrographs were taken with a fluorescent microscope (Nikon Instruments, Melville, NY, USA). Microscopic examination was performed by at least two investigators, who were blinded to the sample identification.

Caspase-3 activity

Caspase-3 activity in the cochlear tissue was measured with a caspase-3/CPP32 Fluorometric Assay Kit (Biovision Research Products, Mountain View, CA, USA) 24 h after ouabain or saline administration[9]. All assays were run in duplicate.

Statistical analysis

All data are expressed as the mean±SEM. The data were analyzed by one-way ANOVA followed by an LSD-*t* test for multiple comparisons. The statistical analysis was performed with SPSS (Statistical Package for the Social Sciences) 16.0 software. In all tests, a *P* value less than 0.05 was considered statistically significant.

Results

Click and tone burst-evoked ABR threshold shift

In this study, we first investigated the effects of H_2 treatment on hearing impairment in gerbils with ouabain-induced AN. The H_2 treatment was given twice with 1%, 2%, or 4% H_2 inhalation for 60 min starting at 1 h and again at 6 h after ouabain or saline administration. Based on our preliminary experiment, hearing status was evaluated before and 7 d after ouabain or saline administration by measuring the click and tone burst-evoked ABR threshold shift; these data are shown in Figures 1 and 2. The administration of ouabain significantly increased the click-evoked ABR threshold and tone burst-evoked ABR threshold at 4, 8, and 16 kHz when compared with the saline group ($P<0.05$, $n=6$ per group), suggesting that ouabain caused significant hearing impairment. However, the H_2 treatment markedly attenuated the click and tone burst-evoked ABR threshold shift at 4, 8, and 16 kHz in ouabain-exposed animals ($P<0.05$, $n=6$ per group). In addition, the H_2 treatment had no effects on the click and tone burst-evoked ABR threshold at 4, 8, and 16 kHz in the animals with saline administration ($P>0.05$, $n=6$ per group). These results demonstrate that local administration of ouabain causes a hearing disorder in gerbils, which can be significantly attenuated by H_2 treatment.

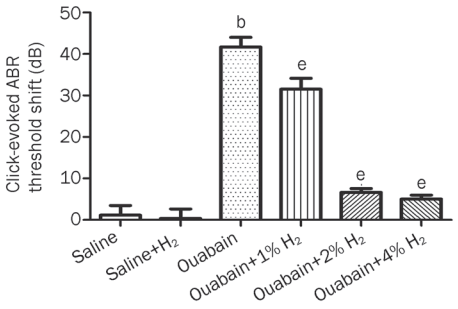

Figure 1. H_2 treatment attenuated ouabain-induced click-evoked auditory brainstem response (ABR) threshold shift. H_2 treatment was given twice with 1%, 2%, or 4% H_2 inhalation for 60 min starting at 1 h and 6 h after ouabain or saline injection, respectively. The click-evoked ABR threshold was measured at baseline just before and again 7 d after ouabain or saline administration. The values are expressed as mean±SEM (n=6 per group). $^bP<0.05$ *vs* Saline group. $^eP<0.05$ *vs* Ouabain group.

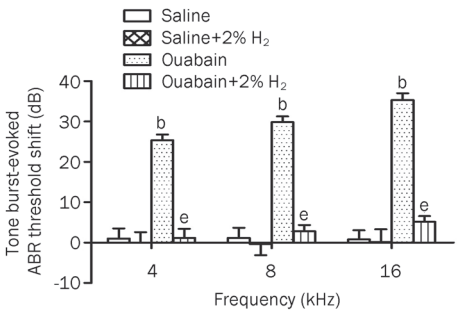

Figure 2. H_2 treatment attenuated ouabain-induced tone burst-evoked auditory brainstem response (ABR) threshold shift. H_2 treatment was given twice with 2% H_2 inhalation for 60 min starting at 1 h and 6 h after ouabain or saline injection, respectively. The tone burst-evoked ABR threshold was measured at baseline just before and again 7 d after ouabain or saline administration. The values are expressed as mean±SEM (n=6 per group). $^bP<0.05$ *vs* Saline group. $^eP<0.05$ *vs* Ouabain group.

DPOAE audiograms

We further investigated the effects of the H_2 treatment on hair cell function in gerbils with ouabain-induced AN. Hair cell function was evaluated before and 7 d after ouabain or saline

administration by distortion product otoacoustic emissions (DPOAE), which are shown in Figure 3. Here, we found that local administration of ouabain did not change the amplitude of DPOAE at 4, 8, and 16 kHz (P>0.05 *vs* Saline group, n=6 per group), which was not influenced by the H_2 treatment (P>0.05 *vs* Ouabain group, n=6 per group). This result demonstrates that ouabain does not damage hair cell function, and H_2 treatment also has no effects on hair cell function in this model.

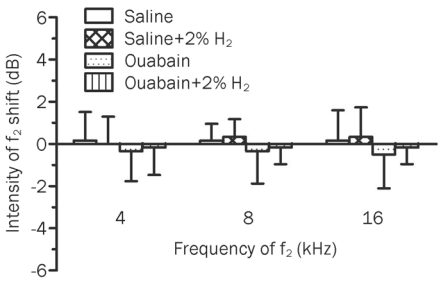

Figure 3. Distortion product otoacoustic emissions (DPOAE) measurements at f_2=4, 8, and 16 kHz. H_2 treatment was given as Figure 2. The hear cell function was evaluated before and 7 d after ouabain or saline injection by DPOAE. The values are expressed as mean±SEM (n=6 per group).

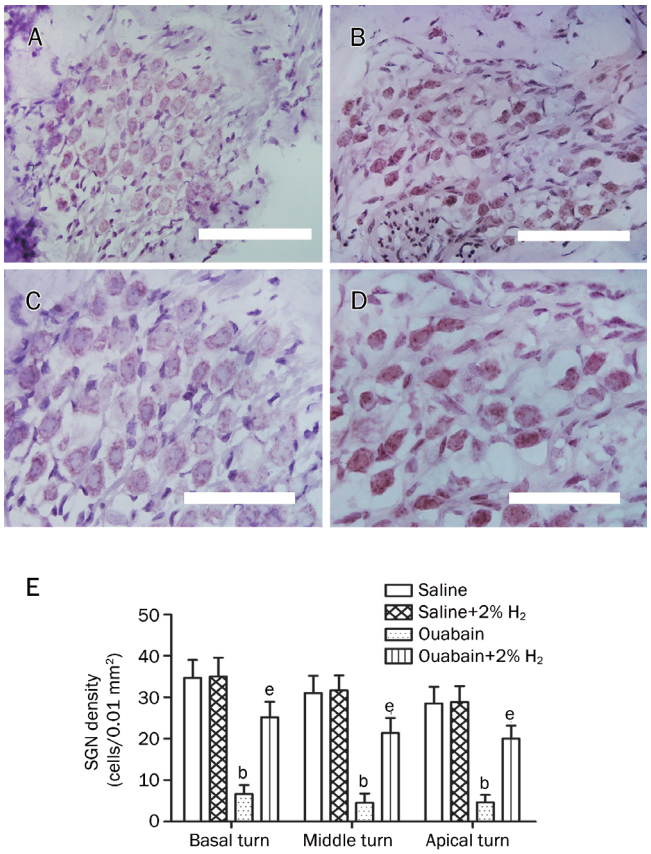

Figure 4. H_2 treatment attenuated ouabain-induced damage of spiral ganglion neurons (SGN). H_2 treatment was given as Figure 2. The SGN damage was evaluated with hematoxylin and eosin staining 7 d after ouabain or saline administration. Representative micrographs in the middle turn are shown in 4A–4D (A and C: Saline group; B and D: Ouabain group). E is the quantitative analysis of spiral ganglion neuronal density for each turn in the cochlea. The values are expressed as mean±SEM (n=6 per group). ^bP<0.05 *vs* Saline group. ^eP<0.05 *vs* Ouabain group. Scale bar for A and B is 50 μm; Scale bar for C and D is 30 μm.

Histological assessment

Furthermore, we investigated the morphological changes in the cochleae, especially the SGNs, 7 d after ouabain or saline administration (Figure 4A–4D). Ouabain caused significant damage to the SGNs, such as edema, as well as the occurrence of vacuole-like structures, condensed pyknotic nuclei and shrinking of the cytoplasm. The H_2-treated, ouabain-exposed animals exhibited normal morphological profiles of the SGNs. In addition, we measured the spiral ganglion neuronal density for each turn in the cochlea (Figure 4E). Ouabain drastically decreased the SGN density in the basal, middle and apical turns in cochlea when compared with the saline group (P<0.05, n=6 per group). However, the H_2 treatment significantly increased the SGN density of the basal, middle and apical turns in the cochleae of the ouabain-exposed animals (P<0.05, n=6 per group). These results demonstrate that ouabain causes significant damage to the SGNs, which can be attenuated by H_2 treatment.

In addition, we observed the morphology of the cochlear hair cells by staining with Alexa Fluor 488 conjugated to phalloidin (green fluorescence). There was no significant damage in the inner and outer hair cells of the cochleae in ouabain-exposed animals (Figure 5).

TUNEL staining and caspase-3 activity

In addition, we detected apoptosis of the SGNs 24 h after ouabain or saline administration by TUNEL staining and caspase-3 activity. The results are shown in Figures 6 and 7. TUNEL staining identified no apoptotic cells in the cochleae of the saline-exposed animals. There was a high number of TUNEL-positive SGNs in the ouabain-treated animals, but these numbers were significantly lower in the animals receiving the H_2 treatment. The number of SGNs that were positive for TUNEL staining was recorded in each specimen in a blind fashion. We found that ouabain-exposed animals had significantly more apoptotic SGNs (P<0.05 *vs* Saline group, n=6 per group). However, H_2 treatment resulted in significantly fewer apoptotic SGNs in the ouabain-exposed animals (P<0.05 *vs* Ouabain group, n=6 per group). Furthermore, we found that the caspase-3 activity in the cochlea was significantly greater in the ouabain-exposed animals than in the saline-only animals (P<0.05 *vs* Saline group, n=6 per group, Figure 7). The H_2–treated animals that had been exposed to ouabain had significantly less caspase-3 activity than the animals exposed to ouabain alone (P<0.05 *vs* Ouabain group, n=6 per group, Figure 7). This result was confirmed by immunofluorescent staining for cleaved caspase-3 (red) (Figure 7). The results suggest

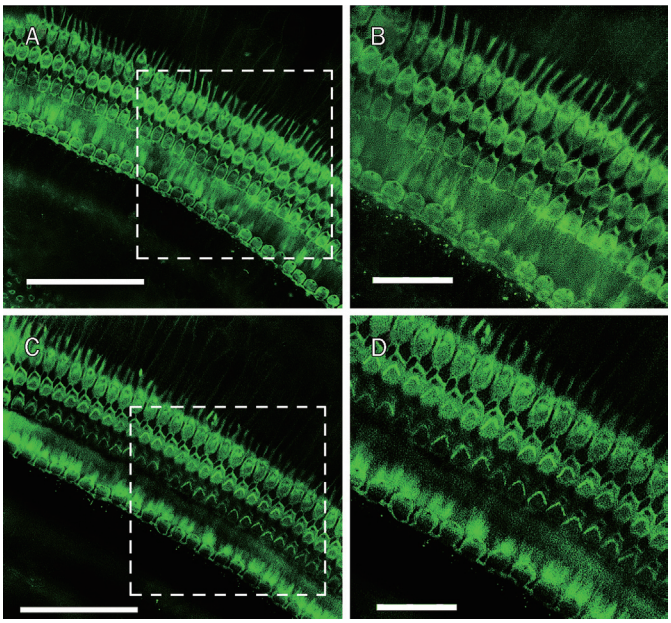

Figure 5. Morphology of cochlear hair cells in ouabain-exposed animals. The organ of corti was stained for filamentous actin with Alexa Fluor 488 conjugated to phalloidin (green fluorescence) (Molecular Probes, Eugene, OR, USA) for 40 min to outline hair cells (A and B: Saline group; C and D: Ouabain group). This figure showed that local administration of ouabain did not damage the outer and inner hair cells. Scale bar for A and C is 50 μm; Scale bar for B and D is 15 μm.

that local administration of ouabain significantly increases the occurrence of cochlear SGN apoptosis, which can be alleviated by H_2 treatment.

Discussion

In this study, we found that H_2 treatment could reduce the click and tone burst-evoked ABR threshold shift induced by local administration of ouabain in gerbils. Furthermore, H_2 treatment significantly attenuated ouabain-induced SGN damage and apoptosis. In addition, the local application of ouabain did not affect the morphology and function of the cochlear hair cells. These results strongly suggest that H_2 might be a useful therapeutic agent for ouabain-induced AN through its capacity to inhibit apoptosis.

AN is a hearing disorder characterized by absent or severely impaired ABR in the presence of normal outer hair cell function and is evaluated by otoacoustic emissions and/or cochlear microphonics[3]. Some possible sites of lesions that can produce the audiometric and electrophysiological profile of AN include: the inner hair cells, the synaptic junction between the inner hair cells and type I afferent nerve fibers, the SGNs and the specific damage or demyelination of type I auditory nerve fibers[3]. The clinical features of AN can vary considerably with respect to the age of onset, etiology, severity of hearing loss and site of lesions[3]. Although the underlying mechanisms of AN are key to understanding and treating the disease, these mechanisms are still largely unknown.

In this study, we found that ouabain-exposed animals had significantly higher click and tone burst-evoked ABR thresholds. However, the local administration of ouabain did not change the amplitude of the DPOAE. In addition, the histological analysis showed that the local administration of ouabain led to significant damage to the SGNs and decreased the spiral ganglion neuronal density for each turn in the cochlea. However, ouabain did not damage the morphology of the cochlear hair cells. These results demonstrate that the local

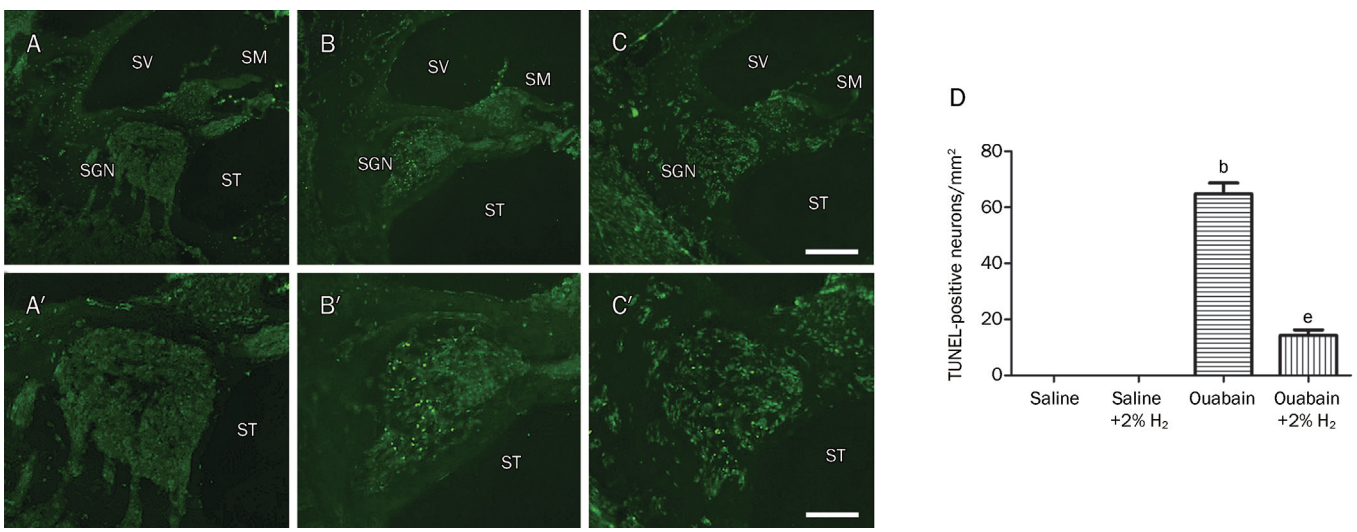

Figure 6. H_2 treatment reduced the ouabain-induced cochlear SGN apoptosis evidenced by TUNEL staining. H_2 treatment was given as Figure 2. The SGN apoptosis was detected by TUNEL staining (A–C, A′–C′) 24 h after ouabain or saline administration. For quantitative measurement, the number of SGN that was positive for TUNEL staining (green) was recorded in each specimen in a blind fashion (D). The values are expressed as mean±SEM (n=6 per group). $^bP<0.05$ *vs* Saline group. $^eP<0.05$ *vs* Ouabain group. ND=not detected. SGN, spiral ganglion neuron; SM, scala media; ST, scala tympani; SV, scala vestibuli. Scale bar for A, B, and C is 100 μm; Scale bar for A′, B′, and C′ is 50 μm.

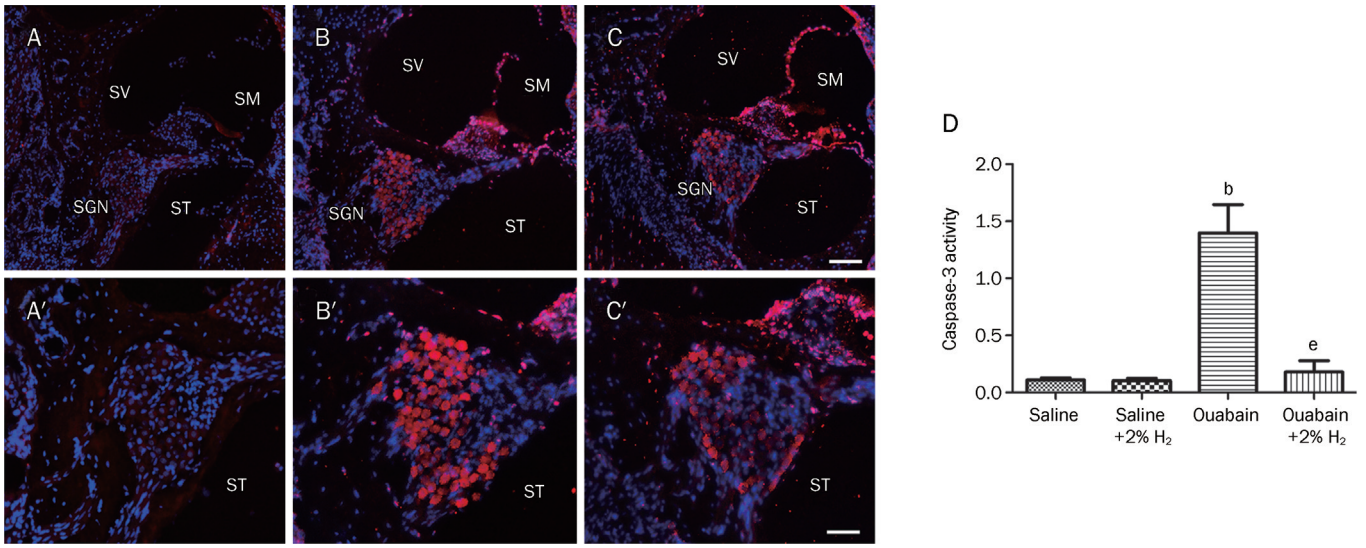

Figure 7. H_2 treatment reduced the ouabain-induced cochlear SGN apoptosis evidenced by immunofluorescent staining for activated caspase-3 and measurement of caspase-3 activity. H_2 treatment was given as Figure 2. The SGN apoptosis was detected by immunofluorescent staining for cleaved caspase-3 (A–C, A′–C′) as well as caspase-3 activity (D) 24 h after ouabain or saline administration. Positive signals are indicated by red fluorescence in contrast to blue fluorescence of Hoechst 33342-stained nuclei (A–C, A′–C′). The caspase-3 activity is expressed as mean±SEM (n=6 per group). $^bP<0.05$ *vs* Saline group. $^eP<0.05$ *vs* Ouabain group. SGN, spiral ganglion neuron; SM, scala media; ST, scala tympani; SV, scala vestibule. Scale bar for A, B, and C is 100 μm; Scale bar for A′, B′, and C′ is 50 μm.

administration of ouabain successfully induced the AN model in gerbils in this study, which is consistent with previous studies[17–19].

Recently, we and other researchers have found that H_2 treatment could effectively protect against damage to organs such as the brain, spinal cord, heart, lungs, liver and kidneys through reducing oxidative stress, inflammation and apoptosis. These findings suggest that H_2 could play a role in preventive and therapeutic applications for organ damage[4–13, 21, 22]. Furthermore, an *in vitro* study has demonstrated that H_2 can protect both the inner and outer hair cells from oxidant damage induced by different concentrations of antimycin A[15]. Incubation with a hydrogen-saturated medium also significantly reduced ROS generation and subsequent lipid peroxidation in the auditory epithelia, leading to the increased survival of hair cells[15]. In addition, a more recent study has shown that pretreatment with H_2-rich water can prevent noise-induced hearing loss[16]. In the present study, we found that H_2 treatment significantly attenuated the ouabain-induced increase in the click and tone burst-evoked ABR threshold. In addition, H_2 treatment significantly mitigated damage to the SGNs and prevented a decreased spiral ganglion neuronal density for each turn of the cochlea in ouabain-exposed animals. Also, H_2 treatment did not change the morphology and function of cochlear hair cells. These results demonstrate that H_2 treatment is beneficial for ouabain-induced AN.

The degeneration of SGNs is a common pathologic feature correlated with permanent hearing loss. SGN apoptosis plays an important role in the ouabain-induced AN model[18]. Apoptosis is a programmed cell death that is characterized by specific ultrastructural changes including cell shrinkage, nuclear condensation and DNA fragmentation[23]. It has been reported that the application of ouabain to the RW membrane of the cochlea results in a rapid loss of SGNs, as indicated both by TUNEL staining and direct observation of the nuclear morphology[17]. In addition, ouabain-induced AN in gerbils is associated with the release of cytochrome *c* and the activation of caspase-3 in SGN[18]. In the present study, we also found that the local administration of ouabain resulted in significant levels of cochlear SGN apoptosis as evidenced by TUNEL staining and caspase-3 activity, which could be significantly attenuated by H_2 treatment. Several previous studies have reported that H_2 has an anti-apoptotic role in many diseases[4, 5, 9]. Therefore, the results suggest that the protective roles of H_2 treatment may be associated with reduced SGN apoptosis. In addition, H_2 treatment can reduce the levels of oxidative products and inflammatory cytokines, as well as increase antioxidant enzymatic activities in many diseases[4, 6, 8–14]. Further studies are needed to determine whether these mechanisms contribute to the protective effects of H_2 treatment against AN.

H_2 is one of the most plentiful gasses in the universe. It is neither explosive nor dangerous at a concentration of less than 4.7% in air and 4.1% in pure oxygen. This study supports the observation that H_2 inhalation may be an effective therapeutic agent for attenuating ouabain-induced AN via the reduction of SGN apoptosis. Therefore, H_2 may be a potential therapy for sensorineural hearing impairment in AN patients.

Abbreviations

ABR, auditory brainstem response; AD, auditory dys-synchrony; AN, auditory neuropathy; CAP, compound action

potential; DPOAE, distortion product otoacoustic emission; EDTA, ethylenediaminetetraacetic acid; H_2, hydrogen gas; ·OH, hydroxyl radicals; PBS, phosphate-buffered saline; ROS, reactive oxygen species; RW, round window; SGN, spiral ganglion neuron; SPL, sound pressure level; TUNEL, terminal deoxynucleotidyl transferase-mediated dUTP-biotin nick-end labeling.

Acknowledgements

This work was supported by the State Key Program of the National Natural Science Foundation of China (No 30930098 to Jian-hua QIU), the Major State Basic Research Development Program of China (973 Program) (No 2011CB504505 to Jian-hua QIU) and the Young Scientists Fund of the National Natural Science Foundation of China (No 30801287 to Juan QU; 81101409 to Ke-liang XIE).

Author contribution

Jian-hua QIU and Ke-liang XIE designed research; Juan QU, Yun-na GAN, Ke-liang XIE, Wen-bo LIU, Ya-fei WANG, and Ren-yi HEI performed research; Wen-juan MI and Jian-hua QIU contributed new reagents or analytic tools; Jian-hua QIU analyzed data; Juan QU, Ke-liang XIE, and Jian-hua QIU wrote the paper.

References

1 Rance G. Auditory neuropathy/dys-synchrony and its perceptual consequences. Trends Amplif 2005; 9: 1–43.
2 Starr A, Picton TW, Sininger Y, Hood LJ, Berlin CI. Auditory neuropathy. Brain 1996; 119: 741–53.
3 Vlastarakos PV, Nikolopoulos TP, Tavoulari E, Papacharalambous G, Korres S. Auditory neuropathy: endocochlear lesion or temporal processing impairment? Implications for diagnosis and management. Int J Pediatr Otorhinolaryngol 2008; 72: 1135–50.
4 Ohsawa I, Ishikawa M, Takahashi K, Watanabe M, Nishimaki K, Yamagata K, *et al*. Hydrogen acts as a therapeutic antioxidant by selectively reducing cytotoxic oxygen radicals. Nat Med 2007; 13: 688–94.
5 Cai J, Kang Z, Liu WW, Luo X, Qiang S, Zhang JH, *et al*. Hydrogen therapy reduces apoptosis in neonatal hypoxia-ischemia rat model. Neurosci Lett 2008; 441: 167–72.
6 Cardinal JS, Zhan J, Wang Y, Sugimoto R, Tsung A, McCurry KR, *et al*. Oral hydrogen water prevents chronic allograft nephropathy in rats. Kidney Int 2010; 77: 101–9.
7 Dole M, Wilson FR, Fife WP. Hyperbaric hydrogen therapy: a possible treatment for cancer. Science 1975; 190: 152–4.
8 Huang CS, Kawamura T, Toyoda Y, Nakao A. Recent advances in hydrogen research as a therapeutic medical gas. Free Radic Res 2010; 44: 971–82.
9 Huang Y, Xie K, Li J, Xu N, Gong G, Wang G, *et al*. Beneficial effects of hydrogen gas against spinal cord ischemia-reperfusion injury in rabbits. Brain Res 2011; 1378: 125–36.
10 Ji X, Liu W, Xie K, Qu Y, Chao X, Chen T, *et al*. Beneficial effects of hydrogen gas in a rat model of traumatic brain injury via reducing oxidative stress. Brain Res 2010; 1354: 196–205.
11 Kajiyama S, Hasegawa G, Asano M, Hosoda H, Fukui M, Nakamura N, *et al*. Supplementation of hydrogen-rich water improves lipid and glucose metabolism in patients with type 2 diabetes or impaired glucose tolerance. Nutr Res 2008; 28: 137–43.
12 Xie K, Yu Y, Pei Y, Hou L, Chen S, Xiong L, *et al*. Protective effects of hydrogen gas on murine polymicrobial sepsis via reducing oxidative stress and HMGB1 release. Shock 2010; 34: 90–7.
13 Xie K, Yu Y, Zhang Z, Liu W, Pei Y, Xiong L, *et al*. Hydrogen gas improves survival rate and organ damage in zymosan-induced generalized inflammation model. Shock 2010; 34: 495–501.
14 Cai J, Kang Z, Liu K, Liu W, Li R, Zhang JH, *et al*. Neuroprotective effects of hydrogen saline in neonatal hypoxia-ischemia rat model. Brain Res 2009; 1256: 129–37.
15 Kikkawa YS, Nakagawa T, Horie RT, Ito J. Hydrogen protects auditory hair cells from free radicals. Neuroreport 2009; 20: 689–94.
16 Lin Y, Kashio A, Sakamoto T, Suzukawa K, Kakigi A, Yamasoba T. Hydrogen in drinking water attenuates noise-induced hearing loss in guinea pigs. Neurosci Lett 2011; 487: 12–6.
17 Schmiedt RA, Okamura HO, Lang H, Schulte BA. Ouabain application to the round window of the gerbil cochlea: a model of auditory neuropathy and apoptosis. J Assoc Res Otolaryngol 2002; 3: 223–33.
18 Lang H, Schulte BA, Schmiedt RA. Ouabain induces apoptotic cell death in type I spiral ganglion neurons, but not type II neurons. J Assoc Res Otolaryngol 2005; 6: 63–74.
19 Lang H, Schulte BA, Goddard JC, Hedrick M, Schulte JB, Wei L, *et al*. Transplantation of mouse embryonic stem cells into the cochlea of an auditory-neuropathy animal model: effects of timing after injury. J Assoc Res Otolaryngol 2008; 9: 225–40
20 Gorga MP, Johnson TA, Kaminski JR, Beauchaine KL, Garner CA, Neely ST. Using a combination of click- and tone burst-evoked auditory brain stem response measurements to estimate pure-tone thresholds. Ear Hear 2006; 27: 60–74..
21 Li J, Wang C, Zhang JH, Cai JM, Cao YP, Sun XJ. Hydrogen-rich saline improves memory function in a rat model of amyloid-beta-induced Alzheimer's disease by reduction of oxidative stress. Brain Res 2010; 1328: 152–61.
22 Sun H, Chen L, Zhou W, Hu L, Li L, Tu Q, *et al*. The protective role of hydrogen-rich saline in experimental liver injury in mice. J Hepatol 2011; 54: 471–80.
23 Elmore S. Apoptosis: a review of programmed cell death. Toxicol Pathol 2007; 35: 495–516.

Acta Pharmacologica Sinica (2012) 33: 452–458
 1671-4083/12 $32.00
www.nature.com/aps

Original Article

Plasma ghrelin levels are closely associated with severity and morphology of angiographically-detected coronary atherosclerosis in Chineses patients with diabetes mellitus

Min ZHANG[1], Wei-yi FANG[1, *], Fang YUAN[1], Xin-kai QU[1], Hua LIU[1], Ying-jia XU[1], Hui CHEN[1], Yong-fu YU[2], Yan SHEN[3], Zhi-chun ZHENG[3]

[1]Department of Cardiology, The Affiliated Chest Hospital, Shanghai Jiao Tong University, Shanghai 200030, China; [2]Department of Biostatistics, Fudan University, School of Public Health, Shanghai 200032, China; [3]Department of Radiology, The Affiliated Chest Hospital, Shanghai Jiao Tong University, Shanghai 200030, China

Aim: Low plasma ghrelin level was found to be associated with diabetes, and ghrelin was shown to inhibit pro-atherogenic changes in experimental models of atherosclerosis. The aim of this study was to investigate the relationship between plasma ghrelin levels and coronary atherosclerotic lesions in Chinese patients with diabetes.
Methods: Plasma ghrelin levels were measured using an ELISA kit. The severity of coronary artery disease (CAD) was determined via angiography. Composition of atherosclerotic plaques was detected via coronary CT angiography.
Results: A total of 178 patients with diabetes were recruited. Among the patients, 70 were diagnosed with acute coronary syndrome (ACS), 82 with stable angina pectoris (SAP) and 26 without coronary angiographic finding (controls). A negative correlation was found between ghrelin levels and the severity of the CAD, as determined via the Gensini score (r=-0.2434; P=0.0217). In diabetic patients with CAD and a complex lesion, the plasma ghrelin levels were significantly lower than in those with a simple lesion (ACS group: 3.81±0.49 ng/mL *vs* 4.72±0.50 ng/mL, P<0.0001; SAP group: 4.21±0.52 ng/mL *vs* 4.76±0.59 ng/mL, P=0.0397). Angiographically-detected complex lesion was an independent factor associated with ghrelin levels (adjusted beta coefficient=-0.67, 95% CI -0.97 to -0.37, P<0.0001).
Conclusion: Low plasma ghrelin level is closely related to angiographically-detected severity and the complex lesion morphology in Chinese diabetic patients with CAD.

Keywords: diabetes mellitus; ghrelin; atherosclerosis; coronary artery disease; coronary angiography; 64-slice CT scanner

Acta Pharmacologica Sinica (2012) 33: 452–458; doi: 10.1038/aps.2011.196; published online 27 Feb 2012

Introduction

The coronary atherosclerosis is one of the most common chronic complications of diabetes mellitus that require more accurate diagnoses and judgement of the severity of coronary lesions in diabetic patients. Ghrelin, a 28-amino acid peptide secreted by ghrelin cells of the gastric mucosa, increases appetite and the release of cortisol, anti-diuretic hormone, growth hormone and other homeostatic hormones. Studies previously demonstrated that low plasma ghrelin levels are reported to be associated with diabetes and ghrelin receptor density is higher in the cardiovascular system of atherosclerotic mice than that of normal controls, indicating that ghrelin and its receptor are potential targets for treatment of cardiovascular disease[1, 2]. As previously demonstrated by us and others, ghrelin inhibits pro-atherogenic changes in *in vitro* and *in vivo* experimental models. Ghrelin exhibits protective effects against the development of atherosclerosis by increasing coronary blood flow[3], improving endothelial function[4], inhibiting endothelial injury[5], inducing vasodilation, enhancing cholesterol efflux in macrophages[6], inhibiting smooth muscle cell (SMC) proliferation and apoptosis[7, 8] and exerting anti-inflammatory effects[9–11] on the cardiovascular system. Low plasma ghrelin levels were found in diabetic patients compared to weight-matched non-diabetic subjects[12].

However, there are few reports regarding the relationship between the severity of coronary artery lesions and plasma

* To whom correspondence should be addressed.
E-mail fwychest@126.com
Received 2011-10-11 Accepted 2011-12-12

ghrelin levels in the patients with diabetes. Until now, clinical research on the correlation between ghrelin and atherosclerotic disease mainly focused on the relationship between plasma ghrelin levels and carotid intima-media thickness (c-IMT), and the results of these studies were equivocal[13–17]. Additionally, there are no reports focusing on the association between ghrelin and coronary atherosclerotic lesions in diabetic patients. Therefore, we hypothesized that plasma ghrelin levels may be a risk factor for coronary atherosclerosis and could be used as a new predictive index for the severity of coronary atherosclerosis in patients with diabetes mellitus.

In the present study, we examined whether ghrelin levels could be used to predict the severity of coronary atherosclerotic lesions in diabetic patients with acute coronary syndrome (ACS) and stable angina pectoris (SAP), and investigated whether there is a relationship between plasma ghrelin levels and angiographically-detected coronary lesion morphology. Additionally, in a subgroup of diabetic patients, we examined plaque composition using 64-slice coronary CT angiography, and evaluated the association between plasma ghrelin levels and the plaque composition of coronary lesions.

Materials and methods

Subjects

The present study was approved by the local ethical committee and it was conducted in accordance with the Declaration of Helsinki. All participants signed an informed consent before enrolment. The study was performed at the Department of Cardiovascular Diseases, Shanghai Jiaotong University affiliated Chest Hospital. The subjects were 178 consecutive diabetic patients (65.68±11.62 years old) that underwent coronary angiography (CAG) in our department under the suspected diagnosis of coronary artery disease (CAD) between September 2009 and March 2011. Patients were considered diabetic if they were receiving treatment with insulin or oral hypoglycemic agents or if fasting blood glucose was >7 mmol/L. Patients with previous percutaneous coronary interventions (PCI) and coronary artery by-pass grafts (CABG) were excluded. Patients with concomitant inflammatory diseases, renal failure or neoplastic diseases were also excluded. Patients with diabetes were divided into SAP, ACS, and control groups. All diabetic patients with SAP and ACS that underwent coronary angiography had angiographically-detected narrowing of the luminal diameter of a major coronary artery of at least 50%. SAP was defined as chest pain typical of cardiac ischemia on exertion. Patients with ACS were diagnosed according to ACC/AHA 2007 Guidelines. The control group consisted of diabetic patients with normal luminal diameters of the major coronary arteries. After being admitted, all patients received aspirin, anti-anginal treatment (beta-blockers, nitrates or calcium channel blockers alone or in combination). High-risk patients were also treated with intravenous heparin or nitroglycerin. Prior to admission, lipid-lowering agents were administered to 45% patients.

Biochemical analysis

Fasting blood samples were taken from all patients with diabetes for the measurement of plasma total cholesterol, high-density lipoprotein (HDL)-cholesterol, low-density lipoprotein (LDL)-cholesterol and triglycerides. Total plasma ghrelin levels were measured using a commercially available enzyme immunoassay (EIA) kit (Phoenix Pharmaceuticals, Inc, Belmont, CA, USA), according to the manufacturer's protocol. The inter- and intra-assay coefficients of variance were less than 10%. Serum high sensitivity C-reactive protein (hs-CRP) levels were assayed via latex-enhanced immunonephelometric assays on a BN II analyzer (Dade Behring, Newark, Delaware, USA). Body mass index (BMI) was calculated for all patients. Smokers were defined as subjects who had smoked regularly during the previous 12 months. Systemic hypertension was defined as systolic blood pressure ≥140 mmHg and/or diastolic pressure ≥90 mmHg, based on at least 3 measurements or current use of antihypertensive drugs. Patients with dyslipidemia were assessed as being at risk if their LDL cholesterol was ≥140 mg/dL or their HDL cholesterol was ≤40 mg/dL, or if they were taking a hypolipidemic drug.

Coronary angiography analysis

All participants underwent selective coronary angiography using the Judkins technique. Angiography was performed via the femoral artery or radial artery, under local anesthesia (2% lidocaine) and with the use of contrast media. Angiography was performed so that each lesion could be viewed from at least two angles. Coronary lesions were identified as 'culprit lesions' based on clinical and ECG findings. Coronary angiograms were visually analyzed and scored by an interventional cardiologist, who had no knowledge of the patient characteristics.

The severity and extent of CAD was determined according to the following parameters: (1) Number of main coronary arteries with luminal stenosis exceeding 50%. The degree of coronary stenosis was assessed in the direction that showed the most severe stenosis, according to the American Heart Association standards[18]. Patients were assessed as having significant coronary stenosis if their stenosis was ≥50%. The left anterior descending artery, left circumflex artery, and right coronary artery were examined to evaluate the number of stenotic coronary arteries as 0 to 3-vessel disease (VD). If the left main trunk was involved, this was evaluated as a 2-VD by itself. (2) A modified Gensini Score (GS)[19]. The GS was computed to provide a measure of the extent and severity of CAD. The GS defines the narrowing of the lumen of the coronary arteries as 1 for 1% to 25% stenosis, 2 for 26% to 50% stenosis, 4 for 51% to 79% stenosis, 8 for 76% to 90% stenosis, 16 for 91% to 99% stenosis, and 32 for total occlusion. The score is then multiplied by the factor that represents the importance of the lesion's position in the coronary artery system. For example, 5 for the left main coronary artery, 2.5 for the proximal left anterior descending or proximal left circumflex artery, 1.5 for the mid-region, and 1 for the distal left anterior descending or

mid-distal region of the circumflex artery. (3) Angiographic morphology was divided into two types, specifically either simple or complex, based on the Ambrose classification[20]. In our analysis, total occlusions and intracoronary thrombi were considered complex lesions and not classified as separate angiographic variables.

Coronary CT angiography

CT scans were all performed in our hospital using a 64-slice CT scanner (Brilliance 64-slice CT scanner, Philips Healthcare, The Netherlands), and based on the acquisition protocol previously describes[21]. Axial CT images were reconstructed with a slice thickness of 0.75 mm and increments of 0.4 mm with retrospective ECG gating. Plaque was characterized as calcified or non-calcified plaque, as described previously. When plaque contained both calcified and non-calcified components with neither of them constituting >75% of the plaque volume, it was described as a partially calcified or mixed plaque.

Statistical analyses

Data was analyzed using Stata9.0 and results for normally distributed continuous variables were expressed as mean±SD and continuous variables with non-normal distribution were presented as median (interquartile range). Two groups were compared with an unpaired Student *t* test or Mann Whitney U test when the variance was heterogeneous. Statistical comparisons of three or more groups were performed by a one-way analysis of variance (ANOVA) or Kruskal–Wallis Test , where appropriate. In addition, Bonferroni-corrected *post hoc* test was conducted to adjust the observed significant level for multiple comparisons if the null hypothesis was rejected. Statistical analysis of categorical variables was performed using the chi-square test. Associations between clinical variables were examined by Spearman's rank correlation test and expressed as the Spearman correlation coefficient. Values of $P<0.05$ were considered significant.

Results

Plasma ghrelin levels and clinical severity

The present study included 178 patients with diabetes, with consisted of 58.4% men and 41.6% women. Coronary angiographic findings were negative for CAD in 26 (14.6%) patients, while CAD was confirmed in 152 (85.4%) patients, of which ACS was diagnosed in 70 patients and SAP was determined in 82 patients. Twenty-seven patients without diabetes and CAD was also chosen as negative control. As shown in figure 1A, plasma ghrelin levels were lower in diabetic patients than in non-diabetic subjects (4.74±0.60 ng/mL *vs* 6.72±0.73 ng/mL; $P<0.01$), so diabetic patients had been chosen as this thesis's subject. There were no significant differences in plasma ghrelin levels among diabetic patients with ACS, SAP and control group despite plasma ghrelin levels in ACS group was in the trend of lowering.

Plasma ghrelin levels and coronary angiographic results

There was no significant difference in plasma ghrelin levels among diabetic patients with 1-vessel, 2-vessel, and 3-vessel CAD ($F=1.35$, $P=0.2642$) (Figure 1B).

The Gensini score ranged from 0 to 254, and the median was 31. There was a negative correlation between plasma ghrelin levels and the severity of CAD in diabetic patients, as determined with the Gensini score (Spearman correlation coefficient $r=-0.2434$; $P=0.0217$).

Twelve of the 82 culprit lesions in diabetic patients with SAP and 30 of the 70 culprit lesions in diabetic patients with ACS showed angiographic evidence of a complex lesion. Table 1 shows the characteristics of diabetic patients with angiographically-detected simple and complex lesions. As shown in Figure 1C, plasma ghrelin levels in diabetic patients with CAD and a complex lesion were significantly lower than those with a simple lesion (ACS group: 3.81±0.49 ng/mL *vs* 4.72±0.50 ng/mL; $P<0.01$. SAP group: 4.21±0.52 ng/mL *vs* 4.76 ±0.59 ng/mL; $P=0.0397$).

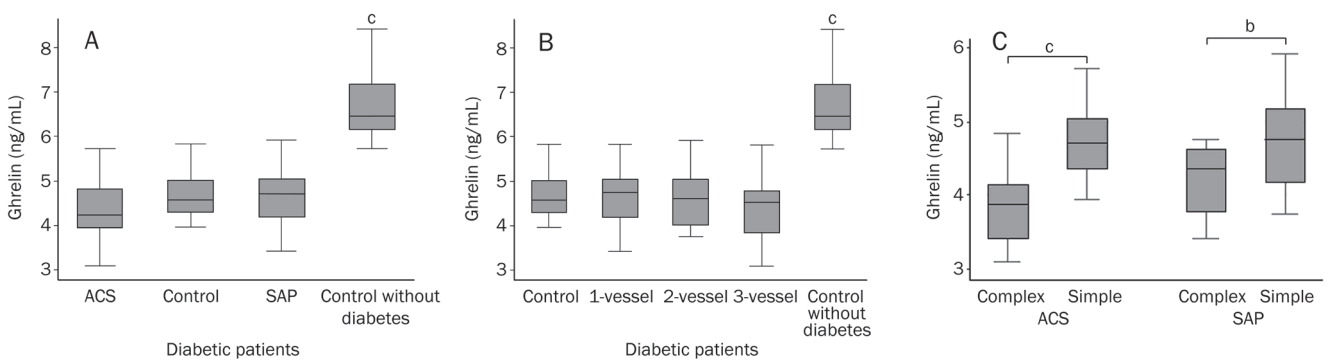

Figure 1. (A) Plasma ghrelin levels in control subjects, and ACS and SAP group in diabetic patients and control without diabetic patients. (B) Plasma ghrelin levels in diabetic patients with 1-vessel, 2-vessel, and 3-vessel CAD , control subjects and control without diabetic patients. (C) Relationship between plasma ghrelin levels and coronary angiographic morphology (*ie* simple or complex) in diabetic patients with SAP and ACS. Mean±SD. $^bP<0.05$, $^cP<0.01$.

Table 1. Clinical and angiographic characteristics of diabetic patients with SAP and UAP, and with angiographically-detected simple and complex lesions.

	SAP			ACS		
	Simple (*n*=70)	Complex (*n*=12)	*P* value	Simple (*n*=40)	Complex (*n*=30)	*P* value
Age (years)	67.03±11.13	71.00±9.42	0.4060	66.40±9.69	66.60±10.08	0.9530
Male (%)	40 (76.92%)	12 (23.08%)	0.0440	18 (45.00%)	22 (55.00%)	0.0937
Hypertension (%)	62 (86.11%)	10 (13.89%)	0.7171	30 (55.56%)	24 (44.44%)	0.7274
Smoking (%)	14 (87.50%)	2 (12.50%)	0.8490	6 (50.00%)	6 (50.00%)	0.6977
Hypercholesterolaemia (%)	18 (81.82%)	4 (18.18%)	0.6971	20 (76.92%)	6 (23.08%)	0.0691
Total cholesterol (mmol/L)	4.45±1.04	4.13±1.09	0.2452	4.66±1.11	4.50±1.15	0.6931
HDL cholesterol (mmol/L)	1.04±0.23	0.94±0.27	0.3405	1.01±0.19	0.91±0.20	0.1316
LDL cholesterol (mmol/L)	2.68±0.84	2.64±0.83	0.6713	2.65±1.09	2.82±0.58	0.5386
Triglycerides (mmol/L)	2.23±2.02	1.52±1.13	0.2528	2.00±1.24	1.95±1.30	0.7015
BMI	23.60±1.17	24.81±2.00	0.1086	23.43±1.01	25.20±1.20	0.0000
The number of stenotic coronary arteries						
1-vessel	36 (94.74%)	2 (5.26%)	0.0069	6 (50.00%)	6 (50.00%)	0.0397
2-vessel	24 (92.31%)	2 (7.69%)		20 (71.43%)	8 (28.57%)	
3-vessel	10 (55.56%)	8 (44.44%)		14 (46.67%)	16 (53.33%)	
Gensini Score (GS)	30.11±35.67	80.67±50.98	0.0022	47.75±32.06	80.60±61.61	0.0510
hs-CRP (mg/dL)	2.64±6.03	2.74±5.38	0.3216	10.21±14.42	15.42±16.00	0.2414
Ghrelin (ng/mL)	4.76±0.59	4.21±0.52	0.0397	4.72±0.50	3.81±0.49	0.0000

Categorical variables are expressed as percentages and continuous variables as mean±SD or median (interquartile ranges), where appropriate. HDL, high density lipoprotein; LDL, low density lipoprotein; hs-CRP, high-sensitivity C-reactive protein.

Stepwise regression analysis

To identify independent factors associated with plasma ghrelin levels and severity of angiographically-detected lesions in diabetic patients with SAP and ACS, a multivariate logistic regression analysis was performed using the following variables: age, gender, risk factors, HDL and LDL cholesterol, TG, serum hs-CRP levels, number of stenotic coronary arteries, Gensini score and angiographically-detected complex or simple lesions. Stepwise regression analysis revealed that angiographically-detected complex lesions, BMI, CH (cholesterol), TG and LDL cholesterol were independent factors associated with plasma ghrelin levels in diabetic patients (angiographically-detected complex or simple lesions: adjusted beta coefficient=-0.67, 95% CI -0.97 to -0.37, $P<0.0001$; BMI: adjusted beta coefficient=-0.12, 95% CI -0.23 to -0.02, $P=0.018$; CH: adjusted beta coefficient=-0.34, 95% CI -0.59 to -0.09, $P=0.008$; TG: adjusted beta coefficient=0.10, 95% CI 0.01 to 0.19, $P=0.048$; LDL: adjusted beta coefficient=0.31, 95% CI 0.03 to 0.60, $P=0.032$).

Plasma ghrelin levels and plaque composition

Thirty-two of the 178 diabetic patients (subgroup analysis) who underwent coronary CT angiography were diagnosed with CAD (*ie* 14 had ACS and 18 had SAP) prior to admission (Figure 2). There were no significant differences between plasma ghrelin levels in patients with calcified (4.56±1.21 ng/mL, $n=11$), non-calcified (4.63±1.18 ng/mL, $n=6$), and mixed plaques (4.47±1.28, $n=15$) ($F=0.06$, $P=0.9456$), as determined by coronary CT angiography (Figure 3).

Discussion

To the best of our knowledge, this is the first study to demonstrate that decreased plasma ghrelin levels are associated with the severity of angiographically-detected coronary lesions in diabetic patients. The reason why we had chosen diabetic patients as this thesis's subject was that plasma ghrelin levels were lower in diabetic patients than in non-diabetic subjects, thereby baseline data were established. The severity of coronary lesion might not be simply implied by clinical diagnosis and 1-, 2-, or 3-vessel CAD involved, so no significant association between ghrelin and the two aspects above was observed. While through analysis of the more sensitive markers such as Gensini scores and Ambrose classification in response to the severity of coronary atherosclerosis and plaque stability, this study showed that there is a relationship between decreased plasma ghrelin levels and severity or complex coronary lesion morphology in diabetic patients with SAP and in those with ACS. These observations strongly support the concept of a direct relationship between plasma ghrelin levels and angiographically-detected severity and morphology of coronary artery atherosclerosis in diabetic patients. Furthermore, in the present study, there were no significant correlations between plasma ghrelin levels and plaque composition of the coronary lesion in patients with SAP or ACS, as determined via coronary CT angiography. There are several probable explanations for the major findings of the present study. One is that ghrelin

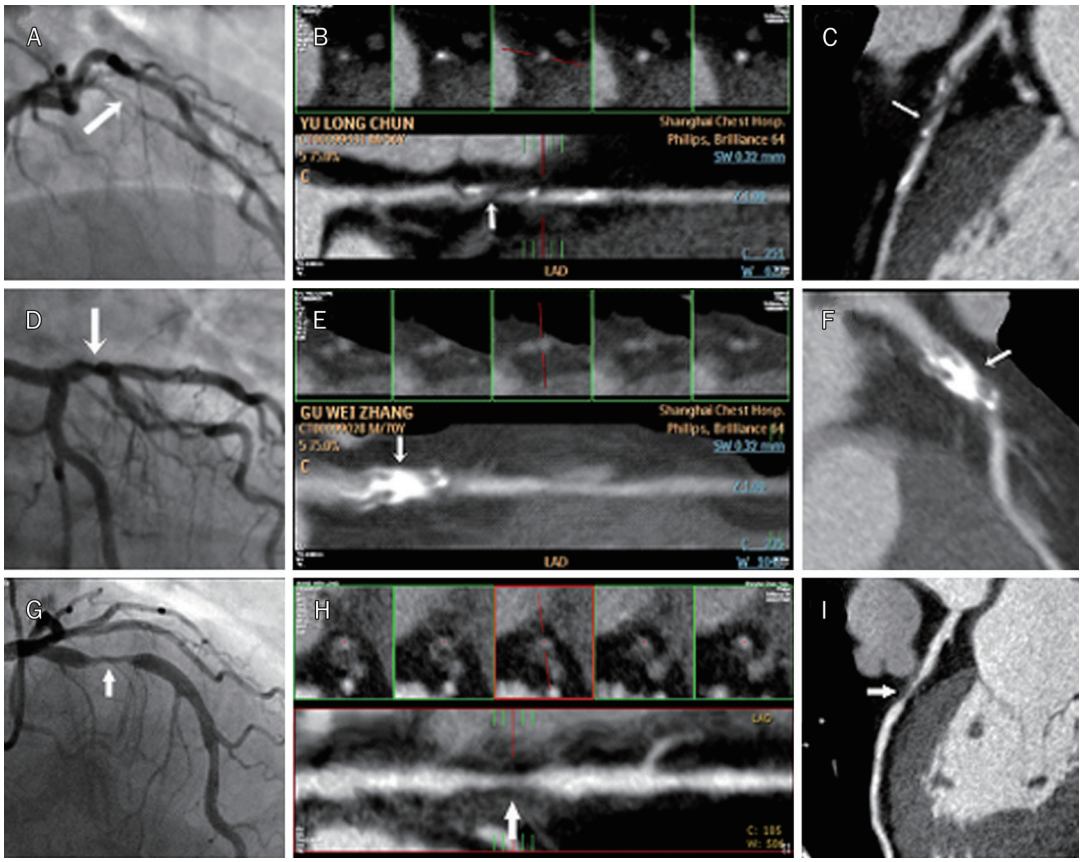

Figure 2. (A) Angiographic images illustrating a long lesion in LAD (arrow). (B–C) Coronary CT angiography depicting a mixed plaque and the lesion in the angiographic image shown in A. (D) Angiographic image illustrating a localized lesion in LAD (arrow). (E–F) Coronary CT angiography depicting a calcified plaque match and the lesion in the angiographic image shown in D. (G) Angiographic image illustrating a localized lesion in LAD (arrow). (H–I) Coronary CT angiography revealing a non-calcified plaque and the lesion in the angiographic image shown in G.

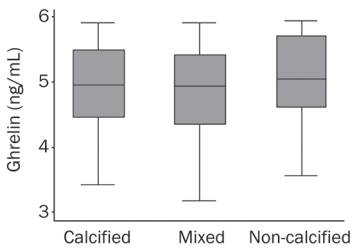

Figure 3. Plasma ghrelin levels in diabetic patients with calcified, non-calcified, and mixed plaques using coronary CT angiography.

appears to have beneficial features in relation to three essential processes of atherosclerotic activity, namely endothelial function, inflammation and apoptosis. Ghrelin increases endothelial nitric oxide synthase expression in growth homone (GH)-deficient rats[4], suggesting that ghrelin has GH-independent cardio-protective effects. Another important finding indicated that ghrelin reversed endothelial dysfunction in patients with metabolic syndrome by increasing nitric oxide bioactivity[22], suggesting that ghrelin may play a role in the pathobiology of atherosclerosis. Recent research also found that ghrelin has an anti-inflammatory effect in the cardiovascular system. Skilton found that ghrelin can upregulate the expression of molecules, such as intercellular adhesion molecule-1 (ICAM-1), vascular cell adhesion molecule-1 (VCAM-1), E-selectin, in human umbilical vein endothelial cells (HUVECs)[10]. LI *et al*[11] also reported that the release of inflammatory factors and upregulation of the nuclear factor, NF-kappaB, through the inducing effects of tumor necrosis factor (TNF)-α in HUVECs could be inhibited by exogenous ghrelin. We previously demonstrated that exogenous ghrelin significantly inhibited cytokine-induced CD40 expression in HUVECs potentially via the regulation of the inflammatory process in atherosclerosis[9]. We also found that ghrelin has both anti-proliferative and anti-apoptotic functions in vascular smooth muscle cells (SMC)[7]. These actions of ghrelin may have significant theoretical and clinically applicable value in the development of coronary aortic stenotic patches, patch stability, and postoperative re-stenosis. Furthermore, GHS-receptor density has been shown to be upregulated in both atherosclerotic carotid arteries and saphenous vein grafts[23], which further supports the beneficial role of ghrelin in atherosclerosis. Secondly, low ghrelin concentrations have been associated with metabolic disturbances, such as insulin resistance, type II diabetes, and metabolic syndrome[12], which are also commonly recognized as risk factors for atherosclerosis. Ghrelin induces a positive energy balance in animal experiments by stimulating feeding and reducing fat utilization. However, in humans, ghrelin levels in obese subjects are low[12]. Therefore, a negative association between ghrelin and coronary atherosclerosis may be expected. Lastly, studies have shown a positive association between ghrelin concentrations and HDL levels[24]. Ghrelin binding to HDL particles may, in part, explain this association,

and be of functional significance in atherogenesis.

Until now, clinical research on the correlation between ghrelin and atherosclerotic disease mainly focused on the relationship between plasma ghrelin levels and carotid IMT. Our findings are different in that plasma ghrelin concentrations were reported to be positively associated with carotid IMT in middle-aged males[13] and children with Prader-Willi Syndrome[14]. However, our findings were consistent with the majority of the currently available data. Specifically, a multivariable regression analysis revealed that des-acyl ghrelin had a significant inverse correlation with cIMT in elderly hypertensives[17]. Low ghrelin serum levels were associated with advanced carotid atherosclerosis in patients with type II diabetes mellitus[15] and elderly patients with metabolic syndrome[16], implicating the role of ghrelin as a novel atherosclerotic biomarker and predictive index of atherosclerosis. A potential reason for the equivocal results may be that previous studies were conducted in normal people and children instead of patients with CAD, and therefore IMT measurements in these people may have less severe atherosclerotic lesions. That is, ghrelin levels are elevated only in advanced states of atherosclerotic disease. This explanation might also be the reason for the lack of association in females in a study conducted by Poykko[12], which found that carotid atherosclerosis in females was less advanced compared to age-matched males, as indicated by the lower IMT-values and number of carotid atherosclerotic plaques in females. While some of the above-mentioned studies are consistent with our findings, these studies had patients with advanced atherosclerosis lesion, such as elderly patients with metabolic syndrome, hypertension, type II diabetes.

To our knowledge, this is the first study of its kind to demonstrate a close correlation between serum ghrelin levels and the extent and severity of coronary atherosclerosis lesions in patients with diabetes. These results point to a prognostic value of serum ghrelin in coronary atherosclerosis. Several studies have reported that angiographically-detected complex lesions in patient with ACS are strongly associated with disrupted plaques and/or thrombus formation, as assessed by ultrasound[25] and angioscopy[26]. This observation supports angiographic assessments of plaque complexity. We also observed a negative correlation between ghrelin levels and angiographically-detected complex lesions in patients with ACS. Therefore, serum ghrelin may be a prognostic tool for determining the extent, severity and instability of atherosclerosis plaques.

One limitation of the present study was that we did not utilize contemporary tools of plaque morphology assessments, such as ultrasound or optical coherence tomography. Furthermore, there were no significant correlations between plasma ghrelin levels and plaque composition with calcified, non-calcified and mixed plaques using coronary CT angiography. Possible explanations for this may be the relatively small number of patients that had a coronary CT scan performed, and the limitation of CT in differentiating the characteristics and stability of plaque, with the exception of diagnosing calcification. Future studies using ultrasound or optical coherence tomography are necessary to confirm the association between plasma ghrelin levels and plaque morphology.

Acknowledgements

This work was supported by The National Natural Science Foundation of China (81000087), Fund of Basic Research of Science and Technology Commission of Shanghai Municipality (10JC1414000), Fund of Shanghai Health Department (2008Y049) and The PhD Programs Foundation of Shanghai Jiao Tong University (BXJ201142).

Author contribution

Wei-yi FANG designed research; Min ZHANG performed research and wrote the paper; Fang YUAN and Hua LIU analyzed biochemical examination data; Xin-kai QU and Hui CHEN performed coronary angiography and analyzed coronary angiographic results; CT scans were performed and analyzed by Zhi-chun ZHENG and Yan SHEN; Yong-fu YU accomplished statistical analyses; Ying-jia XU revised the english.

References

1 Kojima M, Hosoda H, Date Y, Nakazato M, Matsuo H, Kangawa K. Ghrelin is a growth-hormone-releasing acylated peptide from stomach. Nature 1999; 402: 656–60.

2 Katugampola SD, Pallikaros Z, Davenport AP. [^{125}I-His(9)]-ghrelin, a novel radioligand for localizing GHS orphan receptors in human and rat tissue: up-regulation of receptors with atherosclerosis. Br J Pharmacol 2001; 134: 143–9.

3 Chang L, Ren Y, Liu X, Li WG, Yang J, Geng B, *et al*. Protective effects of ghrelin on ischemia/reperfusion injury in the isolated rat heart. J Cardiovasc Pharmacol 2004; 43: 165–70.

4 Shimizu Y, Nagaya N, Teranishi Y, Imazu M, Yamamoto H, Shokawa T, *et al*. Ghrelin improves endothelial dysfunction through growth hormone-independent mechanisms in rats. Biochem Biophys Res Commun 2003; 310: 830–5.

5 Caliskan Y, Gorgulu N, Yelken B, Yazici H, Oflaz H, Elitok A, *et al*. Plasma ghrelin levels are associated with coronary microvascular and endothelial dysfunction in peritoneal dialysis patients. Ren Fail 2009; 31: 807–13.

6 Demers A, Caron V, Rodrigue-Way A, Wahli W, Ong H, Tremblay A. A concerted kinase interplay identifies PPARgamma as a molecular target of ghrelin signaling in macrophages. PLoS One 2009; 4: e7728.

7 Zhang M, Yuan F, Liu H, Chen H, Qiu X, Fang W. Inhibition of proliferation and apoptosis of vascular smooth muscle cells by ghrelin. Acta Biochim Biophys Sin 2008; 40:769–76.

8 Baldanzi G, Filigheddu N, Cutrupi S, Catapano F, Bonissoni S, Fubini A, *et al*. Ghrelin and des-acyl ghrelin inhibit cell death in cardiomyocytes and endothelial cells through ERK1/2 and PI 3-kinase/AKT. J Cell Biol 2002; 159: 1029–37.

9 Zhang M, Yuan F, Chen H, Qiu X, Fang W. Effect of exogenous ghrelin on cell differentiation antigen 40 expression in endothelial cells. Acta Biochim Biophys Sin 2007; 39: 974–81.

10 Skilton MR, Nakhla S, Sieveking DP, Caterson ID, Celermajer DS. Pathophysiological levels of the obesity related peptides resistin and ghrelin increase adhesion molecule expression on human vascular endothelial cells. Clin Exp Pharmacol Physiol 2005; 32: 839–44.

11 Li WG, Gavrila D, Liu X, Wang L, Gunnlaugsson S, Stoll LL, *et al*. Ghrelin inhibits proinflammatory responses and nuclear factor-kappaB activation in human endothelial cells. Circulation 2004; 109: 2221–6.
12 Poykko SM, Kellokoski E, Horkko S, KaumaH, Kesaniemi YA, Ukkola O. Low plasma ghrelin is associated with insulin resistance, hypertension, and the prevalence of type 2 diabetes. Diabetes 2003; 52: 2546–53.
13 Poykko SM, Kellokoski E, Ukkola O, kauma H, Paivansalo M, Kesaniemi YA, *et al*. Plasma ghrelin concentrations are positively associated with carotid artery atherosclerosis in males. J Int Med 2006; 260: 43–52.
14 Kim SJ, Paik KH, Kim DI, Choe YH, Kim SW, Jin DK. Correlation between hyperghrelinemia and carotid artery intima-media thickness in children with prader-willi syndrome. Yonsei Med J 2010; 51: 339–44.
15 Kadoglou NP, Sailer N, Moumtzouoglou A, Kapelouzou A, Tsanikidis H, Vitta I, *et al*. Visfatin (nampt) and ghrelin as novel markers of carotid atherosclerosis in patients with type 2 diabetes. Exp Clin Endocrinol Diabetes 2010; 118: 75–80.
16 Kotani K, Sakane N, Saiga K, Adachi S, Mu H, Kurozawa Y, *et al*. Serum ghrelin and carotid atherosclerosis in older Japanese people with metabolic syndrome. Arch Med Res 2006; 37: 903–6.
17 Yano Y, Toshinai K, Inokuchi T, Kangawa K, Shimada K, Kario K, *et al*. Plasma des-acyl ghrelin, but not plasma HMW adiponectin, is a useful cardiometabolic marker for predicting atherosclerosis in elderly hypertensive patients. Atherosclerosis 2009; 204: 590–4.
18 Austen WG, Edwards JE, Frye RL, Gensini GG, Gott VL, Grifith LS, *et al*. A reporting system on patients evaluated for coronary artery disease: Report of the Ad Hoc committee for grading of coronary artery disease, council on cardiovascular surgery, American Heart Association. Circulation 1975; 51: 5–40.
19 Gensini GG. A more meaningful scoring system for determining the severity of coronary heart disease. Am J Cardiol 1983; 51: 606.
20 Ambrose JA, Winters SL, Stern A, Eng A, Teichholz LE, Gorlin R, *et al*. Angiographic morphology and the pathogenesis of unstable angina pectoris. J Am Coll Cardiol 1985; 5: 609–16.
21 Hoffmann U, Bamberg F, Chae CU, Nichols JH, Rogers IS, Seneviratne SK, *et al*. Coronary computed tomography angiography for early triage of patients with acute chest pain: the ROMICAT (rule out myocardial infarction using computer assisted tomography) trial. J Am Coll Cardiol 2009; 53: 1642–50.
22 Tesauro M, Schinzari F, Iantorno M, Rizza S, Melina D, Lauro D, *et al*. Ghrelin improves endothelial function in patients with metabolic syndrome. Circulation 2005; 112: 2986–92.
23 Katugampola SD, Maguire JJ, Kuc RE, Wiley KE, Davenport AP. Discovery of recently adopted orphan receptors for apelin, urotensin II, and ghrelin identified using novel radioligands and functional role in the human cardiovascular system. Can J Physiol Pharmacol 2002; 80: 369–74.
24 Purnell JQ, Weigle DS, Breen P, Cummings DE. Ghrelin levels correlate with insulin levels, insulin resistance, and high-density lipoprotein cholesterol, but not with gender, menopausal status, or cortisol levels in humans. J Clin Endocrinol Metab 2003; 88: 5747–52.
25 Maehara A, Mintz GS, Bui AB, Walter OR, Castagna MT, Canos D, *et al*. Morphologic and angiographic features of coronary plaque rupture detected by intravascular ultrasound. J Am Coll Cardiol 2002; 40: 904–10.
26 Waxman S, Mittleman MA, Zarich SW, Fitzpatrick PJ, Lewis SM, Leeman DE, *et al*. Plaque disruption and thrombus in Ambrose's angiographic coronary lesion types. Am J Cardiol 2003; 92: 16–20.

Acta Pharmacologica Sinica (2012) 33: 459–469
 1671-4083/12 $32.00
www.nature.com/aps

Original Article

Chronic cardiotoxicity of doxorubicin involves activation of myocardial and circulating matrix metalloproteinases in rats

Monika IVANOVÁ[1], Ima DOVINOVÁ[2], Ľudmila OKRUHLICOVÁ[1], Narcisa TRIBULOVÁ[1], Petra ŠIMONČÍKOVÁ[1], Monika BARTEKOVÁ[1], Jana VLKOVIČOVÁ[1], Miroslav BARANČÍK[1, *]

[1]*Institute for Heart Research, Slovak Academy of Sciences, Dúbravská cesta 9, Bratislava, 840 05, Slovakia;* [2]*Institute of Normal and Pathological Physiology, Slovak Academy of Sciences, Sienkiewiczova 1, Bratislava, 813 71, Slovakia*

Aim: To investigate the role of matrix metalloproteinases (MMPs) in the responses of rats to a prolonged doxorubicin (DOX) treatment.
Methods: Male Wistar rats were used. DOX was administered by intraperitoneal injections of seven doses (cumulative dose was 15 mg/kg). Control animals were treated with saline. Tissue or plasma samples were collected at four and eight weeks after the application of the last dose. Protein levels were determined by immunoblot assay, and MMP activities were measured by gelatin zymography. Superoxide content was analyzed using a lucigenin chemiluminescence assay and superoxide dismutase (SOD) activities with a SOD assay kit. Qualitative structural alterations of the heart were characterized by transmission electron microscopy.
Results: Systolic blood pressure was higher in DOX-treated rats as compared with the control rats at 8 weeks after treatment. In contrast, there were no differences in the heart rate between the control and DOX-treated rats. DOX treatment caused marked heterogeneous subcellular alterations of cardiomyocytes and structural disorganizations of the cardiac extracellular space. The effects of DOX were linked to a stimulation of plasma MMP-2 and MMP-9 activities that had already increased by 4 weeks after the end of the treatment. In the left ventricle, however, DOX only led to increased MMP-2 activation at 8 weeks after the end of treatment. These changes in tissue MMP-2 were connected with stimulation of Akt kinase activation, inhibition of SOD, an increase in superoxide levels, induction of iNOS protein expression and caspase-3 activation.
Conclusion: Our results show that MMPs are involved in the chronic cardiotoxicity of DOX in rats. The data also suggest that reactive oxygen species (superoxide), NO production (iNOS) and the Akt kinase pathway can modulate MMP-2 activities in rat hearts influenced by DOX.

Keywords: doxorubicin; cardiotoxicity; matrix metalloproteinases; Akt kinase; heart; reactive oxygen species

Acta Pharmacologica Sinica (2012) 33: 459–469; doi: 10.1038/aps.2011.194; published online 26 Mar 2012

Introduction

The anthracycline compound doxorubicin (DOX) is an anticancer drug with limited clinical use due to its serious adverse effects, including cumulative dose-dependent cardiac toxicity. The specific mechanisms of doxorubicin cardiotoxicity are complex and, despite decades of research, remain unclear. Several mechanisms may play a role in the effects induced by DOX, including inhibition of nucleic acid and protein synthesis, changes in adrenergic function, mitochondrial abnormalities, lysosomal alterations, altered sarcolemmal Ca^{2+} transport, and an imbalance of myocardial electrolytes[1]. Oxidative/nitrosative stress plays an important role in the realization of the effects of DOX. Due to this stress, there is an increased production of free radicals and a modulation of downstream effector signaling pathways[2]. The effects of DOX are mediated through the induction of reactive oxygen species (ROS) or via a DOX-mediated induction of nitric oxide synthases (NOS), leading to nitric oxide (NO) formation. Identification of the proteins with altered expression and/or activities following DOX treatment and an understanding of their effector cell signaling pathways may provide new insights into the mechanisms responsible for the toxic effects of DOX.

DOX treatment can produce a number of consequences at the subcellular level that may persist for a prolonged time after its application. For example, the delay between anthracycline administration and the occurrence of clinical symptoms is generally 1–2 years in adults but may extend to much longer periods in children[3]. In experimental animal models,

* To whom correspondence should be addressed.
E-mail Miroslav.Barancik@savba.sk
Received 2011-08-06 Accepted 2011-12-06

Acta Pharmacologica Sinica (2012) 33: 468–478
 1671-4083/12 $32.00
www.nature.com/aps

some side effects of DOX treatment can take weeks or months to occur[4]. The cardiotoxic effects of DOX often result in a cardiomyopathy that is similar to dilated cardiomyopathy. This cardiomyopathy manifests as a dilation of all of the chambers of the heart and a severe impairment of left ventricular systolic function that eventually leads to congestive heart failure[5]. Heart failure develops over a prolonged time period and is associated with myocardial remodeling, which also involves changes in the major structural proteins of the extracellular matrix (ECM). The matrix metalloproteinases (MMPs) play an important role in remodeling of the ECM. These enzymes belong to the zinc-dependent endopeptidases family and are synthesized as zymogens that can be activated by proteolytic cleavage of an amino-terminal domain or through an oxidant-induced conformational change (with no change in molecular weight). The activities of MMPs in tissues are also tightly regulated by the endogenous tissue inhibitors of matrix metalloproteinases (TIMPs) [6].

MMPs are involved in the degradation and remodeling of the ECM matrix under physiological and pathological conditions. Moreover, there is emerging evidence that MMPs can also degrade other non-matrix substrates, including specific cardiac proteins[7, 8], to affect a number of biological processes within the myocardium. Circulating MMPs have been found to be increased in patients with heart failure and have been proposed to be a prognostic factor for survival in such patients[9]. It has also been shown that the intracellular actions of MMP-2 are associated with acute ischemia and reperfusion injury[7]. Furthermore, using isolated heart preparations, it was demonstrated that myocardial injury induced by peroxynitrite, a product of the reaction of superoxide anion and NO, is mediated through the release and activation of MMP-2 within the coronary circulation[10]. The activation of MMPs has also been implicated in the realization of acute effects of DOX. In mice, it was found that an acute cardiotoxicity induced by doxorubicin applied in a single dose was connected with the increased activities of MMP-2 and MMP-9[11]. However, the role of MMPs in processes associated with the chronic effects of DOX remains unclear.

The increase in ROS and the dysregulation of nitric NO production play very essential roles in promoting the toxic effects of DOX[2]. The effects of ROS and NO on MMPs can occur in different ways, including direct posttranslational modifications of MMPs, the induction of intracellular factors that can modulate MMP transcription, and as the induction of signaling molecules, which in turn alter the MMP transcription. Several studies have demonstrated that the expression and activation of MMPs is regulated by protein kinases, such as the MAPKs and PI3K/Akt[12, 13], and emerging evidence indicates that some protein kinases modulate MMPs in response to DOX in cardiac cells [14].

This study investigated the involvement of MMPs on the chronic effects induced by repeated application of DOX in rats. Our aim was to characterize the alterations in MMP levels, activation and release several weeks after the application of DOX, and to assess the specific mechanisms involved in the modulation of MMPs as a consequence of DOX treatment.

Materials and methods

Experimental model

Ten-week-old male Wistar rats were purchased from Dobra Voda (Slovakia). The animals were acclimatized to laboratory conditions for one week prior to the start of the study. In the study, 11-weeks old animals weighing 230–260 g were used. All animals were housed at a temperature of 22–24 °C in individual cages and fed a regular pellet diet *ad libitum*. The rats used in the studies were divided into four experimental groups — two control (C — 4 and 8 weeks) groups and two doxorubicin (DOX — 4 and 8 weeks) groups. Eight animals were used for each experimental group. In the DOX groups, the rats received seven intraperitoneal injections of 2.15 mg/kg of DOX over a 3-week period (the total cumulative dose of DOX was 15 mg/kg). The control animals were treated with saline. The animals were anaesthetized with thiopental (50 mg/kg, ip), and samples of tissues or plasma were collected four or eight weeks after the application of the final dose of DOX or saline. All animal experiments were performed in accordance with the rules issued by the State Veterinary Administration of the Slovak Republic, legislation No 289/2003, according to the regulations of the Animal Research and Care Committee of Institute for Heart Research SAS.

Systolic blood pressure and heart rate measurements

Systemic blood pressure (SBP) and heart rate (HR) were measured non-invasively through tail cuff plethysmography (PowerLab 4/30, ADInstruments) in both the control and DOX-treated groups. For the blood pressure measurements, eight animals in each experimental group were used. The measurements were performed prior to the first DOX or saline application and four or eight weeks after the final application.

Sample collection

At the end of the experiment, the animals were anesthetized with injection with thiopental (50 mg/kg, ip) and were euthanized by thoracotomy and a rapid excision of their hearts. The excised hearts were weighed and separated into the left ventricle (LV) and right ventricle (RV). The whole heart weights (HW) and left ventricular weights (LVW) were registered. The LV is the largest part of the rat heart, comprising nearly the entire heart, and its function is critical for physiological function. Moreover, different pathological stimuli significantly affect the physiological and biochemical parameters of the LV and its function. Therefore, our present measurements were focused on changes in the left ventricular tissue. Further processing of the collected left ventricular tissue samples was dependent on the following assay: The tissue ventricular samples for biochemical analysis were immediately frozen in liquid nitrogen and stored at -75 °C until use. For the transmission electron microscopy studies, small blocks of transmural left ventricular tissues were fixed in buffered 2.5% glutaraldehyde immediately after collection. For measurements of superoxide levels, tissues of the left ventricle were collected

and placed into ice-cold, Krebs-Henseleit buffer.

The plasma samples were prepared from whole artery blood drawn from the chest of the rats immediately after excision of the heart. Citrate was immediately added to the collected blood (resulting concentration 0.76%), followed by centrifugation of the blood for 5 min at 1200×*g* to obtain the plasma. The prepared plasma samples were stored at -20 °C until further analysis.

Transmission electron microscopy

Small (1–2 mm^3) transmural ventricular heart tissue samples were routinely processed for electron microscopy. The samples were fixed in 2.5% glutaraldehyde in 100 mmol/L cacodylate buffer at 40 °C, washed, and then subsequently postfixed in 1% OsO_4 and embedded in Epon812. Ultrathin sections of the tissue were stained with uranyl acetate and lead citrate. The ultrastructure of the myocardial tissue was evaluated using a transmission electron microscope Tesla 500 (Brno, Czech Republic).

Measurement of superoxide levels

The production of superoxide (O_2^-) was evaluated using a Lucigenin Enhanced Chemiluminiscence assay[15]. Left ventricle tissue samples were cut into small pieces of up to 15 mg wet weight and stored in Krebs-Henseleit buffer on ice until measured. Prior to the assay, the tissues were equilibrated for 20 min at 37 °C. During the assay, the tissue samples were incubated in a 50 mmol/L solution of lucigenin in Krebs-Henseleit buffer at 37 °C and chemiluminiscence was measured every 30 s for 5 min using a Turner Designs TD-20/20 luminometer. The data were expressed as relative luminiscence units per mg of tissue (RLU·mg^{-1} tissue).

Determination of superoxide dismutase activity

The superoxide dismutase (SOD) activity in the LV was analyzed using a SOD Assay kit (Fluka), which assays SOD activity by utilizing a highly water-soluble tetrazolium salt, WST-1 (2-(4-Iodophenyl)-3-(4-nitrophenyl)-5-(2,4-disulfophenyl)-2*H*-tetrazolium, monosodium salt) that produces a water-soluble formazan dye upon reduction with superoxide anion. The rate of WST-1 reduction with O_2^- is linearly related to the xanthine oxidase activity and is inhibited by SOD. Therefore, the SOD activity was determined to be inhibition activity and was quantified by measuring the color decrease of WST-1-formazan production at 450 nm. Tissue homogenates from isolated left ventricles were analyzed. The tissue was homogenized in phosphate buffer (pH 7.4). The changes in formazan production were analyzed for 30 min at 37 °C using a microplate reader (Thermo Scientific Multiscan FC, Finland). The SOD activities were calculated using a SOD standard curve and expressed as U·mg^{-1} protein.

Determination of total antioxidant status

The total antioxidant status (TAS) of the samples from the LV was determined using a decolorization assay. This assay makes use of a stable ABTS (2,2′-azinobis-(3-ethylbenzothiazoline-6-sulfonic acid)) radical prepared by the reaction of ABTS and potassium persulfate, as described previously[16]. It is known that the amount of ABTS radical is reduced in the presence of hydrogen-donating antioxidants, and these changes can be measured spectrophotometrically. We incubated the tissue sample homogenates (used also for assay of the SOD activities) with ABTS radical for 3 min at 37 °C. A decrease in absorbance caused by antioxidant addition was registered spectrophotometrically at 720 nm, calculated to the concentration of the antioxidant standard Trolox (6-hydroxy-2,5,7,8-tetramethylchroman-2-carboxylic acid) and expressed as μmol/L of Trolox equivalent.

Preparation of tissue protein fractions

The tissue samples used for Western blot analysis and zymography were obtained from saline-treated and DOX-treated rats at four or eight weeks after the end of the application period. The tissues from the LV were pulverized in liquid nitrogen, resuspended in ice-cold buffer A (20 mmol/L Tris-HCl, 250 mmol/L sucrose, 1.0 mmol/L EGTA, 1.0 mmol/L dithiothreitol (DTT), 1.0 mmol/L phenylmethylsulphonylfluoride (PMSF) and 0.5 mmol/L sodium orthovanadate, pH 7.4) and homogenized with a Teflon homogenizer. The homogenates were centrifuged at 800×*g* for 5 min at 4 °C. After centrifugation, the pellets were discarded, and the supernatants were centrifuged again at 16100×*g* for 30 min. The postmitochondrial supernatants after the second centrifugation, termed as soluble fractions, were used for further analysis. The protein concentrations were estimated using the Bradford assay[17].

Electrophoresis and immunochemical Western blot analysis

Samples of protein fractions containing equivalent amounts of protein per lane (30 μg per lane) or plasma samples were separated by sodium dodecyl sulfate-polyacrylamide gel electrophoresis (SDS-PAGE). For Western blot assays, after an electrophoretic separation, the proteins were transferred onto a nitrocellulose membrane. The quality of the transfer was verified by Ponceau S staining of the nitrocellulose membranes after transfer, and equal protein loading was verified by blotting glyceraldehyde-3-phosphate dehydrogenase (GAPDH) as the loading control. Specific anti-Akt, anti-MMP-2, anti-SOD-1, anti-NOS-2 (iNOS), anti-GAPDH (all from Santa Cruz Biotechnology), anti-phospho-Akt, anti-cleaved caspase-3 (from Cell Signaling Technology) antibodies were used for the primary antibody immunodetection. Peroxidase-labeled anti-rabbit immunoglobulins (Cell Signaling Technology) were used as the secondary antibodies. The bound antibodies were detected by the enhanced chemiluminescence (ECL) detection method.

Measurement of MMP activities by gelatin zymography

The gelatinolytic activities of MMPs were analyzed by zymography in polyacrylamide gels containing gelatin as a substrate. Laemmli buffer without 2-mercaptoethanol was added to the protein samples, and non-heated samples were subjected to electrophoresis in SDS-polyacrylamide gels co-polymerized

with gelatin (2 mg/mL). After electrophoresis, the gels were washed twice for 20 min each with 50 mmol/L Tris-HCl (pH 7.4), containing 2.5% Triton X-100, and then incubated overnight at 37 °C in a substrate buffer containing 50 mmol/L Tris-HCl, 10 mmol/L $CaCl_2$ and 1.25% Triton X-100, pH 7.4. After incubation, the gels were stained with 1% Coomassie Brilliant Blue G-250 and then destained with 40% methanol and 10% acetic acid. The gelatinolytic activities of the MMPs were detected as transparent bands against a dark blue background.

Statistical evaluation

A quantification of the proteins from the Western blot and zymography studies was performed using a Phosphorimager Thyphoon (Amersham Biosciences). The data were expressed as the means±SD. The statistical significance of the differences between the groups was analyzed by an unpaired Student's *t*-test. The data from measurements of superoxide dismutase activities, superoxide production and TAS were analyzed by one-way ANOVA. Differences were considered as significant at $P<0.05$ for all tests.

Results

Effects of doxorubicin on physiological parameters at four and eight weeks after the end of the treatment

The values of body weight, heart weight, left ventricle weight and heart weight/body weight ratio of saline- and DOX-treated rats obtained at four and eight weeks after the last injection are summarized in Table 1. There were differences in the trends of the body weights of DOX-treated group of rats compared with the control saline-treated animals, and these differences were more pronounced with a prolongation of time after treatment. In animals treated with DOX, the body weights and increases in body weights were lower. However, the weight of the whole heart as well as the weight of LV was not markedly changed compared with control (saline-treated) animals. Eight weeks after the end of treatment, the systolic blood pressure increased in DOX-treated rats compared with control animals (Figure 1A). In contrast, there were no differences in the heart rate between the saline- and DOX-treated groups (Figure 1B).

Table 1. The effect of doxorubicin treatment on body weight (BW), BW increase, heart weight (HW), ventricular weight and ratio of heart to body weight. BW increases are values relative to initial body weights prior to drug treatment. C-4: control group, 4 weeks after the end of saline treatment; C-8: control group, 8 weeks after the end of saline treatment; DOX-4: doxorubicin group, 4 weeks after the end of doxorubicin treatment; DOX-8: doxorubicin group, 8 weeks after the end of doxorubicin treatment. Mean±SD. $^bP<0.05$ *vs* corresponding control value.

	4 weeks		8 weeks	
	C-4	DOX-4	C-8	DOX-8
Body weight (g)	388±29	359±44	418±39	377±52^b
BW increase (g)	132±27	109±33	180±31	152±23^b
Heart weight (g)	0.95±0.15	0.94±0.09	1.03±0.10	0.98±0.11
HW/BW (mg/g)	2.47±0.46	2.65±0.49	2.47±0.32	2.64±0.33
LV weight (g)	0.52±0.12	0.53±0.11	0.66±0.09	0.62±0.08

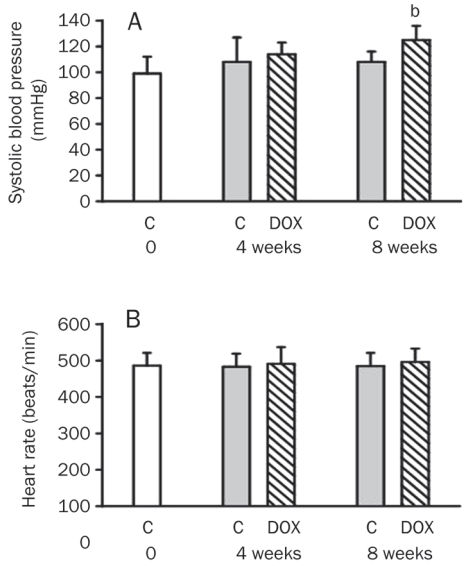

Figure 1. Effect of doxorubicin treatment on the systolic blood pressure (A) and heart rate (B). These parameters were measured by the non-invasive method of tail cuff plethysmography in both control and DOX-treated groups of rats. The measurements were performed before the first DOX or saline application and 4 or 8 weeks after end of their application. In each experimental group, eight animals were used for blood pressure and heart rate measurements and bars represent mean±SD from these independent measurements. C- control saline-treated rats; DOX- doxorubicin-treated rats; 0- rats before start of treatment; 4 weeks- rats 4 weeks after end of treatment; 8 weeks- rats 8 weeks after end of treatment. $^bP<0.05$ *vs* corresponding control value.

Electron microscopic analysis

An electron microscopic examination of the hearts of the control rats showed a classic intact ultrastructure of the myocytes, without any abnormalities in the extracellular space (Figure 2A). DOX induced heterogeneous subcellular alterations, characterized by a degeneration and/or loss of myofibrils, and cytoplasmic vacuolization of cardiomyocytes (Figure 2B). These changes are known structural markers of DOX cardiotoxicity. We also observed a structural disorganization of the cardiac extracellular space (Figure 2C), which was manifested by an increased density of extracellular matrix proteins. Simultaneously, ultrastructural analysis also demonstrated the presence of damaged endothelial cells of the capillaries (Figure 2D). The damage was characterized by the occasional disruption of plasmalemmal integrity, injured mitochondria, changes in cytoplasm density, quantity of ribosomes, pinocytic vesicules, and occasional disorganization and clumping of chromatin, indicating endothelial cell activation and dysfunction. Moreover, in DOX-treated rat hearts, an increased accumulation of interstitial collagen fibers, the presence of macrophages, vacuoles forming large membrane-bound spaces, Cajal cell processes, and proliferating fibroblasts were observed. All the

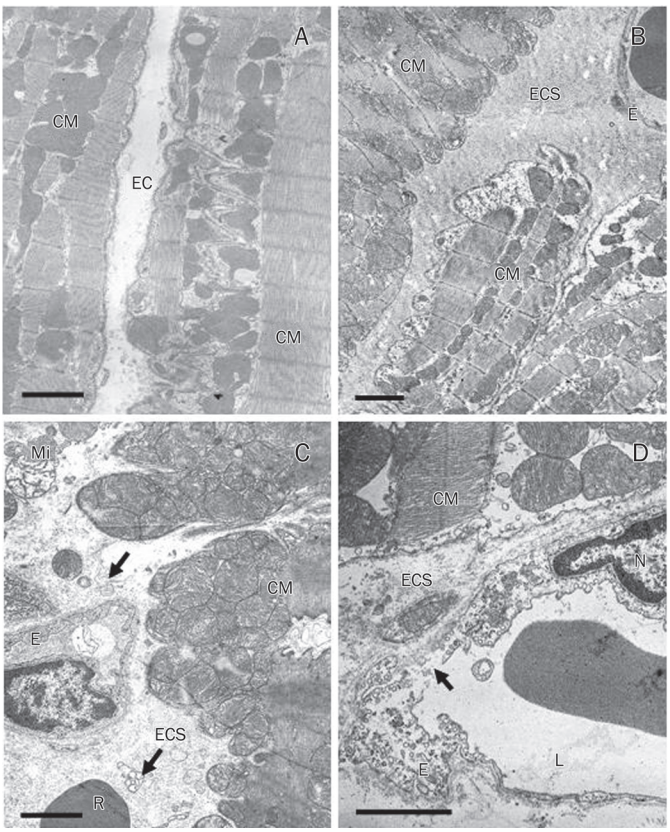

Figure 2. Representative electron microscopic images showing changes in ultrastructure of rat hearts 8 weeks after the application of the last dose of saline or doxorubicin. (A) Electron micrograph of control heart showing normal architecture of cardiomyocytes and without changes in extracellular space. CM – cardiomyocytes; EC – extracellular space. Bar: 1 μm. (B) Electron micrograph of the myocardium affected with doxorubicin demonstrating injury of cardiomyocytes and dense extracellular space. E- capilary endothelial cells; ECS – extracellular space; CM – cardiomyocytes. Bar: 1 μm. (C) Extracellular space (ECS) of the myocardium affected with DOX is filled with irregularly distributed dense material, mitochondria (Mi), vacuoles and myelinized structures (arrows) and extravased red cells (R). E – endothelial cells of capilary; CM – cardiomyocytes. Bar: 1 μm. (D) Subcellular injury of capillary endothelial cell (E) manifested with disrupted plasmalemma (arrow), reduced cytoplasm density and clumping of chromatin. N – nucleus; ECS – extracellular space; CM – cardiomyocytes, L – lumen. Bar: 1 μm.

observed changes had occurred at four weeks after the end of treatment and were more pronounced after eight weeks of treatment.

Doxorubicin treatment modulates the activities of matrix metalloproteinases

In our study, we investigated the consequences of DOX treatment on MMPs present in heart tissue as well as on MMPs that were released into the circulation. The MMPs activities were analyzed by zymography using gelatin as a substrate. As a positive control to identify the 63-kDa MMP-2 we used a recombinant active 63-kDa MMP-2 (Calbiochem). Pro-MMP-2 and MMP-9 were identified using fetal bovine serum containing predominantly activity of the 72-kDa form of MMP-2 and MMP-9.

In ventricular tissue samples, we predominantly detected enzymatic gelatinolytic activities of the 72-kDa MMP-2. DOX treatment markedly increased the activity of this form of the enzyme, as assayed at eight weeks after end of treatment. However, activity of the 72-kDa MMP-2 in the LV did not change at four weeks after the end of DOX treatment (Figure 3A, 3B). For the 63-kDa form of MMP-2 and MMP-9, we did not observe intensive gelatinolytic bands in the samples isolated from the LV, and the application of DOX also did not induce additional activation of these forms of MMPs. As shown in Figure 3C, the observed effects of DOX on activity of the 72-kDa form of MMP-2 were not connected with a modulation of the protein levels of this enzyme. The protein levels of MMP-2 were determined using a specific antibody that reacts with both the 72-kDa and 63-kDa forms of MMP-2, and our results did not show any differences in the protein levels of tissue MMP-2 between saline- and DOX-treated hearts at four or eight weeks after the end of the treatment. The observed increase of 72-kDa MMP-2 activity at eight weeks after the end of the DOX application was also not related to changes in levels of TIMP-2 (tissue inhibitor of MMPs) (Figure 3C).

A zymographic analysis of blood plasma samples revealed several bands corresponding to the gelatinolytic activities of proteinases. Using positive controls, we identified the activities of 72-kDa MMP-2 and 92-kDa MMP-9. We found that the activities of both MMPs increased in the plasma of DOX-treated rats at both four and eight weeks after the end of DOX treatment (Figure 4A, 4C, 4D). Using a specific antibody, we predominantly detected the presence of the 72-kDa form of MMP-2 in the plasma, but we did not observe differences in protein levels of this enzyme between the plasma samples of saline- and DOX-treated rats (Figure 4B).

Doxorubicin treatment increases superoxide production, iNOS levels and cleaved caspase-3 levels in the left ventricle of rat hearts

An activation of the non-cleaved oxidatively activated 72-kDa form of tissue ventricular MMP-2 suggested a potential alteration of its enzyme activity due to the action of radicals. To determine a possible role for superoxide radical formation, we measured the levels of superoxide in the LV after application of DOX in conditions where the 72-kDa MMP-2 had been activated. As shown in Figure 5A, DOX treatment induced an increase in superoxide levels at eight weeks after the end of the DOX application. This increase in superoxide levels was connected with a decreased enzymatic activity of SOD (Figure 5B) and a significant lowering of total antioxidant status (TAS). The TAS was determined using ABTS radical for antioxidant determination, and the value obtained in the DOX group at eight weeks after the end of the DOX application (8.90±1.40 μmol/L Trolox equivalent) represented 73% of the corresponding control value (12.23±0.76 μmol/L Trolox equivalent). However, superoxide levels, SOD activities and TAS had not changed at four weeks after DOX treatment. To

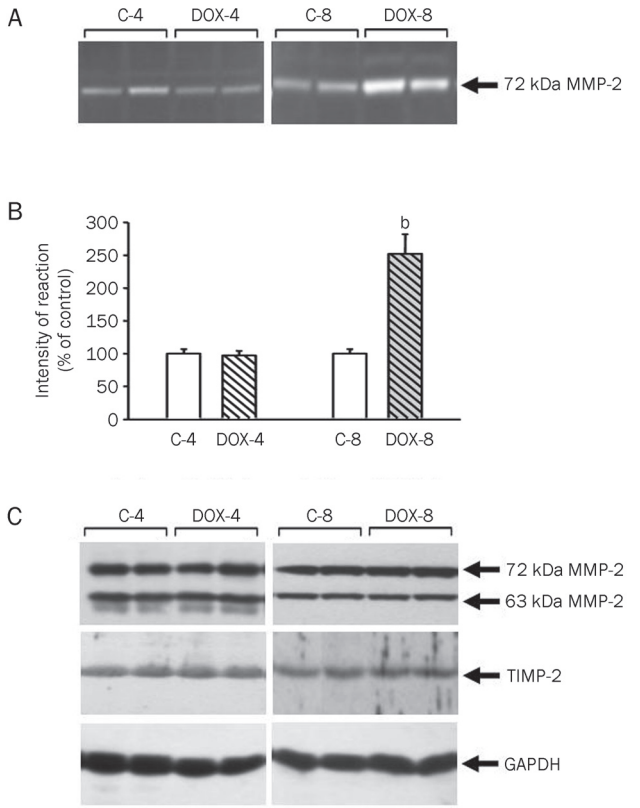

Figure 3. Effect of doxorubicin treatment on tissue matrix metalloproteinases and TIMP-2. The MMPs and TIMP-2 were analyzed in protein fractions isolated from the left ventricular tissue of control (C) and doxorubicin-treated (DOX) rat hearts obtained 4 weeks (C-4, DOX-4) or 8 weeks (C-8, DOX-8) at the end of the treatment. Tissue samples obtained from six animals in each experimental group were used for the analysis. (A) Records showing the influence of DOX-treatment on gelatinolytic activity of tissue 72 kDa MMP-2. The MMP activities were analyzed by zymography in polyacrylamide gels containing gelatin as a substrate and enzymatic gelatinolytic activities of 72 kDa MMP-2 were detected predominantly in samples from left ventricle. (B) Quantitative analysis of MMP-2 activities. Data are expressed as a percentage of value for corresponding control. Each bar represents mean±SD of 6 independent tissue samples per group. $^{b}P<0.05$ vs corresponding control value. (C) Effect of DOX treatment on protein levels of MMP-2, TIMP-2, and GAPDH. The levels of proteins were analyzed by Western blot analysis using specific antibodies. An antibody specific for MMP-2 reacted with both 72 kDa and 63 kDa forms of MMP-2. Protein loading was confirmed by using GAPDH.

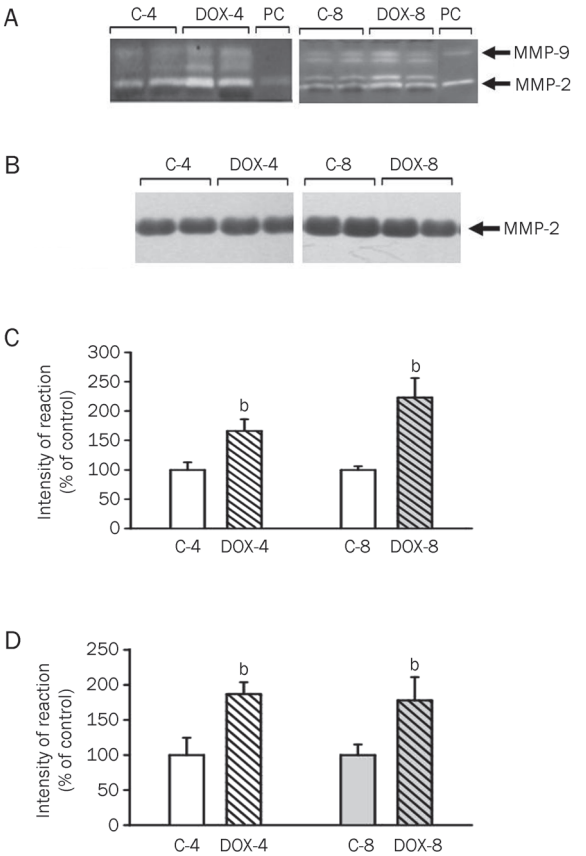

Figure 4. Effect of doxorubicin treatment on plasma matrix metalloproteinases. The MMPs released into circulation were analyzed in plasma samples prepared from whole artery blood of control (C) and doxorubicin-treated (DOX) rats obtained 4 weeks (C-4, DOX-4) or 8 weeks (C-8, DOX-8) after the end of the treatment. Blood plasma samples obtained from six animals in each experimental group were used for the analysis. (A) Records showing the influence of DOX-treatment on gelatinolytic activities of MMPs. Zymographic analysis of blood plasma samples revealed several bands corresponding to the gelatinolytic activities of several proteinases and using positive controls the activities of 72 kDa MMP-2 and 92 kDa MMP-9 were identified. (B) The records showing protein levels of MMP-2 determined in plasma samples by Western blot analysis using a specific antibody which detected predominantly the presence of 72 kDa form of MMP-2 in plasma. (C) Quantitative analysis of MMP-2 activities. Data are expressed as a percentage of value for corresponding control. Each bar represents mean±SD of 6 independent plasma samples per group. $^{b}P<0.05$ vs corresponding control value. (D) Quantitative analysis of MMP-9 activities. The data are expressed as a percentage of value for corresponding control. Each bar represents mean±SD of 6 independent plasma samples per group. $^{b}P<0.05$ *vs* corresponding control value.

investigate whether the changes in superoxide levels and SOD activities are associated with a modulation of SOD expression, we measured the protein levels of SOD-1. We did not observe any changes in SOD-1 protein levels as a consequence of DOX application (Figure 5C, 5D).

Another radical implicated in the toxic effects of DOX is nitric oxide produced by NO synthases (NOS). We assayed for changes in iNOS expression and found that DOX treatment induced an upregulation of iNOS protein levels (Figure 6A, 6B). These changes had already occurred by four weeks after the end of DOX treatment and were more pronounced at eight weeks after the treatment. We also observed an increased amount of cleaved (activated) caspase-3 in the hearts of DOX-treated rats, and these changes were more evident at eight weeks after the end of the treatment (Figure 6C, 6D).

Chronic effects of doxorubicin treatment are connected with stimulation of Akt kinase

To characterize the influence of DOX treatment on the protein

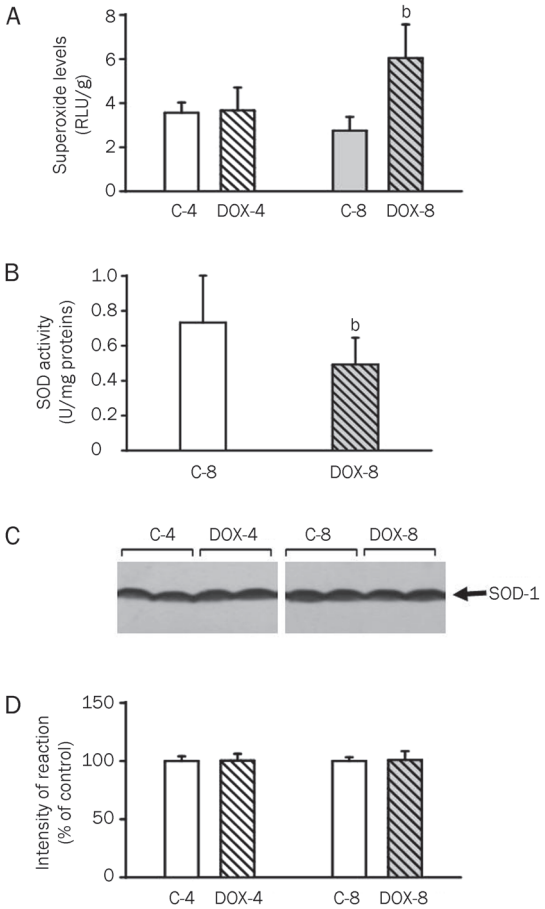

Figure 5. Effect of doxorubicin treatment on levels of superoxide anion (O_2^-), activities of SOD and protein levels of SOD-1. Left ventricular tissue of control (C) and doxorubicin-treated (DOX) rat hearts obtained 4 weeks (C-4, DOX-4) or 8 weeks (C-8, DOX-8) at the end of the treatment was used for the analysis. Tissue of left ventricle obtained from six animals in each experimental group was used for the analysis. (A) Doxorubicin treatment induced increase in levels of superoxide (O_2^-) 8 weeks after the end of the DOX application. On the other hand, superoxide levels were not changed 4 weeks after DOX treatment. The superoxide levels were evaluated using Lucigenin Enhanced Chemiluminiscence assay and the obtained data were expressed as relative luminiscence unit per mg of tissue (RLU·mg^{-1} tissue). Each bar represents mean±SD of six independent measurements. $^bP<0.05$ *vs* corresponding control value. (B) Doxorubicin treatment induced inhibition of enzymatic activities of superoxide dismutase (SOD) 8 weeks after the end of the drug application. The SOD activities in left ventricle were analyzed using the SOD Assay kit (Fluka) and are expressed in U·mg^{-1} of protein. Each bar represents mean±SD of six independent measurements. $^bP<0.05$ *vs* corresponding control value. (C) The record showing the effects of DOX treatment on protein levels of SOD-1. The protein levels of SOD-1 were analyzed by Western blot analysis. (D) Quantitative analysis of SOD-1 protein levels. The data are expressed as a percentage of value for corresponding control. Each bar represents mean±SD of 6 independent tissue samples per group. $^bP<0.05$ *vs* corresponding control value.

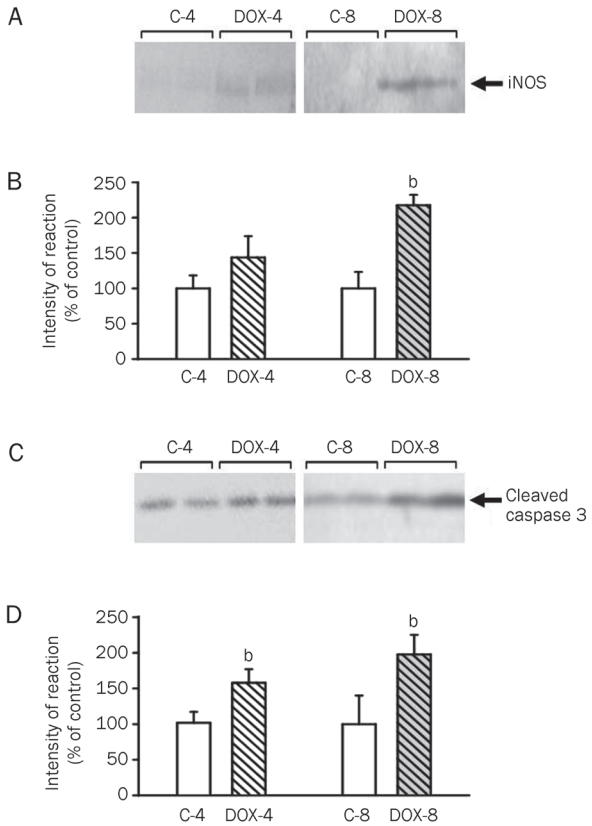

Figure 6. Effect of chronic DOX treatment on protein levels iNOS and cleaved caspase-3. For the analysis protein fractions isolated from the left ventricular tissue of control (C) and doxorubicin-treated (DOX) rat hearts obtained 4 weeks (C-4, DOX-4) or 8 weeks (C-8, DOX-8) at the end of the treatment were used. Tissue samples obtained from six animals in each experimental group were used. (A) Western blot record showing the influence of saline and DOX on iNOS protein levels induction. The protein levels of iNOS were analyzed by Western blot analysis. (B) Quantitative analysis of iNOS protein levels. The data are expressed as a percentage of value for corresponding control. Each bar represents mean±SD of 6 independent tissue samples per group. $^bP<0.05$ *vs* corresponding control value. (C) Western blot record showing the influence of saline and DOX on caspase-3 activation. Levels of fragment of activated caspase-3 resulting from cleavage adjacent to Asp175 were determined using a specific antibody. (D) Quantification of cleaved caspase-3 content in the left ventricular tissue after DOX treatment. The data were obtained from Western blot records and are expressed as a percentage of value for corresponding control. Each bar represents mean±SD of 6 independent tissue samples per group. $^bP<0.05$ *vs* corresponding control value.

blot analysis of heart left ventricular tissue samples obtained at four or eight weeks after treatment with saline (controls) levels and activation of Akt kinase, we performed a Western or DOX (DOX-treated rats). This analysis used an antibody specific for Akt kinase and revealed no differences in the levels of Akt kinase between the control and DOX-treated hearts at either four or eight weeks after the treatment (Figure 7A). However, detection with a phosphospecific antibody (Ser473) showed an increased phosphorylation of Akt kinase specifically on Ser473 in the LV of DOX-treated rat hearts at eight weeks after the end of the treatment (Figure 7A). The observed levels of active Akt kinase at eight weeks after the end of DOX treatment were also increased in relation to total

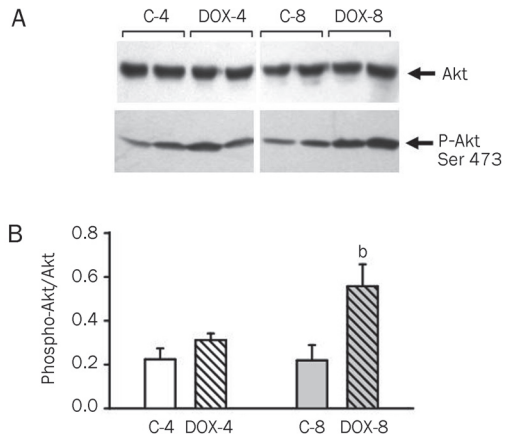

Figure 7. Effect of chronic DOX treatment on protein levels and activation of Akt kinase. For the analysis protein fractions isolated from the left ventricular tissue of control (C) and doxorubicin-treated (DOX) rat hearts obtained 4 weeks (C-4, DOX-4) or 8 weeks (C-8, DOX-8) at the end of the treatment were used. Tissue samples obtained from six animals in each experimental group were used for the analysis. (A) Western blot record showing the influence of saline and DOX on protein levels and specific phosphorylation of Akt kinase. Levels of Akt kinase were determined by Western blot analysis using a specific antibody. The changes in the specific phosphorylation (activation) of Akt kinase were determined by Western blot analysis using an antibody which reacts with Akt kinase phosphorylated specifically on Ser473. (B) The quantification of Akt kinase phosphorylation and activation. The data were obtained from Western blot records and are expressed as a ratio of content of phosphorylated Akt kinase to total Akt kinase. Each bar represents mean±SD of 6 independent tissue samples per group. $^{b}P<0.05$ *vs* corresponding control value.

Akt kinase levels (Figure 7B).

Discussion

The results of this study provide new insights into the chronic effects of prolonged DOX administration on MMPs several weeks after DOX treatment. We have shown that the activation of myocardial and circulating MMPs, especially MMP-2, is closely associated with the progression of the toxic effects of DOX. Our results also add new evidence that specific cellular signaling mechanisms, such as the Akt kinase pathway, are involved in the regulation of myocardial MMP-2 in relation to the chronic effects of DOX.

The consequences of DOX administration in humans can be acute (occurring during or immediately after treatment), early (occurring within one year of exposure), and late (occurring one or more years after initial exposure)[3, 4]. This is important from a clinical point of view because in most patients, the cardiotoxicity of DOX develops long after the patient's initial exposure to the drug. The severity of the toxic effects induced by DOX is also dependent on the specific protocol of the DOX treatment (dosage, time, *etc*). Some strategies to prevent the cardiac toxicity of DOX involve reducing dosages and prolonging the DOX infusion time to limit its serum concentrations. In our animal model, we used repeated administration of lower doses of DOX during a prolonged period of three weeks, and we investigated the effects of a pre-treatment with DOX by assessing the outcomes several weeks after the end of the treatment. The time periods of four weeks and eight weeks after the last dose of DOX for functional and other (morphological, biochemical) assessments in the present study were chosen because during these time periods, chronic changes initiated by DOX can already be observed. DOX treatment is often accompanied by cardiotoxic effects that manifest as cardiomyopathy associated with severe systolic dysfunction of the left ventricle[5]. Our previous study also showed that the application of DOX significantly affected the physiological and several biochemical parameters of the LV[18]. Therefore, the measurements performed in the present study focused on changes in tissues from the LV. Using electron microscopy, tissue and cardiomyocyte damage following DOX treatment was demonstrated, and no such changes were observed in the control rat hearts. Structural disorganizations of the cardiac extracellular space were also observed, and these alterations could be related to the observed changes in activities of MMPs, enzymes that are known to play an important role in processes of extracellular matrix remodeling.

It has been shown that an activation of myocardial MMPs may be an early marker of acute cardiotoxicity induced by a single ip injection of 25 mg/kg DOX in mice[11]. However, the role of MMPs in the processes associated with the chronic effects of DOX remains unknown. In a recent study it was documented that chronic anthracycline cardiotoxicity in rabbits is associated with profound changes in left ventricular morphology and function as well as with alterations in the collagen network[19]. However, despite the alterations of collagen proteins, no changes in MMP activities were found. In the present study, an induction of gelatinolytic activity of the 72-kDa MMP-2 in the LV of DOX-treated rats was found. This increase in MMP activity occurred eight weeks after the end of DOX treatment and was not connected with changes in protein content of this enzyme. The latter finding suggests that the regulation of MMP-2 activity observed in rats exposed to DOX treatment does not occur at the transcriptional level. Moreover, the unchanged protein levels of TIMP-2 suggest that this specific tissue inhibitor also does not play a role in the observed changes of MMP-2. However, the results of some studies indicate that a transcriptional regulation of MMPs, in consequence to DOX action at some time points, cannot be completely ruled out. The increased expression of the genes for myocardial (ventricular) MMP-2 and MMP-9 was documented after an acute treatment with DOX in the mouse model[2, 20], and the transcriptional activation of several MMPs has also been found in pig myocardium[21]. One explanation for the differences obtained in specific experimental animal models could be that the changes in MMPs expression are time dependent. This hypothesis is also supported by the results

of a study where MMP-2 mRNA expression increased significantly in DOX-treated mice on days one and two; however, on day four, the MMP-2 mRNA levels declined[20].

MMP activity can also be regulated through post-translational modifications that include either proteolytic removal of the propeptide domain or zymogen modification by oxidant stress. In the latter mechanism, a powerful endogenous oxidant, such as peroxynitrite, can activate MMPs by reacting with a critical cysteine residue without a loss of the propeptide domain[22]. The observed activity of the 72-kDa MMP-2 corresponds to the form of MMP-2 that is activated through conformational changes induced by oxidative stress. Thus, the observed increase in the activities of the 72-kDa form of MMP-2 in DOX-treated left ventricular tissue can also be explained through the observed reduction of SOD activities and increased levels of superoxide anion. Furthermore, the observed increase in iNOS protein levels in the left ventricle of DOX-treated rats suggests that the induction of NO production from increased iNOS expression is also a consequence of DOX treatment. Recent reports also indicated that elevated iNOS activity and nitrosative stress are involved in DOX-induced cyto- and cardiotoxicity[2, 23]. The findings that at eight weeks after DOX treatment, there are higher levels of superoxide anion as well as increased levels of iNOS in the left ventricular tissue point to an increased formation of peroxynitrite, a product of the reaction between NO and superoxide anion. This powerful oxidant could be involved in the observed MMP-2 activation. Moreover, peroxynitrite was also found to stimulate the release of MMP-2 into the circulation from rat hearts during reperfusion[24].

Our results showed that, in parallel to the observed activation of tissue MMP-2, the levels of the phosphorylated (activated) form of the Akt kinase also increased. The signal transduction pathways linked to DOX-induced ROS formation and oxidative stress have been investigated, and several lines of evidence point to a role for MAPK and PI3K/Akt kinase signaling[14, 25]. The Akt kinase activation observed in the present study can have several possible roles. First, it may represent an attempt to overcome apoptosis induced as a consequence of DOX action. It has been shown that DOX treatment *in vivo* causes cardiomyocyte apoptosis[26], and we also observed increased levels of cleaved (activated) caspase-3 in the hearts of DOX-treated rats. It is also known that oxidative stress induced by ROS is accompanied by an activation of Akt kinase, and this enzyme has been proposed to be a reperfusion injury salvage kinase (RISK), counteracting myocardial cell damage through a compensatory protective pathway[27]. The role of Akt kinase in a salvage pathway to protect against the damaging effects of DOX was documented in rats[28], and other studies have documented that a single injection of DOX can induce the activation of both caspase-3 and Akt in the left ventricles of mice[25]. The activations of these factors in mice were observed five days after the onset of treatment, suggesting that the observed Akt kinase activation likely reflects a protective response to counteract the induction of cardiomyocyte apoptosis. A second possible role for Akt kinase activation may be related to the observed activation of MMP-2. It was demonstrated that the enhancement of MMP-2 and MMP-9 in cardiac myocytes in acute responses to DOX could be mediated through redox-dependent MAPK and PI3K/Akt kinase pathways[14]. The positive influence of PI3K/Akt kinase pathway on the induction of MMP-2 expression and activation was also demonstrated in studies showing that the activation of Akt kinase resulted in upregulation of MMP-2[29, 30]. Similarly, our present results show that Akt kinase activation in cardiac tissue (eight weeks after DOX treatment) is connected with a stimulation of tissue MMP-2 activity. However, in contrast to the above studies, we did not observe changes in MMP-2 protein expression. Moreover, our recent observation that activation of Akt kinase induced by a short cycle of ischemia and reperfusion (realized within several minutes) is associated with inhibition of MMP-2 activation[13] suggests that the roles of Akt kinase in MMP-2 regulation can be different, and this may be attributed to substantial differences in time (acute, chronic effects) and experimental models.

In the present study, we found increased activities of MMP-2 and MMP-9 in the plasma of DOX-treated rats at both four and eight weeks after the end of the treatment. MMPs are synthesized within a wide variety of tissue types. Therefore, the observed changes in plasma MMP activities may not necessarily reflect changes found in the heart. Circulating MMPs have been proposed to be a prognostic factor for survival in patients with heart failure[9], and increased circulating and tissue MMP-2 and MMP-9 levels have also been reported to play a role in the development of hypertension[31]. Thus, the observed increases in plasma MMPs activities can also explain the observed elevation of systolic blood pressure in rats eight weeks after DOX treatment. This finding is also supported by the results of a recent study demonstrating that MMPs inhibition may attenuate increases in systolic blood pressure[32].

In conclusion, our data demonstrate that alterations in MMP activation and release occur several weeks after the application of DOX. These findings suggest that MMPs, especially MMP-2, are closely related to the progression of the toxic effects of DOX and are responsible for the pathogenesis of DOX-induced cardiomyopathy. Moreover, our results show that changes in the activation and release of MMPs can undergo dynamic changes during the time course of developing the toxic effects of DOX. A study of the cellular mechanisms that are involved at the onset of the chronic effects of DOX demonstrated an important role for Akt kinase signaling and oxidative/nitrosative stress. These results also suggest that increased oxidative/nitrosative stress and activation of downstream effector of Akt kinase pathway may play a role in the modulation of MMP-2 activities that occurs in rat hearts as a chronic consequence of DOX treatment.

Acknowledgements

The authors would like to thank Maria Fogarassyova, Iveta Formankova, Iveta Blazickova and Viera Mocsonokyova for their excellent technical assistance. This study was supported by Scientific Grant Agency of the Ministry of Education of Slovak Republic and the Slovak Academy of Sciences (VEGA SR) grants No 2/0205/09, 2/0049/09 and 2/0108/10 and the Joint Research Cooperation of the Slovak Academy of Sciences and National Science Council (SAS-NSC JRP) 2010/01.

Author contribution

Monika IVANOVÁ, Petra ŠIMONČÍKOVÁ, Jana VLKOVIČOVÁ, Monika BARTEKOVÁ and Miroslav BARANČÍK performed the physiological and biochemical experiments; Ľudmila OKRUHLICOVÁ and Narcisa TRIBULOVÁ contributed to the electron microscopic examinations; Ima DOVINOVÁ contributed to the examination of parameters related to oxidative stress; Miroslav BARANČÍK wrote the paper.

References

1 Singal PK, Deally CMR, Weinberg LE. Subcellular effects of adriamycin in the heart: A concise review. J Mol Cell Cardiol 1987; 19: 817–28.

2 Mukhopadhyay P, Rajesh M, Batkai S, Kashiwaya Y, Hasko G, Liaudet L, *et al*. Role of superoxide, nitric oxide, and peroxynitrite in doxorubicin-induced cell death *in vivo* and *in vitro*. Am J Physiol Heart Circ Physiol 2009; 296: H1466–83.

3 Pein F, Sakiroglu O, Dahan M, Lebidois J, Merlet P, Shamsaldin A, *et al*. Cardiac abnormalities 15 years and more after adriamycin therapy in 229 childhood survivors of a solid tumour at the Institut Gustave Roussy. Br J Cancer 2004; 91: 37–44.

4 Robert J. Long-term and short-term models for studying anthracycline cardiotoxicity and protectors. Cardiovasc Toxicol 2007; 7: 135–9.

5 Singal PK, Iliskovic N. Doxorubicin-induced cardiomyopathy. N Engl J Med 1998; 339: 900–5.

6 Nagase H, Woessner JF Jr. Matrix metalloproteinases. J Biol Chem 1999; 274: 21491–4.

7 Wang W, Schulze CJ, Suarez-Pinzon WL, Dyck JR, Sawicki G, Schulz R. Intracellular action of matrix metalloproteinase-2 accounts for acute myocardial ischemia and reperfusion injury. Circulation 2002; 106: 1543–9.

8 Sawicki G, Leon H, Sawicka J, Sariahmetoglu M, Schulze CJ, Scott PG, *et al*. Degradation of myosin light chain in isolated rat hearts subjected to ischemia-reperfusion injury: a new intracellular target for matrix metalloproteinase-2. Circulation 2005; 112: 544–52.

9 Altieri P, Brunelli C, Garibaldi S, Nicolino A, Ubaldi S, Spallarossa P, *et al*. Metalloproteinases 2 and 9 are increased in plasma of patients with heart failure. Eur J Clin Invest 2003; 33: 648–56.

10 Wang W, Sawicki G, Schulz R. Peroxynitrite-induced myocardial injury is mediated through matrix metalloproteinase-2. Cardiovasc Res 2002; 53: 165–74.

11 Bai P, Mabley JG, Liaudet L, Virag L, Szabo C, Pacher P. Matrix metalloproteinase activation is an early event in doxorubicin-induced cardiotoxicity. Oncol Rep 2004; 11: 505–8.

12 Kurata H, Thant AA, Matsuo S, Senga T, Okazaki K, Hotta N, *et al*. Constitutive activation of MAP kinase kinase (MEK1) is critical and sufficient for the activation of MMP-2. Exp Cell Res 2000; 254: 180–8.

13 Spanikova A, Ivanova M, Matejikova J, Ravingerova T, Barancik M. Influence of ischemia/reperfusion and modulation of PI3K/Akt kinase pathway on matrix metalloproteinase-2 in rat hearts. Gen Physiol Biophys 2010; 29: 31–40.

14 Spallarossa P, Altieri P, Garibaldi S, Ghigliotti G, Barisione C, Manca V, *et al*. Matrix metalloproteinase-2 and -9 are induced differently by doxorubicin in H9c2 cells: The role of MAP kinases and NAD(P)H oxidase. Cardiovasc Res 2006; 69: 736–45.

15 Guzik TJ, Channon KM. Measurement of vascular reactive oxygen species production by chemiluminiscence. Methods Mol Med 2005; 108: 73–89.

16 Re R, Pellegrini N, Proteggente A, Pannala A, Yang M, Rice-Evans C. Antioxidant activity applying an improved ABTS radical cation decolorization assay. Free Radic Biol Med 1999; 26: 1231–7.

17 Bradford M. A rapid and sensitive method for the quantitation of microgram quanties of protein utilizing the principle of protein-dye-binding. Anal Biochem 1976; 72: 248–54.

18 Šimončíková P, Ravingerová T, Barančík M. The effect of chronic doxorubicin treatment on mitogen-activated protein kinases and heat stress proteins in rat heart. Physiol Res 2008; 57: S97–101.

19 Adamcová M, Potacova A, Popelova O, Sterba M, Mazurova Y, Aupperle H, *et al*. Cardiac remodeling and MMPs on the model of chronic daunorubicin-induced cardiomyopathy in rabbits. Physiol Res 2010; 59: 831–6.

20 Kizaki K, Ito R, Okadaa M, Kazuki K, Uchide T, Temmac K, *et al*. Enhanced gene expression of myocardial matrix metalloproteinases 2 and 9 after acute treatment with doxorubicin in mice. Pharmacol Res 2006; 53: 341–6.

21 Goetzenich A, Hatam N, Zernecke A, Weber C, Czarnotta T, Autschbach R, *et al*. Alteration of matrix metalloproteinases in selective left ventricular adriamycin-induced cardiomyopathy in the pig. J Heart Lung Transplant 2009; 28: 1087–93.

22 Okamoto T, Akaike T, Sawa T, Miyamoto Y, van der Vliet A, Maeda H. Activation of matrix metalloproteinases by peroxynitrite-induced protein S-glutathiolation via disulfide S-oxide formation. J Biol Chem 2001; 276: 29596–602.

23 Deng S, Kruger A, Schmidt A, Metzger A, Yan T, Godtel-Armbrust U, *et al*. Differential roles of nitric oxide synthase isozymes in cardiotoxicity and mortality following chronic doxorubicin treatment in mice. Naunyn Schmiedebergs Arch Pharmacol 2009; 380: 25–34.

24 Cheung PY, Sawicki G, Wozniak M, Wang W, Radomski MW, Schulz R. Matrix metalloproteinase-2 contributes to ischemia-reperfusion injury in the heart. Circulation 2000; 101: 1833–9.

25 Ichihara S, Yamada Y, Kawai Y, Osawa T, Furuhashi K, Duan Z, *et al*. Roles of oxidative stress and Akt signaling in doxorubicin cardiotoxicity. Biochem Biophys Res Commun 2007; 359: 27–33.

26 Childs AC, Phaneuf SL, Dirks AJ, Phillips T, Leeuwenburgh C. Doxorubicin treatment *in vivo* causes cytochrome *c* release and cardiomyocyte apoptosis, as well as increased mitochondrial efficiency, superoxide dismutase activity, and Bcl-2:Bax ratio. Cancer Res 2002; 62: 4592–8.

27 Hausenloy DJ, Yellon DM. New directions for protecting the heart against ischaemia-reperfusion injury: targeting the reperfusion injury salvage kinase (RISK)-pathway. Cardiovasc Res 2004; 61: 448–60.

28 Das J, Ghosh J, Manna P, Sil PC. Taurine suppresses doxorubicin-triggered oxidative stress and cardiac apoptosis in rat via up-regulation of PI3-K/Akt and inhibition of p53, p38-JNK. Biochem Pharmacol 2011; 81: 891–909.

29 Bae IH, Park MJ, Yoon SH., Kang SW, Lee SS, Choi KM, *et al*. Bcl-w

promotes gastric cancer cell invasion by inducing matrix metalloproteinase-2 expression via phosphoinositide 3-kinase, Akt, and Sp1. Cancer Res 2006; 66: 4991–5.

30 Lee SJ, Bae SS, Kim KH, Lee WS, Rhim BY, Hong KW, *et al*. High glucose enhances MMP-2 production in adventitial fibroblasts via Akt1-dependent NF-kappaB pathway. FEBS Lett 2007; 581: 4189–94.

31 Flamant M, Placier S, Dubroca C, Esposito B, Lopes I, Chatziantoniou C, *et al*. Role of matrix metalloproteinases in early hypertensive vascular remodeling. Hypertension 2007; 50: 212–8.

32 Castro MM, Rizzi E, Figueiredo-Lopes L, Fernandes K, Bendhack LM, Pitol DL, *et al*. Metalloproteinase inhibition ameliorates hypertension and prevents vascular dysfunction and remodeling in renovascular hypertensive rats. Atherosclerosis 2008; 198: 320–31.

Acta Pharmacologica Sinica (2012) 33: 470–478
 1671-4083/12 $32.00
www.nature.com/aps

Original Article

CPU86017-RS attenuate hypoxia-induced testicular dysfunction in mice by normalizing androgen biosynthesis genes and pro-inflammatory cytokines

Guo-lin ZHANG#, Feng YU#, De-zai DAI*, Yu-si CHENG, Can ZHANG, Yin DAI

Faculty of Pharmacy, China Pharmaceutical University, Nanjing 210009, China

Aim: Downregulation of androgen biosynthesis genes StAR (steroidogenic acute regulatory) and 3β-HSD (3β-hydroxysteroid dehydrogenase) contributes to low testosterone levels in hypoxic mice and is possibly related to increased expression of pro-inflammatory cytokines in the testis. The aim of this study is to investigate the effects of CPU86017-RS that block Ca^{2+} influx on hypoxia-induced testis insult in mice.

Methods: Male ICR mice were divided into 5 groups: control group, hypoxia group, hypoxia group treated with nifedipine (10 mg/kg), hypoxia groups treated with CPU86017-RS (60 or 80 mg/kg). Hypoxia was induced by placing the mice in a chamber under 10%±0.5% 02 for 28 d (8 h per day). The mice were orally administered with drug in the last 14 d. At the end of experiment the testes of the mice were harvested. The mRNA and protein levels of StAR, 3β-HSD, connexin 43 (Cx43), matrix metalloprotease 9 (MMP9), endothelin receptor A (ET_AR) and leptin receptor (OBRb) were analyzed using RT-PCR and Western blotting, respectively. The malondialdehyde (MDA), lactate dehydrogenase (LDH), succinate dehydrogenase (SDH) and acid phosphatase (ACP) levels were measured using biochemical kits. Serum testosterone concentration was measured with radioimmunoassay.

Results: Hypoxia significantly increased the MDA level, and decreased the LDH, ACP and SDH activities in testes. Meanwhile, hypoxia induced significant downregulation of StAR and 3β-HSD in testes responsible for reduced testosterone biosynthesis. It decreased the expression of Cx43, and increased the expression of MMP9, ETAR and OBRb, leading to abnormal testis function and structure. These changes were effectively diminished by CPU86017-RS (80 mg/kg) or nifedipine (10 mg/kg).

Conclusion: Low plasma testosterone level caused by hypoxia was due to downregulation of StAR and 3β-HSD genes, in association with an increased expression of pro-inflammatory cytokines. These changes can be alleviated by CPU86017-RS or nifedipine.

Keywords: intermittent hypoxia; testicular injury; CPU86017-RS; nifedipine; StAR; 3β-hydroxysteroid dehydrogenase; matrix metalloprotease 9; endothelin receptor A; connexin 43; OBRb

Acta Pharmacologica Sinica (2012) 33: 470–478; doi: 10.1038/aps.2011.175; published online 19 Mar 2012

Introduction

Oxygen is essential and critical for life in humans and other mammals[1, 2]. When subjected to a low supply of oxygen, a series of pathological changes are initiated in cells and tissues, leading to ischemia, stroke, hemorrhage and many other cardiopulmonary diseases[3, 4]. Certain genes whose transcription is activated by exposure of the cell to hypoxia accelerate the appearance of pro-inflammatory cytokines such as ROS (reactive oxygen species), and induce the activation of the endothelin system[5, 6]. Hypoxia, which is a ubiquitous pathological process, has serious adverse effects on the respiratory and cardiovascular systems[7], and possibly damages the reproductive system as well. A decline in the ability of conceive has frequently been noticed in population lived in highland area.

Male hypogonadism causes degenerative changes in the testes and is characterized by low-concentrations of serum testosterone associated with testicular lesions[8]. An over-activated ET-ROS (endothelin–reactive oxygen species) system enhances activities of some cellular inflammatory factors responsible for the genesis of male hypogonadism. Emerging data suggest that the ET system mediates pathological changes leading to male hypogonadism [9] and testopathy in individuals with diabetic mellitus[10–12]. Matrix metalloprotease (MMPs) are the most important proteases participating in extracellular matrix degradation and remodeling and MMP9 takes an important part in the maintenance of the normal structure and function of the seminiferous tubules. Intercellular gap junction com-

# The two authors contributed equally to this paper.
* To whom correspondence should be addressed.
E-mail dezaidai@vip.sina.com
Received 2011-08-22 Accepted 2011-11-18

munication is operated by a family of proteins known as connexins, among them connexin 43 (Cx43) is the most abundant and extensively distributed of the connexins and it is known to be affected in disease[13, 14]. An alteration of Cx43 is concerned in abnormal function and structure of the testis[15]. Testicular disorders resulting from intermittent hypoxia exposure may be caused by a deficiency in Cx43-mediated gap junctional signaling in the testis.

CPU86017 is synthesized by China Pharmaceutical University through modification of the berberine moiety. In pulmonary hypertension induced by hypoxia, or by the inflammatory reagent monocrotaline, CPU86017 suppresses the activation of the endothelin system and the formation of oxygen free radicals[7, 16]. CPU86017 also blocks L-type calcium channels[17]. This calcium- antagonism activity is thought to underlie its effect of relieving cardiovascular disorder[18]. CPU86017 and its isomer CPU86017-RS were found to act as a protection against tissue damage from various pathological factors. They confer this protection by blocking the ET-ROS pathway and subsequently attenuating the pro-inflammatory cytokines involved in the pathologies caused by hypoxia-induced pulmonary hypertension and cardiovascular abnormalities[7, 16–21]. Hypoxia-induced pulmonary hypertension causes ROS production[22], and nifedipine has been recommended as an effective therapy for managing hypoxic pulmonary hypertension in clinical settings[23–25].

We hypothesized that the male hypogonadism caused by intermittent hypoxia is a result of a chronic inflammatory response in which over-activated cytokines such as ET, leptin, and MMPs, in addition to the downregulation of Cx43, contribute to the pathology in hypoxic testes. We further hypothesized that these changes could be initiated by an increase in calcium influx. In this study, we aimed to determine whether the hypoxia-induced upregulation of inflammatory cytokines and downregulation of testosterone biosynthesis genes in the testis, which are attributed to an enhanced influx of calcium, could respond to nifedipine or CPU 86017-RS.

Materials and methods

Animals and treatment

Male ICR mice, weighing 22–25 g, were bought from the Zhejiang Experimental Animal Center [License Number: SCXK(Z)20080033]. All procedures performed on the animals were conducted in accordance with the Animal Regulations of Jiangsu Province, China.

Mice were randomly divided into 5 groups (n=6). The groups were as follows: a control group, a hypoxia group, a hypoxia group also treated with nifedipine (10 mg/kg *po*, Changzhou Kangpu Pharmaceutical Co, Ltd, China, batch number: 0910004), and two groups treated with CPU86017-RS (RS60, 60 mg/kg; RS80, 80 mg/kg *po*, supplied by the Department of Medicinal Chemistry of China Pharmaceutical University, batch number: 20090301). Chronic exposure to intermittent hypoxia was performed as previously described[6, 7]. Briefly, for 8 h per day for 28 d, the mice were placed in a normobaric hypoxic chamber in which the oxygen content was maintained at 10%±0.5%. The interventions by nifedipine or CPU86017-RS were applied during the last 2 weeks of hypoxia exposure.

Biochemical assays

The testis was harvested from mice after cervical dislocation and 100 mg of testicular tissue was homogenized in 10 volume of physiological saline. MDA, LDH, SDH, and ACP levels were measured by using biochemical kits (Nanjing Jiancheng Institute of Bio-engineering Company, Nanjing, China). Serum testosterone concentrations were measured by radioimmunoassay (RIA) with kits purchased from the institute of Jiuding Medical Bio-engineering company (Tianjin, China). These measurements were made in accordance with previous reports[9–11].

RT-PCR

The testes were harvested and total RNA was extracted using the Trizol solution. cDNA was synthesized as described previously (Invitrogen, Carlsbad, CA, USA)[14]. The primer (Invitrogen Trading Co, Ltd, Shanghai, China) sequences were used as follows: sense: 5′-ATCGGGATCCCCTTGATTAC-3′ and antisense: 5′-ACAGCAACAGAGGCAGGACT-3′ for ET_AR, sense: 5′-CGACATAGACGGCATCCAG-3′ and antisense: 5′-CTGTCGGCTGTGGTTCAGT-3′ for MMP9, sense: 5′-TACCACGCCACCGGCCCA-3′ and antisense: 5′-GCATTTTGGCTGTCGTCAGG-3′ for Cx43, sense: 5′-AGAATTGTTCCTGGGCACAAG-3′ and antisense: 5′-ACACTCATCCTCACAGGTTCC-3′ for OBRb, sense: 5′-AACTTTGGCATTGTGGAAGG-3′ and antisense: 5′-GGAGACAACCTGGTCCTCAG-3′ for GAPDH.

Western blotting

After the mice were sacrificed, proteins of testes were extracted (Biouniquer Biotechnology Co, Ltd, Hangzhou, China) and Western blotting was conducted as described previously[6]. The sources of antibodies were listed as below: polyclonal rabbit anti-ET_AR-IgG, polyclonal rabbit anti-StAR-IgG and polyclonal rabbit anti-MMP9-IgG were purchased from Santa Cruz Biotechnology Inc, USA; polyclonal rabbit anti-Cx43-IgG, polyclonal rabbit anti-β-actin-IgG, polyclonal rabbit anti-OBRb-IgG and horseradish peroxidase (HRP)-conjugated goat secondary antibody IgG were purchased from Wuhan Boster Biological Technology, Wuhan, China.

Assessment of testis pathology

The testis tissues, fixed with neutral 10% formalin, were embedded in paraffin and sliced into 4-μm-thick sections and stained with hematoxylin-eosin (HE). All pictures were viewed under an inverted microscope (Nikon TE 2000-U, Japan) by a pathologist blinded to the experiment.

Immunohistochemical fluorescence assay

The immunohistochemical fluorescence assay were conducted as previously described[26]. Paraffin-embedded testicular tissue was sliced into 4-μm-thick sections, dewaxed with xylene

2 times and dehydrated with decreasing concentrations of ethanol (100%, 95%, 90%, 80%, and 70%). The sections were then placed in a 3:4 ratio solution of sodium-citrate:citrate, microwaved on full power for 8 min and soaked in a 3% H_2O_2-methanol solution for 15 min to inactivate enzymes. The slices were then incubated in primary antibody (1:100, polyclonal rabbit anti-3β-hydroxysteroid dehydrogenase (3β-HSD)-IgG, Novus Biological LLC, USA) for 2 h, washed 3 times with PBS, incubated with FITC-labeled secondary antibodi+es (1:400, KeyGEN BioTECH, Nanjing, China) for 1 h at 37°C, washed 3 times and stained with DAPI (KeyGEN BioTECH, Nanjing, China) for 10 min at room temperature in the dark. All slides were viewed with a fluorescence microscope (OLYMPUS IX51, Japan).

Statistical analysis

All data were analyzed using SPSS11.5 (USA) software and are presented as the mean±SD. Statistics were evaluated using one-way analysis of variance followed by a Dunnett's test. The Student Newman-Keuls test was performed when the variances were equal, and the Games-Howell test was used when the variances were not equal. A probability value of $P<0.05$ was considered statistically significant.

Results

Testicular MDA, ACP, SDH, and LDH

Oxidative stress occurs in testicular tissues following exposure to intermittent hypoxia. In the testis, the production of MDA, an indication of oxidized lipid substances from an excess of reactive oxygen species (ROS), was increased by 177.1% ($P<0.01$) compared to controls. By contrast, the activities of ACP, SDH, and LDH, which are the main energy suppliers for both testosterone biosynthesis and cell maturation during spermatogenesis, were decreased in hypoxic testes by 42.1% ($P<0.01$), 34.3% ($P<0.01$) and 57.1% ($P<0.01$), respectively, compared to controls. A reduction in these enzymatic activities was, at least in part, related to the testicular lesions induced by the 28-d exposure to intermittent hypoxia, which led to low testosterone production in these mice. These abnormalities were decreased by interventions with either CPU86017-RS or nifedipine (Figure 1).

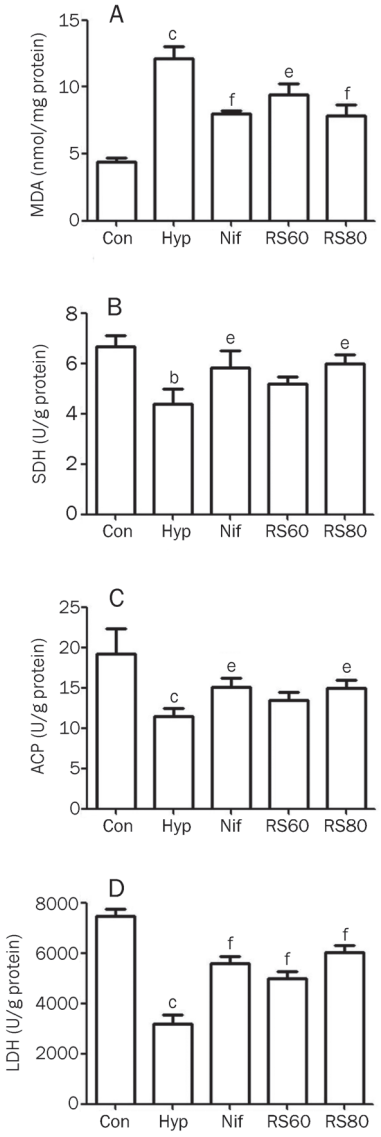

Figure 1. Testicular MDA increased significantly in hypoxic mice, accompanied with a reduction of SDH, ACP, and LDH dramatically, indicating that both oxidative stress and short of energy supply in the hypoxic testis were significant. These changes were obviously alleviated by the medication of CPU86017-RS and nifedipine. $n=6$. Mean±SD. $^bP<0.05$, $^cP<0.01$ *vs* control. $^eP<0.05$, $^fP<0.01$ *vs* hypoxia.

Serum testosterone and StAR

Low serum testosterone has been recognized as the main criterion for clinical diagnosis of male hypogonadism. Therefore, we measured serum testosterone levels. In this study, serum testosterone levels, which are very sensitive to hypoxia, decreased by 85.0% ($P<0.01$) in the hypoxic testis compared to the control group (Figure 2A). The biosynthesis of testosterone depends on a series of gene activities that convert cholesterol to testosterone. The first step in this series of reactions involves the StAR-controlled uptake of cholesterol into the mitochondria. The expression of the testosterone biosynthesis gene StAR was downregulated by 32% ($P<0.01$) at the mRNA level and 36.4% ($P<0.01$) at the protein level relative to controls (Figures 2B, 2C).

Pathological changes

The morphological arrangement of the seminiferous tubules was precisely layered and contained the spermatogenetic and Sertoli's cells associated with an intact basement. As in normal physiological conditions, these tubules were filled with spermatozoa that were concentrated at the center of the lumen and were surrounded by a clearly structured reproductive epithelium. The inter-tubule space contained an abundance of Leydig's cells, which are responsible for the active production of androgen. In contrast, the seminiferous tubules in the hypoxic group were badly damaged; their multi-layer reproductive endothelium was destroyed; they had greatly

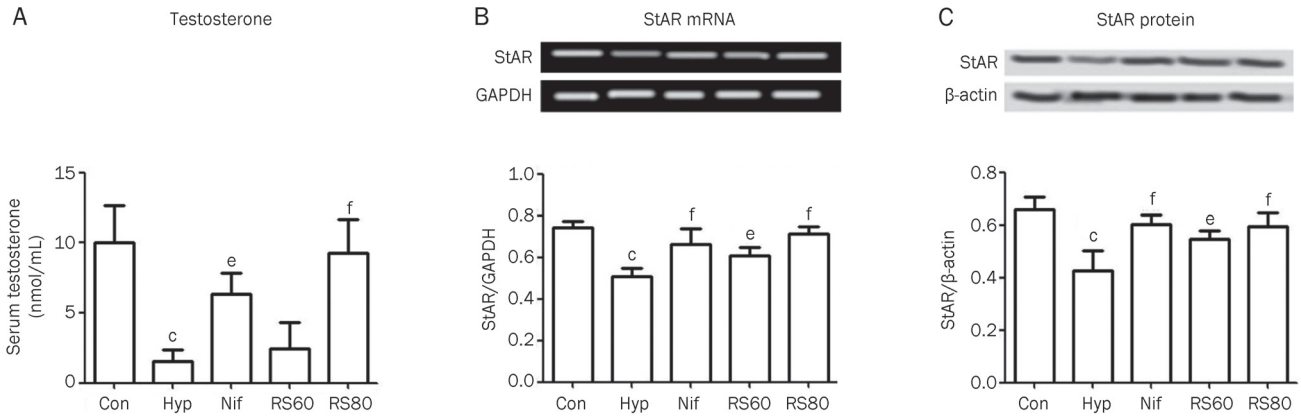

Figure 2. Serum testosterone content and expressions of StAR were decreased distinctly in mice suffering from hypoxia, which were neutralized by medication of CPU86017-RS. n=6. Mean±SD. ^{c}P<0.01 *vs* control. ^{e}P<0.05, ^{f}P<0.01 *vs* hypoxia.

decreased amounts of spermatozoa in the lumen; and they had distorted reproductive epithelial and Sertoli's cells. The hypoxic mice also had a decreased number of Leydig's cells in the intra-tubular space. CPU86017-RS and nifedipine treatment preserved the normal appearance of the seminiferous tubules and the number of Leydig's cells in the inter-tubular space (Figure 3A–3E).

Immunofluorescence imaging and Western blotting of 3β-HSD

To collect further evidence of the existence of hypoxic lesions in the testis, 3β-HSD, a specific biomarker of Leydig's cell in the testis, was targeted. 3β-HSD is involved in many of the steps in the synthesis of testosterone from cholesterol that occur in the mitochondria of Leydig's cells and is therefore critical for androgen biogenesis. The location and abundance of 3β-HSD conjugated to Leydig's cells in the space within the tubules were clearly observed with the green signal from the immunofluorescence assay, and functioning Leydig's cells were clearly observed in the control mice (Figure 3F). The green fluorescence intensity of Leydig's cells was greatly reduced following exposure to intermittent hypoxia, in agreement with the changes in histology and biomarkers and the reduced serum testosterone concentration. The recovery of the Leydig's cells labeled with immunofluorescence was significant in mice treated with either nifedipine or CPU86017-RS (Figure 3G–3K). In parallel experiments, Western blots revealed a significant decrease in the protein expression of 3β-HSD (P<0.01) compared to controls. CPU86017-RS and nifedipine treatment increased the mRNA and protein expression of 3β-HSD (Figure 3L, 3M).

ET_AR and OBRb expression

Leptin and its receptors greatly affect the male reproductive epithelium during developmental and postnatal periods. In the present study, we found elevated levels of OBRb mRNA and protein expression in the testis (Figure 4A, 4B), as well as an upregulation of mRNA and protein levels of ET_AR (Figure 4C, 4D). Activated ET_AR is always accompanied by an increase in oxidants. Therefore, the upregulation of ET_AR is indicative of a state of oxidative stress in the hypoxic testes. CPU86017-RS and nifedipine neutralized the abnormal expression of OBRb (P<0.01) and ET_AR (P<0.01) compared with hypoxic mice that did not receive treatment (Figure 4).

Cx43 and MMP9

Hypoxia-induced male hypogonadism may be the consequence of impairment of the extracellular matrix. This is relevant because the extracellular matrix is important in gap junctional communication through the intercellular space of cells in the testes. Cx43 mRNA and protein expression decreased by 43.6% and 42.7% (P<0.01), respectively, in the hypoxia group compared to controls (Figure 5A, 5B), indicating that the intercellular gap junctional communications in the testis were insufficient. This finding coincided with the depressed testicular function observed after episodes of hypoxia. This Cx43 impairment contributed to the decreased testosterone production in the testes. In contrast, MMP9 mRNA and protein expression was increased by 70.8% and 93.8% (P<0.01), respectively (Figure 5C, 5D), providing evidence for the idea that intermittent hypoxia induces remodeling of the extracellular matrix. Extracellular matrix remodeling was significant and resulted in an alteration in the intercellular space that affected signal transduction through intercellular gap junctions. CPU86017-RS and nifedipine relieved the hypoxia-induced insults to the reproductive system, partly by normalizing the extracellular matrix and gap junctional communication in the testes.

Discussion

Normobaric hypoxia is a common pathological process that damages multiple metabolic and cardiovascular systems[27]. Hypoxia inhibits spermatogenesis by damaging the seminiferous epithelium and promoting the apoptosis of spermatogenic cells in the reproductive system.

Serum testosterone concentrations less than 300 ng/dL serve as a criterion for the diagnosis of male hypogonadism[28].

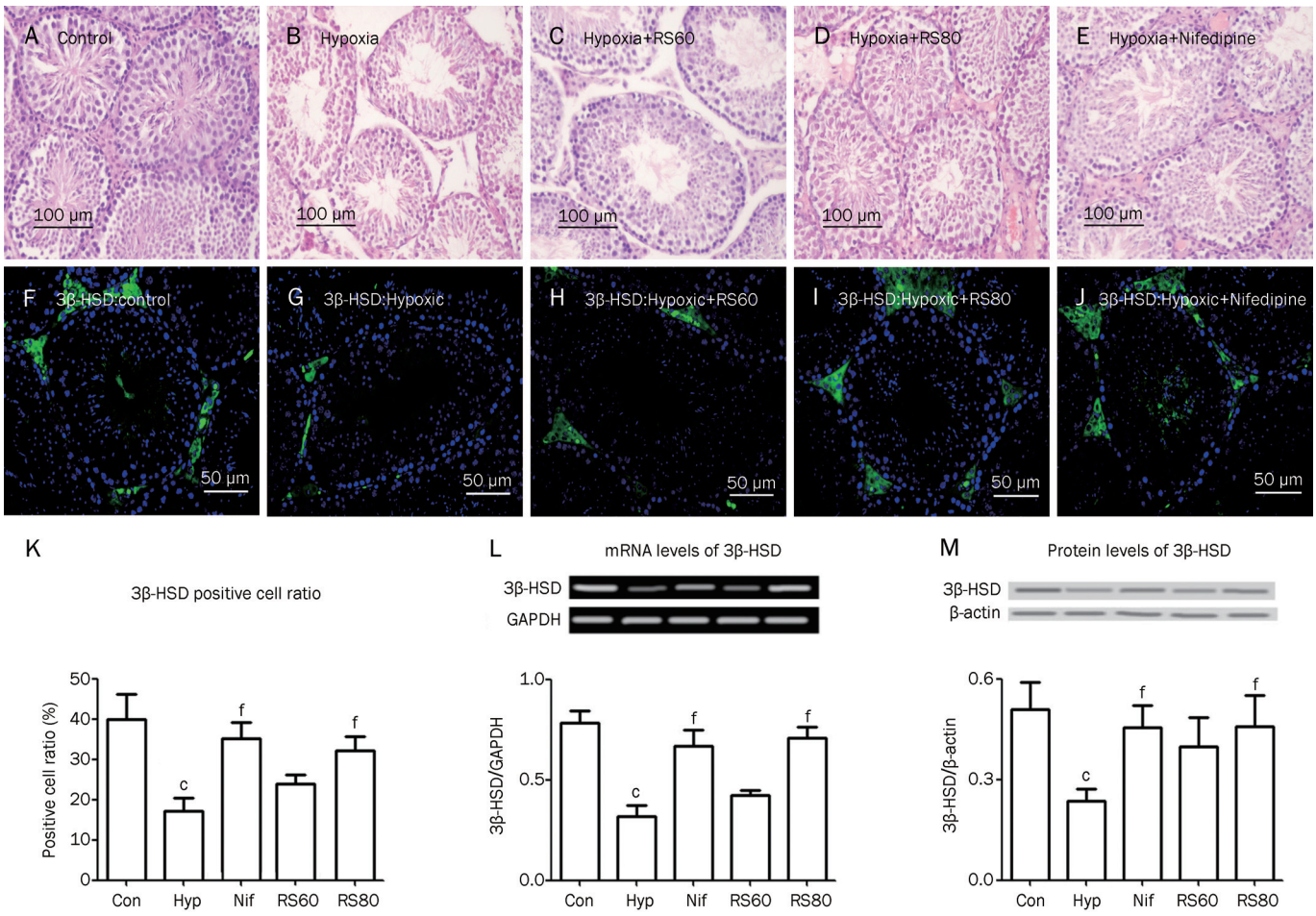

Figure 3. Histological changes of the testes and abnormal expression of 3β-HSD (green fluorescence) were observed. A–E: Histological changes in the testis were found in H+E stained slices. (A) Control; (B) Hypoxia; (C) Hypoxia+RS60; (D) Hypoxia+RS80; (E) Hypoxia+nifedipine. The cellular distribution and expression of 3β-HSD were detected by immunofluorescence assay in green color (F–J), and RT-PCR and western blotting were also employed. (F) 3β-HSD in normal control; (G) in hypoxic mice; (H) Hypoxia+RS60; (I) Hypoxia+RS80; (J) Hypoxia+nifedipine; (K) positive cell ratio of 3β-HSD; (L and M) mRNA and protein levels of 3β-HSD.

Testosterone serum concentrations decreased significantly after exposure to intermittent hypoxia, and this decrease was due to decreased expression of the androgen biosynthesis genes, StAR and 3β-HSD. Decreased testosterone production induced by intermittent hypoxia may result from inhibition of cholesterol desmolase activity (cleavage of cholesterol side-chains by cytochrome P450 and P450scc) and the cAMP pathway; therefore, decreased testosterone production may be related to abnormal intracellular calcium levels[29, 30]. Testosterone replacement therapy, which is widely used to treat male hypogonadism in clinical settings, elevates serum testosterone levels directly and improves erectile dysfunction. However, although this therapeutic approach suppresses the hypothalamus-pituitary-testis feed back loop, it does not alleviate testicular lesions[10, 11]. Increasing the gene expression of both StAR and 3β-HSD represents a basic approach to normalize the hypoxia-induced decrease in testicular function. In the present study, the hypoxia-induced downregulation of these two genes was significantly attenuated by the calcium antagonists nifedipine and CPU86017-RS.

In the testes, the activity of ACP, LDH, and SDH is a crucial source of energy for both testosterone biosynthesis and spermatogenic epithelium maturation. Therefore, the activities of ACP, LDH, and SDH can be used as markers for predicting testis function. ACP is essential for protein synthesis and is actively involved in germ development and Sertoli's cell function. LDH and SDH are present during spermatogenesis and are found in Sertoli's cells, where they take an active part in supplying energy by metabolizing glucose[28]. They also play an important role in the transformation of testosterone from cholesterol in Leydig's cells.

Calcium channels in the cell membrane actively control the influx of Ca^{2+}, which influences the intracellular levels of free Ca^{2+}. Consequently, the intracellular levels of free Ca^{2+} markedly affect the genesis and maturation of sperm cells[31, 32]. Sperm and Leydig's cells containing L-type voltage-dependent calcium channels are crucial for sperm-egg fusion and testosterone biosynthesis. In this study, nifedipine served as the

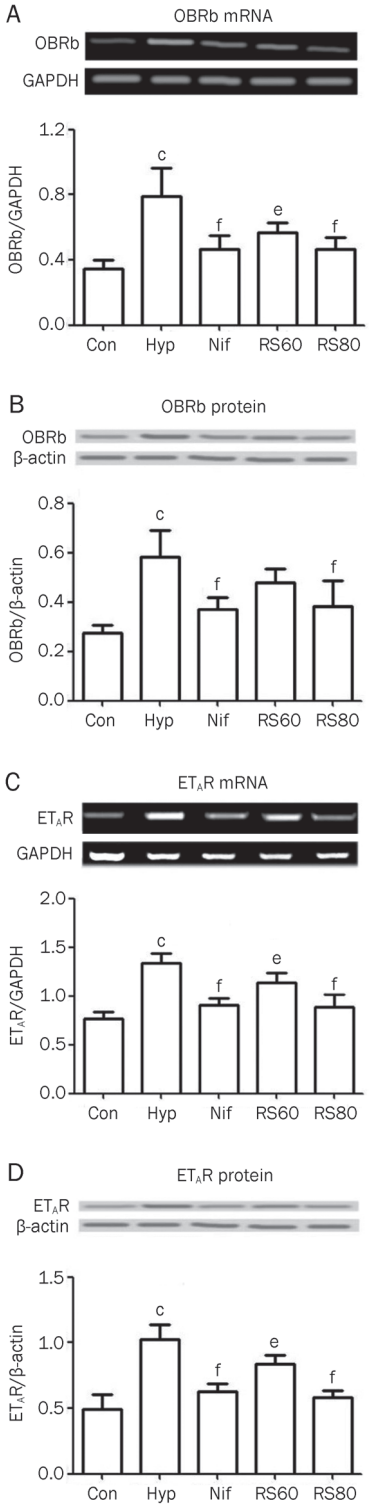

Figure 4. An increase in expression of ET_AR and OBRb was found in hypoxic mice, which was blunted by CPU86017-RS compound and nifedipine respectively. *n*=6. Mean±SD. $^cP<0.01$ *vs* dontrol. $^eP<0.05$, $^fP<0.01$ *vs* hypoxia.

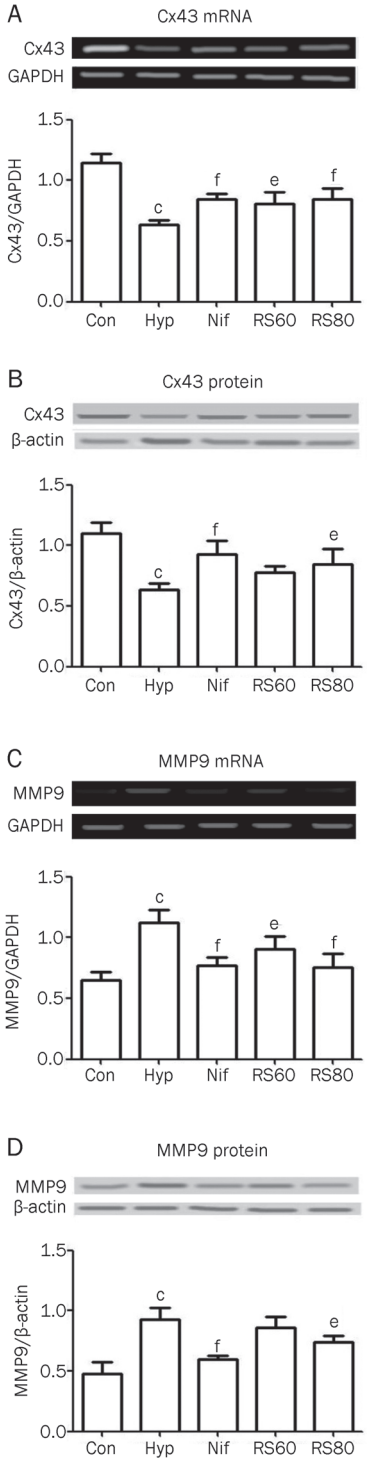

Figure 5. Abnormal expressions of MMP9 and Cx43 were found in the testis after hypoxia exposure and were reversed by CPU86017-RS and nifedipine dramatically. *n*=6. Mean±SD. $^cP<0.01$ *vs* control. $^eP<0.05$, $^fP<0.01$ *vs* hypoxia.

positive control that limited the calcium influx and reversed the increase in calcium influx observed following exposure to low levels of oxygen. Under physiological conditions, calcium concentrations in the extracellular space are about a million times higher than those in the cytosol. Voltage-dependent L-type channels are important in living cells, and upon activa-

tion under physiological conditions, a small amount of Ca^{2+} moves through these channels and promotes a series of Ca^{2+}-activated events necessary for normal testicular function. An overload of Ca^{2+} influx caused by hypoxia contributes significantly to hypoxia-induced testicular damage. Blocking this calcium influx with nifedipine reverses the hypoxia-induced increase in overloaded free Ca^{2+} levels in the testicular cells, thereby decreasing the pathological changes secondary to hypoxia. In addition, CPU86017 has been found to act as a calcium antagonist in the cardiovascular system[17, 18], and this calcium antagonism may underlie the mechanism by which this compound acts to relieve hypoxia-induced testicular abnormalities. The disturbance of calcium homeostasis in reproductive cells is the main cause of the low testosterone concentrations and abnormal pro-inflammatory biomarkers observed in hypoxic testes. These changes were relieved by the CPU86017-RS isomer, and the relief was comparable to that observed with nifedipine. We also emphasize that under physiological conditions calcium influx is necessary for the maintenance of normal testicular size and function. Large doses of nifedipine caused a decrease in testosterone biosynthesis and a reduction in testicular size in prepubertal mice[33].

An over-activated endothelin system has been found to be involved in several pathologies in the cardiovascular system and to participate in myocardium fibrosis through the activation of MMP2/9 in heart fibroblasts[14]. Our previous studies have suggested that an upregulation of ET_AR is closely linked to an increase in ROS production, which forms a so-called ET-ROS pathway in diabetic cardiomyopathy, vascular disorder and nephropathy[34, 35]. ROS are over-produced in hypoxia and facilitates the activation of ET_AR. ET_AR then provides positive feedback to stimulate the NADPH oxidase and to initiate oxidative stress in the testis. The rhythmic contraction of seminiferous tubules propels sperm cells to the epididymis and depends on the stimulation of ET-1, which is secreted mainly by Sertoli's cells and Leydig's cells. Under intermittent hypoxia conditions, over-activation of ET_AR leads to an impairment in the movement of the tubules, impeding the final maturation of sperm cells in the epididymis.

Abnormal expression of MMP9 and Cx43 in isoproterenol-induced cardiovascular abnormality is related to ET_AR activation[14]. Spermatogenesis is a highly programmed process that requires well-regulated degradation and remodeling of the extracellular matrix. The regulation of CD147 by MMP2 and MMP9 is essential for germ cell migration during spermatogenesis[36]. MMP9 is a key effector molecule in the increased neural stem cell proliferation and migration that occur during low O_2 conditions. Decreased MMP9 expression adversely influences cell proliferation, cell migration and cell cycle kinetics in the testes. Gap junctional communication is achieved through a family of proteins named connexins, through which small molecules, such as ions and second messengers, and various other signaling molecules can be exchanged between cells[37]. Cx43 is found in a variety of tissues, including the testes, and is responsible for conducting cell-to-cell communication via electrical and chemical coupling. Gap junctional communication via Cx43 plays an important role in normal testicular function because it normalizes the distribution of electrical heterogeneity[38]. The effectiveness of nifedipine and CPU86017-RS in relieving the hypoxia-induced abnormality of testicular Cx43 is likely the same as diltiazem[39]. Cx43 function is dependent on the connection of the two halves of the channels across the extracellular space; therefore, changes in the extracellular matrix may greatly impair this connection, resulting in a blockade of gap junctional communication and a dysfunctional testis.

Leptin, and its receptor OBRb, significantly modulates the function of reproductive cells in the testis. Leptin also affects the proliferation and differentiation of germ cells and modulates testicular steroidogenesis through autocrine/paracrine factors[40]. Over-activation of testicular OBRb caused by intermittent hypoxia reflects a status of hyperleptinemia, which indicates the presence of oxidative stress related to over-activity of ET_AR and the sympathetic nerve system. As a result, over-expressed OBRb may damage testosterone biosynthesis by increasing Ca^{2+} influx in the testis. Therefore, treatment with nifedipine and CPU86017-RS is appropriate for the treatment of abnormal OBRb and ET_AR, thereby ameliorating the dysfunction observed in hypoxic testes.

In conclusion, hypoxic testopathy is characterized by a downregulation of StAR, 3β-HSD, and Cx43 expression and an upregulation of ET_AR, MMP9 and OBRb expression. These changes are sensitive to both nifedipine and CPU86017-RS, which implies that the primary cause of the hypoxia-induced damage to the testicular cells is likely mediated by an increase in Ca^{2+} influx. CPU86017-RS and nifedipine attenuated the hypoxia-induced testicular dysfunction by normalizing the testicular expression of genes and pro-inflammatory biomarkers. Further investigation is needed to obtain direct evidence of the calcium-influx-blocking effect of CPU86017-RS and nifedipine in Leydig's cells.

Acknowledgements

This work was supported by the National Key New Drug Innovation Program, the Ministry of Science and Technology of China (Grant No: 2009ZXJ09004-070) and the National Natural Science Foundation of China (Grant No: 81070145).

Author contribution

Guo-lin ZHANG conducted the project, processed the data and prepared the manuscript. Feng YU assisted with the data processing. Yu-si CHENG and Can ZHANG provided the compounds. De-zai DAI and Yin DAI designed the project, discussed the underlying mechanisms and revised the manuscript.

References

1 Webb JD, Coleman ML, Pugh CW. Hypoxia, hypoxia-inducible factors (HIF), HIF hydroxylases and oxygen sensing. Cell Mol Life Sci 2009; 66: 3539–54.

2 Fahling M. Cellular oxygen sensing, signalling and how to survive translational arrest in hypoxia. Acta Physiol 2009; 195: 205–30.

3 Sheldon RA, Osredkar D, Lee CL, Jiang X, Mu D, Ferriero DM. HIF-1 alpha-deficient mice have increased brain injury after neonatal hypoxia-ischemia. Dev Neurosci 2009; 31: 452–8.
4 Takasawa M, Moustafa RR, Baron JC. Applications of nitroimidazole *in vivo* hypoxia imaging in ischemic stroke. Stroke 2008; 39: 1629–37.
5 Guo S, Miyake M, Liu KJ, Shi H. Specific inhibition of hypoxia inducible factor 1 exaggerates cell injury induced by *in vitro* ischemia through deteriorating cellular redox environment. J Neurochem 2009; 108: 1309–21.
6 Li N, Dai DZ, Dai Y. CPU86017 and its isomers improve hypoxic pulmonary hypertension by attenuating increased ET_A receptor expression and extracellular matrix accumulation. Naunyn Schmiedebergs Arch Pharmacol 2008; 378: 541–52.
7 Zhang TT, Cui B, Dai DZ, Tang XY. Pharmacological efficacy of CPU 86017 on hypoxic pulmonary hypertension in rats: mediated by direct inhibition of calcium channels and antioxidant action, but indirect effects on the ET-1 pathway. J Cardiovasc Pharmacol 2005; 46: 727–34.
8 Taniguchi H, Kawa G, Kinoshita H, Matsuda T, Asai A. Male hypogonadotropic hypogonadism (MHH) outpatient with testosterone deficiency syndrome: a case report. Hinyokika kiyo 2009; 55: 107–9.
9 Feng Y, Zhang Q, Dai DZ, Ying HJ, Dai Y. Strontium fructose 1,6-diphosphate rescues adenine-induced male hypogonadism and upregulates the testicular endothelin-1 system. Clin Exp Pharmacol Physiol 2007; 34: 1131–7.
10 Xu M, Dai DZ, Zhang Q, Cheng YS, Dai Y. Upregulated NADPH oxidase contributes to diabetic testicular complication and is relieved by strontium fructose 1,6-diphosphate. Exp Clin Endocrinol Diabetes 2010; 118: 459–65.
11 Tang XY, Zhang Q, Dai DZ, Ying HJ, Wang QJ, Dai Y. Effects of strontium fructose 1,6-diphosphate on expression of apoptosis-related genes and oxidative stress in testes of diabetic rats. Int J Urol 2008; 15: 251–6.
12 Zhang Q, Liu HR, Ying HJ, Dai DZ, Tang XY, Dai Y. Strontium fructose 1,6-diphosphate alleviates early diabetic testopathy by suppressing abnormal testicular matrix metalloproteinase system in streptozocin-treated rats. J Pharm Pharmacol 2009; 61: 229–36.
13 Hu C, Cong XD, Dai DZ, Zhang Y, Zhang GL, Dai Y. Argirein alleviates diabetic nephropathy through attenuating NADPH oxidase, Cx43, and PERK in renal tissue. Naunyn Schmiedebergs Arch Pharmacol 2011; 383: 309–19.
14 Peng HJ, Dai DZ, Ji H, Dai Y. The separate roles of endothelin receptors participate in remodeling of matrix metalloproteinase and connexin 43 of cardiac fibroblasts in maladaptive response to isoproterenol. Eur J Pharmacol 2010; 634: 101–6.
15 Steiner M, Weipoltshammer K, Viehberger G, Meixner EM, Lunglmayr G, Schöfer C. Immunohistochemical expression analysis of Cx43, Cx26, c-KIT and PlAP in contralateral testis biopsies of patients with non-seminomatous testicular germ cell tumor. Histochem Cell Biol 2011; 135: 73–81.
16 Zhang TT, Cui B, Dai DZ, Su W. CPU 86017, *p*-chlorobenzyltetrahyd roberberine chloride, attenuates monocrotaline-induced pulmonary hypertension by suppressing endothelin pathway. Acta Pharmacol Sin 2005; 26: 1309–16.
17 Dai DZ, Hu HJ, Zhao J, Hao XM, Yang DM, Zhou PA, *et al*. Blockade of L-type calcium channel in myocardium and calcium-induced contractions of vascular smooth muscle by CPU 86017. Acta Pharmacol Sin 2004; 25: 416–23.
18 Dai DZ. CPU86017: a novel class III antiarrhythmic agent with multiple actions at ion channels. Cardiovasc Drug Rev 2006; 24: 101–15.
19 Du RH, Yi HW, Dai DZ, Tang WH, Dai Y. Inflammatory factors that contribute to upregulation of ERG and cardiac arrhythmias are suppressed by CPU86017, a class III antiarrhythmic agent. J Pharm Pharmacol 2008; 60: 1089–95.
20 Li N, Yang L, Dai DZ, Wang QJ, Dai Y. Chiral separation of racemate CPU86017, an anti-arrhythmic agent, produces stereoisomers possessing favourable ion channel blockade and less alpha-adrenoceptor antagonism. Clin Exp Pharmacol Physiol 2008; 35: 643–50.
21 Na T, Huang ZJ, Dai DZ, Zhang Y, Dai Y. Abrupt changes in FKBP12.6 and SERCA2a expression contribute to sudden occurrence of ventricular fibrillation on reperfusion and are prevented by CPU86017. Acta Pharmacol Sin 2007; 28: 773–82.
22 Bailey DM, Dehnert C, Luks AM, Menold E, Castell C, Schendler G, *et al*. High-altitude pulmonary hypertension is associated with a free radical-mediated reduction in pulmonary nitric oxide bioavailability. J Physiol 2010; 588: 4837–47.
23 Andreassen AK, Geiran O, Madsen S, Hognestad A, Simonsen S. Pulmonary arterial hypertension treated with prostacyclin or calcium blockers. Tidsskr Nor Laegeforen 2003; 123: 3393–6.
24 Rosati E, Butera G, Bossone E, De Felice C, Latini G. Inhaled nitric oxide and oral nifedipine in a preterm infant with bronchopulmonary dysplasia and pulmonary hypertension. Eur J Pediatr 2007; 166: 737–8.
25 Maggiorini M. High altitude-induced pulmonary oedema. Cardiovasc Res 2006; 72: 41–50.
26 Richardson A, Watt P, Maxwell N. Hydration and the physiological responses to acute normobaric hypoxia. Wild Environ Med 2009; 20: 212–20.
27 Hodkinson PD, Hunt BJ, Parmar K, Ernsting J. Is mild normobaric hypoxia a risk factor for venous thromboembolism? J Thromb Haemost 2003; 1: 2131–3.
28 Cheng YS, Dai DZ, Dai Y. Testis dysfunction by isoproterenol is mediated by upregulating endothelin receptor A, leptin and protein kinase Cvarepsilon and is attenuated by an endothelin receptor antagonist CPU0213. Reprod Toxicol 2010; 29: 421–6.
29 Luo L, Chen H, Zirkin BR. Temporal relationships among testosterone production, steroidogenic acute regulatory protein (StAR), and P450 side-chain cleavage enzyme (P450scc) during Leydig cell aging. J Androl 2005; 26: 25–31.
30 Rangel PL, Rodriguez A, Rojas S, Sharp PJ, Gutierrez CG. Testosterone stimulates progesterone production and STAR, P450 cholesterol side-chain cleavage and LH receptor mRNAs expression in hen (*Gallus domesticus*) granulosa cells. Reproduction 2009; 138: 961–9.
31 Lawson C, Goupil S, Leclerc P. Increased activity of the human sperm tyrosine kinase SRC by the cAMP-dependent pathway in the presence of calcium. Biol Reprod 2008; 79: 657–66.
32 Boni R, Gualtieri R, Talevi R, Tosti E. Calcium and other ion dynamics during gamete maturation and fertilization. Theriogenology 2007; 68: S156–64.
33 Lee JH, Ahn HJ, Lee SJ, Gye MC, Min CK. Effects of L- and T-type Ca^{2+} channel blockers on spermatogenesis and steroidogenesis in the prepubertal mouse testis. J Assist Reprod Genet 2011; 28: 23–30.
34 Tang XY, Liu Q, Dai DZ, Dai Y. CPU0213, a novel endothelin receptor antagonist, suppresses the upregulation of matrix metalloproteinases and connexin 43 in hyperthyroid myocardium. Pharmacol Rep 2008; 60: 524–31.
35 Su W, Dai DZ, Liu HR, Na T, Dai Y. Upregulated endothelin system in diabetic vascular dysfunction and early retinopathy is reversed by CPU0213 and total triterpene acids from Fructus Corni. Clin Exp Pharmacol Physiol 2007; 34: 1228–33.
36 Chen H, Fok KL, Yu S, Jiang J, Chen Z, Gui Y, *et al*. CD147 is required for matrix metalloproteinases-2 production and germ cell migration during spermatogenesis. Mol Hum Reprod 2011; 17: 405–14.

37 Izzo G, Ferrara D, Delrio G, d'Istria M, Minucci S. Connexin43 expression in the testis of frog *Rana esculenta*: sex hormonal regulation. Ann NY Acad Sci 2009; 1163: 425–7.

38 Guan K, Wagner S, Unsold B, Maier LS, Kaiser D, Hemmerlein B, *et al*. Generation of functional cardiomyocytes from adult mouse spermatogonial stem cells. Circ Res 2007; 100: 1615–25.

39 Matsushita S, Kurihara H, Watanabe M, Okada T, Sakai T, Amano A. Inhibition of connexin43 dephosphorylation is involved in protective effects of diltiazem on cardiac function during hypoxic injury. Histol Histopathol 2011; 26: 315–22.

40 Herrid M, O'Shea T, McFarlane JR. Ontogeny of leptin and its receptor expression in mouse testis during the postnatal period. Mol Reprod Dev 2008; 75: 874–80.

Acta Pharmacologica Sinica (2012) 33: 479–489
 1671-4083/12 $32.00
www.nature.com/aps

Original Article

Strontium fructose 1,6-diphosphate prevents bone loss in a rat model of postmenopausal osteoporosis via the OPG/RANKL/RANK pathway

Bo MA[1], Qi ZHANG[1, 2, *], Di WU[3], Yong-lu WANG[1, 2], Ying-ying HU[1], Yan-ping CHENG[1], Zhen-dong YANG[1], Ya-ya ZHENG[1], Han-jie YING[4, *]

[1]School of Pharmaceutical Sciences, Nanjing University of Technology, Nanjing 210009, China; [2]Jiangsu Provincial Institute of Material Medica, Nanjing University of Technology, Nanjing 210009, China; [3]Laboratory for Applied PK/PD, Division of Clinical Pharmacology and Therapeutics, The Children's Hospital of Philadelphia; Kinetic Modeling and Simulation Core, Institute of Translational Medicine and Therapeutics, University of Pennsylvania, Philadelphia, PA 19104, USA; [4]School of Life Science & Pharmaceutical Engineering, Nanjing University of Technology, Nanjing 210009, China

Aim: To evaluate the protective effects of strontium fructose 1,6-diphosphate (FDP-Sr), a novel strontium salt that combined fructose 1,6-diphosphate (FDP) with strontium, on bone in an ovariectomy-induced model of bone loss.
Methods: Eighty female Sprague-Dawley rats were ovariectomized (OVX) or sham-operated. Three months later, the rats were assigned to six groups (10 for each): sham-operated, OVX control, OVX+FDP-Sr (110, 220, or 440 mg/kg), or OVX+strontium ranelate (SR, 180 mg/kg). Drugs were administered orally for 3 months. When the treatment was terminated, the following parameters were assessed: bone mineral density (BMD), the biomechanical properties of the femur and lumbar vertebrae, trabecular histomorphology, serum phosphorus, calcium, bone-specific alkaline phosphatase (B-ALP), tartrate-resistant acid phosphatase 5b (TRACP5b), N-telopeptide of type I collagen (NTx) and a series of markers for oxidative stress. Receptor activator of NF-κB ligand (RANKL) and osteoprotegerin (OPG) levels in serum were measured using ELISA and their gene expression levels in the bone were measured using R-T PCR.
Results: Treatment with FDP-Sr (220 or 440 mg/kg) or SR (180 mg/kg) significantly increased the BMD and improved the bone micro-architecture and bone strength in OVX rats. The treatments also decreased in the levels of H_2O_2 and MDA, restored the CAT level in serum and bone marrow, increased the serum B-ALP and decreased NTx and TRACP 5b in OVX rats. Treatment with FDP-Sr decreased the RANKL level, and increased the OPG level in serum in a dose-dependent manner. It also significantly down-regulated the RANKL expression and up-regulated OPG expression in bone marrow.
Conclusion: FDP-Sr may be an effectve treatment for postmenopausal osteoporosis that acts, in part, via a decrease in osteoclastogenesis through the OPG\RANKL\RANK pathway.

Keywords: osteoporosis; ovariectomy; strontium fructose 1,6-diphosphate; strontium ranelate; osteoprotegerin (OPG); receptor activator of NF-κB ligand (RANKL); bone mineral density; tartrate-resistant acid phosphatase 5 (TRACP5); N-telopeptide of type I collagen (NTx)

Acta Pharmacologica Sinica (2012) 33: 479–489; doi: 10.1038/aps.2011.177; published online 19 Mar 2012

Introduction

Osteoporosis is a major clinical condition in the elderly population and is a skeletal disorder characterized by bone mass reduction, increased bone fracture risk and potential bone architecture alterations[1, 2]. The incidence of osteoporosis is increasing owing to the increasing elderly population. Currently, osteoporosis and its complications affect approximately 200 million people worldwide. Hip fracture is one of the most serious complications of osteoporosis and a measure of osteoporosis severity. By 2050, the incidence of hip fracture is predicted to double in North America and Europe, whereas higher incidences are predicted in other countries, including a five-fold increase in Asia and up to a seven-fold increase in Latin America[3]. Although these estimates are for the general population, women are more prone to bone loss than men, owing to postmenopausal estrogen deficiency, which results in osteoporosis.

* To whom correspondence should be addressed.
E-mail nancyzhang03@hotmail.com (Qi ZHANG);
yinghanjie134@163.com (Han-jie YING)
Received 2011-09-13 Accepted 2011-11-23

The mechanisms through which estrogen deficiency induces bone loss remain unclear. Bone remodeling has been suggested to play a fundamental role in the maintenance of skeletal mechanical integrity via a balance between bone formation and bone resorption[4, 5]. Estrogen deficiency leads to a negative bone remodeling balance, in which bone resorption exceeds bone formation. This imbalance aggravates the loss of bone mass and increases the incidence of osteopenia. Thus, estrogen deficiency is a major risk factor for osteoporosis. Conventional therapeutic agents that aim to stimulate bone formation or inhibit bone resorption fail to re-establish bone turnover equilibrium even after long-term usage. Furthermore, these agents have multiple side effects, including bisphosphonate-induced osteonecrosis of the jaw[6, 7], estrogen replacement therapy (ERT)-induced malignancies[8, 9], and increased stroke rates[10, 11]. Therefore, it is necessary to develop novel drugs with the "dual effect" of stimulating bone formation and inhibiting bone resorption while causing fewer side effects.

Strontium, a significant component of the skeleton, can decrease bone resorption and increase bone formation and bone mass without affecting bone mineralization. Thus, strontium may be of potential benefit for the treatment of osteoporosis[12]. Following the formulation of strontium ranelate (Protelos; Servier Laboratories, France), strontium treatment has been considered to be an important advance in the pharmacotherapy of osteoporosis because strontium has demonstrated both anti-resorptive and bone-forming effects[13–16].

Many strontium salts have been synthesized and studied in the context of osteoporosis. To date, strontium ranelate is the only drug on the market and has been highly evaluated for clinical use. Ranelic acid serves as a carrier for strontium ranelate, but the biologic activity and toxicity of ranelic acid are unclear. Some side effects of ranelic acid, such as toxic epidermal necrolysis, have been reported[17]. Researchers remain uncertain if these side-effects are caused by strontium or ranelic acid. It would be of great interest to couple the Sr^{2+} with a natural, non-toxic acid radical that could increase the safety and efficacy of the strontium compound. Strontium fructose 1,6-diphosphate (FDP-Sr) is designed following the above principle.

FDP-Sr is a novel compound synthesized by combining fructose 1,6-diphosphate (FDP) with strontium (Figure 1). FDP serves as both a glycolytic intermediate and an important adenosine triphosphate supplier in energy metabolism. It exerts protective effects against ischemia[18] or hypoxia[19] and facilitates the recovery of relevant tissue[20]. FDP also has advantages, in terms of safety, over other chemical acid radicals due to its endogenous nature. In addition, FDP induces calcium uptake in bone formation and modulates bone metabolism *in vitro*[21]. Therefore, FDP may be especially suitable for elderly patients. FDP-Sr also showed a favorable pharmacokinetic profile as a promising anti-osteoporosis drug candidate (rapid oral absorption, modest protein-binding, and a significantly higher affinity for and longer retention in the bone than in other organs)[22]. As such, the combination of FDP with strontium may potentially improve the effect of strontium against osteoporosis.

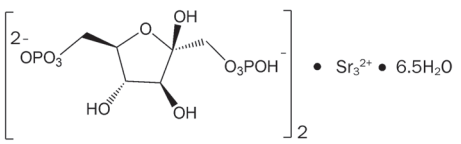

Figure 1. The chemical structure of FDP-Sr.

The aim of this study was to investigate the protective effect of FDP-Sr on bone loss in ovariectomized (OVX) rats. Bone mineral density (BMD), biomechanical testing, bone histomorphology, bone turnover and oxidative stress were examined in OVX rats treated with FDP-Sr. OPG and RANKL mRNA expression in the bone was examined by real-time PCR to determine the mechanism of osteoblasts (OB) coupled with osteoclasts (OC) under FDP-Sr treatment.

Materials and methods

Animals

Eighty specific-pathogen-free (SPF) virgin female Sprague–Dawley rats (6 months old, body weight 280±20.0 g) were obtained from the Animal Center of Nanjing Medical University for this study. Rats were housed under controlled conditions; room temperature was maintained at 22±1 °C, and standard solid food with water *ad libitum* was provided during the experiment. This study was reviewed and approved by the Animal Ethical Committee of Nanjing University of Technology.

Experimental design and treatments

After 7 days of acclimatization, all animals were anesthetized with 30 mg/kg pentobarbital sodium (Fluka, Germany), injected intraperitoneally, and then a bilateral ovariectomy (n=60) or a sham operation (n=20) was performed. Three months later, 20 rats were randomly chosen from sham-operated (n=10) and OVX (n=10) operated animals, and the BMD and biomechanical properties were examined to confirm the occurrence of osteoporosis in the rats. Subsequently, the remaining sham-operated animals (n=10) were treated with vehicle (deionized water), and the remaining OVX rats were randomly assigned to 5 groups (n=10 per group): OVX control (vehicle), OVX+FDP-Sr (FDP-Sr 110, 220 of 440 $mg \cdot kg^{-1} \cdot d^{-1}$), OVX+Strontium Ranelate (SR, 180 $mg \cdot kg^{-1} \cdot d^{-1}$, Osseor, Les Laboratories Servier Industrie, 45520 Gidy, France). The body weights of the rats were measured weekly and used to adjust the quantity of the FDP-Sr or SR treatments. After three months of treatment, all rats were weighed, anesthetized and bled from the carotid arteries. The tibia, femur and lumbar vertebrae were de-fleshed from adjacent tissues, wrapped in saline-soaked gauze bandages to prevent dehydration, and stored frozen at -20 °C in small Ziploc freezer bags until the BMD and biomechanical properties were measured. Blood samples were collected, and plasma was then prepared by centrifugation at 2000×g for 10 min. The plasma samples were

then frozen at -80 °C for the analysis of biochemical markers. The uterus was removed from each rat and immediately weighed.

Bone mineral density assessment

After the rats were sacrificed, the complete left femur and lumbar vertebrae (L1-L5) were removed. BMD was determined by dual-energy X-ray absorptiometry (GE, Lunar Prodigy^{TM}) equipped with the appropriate small animal software for bone density assessment. BMD was calculated from the bone mineral content (BMC) of the measured area.

Biomechanical three-point bending testing and compression measurements

Prior to mechanical testing, the lumbar vertebrae (L3) and left femur were slowly thawed at 37 °C, and then the soft tissue around the bone was removed. Subsequently, the left femur was placed on the lower supports of a three-point bending fixture with the posterior side facing down in an Instron Mechanical Testing Instrument (Instron 5544; Instron, Norwood, MA, USA). The span between the two lower supports was set at 18 mm. The upper loading device was aligned to the center of the femoral shaft. Load was applied at a constant displacement rate of 10 mm/min (temperature: 23°C, humidity: 60%–70%) until the femur broke. Simultaneously, the upper and lower end of the L3 was polished so that they were parallel, and all of the L3 were maintained at the same high degree. They were placed between two platens; the load and displacement were recorded on an Instron Mechanical Testing Instrument until the specimen broke. Maximum load (ultimate strength, F_{max}), stiffness (slope of the linear part of the curve representing elastic deformation), and energy absorption (area under the curve, Wabs) were obtained.

Bone histomorphometric analysis

The fourth lumbar vertebra were removed and fixed with a 10% tetraacetic acid (EDTA) solution (pH 7.4) at 4 °C for 3 weeks. After decalcification, each bone sample was cut along the coronal plane and embedded in paraffin for tissue sectioning and histological staining. A histomorphometric study of the lumbar vertebra was performed using image analysis software (Image Pro Plus 6.1 for Windows; Media Cybernetics, USA). Parameters measured included mean thickness of the trabeculae (Tb.Th, μm), trabecular area percentage (Tb.Ar, %) and trabecular separation (Tb.Sp, mm).

Bone metabolic biochemical markers

Serum calcium (S-Ca) and phosphorus (S-P) concentrations were measured on an automatic biochemical analyzer (Hitachi 7170, Hitachi, Japan). Serum bone-specific alkaline phosphatase (B-ALP, a bone resorption marker and indicator of bone formation), and the bone resorption markers serum tartrate-resistant acid phosphatase 5b (TRACP 5b) and N-telopeptide of type I collagen (NTx) were estimated using an ELISA kit (Quantikine, R&D Systems, Minneapolis, MN, USA) according to the manufacturer's instructions. B-ALP has 4.7% intra- and 3.4% inter-assay variabilities, TRACP 5b has 7.3% intra- and 3.5% inter-assay variabilities, and NTx has 4.0% intra- and 6.7% inter-assay variabilities.

Oxidative stress assays

Bone marrow was isolated from lumbar vertebrae, homogenized (100 mg/mL) at 4 °C in 0.1 mol/L Tris-HCl buffer pH 7.4 and centrifuged at 2000×*g* for 10 min. The supernatant was collected and promptly frozen at -80 °C until analysis. Oxidative stress was analyzed in bone marrow and serum. Superoxide dismutase (SOD, an enzyme that repairs cells and tissues as well as reduces superoxide induced damage), hydrogen peroxide (H_2O_2, an oxidizer), malondialdehyde (MDA, a marker for oxidative stress) and catalase (CAT, an enzyme rapidly catalyze the decomposition of hydrogen peroxide) concentrations were determined by colorimetric methods using the appropriate kits (Nanjing Jiancheng Bioengineering Institute, Nanjing, China). Protein levels in the bone marrow were determined by standard Coomassie brilliant blue staining (Nanjing Jiancheng Bioengineering Institute, Nanjing, China).

Serum OPG, RANKL, and IGF-I

Serum levels of OPG, IGF-I, and RANKL were assessed by ELISA (Quantikine, R&D Systems, Minneapolis, MN, USA) according to the manufacturer's instructions. The OPG ELISA had 3.4% intra- and 5.0% inter-assay variabilities, the IGF-I ELISA had 8.2% intra- and 7.9% inter-assay variabilities and the RANKL ELISA had 7.4% intra- and 8.6% inter-assay variabilities. The ratio of OPG to RANKL, expressed as OPG/RANKL, was used to explain the process of bone formation coupled with bone resorption.

Real-time PCR analyses of bone OPG and RANKL

The metaphyseal portion of the tibia was cut and homogenized using a Mixer Mill MM400 (Retsch, Germany) to isolate the mRNA. Total RNA was isolated using TRIzol following the manufacturer's guidelines (Invitrogen, Rockville, MD, USA). The concentration and purity of the RNA were determined by measuring the absorbance at 260 nm and 280 nm. The amount of RANKL and OPG mRNA was determined with ABI Prism 7900HT quantitative real-time PCR (Applied Biosystems, Foster City, CA). The primers were as follows: RANKL (forward, 5′-ACC AGC ATC AAA ATC CCA AG-3′; reverse, 5′-TTT GAA AGC CCC AAA GTA CG-3′) and OPG (forward, 5′-GTT CTT GCA CAG CTT CAC CA-3′; reverse, 5′-AAA CAG CCC AGT GAC CAT TC-3′). PCR amplification was carried out in a 20 μL reaction mixture (2 μL of cDNA and 200 nmol/L primers for OPG and RANKL, respectively, and 1 μL SYBR green). The temperature program was as follows: inactivation of reverse transcriptase at 95 °C for 30 s, followed by 45-cycles of 95 °C for 10 s, 60 °C for 20 s, and 72 °C for 20 s. The specificity of the PCR results was confirmed by melting curve analysis. The mRNA levels for each gene were calculated using a standard curve generated from 10-fold dilutions

of a control RNA (Roche, Penzberg, Germany). The expression levels of RANKL and OPG were normalized to S18 RNA levels, and all samples were analyzed in triplicate.

Statistical analysis

All data are presented as the mean±SD. One-way ANOVA followed by the least-significant difference (LSD) was used to determine statistical differences. $P<0.05$ was used as the criteria for statistical significance.

Results

Body weight and uterine index

There was no difference in the body weight observed among all groups in the initial experimental period. Following the initial experimental period, the body weights in the OVX-control group and OVX+FDP-Sr/SR group significantly increased compared to the sham-operated group; no adverse effects from FDP-Sr treatment were observed (Figure 2A). Atrophy of the uterine tissue was caused by bilateral ovariectomy after 6 months, and the uterine index (uterine wet weight/body weight) and E_2 levels (Figure 2B, 2C) in the OVX control and treatment groups were markedly decreased compared with the sham-operated group ($P<0.01$). These data indicated the success of the surgical procedure and confirmed that the FDP-Sr treatment did not have estrogenic effects.

Bone mineral density measurements

Ovariectomy caused significant BMD reduction in the rat femur and lumbar vertebrae compared to that in the sham-operated group ($P<0.05$ CV: 5.23% and $P<0.01$, CV: 6.25%, respectively) three months following the operation (Figure 3). At the end of the treatment period, the BMD values for the femur ($P<0.01$) and lumbar vertebrae ($P<0.01$) in the OVX-control group (CV: 8.13% and 7.30%) were significantly lower than those in the sham-operated group. Treatment with 220 or 440 $mg \cdot kg^{-1} \cdot d^{-1}$ of FDP-Sr markedly inhibited OVX-induced decreases (0.173±0.011 CV: 6.36% and 0.175±0.013 CV: 7.43%, respectively) in BMD of the femur ($P<0.05$ for both). All three FDP-Sr doses were shown to significantly inhibit the decrease in lumbar vertebrae BMD in a dose-dependent manner in

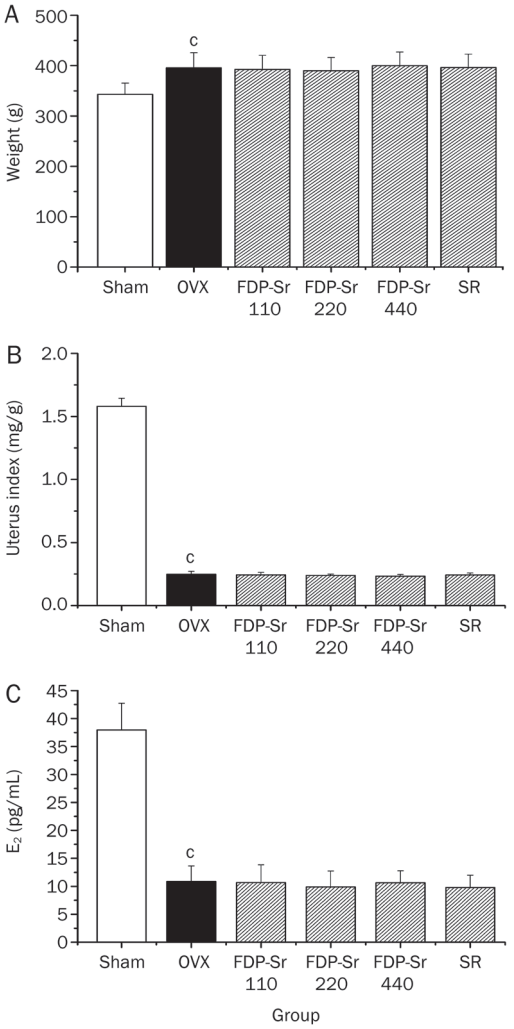

Figure 2. Effect of a 3-week treatment with FDP-Sr or SR on E2, and body and uterus weights of OVX rats. (A) The body weights of the rats were recorded at the end of the experimental period. (B) The uterus index is represented as the uterus weight divided by the body weight. (C) E2 was recorded after 3 weeks of treatment. Values with a superscript are significantly different from those of the sham-operated group ($^bP<0.05$, $^cP<0.01$) or OVX group ($^eP<0.05$, $^fP<0.01$).

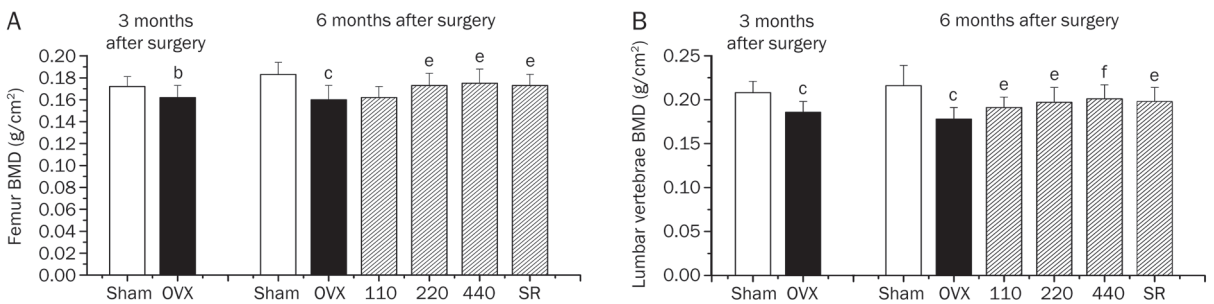

Figure 3. Bone mineral density of the femur and the lumbar vertebrae. (A) Femur. (B) Lumbar vertebrae (L1–L5). Each column and bar represents mean±SD. $n=10$. Values with a superscript are significantly different from those of the sham-operated group ($^bP<0.05$, $^cP<0.01$) or OVX group ($^eP<0.05$, $^fP<0.01$).

comparison with the OVX control group (P<0.05, P<0.05, and P<0.01, respectively). There were no differences in BMD between the FDP-Sr and SR treatment groups.

Mechanical tests of femur and lumbar vertebrae

After three months of estrogen deficiency, maximum load, stiffness and energy were significantly decreased (P<0.05 for all) in the OVX control group compared with the sham-operated group as demonstrated in the femoral three-point bending test (Table 1). Compression testing of the third lumbar vertebra demonstrated that the bone strength of rats in the OVX control group was reduced. Significant decreases were observed in the maximum load (P<0.01), stiffness (P<0.05) and energy to failure (P<0.05) when compared with the sham-operated group.

At the end of the treatment period, the maximum load (P<0.05), stiffness (P<0.05) and energy (P<0.01) of the femoral three-point bending test were significantly decreased in the OVX control group compared with the sham-operated group. This decrease was dose-dependently attenuated by FDP-Sr treatment. Treatment with 220 mg/kg or 440 mg/kg FDP-Sr improves femoral three-point bending test parameters by increasing the maximum load (P<0.05 for both), stiffness (P<0.05 and P<0.01, respectively) and energy to failure (P<0.05 for both) compared with those in the OVX control group. Compression testing of the third lumbar vertebrae showed that the maximum load, stiffness and energy to failure also notably decreased (P<0.01 for all) in the OVX control group compared with the sham-operated group six months after surgery. Treatment with 220 or 440 mg/kg FDP-Sr increased the value of maximum load (P<0.05 and P<0.01, respectively), stiffness (P<0.05 and P<0.01, respectively) and energy to failure (P<0.05 for both) compared with the OVX control group.

Histomorphometry study

As shown in Figure 4 and Table 2, the ovariectomy procedure induced significant reductions in trabecular area percentage (Tb.Ar, Table 2) and trabecular thickness (Tb.Th μm, Table 2) compared to the sham-operated group. These reductions were accompanied by significant increases in trabecular separation (Tb.Sp, Table 2) (P<0.001 for all).

After three months of FDP-Sr treatment, positive effects on the trabecular microarchitecture of lumbar vertebra were observed. Compared to the OVX control group, 220 or 440 $mg{\cdot}kg^{-1}{\cdot}d^{-1}$ FDP-Sr can prevent the further loss of Tb.Ar (P<0.05 for 440 mg/kg) and Tb.Th (P<0.05 for both). The increased Tb.Sp in the lumbar vertebrae was significantly inhibited at the end of the 220 (P<0.05) and 440 $mg{\cdot}kg^{-1}{\cdot}d^{-1}$

Table 1. Effect of FDP-Sr on bone mechanical strength of lumbar vertebrae (L3) and femur. Mean±SD. n=10. Values with a superscript are significantly different from those in the sham (^{b}P<0.05, ^{c}P<0.01) or OVX group (^{e}P<0.05, ^{f}P<0.01).

	3 months after surgery		6 months after surgery					
	Sham	OVX	Sham	OVX	FDP-Sr 110	FDP-Sr 220	FDP-Sr 440	SR
Three point bending femur								
Maximum load (N)	119.2±13.2	101.5±14.3^{b}	137.2±22.4	107.0±18.3^{b}	122.4±14.7	127.9±21.4^{e}	127.9±14.2^{e}	126.6±12.5^{e}
Stiffness (N/mm)	195.2±19.8	175.8±13.4^{b}	221.0±32.2	183.2±26.4^{b}	200.1±37.0	213.2±30.8^{e}	219.1±24.3^{f}	216.8±28.4^{e}
Energy (N×mm)	28.7±4.6	23.0±4.6^{b}	29.4±4.1	23.8±4.1^{c}	24.8±4.2	28.2±4.9^{e}	27.8±3.9^{e}	28.0±3.2^{e}
Compression lumbar vertebrae (L3)								
Maximum load (N)	196.2±18.9	171.1±14.8^{c}	202.8±22.6	152.9±25.4^{c}	168.1±26.3	184.8±25.3^{e}	192.5±16.2^{f}	184.9±20.9^{e}
Stiffness (N/mm)	761.1±79.1	665.0±88.5^{b}	814.1±83.1	641.3±90.7^{c}	717.1±90.6	754.4±91.4^{e}	764.6±83.6^{f}	756.6±97.6^{e}
Energy (N×mm)	31.6±4.9	25.6±4.4^{b}	33.4±5.0	22.7±5.8^{c}	25.8±6.9	29.3±6.7^{e}	29.2±5.1^{e}	29.0±5.1^{e}

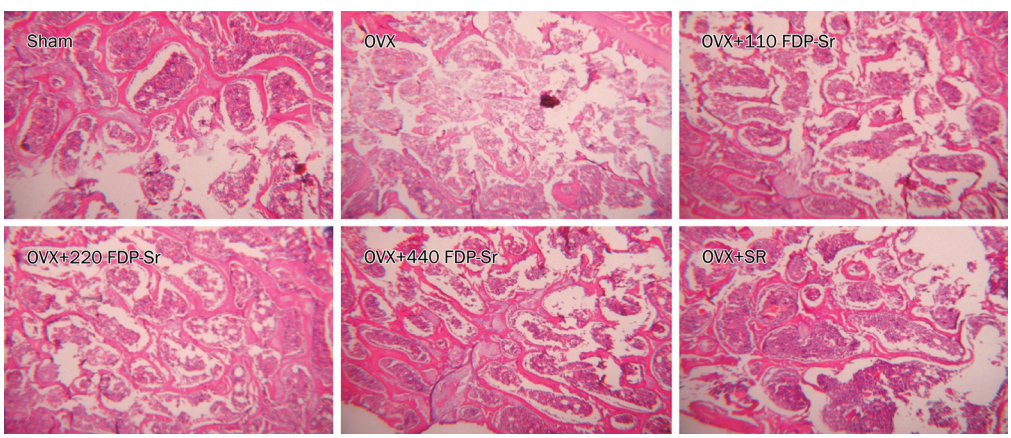

Figure 4. Histological sections [stained with H&E (40×)] of bone trabeculae from the 4th lumbar vertebra in rats from different groups. The ovariectomy caused a loss of trabeculae in the lumbar vertebra of the OVX group, but SR and 220 or 440 $mg{\cdot}kg^{-1}{\cdot}d^{-1}$ FDP-Sr significantly protected bone from ovariectomy-induced osteopenia.

Table 2. Histomorphometric analysis of lumbar vertebrae (L4) in groups. Mean±SD. n=10. Values with a superscript are significantly different from those in the sham (^bP<0.05, ^cP<0.01) or OVX group (^eP<0.05, ^fP<0.01).

			FDP-Sr			
	Sham	OVX	OVX+110	OVX+220	OVX+440	OVX+SR
Tb.Th (μm)	76.12±7.59	58.24±5.66^c	60.58±5.44	63.79±5.81^e	64.49±5.54^e	63.61±3.89^e
Tb.Ar (%)	53.37±2.91	44.52±3.87^c	45.46±3.96	46.64±3.73	48.33±4.14^e	48.18±2.91^e
Tb.Sp (mm)	60.68±3.93	80.59±10.66^c	75.72±10.55	71.46±6.95^e	66.61±5.63^f	68.87±6.27^e

(P<0.01) FDP-Sr treatment.

Biochemical parameters

Serum calcium (Ca) levels were significantly decreased in the OVX rats compared with the sham-operated rats (P<0.01). Administration of 220 mg·kg^{-1}·d^{-1} FDP-Sr significantly enhanced the serum Ca levels in OVX rats (P<0.05), whereas the values of serum P (phosphorus) did not show significant differences among the groups.

Serum B-ALP, NTx, and TRACP 5b were significantly increased in the OVX control group compared with the sham-operated group six months after bilateral ovariectomy (P<0.01, P<0.01, and P<0.05, respectively), suggesting that bone turnover was elevated because of estrogen deficiency; this has been previously reported[5]. After three months of treatment, FDP-Sr was able to maintain an increase in serum B-ALP level in a dose-dependent manner (5.7%, 12.6%, and 15.4%, and all three doses resulted in a significant difference compared to those in the OVX control group (P<0.05, P<0.01, and P<0.01, respectively). However, treatment with FDP-Sr can markedly suppress the ovariectomy-induced increase in serum NTx (P<0.05 for 110 and 220 mg·kg^{-1}·d^{-1}, P<0.01 for 440 mg·kg^{-1}·d^{-1}) and TRACP 5b (P<0.05 for 220 mg·kg^{-1}·d^{-1}, P<0.01 for 440 mg·kg^{-1}·d^{-1}) (Table 3).

Oxidative stress assays

Estrogen deficiency induced abnormal changes in free radical parameters, significantly increased levels of H_2O_2 and MDA in serum and bone tissue, respectively (P<0.05 for all), and biomarkers of anti-oxidant such as CAT in serum (P<0.01) and bone tissue (P<0.05) were significantly decreased compared to those in the sham-operated group six months after the surgery. Treatment with FDP-Sr decreased both H_2O_2 and MDA levels in serum and bone tissue in a dose-dependent manner. Additionally, FDP-Sr inhibited the decrease of CAT in serum and bone tissue after three months of treatment, but this anti-oxidant effect was not observed in the strontium ranelate group, which suggests that this effect is due to FDP (Table 4).

Serum OPG, RANKL, and IGF-I

Serum OPG was 38.5% lower (P<0.01) in the OVX animals (506.75±75.826 pg/mL) compared to the sham-operated animals (724.0±42.55 pg/mL). In contrast, estrogen deficiency inncrease serum RANKL (P<0.01), and the ratio of OPG to RANKL (P<0.01) was significantly decreased compared with the sham-operated group. Meanwhile, OVX significantly induced a decrease in serum IGF-I (P<0.05) 6 months after surgery compared to the sham-operated group. Treatment with FDP-Sr reversed the above findings. Treatment with FDP-Sr 220 or 440 mg·kg^{-1}·d^{-1} resulted in a significant OPG increase (P<0.01, 812.75±138.87 pg/mL for 220 mg·kg^{-1}·d^{-1}, P<0.01, 969.05±61.57 pg/mL for 440 mg/kg) and RANKL decrease (P<0.01 49.27±6.85 pg/mL for 220 mg/kg, P<0.01, 43.44±6.51 pg/mL for 440 mg/kg) 3 months after treatment. Thus, the ratio of OPG to RANKL was significantly increased in both the 220 and 440 FDP-Sr mg·kg^{-1}·d^{-1} treatment groups compared to the OVX animals. Additionally, the medium (4.29±0.46 ng/mL) and high (4.18±0.47 ng/mL) doses of FDP-Sr significantly increased serum IGF-I after 3 months compared to the OVX control group (3.34±0.34 ng/mL). Significant differences in OPG and RANKL were also

Table 3. Effects of FDP-Sr or SR on bone biochemical parameters in serum of ovariectomized rats. Mean±SD. n=10. Values with a superscript are significantly different from those in the sham (^bP<0.05, ^cP<0.01) or OVX group (^eP<0.05, ^fP<0.01).

			FDP-Sr			
	Sham	OVX	OVX+110	OVX+220	OVX+440	OVX+SR
S-Ca (mmol/L)	2.26±0.16	2.09±0.13^b	2.06±0.11	2.16±0.12	2.07±0.16	2.08±0.12
S-P (mmol/L)	1.67±0.14	1.69±0.18	1.72±0.21	1.71±0.17	1.79±0.20	1.75±0.13
B-ALP (μg/L)	0.994±0.073	1.33±0.034^c	1.406±0.062^e	1.498±0.045^f	1.535±0.078^f	1.423±0.045^e
NTx (nmol/L)	2.179±0.123	3.036±0.347^c	2.600±0.174^e	2.426±0.235^e	2.261±0.071^f	2.395±0.265^e
TRACP-5b (U/L)	1.877±0.169	2.056±0.184^b	1.982±0.138	1.891±0.089^e	1.835±0.145^f	1.874±0.105^e

Table 4. Effect of FDP-Sr on marker of oxidative stress in serum and tibia metaphysis. Mean±SD. *n*=10. Values with a superscript are significantly different from those in the Sham ($^{b}P<0.05$, $^{c}P<0.01$) or OVX group ($^{e}P<0.05$, $^{f}P<0.01$).

			FDP-Sr			
	Sham	OVX	OVX+110	OVX+220	OVX+440	OVX+SR
Serum						
H_2O_2 (mmol/L)	18.62±2.22	21.59±3.13^{b}	19.20±3.11	18.98±3.29	18.72±2.67^{e}	21.26±1.99
CAT (U/mL)	0.637±0.122	0.444±0.102^{c}	0.485±0.102	0.563±0.127^{e}	0.605±0.100^{f}	0.422±0.101
SOD (U/mL)	141.4±4.89	139.9±5.29	140.5±6.10	140.5±5.68	140.3±5.25	137.9±4.53
MDA (nmol/mL)	8.18±0.807	9.13±0.958^{b}	8.33±1.103	8.57±1.258	8.21±0.770^{e}	8.63±0.900
Metaphysis						
H_2O_2 (mmol/g prot)	4.83±1.93	6.50±1.33^{b}	5.49±0.99	5.13±0.88^{e}	4.82±1.39^{e}	5.99±1.05
CAT (U/mg prot)	1.55±0.28	1.18±0.34^{b}	1.09±0.47	1.41±0.55	1.59±0.49^{e}	1.37±0.50
SOD (U/mg prot)	42.61±12.77	36.55±11.45	36.71±6.38	39.16±14.42	40.25±12.90	35.21±7.28
MDA (nmol/mg prot)	2.14±0.81	3.08±0.74^{b}	2.66±0.37	2.52±0.48	2.34±0.48^{e}	3.04±0.45

observed in the middle- and high-dose FDP-Sr treatment groups compared to the SR group (Figure 5).

Real-time PCR analyses of bone OPG and RANKL

To investigate the role of FDP-Sr in the OPG/RANKL/RANK pathway and to identify the mechanism regulating bone formation and resorption, we performed real-time RT-PCR on bone tissues to examine OPG and RANKL expression. Our results demonstrated that the metaphyseal portion of the tibia bone from the OVX rats produced more RANKL and less OPG than the sham-operated rats and that the OPG/RANKL ratio was lower in OVX rats than in sham-operated rats. All three doses of FDP-Sr significantly increased OPG expression, reduced RANKL and elevated the OPG/RANKL ratio in OVX rats. Additionally, significant increases in OPG expression and reduced RANKL expression were found in middle and high FDP-Sr doses compared to the SR group (Figure 6).

Discussion

Osteoporosis associated with ovarian hormone deficiency following menopause can be caused by inadequate peak bone mass, excessive bone resorption and inadequate bone formation[23, 24]. The ovariectomized rat model is a classic model for conducting osteoporosis studies[25, 26]. In the current study, FDP-Sr counteracted the bone loss induced by ovariectomy, preserved bone microarchitecture and maintained bone strength in OVX rats. Estrogen deficiency leading to endocrine dysfunction significantly increased body weight, although feed consumption was similar among all groups. A recent study by Rogers *et al* indicated that adiposity induced by ovariectomy is associated with decreased energy expenditure, adipose tissue (AT) expansion, and hepatic steatosis[27]. No dose of FDP-Sr prevented the body weight gain induced by estrogen deficiency. Estrogen deficiency was confirmed by atrophy of the uterine tissue, another key marker of estrogen deficiency, on six months after bilateral ovariectomy surgery. FDP-Sr was unable to slow ovariectomy-induced atrophy of the uterine tissue. These results indicate that FDP-Sr differed from estrogen replacement therapy in the regulation of body weight and uterine growth in the OVX rats.

Osteoporosis is a metabolic disorder in which a loss of bone mass and strength leads to fragility fractures[28]. In this study, BMD and biomechanical properties were chosen as indexes to evaluate the establishment of osteoporosis due to ovariectomy[29, 30]. As expected, OVX resulted in a significant BMD decrease in the femur and lumbar vertebra following three months of treatment after bilateral ovariectomy surgery. Estrogen is important for maintaining bone density, and when estrogen levels drop after menopause, bone loss accelerates[5]. Additionally, a significant reduction in biomechanical parameters was observed including the compression strength of the lumbar vertebra and the three-point bending test of the femur compared to values in the sham-operated group. Three months of FDP-Sr therapy dose-dependently increased the BMD of the lumbar vertebrae and femur. Elevated biomechanical properties of the femur and vertebrae further indicated that FDP-Sr was effective at restoring bone strength in OVX rats. Physiological analyses indicated that the turnover rate for cancellous bone is higher than that for cortical bone. Cancellous bone is the major component of vertebrae, and cortical bone is the chief component of the femur. Therefore, the lumbar vertebrae play a critical role in predicting osteoporosis and monitoring the response to pharmacotherapy. The findings in this study are in agreement with previous reports in OVX rats in demonstrating that decreases in BMD and biomechanical properties occur faster in the vertebrae than in the femur. The protective effect of FDP-Sr on bone is more easily observed in the lumbar spine, although this protective effect was observed in the femur after three months of treatment.

Histomorphometric analysis of the trabecular bone in lumbar vertebral bodies was performed at the end of the study. Deterioration of the trabecular architecture has been implicated in decreased bone strength and increased fracture incidence in humans. Thus, the assessment of trabecular architectural properties is necessary to evaluate the treatment impact on the quality of the lumbar vertebrae in addition to BMD

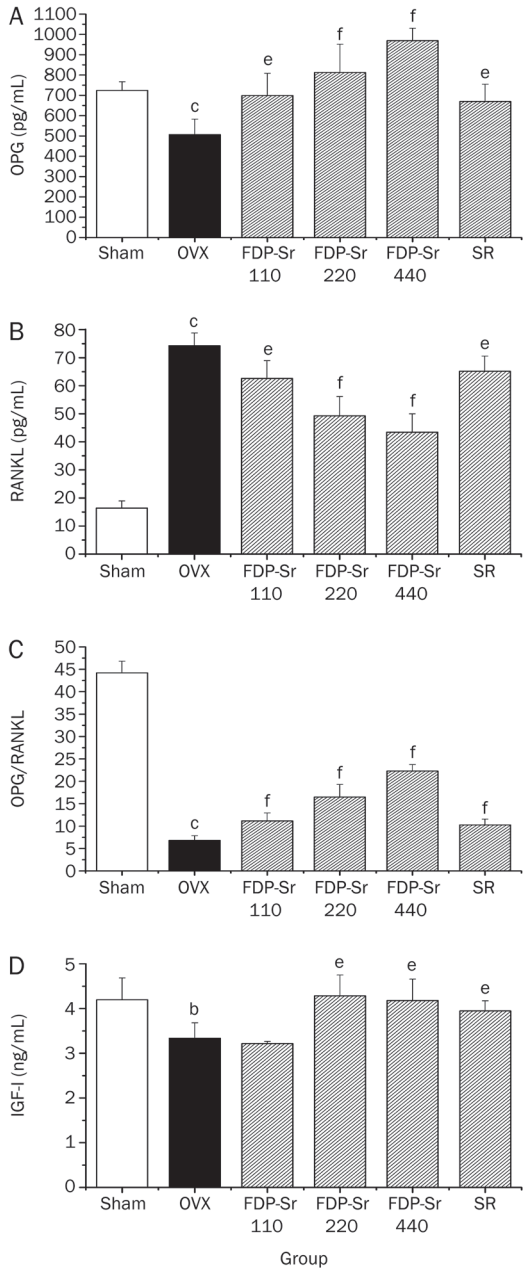

Figure 5. Effect of FDP-Sr on OPG (A), RANKL (B), OPG/RANKL (C) and IGF-I (D) in serum. Each column and bar represents the mean±SD. n=10. Values with a superscript are significantly different from those of the sham-operated group (^{b}P<0.05, ^{c}P<0.01) or OVX group (^{e}P<0.05, ^{f}P<0.01).

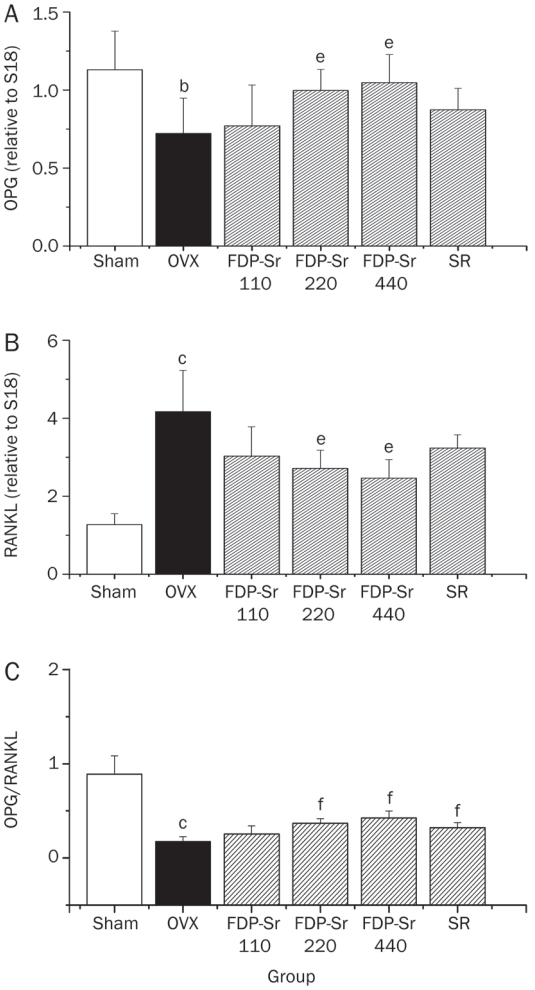

Figure 6. Effect of FDP-Sr on OPG (A), RANKL (B), and OPG mRNA/RANKL mRNA (C) expression in the metaphyseal portion of the tibia. Each column and bar represents the mean±SD. n=10. Values with a superscript are significantly different from those of the sham-operated group (^{b}P<0.05, ^{c}P<0.01) or OVX group (^{e}P<0.05, ^{f}P<0.01).

and biomechanical properties. In this study, Tb.Th and Tb.N decreased and Tb.Sp increased in the OVX control group compared to the sham-operated group. The results indicate that trabecular bone was readily lost as a result of estrogen deficiency, which is typical of cancellous bone loss and has been reported previously. However, this deterioration was ameliorated by FDP-Sr treatment. A gradual increase in Tb.Th and Tb.N and a decrease in Tb.Sp were observed after 3 months of treatment. These findings suggest that FDP-Sr can significantly improve these structural indices, repair lost trabecular connectivity, and prevent the progression of trabecular architecture deterioration. Moreover, these results indicate that FDP-Sr contributes to the restoration of deteriorated trabecular architecture and lumbar morphology.

The loss of bone mass and the deterioration of bone microstructure have been linked to an imbalance between bone formation and bone resorption. Biochemical markers of bone turnover have been widely used to measure the effects of various drugs on bone remodeling[31]. The dual effect of Sr in the treatment of osteoporosis was successfully duplicated *in vivo* in this study. B-ALP activity, an indicator of bone formation, was found throughout the body, and its activity in plasma increased sharply after the ovariectomy surgery. FDP-Sr treatment increased B-ALP by 5.7%, 12.6%, and 15.4% in OVX rats. TRACP 5b is one isoform of TRACP 5 and serum TRACP 5b is derived only from osteoclasts. Thus, TRACP 5b activity can be used as a marker to monitor osteoclastic activ-

ity and bone resorption rates[32]. As expected, the TRACP 5b activity in serum increased sharply after the ovariectomy surgery. FDP-Sr potently inhibited the increase in TRACP 5b levels in plasma and thereby favors bone metabolism. Meanwhile, serum NTx, which also represents a bone resorption biomarker derived from N-telopeptide of type I collagen, rapidly declined after oral administration of FDP-Sr. Overall, these results indicated a positive effect on bone formation and a negative effect on bone resorption and confirmed the dual effect of FDP-Sr *in vivo*.

Physiologically, the balance of bone formation and resorption plays a key role in bone metabolism in healthy individuals. When resorption increases after menopause, bone formation is not able to compensate, leading to the degradation of bone biomechanical properties. Ideally, to reverse this process, treatments should be able rebalance bone remodeling. Fortunately, strontium, a naturally occurring anti-osteoporosis drug, has a dual effect on bone remodeling unlike other drugs. However, the optimal usage of strontium treatment to rebalance bone remodeling and repair bone mass remains unclear. Strontium can directly interact with the calcium-sensing receptor (CaSR), a G protein-coupled receptor first cloned from the parathyroid gland[33–35], as recent work by Naibedya *et al* found that Sr^{2+} is a CaSR agonist, even though strontium's affinity for the receptor is lower than that of calcium[36]. Other studies have demonstrated that the PKC/PKD and p38 pathways could be involved as potential mediators of osteoblast cell replication[37]. In addition, IGF-I can play a role as a key cytokine in bone formation stimulated by strontium[38, 39]. Previous studies have indicated that strontium can inhibit osteoclast proliferation, differentiation and activity[40]; however, the mechanism remains controversial. Strontium was thought to cause osteoclast apoptosis either directly[41] or indirectly through CaSR[42]. Hofbauer *et al* suggest that although multiple hormones and cytokines regulate various aspects of osteoclast formation, the final effectors are in the OPG/RANK/RANKL system, which was regarded as a key factor in inhibiting bone proliferation and directly participates in the process of bone formation and bone resorption[43]. This hypothesis explains the process of bone formation coupled with bone resorption. Our research indicated that FDP-Sr up-regulates OPG and down-regulates RANKL secreted from osteoblasts, thereby inhibiting osteoclastogenesis and promoting bone formation.

Alternatively, oxidative stress is an indirect effect of estrogen deficiency and can be associated with one of several mechanisms related to bone loss[44]. A study by Sridhar *et al* confirmed that estrogen deficiency increases hydrogen peroxide and lipid peroxide in the femur bone and impairs bone antioxidant systems, thereby contributing to accelerated bone loss[45]. Therefore, concentrations of several markers of oxidative stress were determined in plasma and bone marrow six months after surgery. Increased H_2O_2 and MDA in the plasma and bone marrow were found in the rats with estrogen deficiency, and as previously reported, hydrogen peroxide served as the reactive oxygen species responsible for bone loss and the inhibition of osteoblast proliferation[46]. Both decreased H_2O_2 and MDA increased CAT in plasma and bone marrow were observed following FDP-Sr treatment, indicating that FDP-Sr may be a substantial contributor to counteract oxidative stress caused by estrogen deficiency in our study. According to previous reports[47, 48], FDP preserved antioxidant capacity, including CAT activity and GSH content, by indirect radical scavenging. Thus, FDP acting as an anti-oxidant may provide an additional benefit to reduce the risk of bone loss.

Osteoporosis is a chronic bone remodeling disease with increased risk of fracture, which can significantly affect quality of life and life expectancy, and patients suffering from it require long-term medication. Therefore, it is important to carefully evaluate the safety and tolerance of anti-osteoporotic agents. Toxic symptoms from appropriate doses of Sr have not been reported in humans. The only stable Sr-containing acid radical considered to be harmful to humans in small amounts is strontium chromate. In this compound, the toxicity is caused by the chromium, which is a genotoxic carcinogen[49]. Strontium ranelate was selected from among 20 different salts (*eg*, lactate, carbonate or gluconate salts) to treat osteoporosis in the clinical setting. Considerations were based on Sr bioavailability, the gastric tolerance, and the high ratio between Sr and different chemical acid radicals[50]. The biologic activity of ranelic acid as a carrier is unclear. The choice of eligible acid radicals plays a vital role in evaluating the therapeutic effectiveness and safety of a strontium compound. FDP, an endogenous intermediate molecule, has low toxicity[51] and can provide energy[52] and anti-oxidant capabilities[48]. FDP combined with strontium has potential as an anti-osteoporosis drug.

Conclusion

In summary, estrogen deficiency was observed in OVX-rats, similar to that found in postmenopausal women. Three months of FDP-Sr treatment resulted in significant protection against bone loss in both cortical and cancellous bone, as well as maintenance of bone microarchitecture and prevention of deterioration in mechanical parameters. These results suggest that FDP-Sr can prevent vertebral and hip fractures through its protective effects on both trabecular and cortical bone and thereby has potential as an alternative treatment for osteoporosis. In addition, the combination of Sr with fructose 1,6-diphosphate was well tolerated by the rats and did not adversely affect bone quality. Further research is needed to identify the mechanisms of action of FDP-Sr and to explore the potential synergistic functions of FDP in the treatment of osteoporosis.

Acknowledgements

The study was supported by a grant from the National Natural Science Foundation of China (Grant No 30873112) and the Six Talent Peek Project of Jiangsu Province (No 07-C-018).

Author contribution

Bo MA and Qi ZHANG have been involved in all phases

of this project; Qi ZHANG and Han-jie YING designed the research; Yong-lu WANG and Ying-ying HU performed the ELISA and real-time PCR; Yan-ping CHENG, Zhen-dong YANG and Ya-ya ZHENG performed the animal experiments for the project; Di WU wrote and revised the manuscript.

References

1 An overview of osteoporosis. Lancet 1982; 2: 423–4.
2 Yasothan U, Kar S. Osteoporosis: overview and pipeline. Nat Rev Drug Discov 2008; 7: 725–6.
3 Cooper C, Campion G, Melton LJ 3rd. Hip fractures in the elderly: a world-wide projection. Osteoporos Int 1992; 2: 285–9.
4 Boyle WJ, Simonet WS, Lacey DL. Osteoclast differentiation and activation. Nature 2003; 423: 337–42.
5 Petrovic O. Estrogen and postmenopausal osteoporosis. Ann Intern Med 1993; 118: 155–6.
6 Rizzoli R, Burlet N, Cahall D, Delmas PD, Eriksen EF, Felsenberg D, *et al*. Osteonecrosis of the jaw and bisphosphonate treatment for osteoporosis. Bone 2008; 42: 841–7.
7 Hong JW, Nam W, Cha IH, Chung SW, Choi HS, Kim KM, *et al*. Oral bisphosphonate-related osteonecrosis of the jaw: the first report in Asia. Osteoporos Int 2010; 21: 847–53.
8 Bush TL, Helzlsouer K. Estrogen replacement therapy and risk of breast cancer. JAMA 1991; 266: 1357–8.
9 Porch JV, Lee IM, Cook NR, Rexrode KM, Burin JE. Estrogen-progestin replacement therapy and breast cancer risk: the Women's Health Study (United States). Cancer Causes Control 2002; 13: 847–54.
10 Wassertheil-Smoller S, Hendrix SL, Limacher M, Heiss G, Kooperberg C, Baird A, *et al*. Effect of estrogen plus progestin on stroke in postmenopausal women: the Women's Health Initiative: a randomized trial. JAMA 2003; 289: 2673–84.
11 Hendrix SL, Wassertheil-Smoller S, Johnson KC, Howard BV, Kooperberg C, Rossouw JE, *et al*. Effects of conjugated equine estrogen on stroke in the Women's Health Initiative. Circulation 2006; 113: 2425–34.
12 Cabrera WE, Schrooten I, De Broe ME, D'Haese PC. Strontium and bone. J Bone Miner Res 1999; 14: 661–8.
13 Meunier PJ, Roux C, Seeman E, Ortolani S, Badurski JE, Spector TD, *et al*. The effects of strontium ranelate on the risk of vertebral fracture in women with postmenopausal osteoporosis. N Engl J Med 2004; 350: 459–68.
14 Reginster JY, Bruyere O, Sawicki A, Roces-Varela A, Fardellone P, Roberts A, *et al*. Long-term treatment of postmenopausal osteoporosis with strontium ranelate: results at 8 years. Bone 2009; 45: 1059–64.
15 Collette J, Bruyere O, Kaufman JM, Lorenc R, Felsenberg D, Spector TD, *et al*. Vertebral anti-fracture efficacy of strontium ranelate according to pre–treatment bone turnover. Osteoporos Int 2010; 21: 233–41.
16 Liu JM, Wai–Chee KA, Pheng CS, Zhu HM, Zhang ZL, Wu YY, *et al*. Efficacy and safety of 2 g/day of strontium ranelate in Asian women with postmenopausal osteoporosis. Bone 2009; 45: 460–5.
17 Lee HY, Lie D, Lim KS, Thirumoorthy T, Pang SM. Strontium ranelate-induced toxic epidermal necrolysis in a patient with post-menopausal osteoporosis. Osteoporos Int 2009; 20: 161–2.
18 Yin H, Jin XB, Gong Q, Yang H, Hu LY, Gong FL, *et al*. Fructose-1,6-diphosphate attenuates acute lung injury induced by lipopolysaccharide in mice. Int Immunopharmacol 2008; 8: 1842–7.
19 Marangos PJ, Fox AW, Riedel BJ, Royston D, Dziewanowska ZE. Potential therapeutic applications of fructose-1,6-diphosphate. Expert Opin Investig Drugs 1998; 7: 615–23.
20 Chien S, Zhang F, Niu W, Ehringer W, Chiang B, Shi X, *et al*. Fructose-1,6-diphosphate and a glucose-free solution enhances functional recovery in hypothermic heart preservation. J Heart Lung Transplant 2000; 19: 277–85.
21 Tenenbaum HC, Palangio K. Phosphoethanolamine- and fructose 1,6-diphosphate-induced calcium uptake in bone formed *in vitro*. Bone Miner 1987; 2: 201–10.
22 Ma B, Zhang Q, Wang G, Wu Z, Shaw JP, Hu Y, *et al*. Synthesis and pharmacokinetics of strontium fructose 1,6-diphosphate (Sr-FDP) as a potential anti-osteoporosis agent in intact and ovariectomized rats. J Inorg Biochem 2011; 1054: 563–8.
23 Kamel HK. Postmenopausal osteoporosis: etiology, current diagnostic strategies, and nonprescription interventions. J Manag Care Pharm 2006; 12: S4–9; quiz S26–8.
24 Raisz LG. Pathogenesis of osteoporosis: concepts, conflicts, and prospects. J Clin Invest 2005; 115: 3318–25.
25 Yamazaki I, Yamaguchi H. Characteristics of an ovariectomized osteopenic rat model. J Bone Miner Res 1989; 4: 13–22.
26 Omi N, Ezawa I. The effect of ovariectomy on bone metabolism in rats. Bone 1995; 17: 163S–168S.
27 Rogers NH, Perfield JW 2nd, Strissel KJ, Obin MS, Greenberg AS. Reduced energy expenditure and increased inflammation are early events in the development of ovariectomy-induced obesity. Endocrinology 2009; 150: 2161–8.
28 Jakubowitz E, Seeger JB, Kretzer JP, Heisel C, Kleinhans JA, Thomsen M. The influence of age, bone quality and body mass index on periprosthetic femoral fractures: a biomechanical laboratory study. Med Sci Monit 2009; 15: BR307–12.
29 Vasikaran SD. Utility of biochemical markers of bone turnover and bone mineral density in management of osteoporosis. Crit Rev Clin Lab Sci 2008; 45: 221–58.
30 Turner CH. Biomechanics of bone: determinants of skeletal fragility and bone quality. Osteoporos Int 2002; 13: 97–104.
31 Bhattacharyya S, Siegel ER, Achenbach SJ, Khosla S, Suva LJ. Serum biomarker profile associated with high bone turnover and BMD in postmenopausal women. J Bone Miner Res 2008; 23: 1106–17.
32 Nenonen A, Cheng S, Ivaska KK, Alatalo SL, Lehtimaki T, Schmidt–Gayk H, *et al*. Serum TRACP 5b is a useful marker for monitoring alendronate treatment: comparison with other markers of bone turnover. J Bone Miner Res 2005; 20: 1804–12.
33 Coulombe J, Faure H, Robin B, Ruat M. *In vitro* effects of strontium ranelate on the extracellular calcium-sensing receptor. Biochem Biophys Res Commun 2004; 323: 1184–90.
34 Pi M, Quarles LD. A novel cation-sensing mechanism in osteoblasts is a molecular target for strontium. J Bone Miner Res 2004; 19: 862–9.
35 Pi M, Faber P, Ekema G, Jackson PD, Ting A, Wang N, *et al*. Identification of a novel extracellular cation-sensing G-protein-coupled receptor. J Biol Chem 2005; 280: 40201–9.
36 Chattopadhyay N, Quinn SJ, Kifor O, Ye C, Brown EM. The calcium-sensing receptor (CaR) is involved in strontium ranelate-induced osteoblast proliferation. Biochem Pharmacol 2007; 74: 438–47.
37 Caverzasio J. Strontium ranelate promotes osteoblastic cell replication through at least two different mechanisms. Bone 2008; 42: 1131–6.
38 Henrotin Y, Labasse A, Zheng SX, Galais P, Tsouderos Y, Crielaard JM, *et al*. Strontium ranelate increases cartilage matrix formation. J Bone Miner Res 2001; 16: 299–308.
39 Gulhan I, Bilgili S, Gunaydin R, Gulhan S, Posaci C. The effect of strontium ranelate on serum insulin like growth factor-1 and leptin levels in osteoporotic post-menopausal women: a prospective study.

Arch Gynecol Obstet 2008; 278: 437–41.
40 Takahashi N, Sasaki T, Tsouderos Y, Suda T. S 12911-2 inhibits osteoclastic bone resorption *in vitro*. J Bone Miner Res 2003; 18: 1082–7.
41 Bonnelye E, Chabadel A, Saltel F, Jurdic P. Dual effect of strontium ranelate: stimulation of osteoblast differentiation and inhibition of osteoclast formation and resorption *in vitro*. Bone 2008; 42: 129–38.
42 Hurtel-Lemaire AS, Mentaverri R, Caudrillier A, Cournarie F, Wattel A, Kamel S, *et al*. The calcium-sensing receptor is involved in strontium ranelate-induced osteoclast apoptosis. New insights into the associated signaling pathways. J Biol Chem 2009; 284: 575–84.
43 Hofbauer LC, Schoppet M. Clinical implications of the osteoprotegerin/RANKL/RANK system for bone and vascular diseases. JAMA 2004; 292: 490–5.
44 Wauquier F, Leotoing L, Coxam V, Guicheux J, Wittrant Y. Oxidative stress in bone remodelling and disease. Trends Mol Med 2009; 15: 468–77.
45 Muthusami S, Ramachandran I, Muthusamy B, Vasudevan G, Prabhu V, Subramaniam V, *et al*. Ovariectomy induces oxidative stress and impairs bone antioxidant system in adult rats. Clin Chim Acta 2005; 360: 81–6.
46 Lean JM, Jagger CJ, Kirstein B, Fuller K, Chambers TJ. Hydrogen peroxide is essential for estrogen-deficiency bone loss and osteoclast formation. Endocrinology 2005; 146: 728–35.
47 Tang XY, Zhang Q, Dai DZ, Ying HJ, Wang QJ, Dai Y. Effects of strontium fructose 1,6-diphosphate on expression of apoptosis–related genes and oxidative stress in testes of diabetic rats. Int J Urol 2008; 15: 251–6.
48 Ahn SM, Hwang JS, Lee SH. Fructose 1,6-diphosphate alleviates UV-induced oxidative skin damage in hairless mice. Biol Pharm Bull 2007; 30: 692–7.
49 Pors NS. The biological role of strontium. Bone 2004; 353: 583–8.
50 Reginster JY. Strontium ranelate in osteoporosis. Curr Pharm Des 2002; 8: 1907–16.
51 Wang M, Yao J, Chen JY, Bai WX, Mei SY, Pan WN, *et al*. A subchronic intravenous toxicity study of magnesium fructose-1,6-diphosphate in beagle dogs. Basic Clin Pharmacol Toxicol 2009; 104: 93–100.
52 Hua D, Zhuang X, Ye J, Wilson D, Chiang B, Chien S. Using fructose-1,6-diphosphate during hypothermic rabbit-heart preservation: a high-energy phosphate study. J Heart Lung Transplant 2003; 22: 574–82.

Acta Pharmacologica Sinica (2012) 33: 490–495
 1671-4083/12 $32.00
www.nature.com/aps

Original Article

Comparison of the effects of cholecalciferol and calcitriol on calcium metabolism and bone turnover in Chinese postmenopausal women with vitamin D insufficiency

Hao ZHANG, Qi-ren HUANG*, Jie-mei GU, Wei-wei HU, Yu-juan LIU, Yun-qiu HU, Zhen-lin ZHANG

Metabolic Bone Disease and Genetic Research Unit, Department of Osteoporosis and Bone Diseases; Shanghai Jiao Tong University, Affiliated Sixth People's Hospital; Shanghai 200233, China

Aim: To compare the effects of cholecalciferol (800 IU/d) and calcitriol (0.25 μg/d) on calcium metabolism and bone turnover in Chinese postmenopausal women with vitamin D insufficiency.
Methods: One hundred Chinese postmenopausal women aged 63.8±7.0 years and with serum 25-hydroxyvitamin D [25(OH)D] concentration <30 ng/mL were recruited. The subjects were divided into 2 groups based on the age and serum 25(OH)D concentration: 50 subjects (group A) received cholecalciferol (800 IU/d), and 50 subjects (group B) received calcitriol (0.25 μg/d) for 3 months. In addition, all the subjects received Caltrate D (calcium plus 125 IU cholecalciferol) daily in the form of one pill. The markers of calcium metabolism and bone turnover, including the serum levels of calcium, phosphorus, alkaline phosphatase, intact parathyroid hormone, 25(OH)D and β-CrossLaps of type I collagen containing cross-linked C-telopeptide (β-CTX), were measured before and after the intervention.
Results: After the 3-month intervention, the serum 25(OH)D concentration in group A was significantly increased from 16.01±5.0 to 20.02±4.5 ng/mL, while that in group B had no significant change. The serum calcium levels in both the groups were significantly increased (group A: from 2.36±0.1 to 2.45±0.1 mmol/L; group B: from 2.36±0.1 to 2.44±0.1 mmol/L). The levels of serum intact parathyroid hormone in both the groups were significantly decreased (group A: from 48.56±12.8 to 39.59±12.6 pg/mL; group B: from 53.67±20.0 to 40.32±15.4 pg/mL). The serum levels of β-CTX in both the groups were also significantly decreased (group A: from 373.93±135.3 to 325.04±149.0 ng/L; group B: from 431.00±137.1 to 371.74±185.0 ng/L).
Conclusion: We concluded that both cholecalciferol (800 IU/d) and calcitriol (0.25 μg/d) plus Caltrate D modifies the serum calcium and bone turnover markers in Chinese postmenopausal women with vitamin D insufficiency. In addition, cholecalciferol (800 IU/d) plus Caltrate D significantly increased the serum 25(OH)D concentration.

Keywords: cholecalciferol; calcitriol; calcium metabolism; bone turnover; parathyroid hormone; 25-hydroxyvitamin D; β-CrossLaps of type I collagen containing cross-linked C-telopeptide (β-CTX); postmenopausal women

Acta Pharmacologica Sinica (2012) 33: 490–495; doi: 10.1038/aps.2011.172; published online 12 Mar 2012

Introduction

The vitamin D receptor is found in bone, most tissues and cells in the body. Vitamin D deficiency is a common health problem that increases the risk of many common and serious diseases, including some cancers, type 1 diabetes, cardiovascular disease, and osteoporosis[1]. Vitamin D is important for maintaining bone health because it stimulates the synthesis of osteopontin and alkaline phosphatase and inhibits osteoblast apoptosis[2]. Vitamin D status is best evaluated by measuring the serum concentration of 25-hydroxyvitamin D [25(OH)D][3]. Most specialties define vitamin D deficiency as 25(OH)D levels below 20 ng/mL[4]. A level of 25(OH)D of 21–29 ng/mL indicates a vitamin D insufficiency whereas a level of 30 ng/mL or greater indicates vitamin D sufficiency[5]. The prevalence of atrophic skin changes in older adults is concomitant with an increased probability of lower 25(OH)D levels[6]. Unlike those of other nutrients, dietary sources of vitamin D are limited. Therefore, most people require supplements such as cholecalciferol (vitamin D_3) to meet the recommended intake[7]. Current guidelines for vitamin D intakes vary around the world.

* To whom correspondence should be addressed.
E-mail qirenhuang@yahoo.com
Received 2011-10-10 Accepted 2011-11-15

The National Osteoporosis Foundation (NOF) recommends an intake of 800 to 1000 international units (IU) of vitamin D per day for adults 50 years and older[8]. Hanley *et al*[9] have suggested that adults over 50 years old are at a moderate risk for vitamin D deficiency and recommended the use of a supplement with at least 800–1000 IU of vitamin D_3. In an expert roundtable discussion, it was agreed that the daily vitamin D intake should be approximately 800 IU for most postmenopausal women[10]. One study indicated that serum 25(OH)D increased with cholecalciferol supplementation and nearly plateaued after 3–4 months of intervention[11]. In elderly people, diminished renal function due to aging leads to a decrease in renal conversion to $1,25(OH)_2D_3$[12]. Calcitriol [$1,25(OH)_2D_3$] plays an important role in promoting bone formation, and D-hormone analogs prevent falls to a greater extent than does ordinary vitamin D. Therefore, the use of D-hormone analogs has been advocated for the treatment of osteoporosis in many studies[13–15]. Because patients who are treated with 0.5 μg/d or 1.0 μg/d of calcitriol tend to develop hypercalcinuria, serum and urinary calcium levels should be examined regularly, and the calcitriol regime should be examined intermittently. Patients are frequently treated with 0.25 μg/d of calcitriol in China, especially elderly patients with osteoporosis. Hurst *et al*[16] concluded that correcting vitamin D deficiency in older women may suppress the age-induced acceleration in bone turnover and may reduce bone resorption. However, Seemans *et al*[17] observed that despite the stratification of different vitamin D receptor genotypes, cholecalciferol supplementation throughout the winter months did not affect bone turnover markers in young or old people. The aim of the current study was to compare the effects of cholecalciferol at 800 IU per day and calcitriol at 0.25 μg per day on calcium metabolism and bone turnover in Chinese postmenopausal women who are vitamin D insufficient.

Materials and methods

Subjects and study design

This was an open-label, controlled clinical trial. The study was approved by the Ethics Committee of the Shanghai Jiao Tong University Affiliated Sixth People's Hospital.

One hundred healthy, independent, ambulatory, postmenopausal female volunteers were recruited from community centers. All participants were of Han ethnicity and had lived in Shanghai for more than 30 years. Postmenopausal women over 50 years of age were eligible for the study, and the serum 25(OH)D concentrations of all subjects were less than 30 ng/mL. All subjects were given a physical examination and were found to be in good health. No participant was receiving treatment or had medical complications that were known to affect bone metabolism, including hyperthyroidism, diabetes mellitus, primary hyperparathyroidism, renal failure, pituitary diseases, and adrenal diseases. All the women had taken less than 600 mg/day of calcium and less than 600 IU/day of vitamin D within the 3 months prior to enrollment. The subjects were divided into two groups based on age and serum 25(OH)D concentrations. Fifty of the subjects received 800 IU/day of cholecalciferol (Cholecalciferol, Xingsha Pharmaceuticals Co, Xiamen, China), and the other fifty matched subjects received 0.25 μg/day of calcitriol (Calcitriol, Roche Pharmaceuticals Co, Shanghai, China), as group A and group B, respectively. All subjects received 1 pill/day of Caltrate D (containing 600 mg of calcium and 125 IU of vitamin D_3, Wyeth Pharmaceuticals, Health Care Products, Suzhou, China). Because the Caltrate D contained 125 IU of vitamin D_3, group A was provided 925 IU of cholecalciferol altogether. The study period was from December 2009 to March 2010, which was during the end of winter and the beginning of spring in China.

Laboratory tests

Fasting blood samples were obtained at baseline and at the end of the study. Blood routine, erythrosedimentation, liver function, renal function and fasting blood-glucose were examined to exclude subjects who had other factors that may affect their vitamin D status. Markers of calcium metabolism and bone turnover were assessed before and after the three-month intervention, including serum calcium (Ca), phosphorus (P), alkaline phosphatase (AKP) (using the HITACHI7600-020 automatic biochemistry analyzer), intact parathyroid hormone (normal, 15–65 pg/mL, intact PTH Kit, Roche Diagnostics, Mannheim, Switzerland), concentrations of 25(OH)D (25 hydroxy vitamin D3 Kit, Roche Diagnostics, Mannheim, Switzerland; using a Cobase 6000 electrochemiluminescence analyzer) and β-CrossLaps of type I collagen containing cross-linked C-telopeptide (β-CTX) (β-CrossLaps Kit, Roche Diagnostics, Mannheim, Switzerland). The coefficients of variability (CV) of serum Ca, P, AKP, PTH, 25(OH)D, and β-CTX were 2.4%, 3.3%, 5.1%, 9.5%, 4.0%, and 3.4%, respectively.

Statistical analysis

Data are represented as the mean±standard deviation (SD). Comparisons of the result before and after treatments were calculated using paired Student's *t*-test for the parametric data of each group. The independent sample *t*-tests were used to compare the serum parameters before and after the treatments of groups A and B, respectively. The independent sample *t*-test was used to compare the difference in the change pattern over time between group A and group B, starting at the treatment baseline. All calculations were performed using SPSS ver 11.0 software (SPSS Inc, Chicago, IL, USA). Data were considered statistically significant at a value of $P<0.05$.

Results

The baseline characteristics of 100 postmenopausal women are shown in Table 1. The mean age of the subjects was 63.8±7.0 years old, the mean menopausal period was 13.7±8.7 years, and the mean 25(OH)D level was 16.84±5.4 ng/mL.

Serum parameters of groups A and B

The baseline characteristics showed no differences between the two groups, except that β-CTX was significantly higher in group B than that in group A ($P<0.05$) (Table 2).

Table 1. Baseline characteristics of 100 postmenopausal women.

	Mean	SD	Range (upper limit, lower limit)
Age (year)	63.8	7.0	(51.3, 79.9)
Duration of menopause (year)	13.7	8.7	(1.0, 40.0)
Height (cm)	154.5	5.5	(139.0, 166.5)
Weight (kg)	58.1	9.5	(36.0, 80.0)
BMI (kg/cm^2)	24.3	3.5	(15.6, 33.3)
Ca (mmol/L)	2.36	0.1	(2.14, 2.58)
P (mmol/L)	1.19	0.1	(0.91, 1.47)
AKP (mmol/L)	66.78	19.3	(20.00, 113.00)
25(OH)D (ng/mL)	16.84	5.4	(5.34, 29.48)
PTH (pg/mL)	51.46	17.1	(20.41, 101.3)
β-CTX (ng/L)	403.54	137.8	(127.00, 837.00)

BMI: bone mass index.

Table 2. Baseline characteristics of group A and B.

	Group A	Group B	*P* value
n	45	47	
Age (year)	63.3±6.8	64.5±6.9	>0.05
Duration of menopause (year)	13.4±8.1	14.3±9.3	>0.05
Height (cm)	155.0±5.4	154.0±5.6	>0.05
Weight (kg)	58.2±9.4	57.3±9.8	>0.05
BMI (kg/cm^2)	24.2±3.6	24.1±3.4	>0.05
Ca (mmol/L)	2.36±0.1	2.36±0.1	>0.05
P (mmol/L)	1.19±0.1	1.20±0.2	>0.05
AKP (mmol/L)	67.78±19.4	66.55±20.6	>0.05
25(OH)D (ng/mL)	16.01±5.0	17.31±5.5	>0.05
PTH (pg/mL)	48.56±12.8	53.67±20.0	>0.05
β-CTX (ng/L)	373.93±135.3	431.00±137.1	**<0.05**

BM: bone mass index. Values shown in boldface are statistically significant.

After the 3-month intervention, the mean serum 25(OH)D increased from 16.01±5.0 ng/mL to 20.02±4.5 ng/mL in group A (P<0.01). However, the mean serum 25(OH)D showed no significant difference before and after the intervention performed on group B (P>0.05) (Table 3). In group A, serum 25(OH)D less than 20 ng/mL was detected in 76% of women (34/45), including 18% of women (8/45) with less than 10 ng/mL vitamin D, and 25(OH)D between 20 and 30 ng/mL was indicated in 24% of women (11/45) previous to the intervention. Serum 25(OH)D less than 20 ng/mL was indicated in 49% of group A (22/45), including 2% of women (1/45) with less than 10 ng/mL vitamin D, and 25(OH)D between 20 and 30 ng/mL was indicated in 51% of group A (23/45) after the intervention. In group B, serum 25(OH)D less than 20 ng/mL was indicated in 66% of women (31/47), including 13% of women (6/47) with less than 10 ng/mL vitamin D, and 25(OH)D between 20 and 30 ng/mL was indicated in 34% of women (16/47) before the intervention. Serum 25(OH)D less than 20 ng/mL was indicated in 85% of group B (40/47), including 6% of group B (3/47) with less than 10 ng/mL vitamin D, and vitamin D 25(OH)D between 20 and 30 ng/mL was indicated in 15% of group B (7/47) after the intervention.

After the three-month intervention, both groups showed a significant increase in serum Ca levels (all P<0.01) that were within the normal range. The AKP levels of groups A and B also showed a significant increase (P<0.05 and P<0.01, respectively). The serum PTH and β-CTX levels showed a significant decrease in both groups (all P<0.01 and all P<0.05) (Table 3).

We compared the serum parameters between the two groups after the 3-month intervention and identified significantly higher levels of serum 25(OH)D in group A than those of group B (P<0.01) (Table 4). We compared the difference in

Table 4. Compared serum parameters of the two groups after the treatment.

	After intervention of group A (*n*=45)	After intervention of group B (*n*=47)	*P* value
Ca (mmol/L)	2.45±0.1	2.44±0.1	>0.05
P (mmol/L)	1.22±0.1	1.24±0.1	>0.05
AKP (mmol/L)	73.27±16.8	74.02±17.3	>0.05
25(OH)D (ng/mL)	20.02±4.5	16.22±3.8	**<0.01**
PTH (pg/mL)	39.59±12.6	40.32±15.4	>0.05
β-CTX (ng/L)	325.04±149.0	371.74±185.0	>0.05

Values shown in boldface are statistically significant.

Table 3. Changes in the serum parameters of the two groups before and after treatment.

	Baseline of group A (*n*=45)	After intervention of group A (*n*=45)	*P* value	Baseline of group B (*n*=47)	After intervention of group B (*n*=47)	*P* value
Ca (mmol/L)	2.36±0.1	2.45±0.1	**<0.01**	2.36±0.1	2.44±0.1	**<0.01**
P (mmol/L)	1.19±0.1	1.22±0.1	>0.05	1.20±0.2	1.24±0.1	>0.05
AKP (mmol/L)	67.78±19.4	73.27±16.8	**<0.05**	66.55±20.6	74.02±17.3	**<0.01**
25(OH)D (ng/mL)	16.01±5.0	20.02±4.5	**<0.01**	17.31±5.5	16.22±3.8	>0.05
PTH (pg/mL)	48.56±12.8	39.59±12.6	**<0.01**	53.67±20.0	40.32±15.4	**<0.01**
β-CTX (ng/L)	373.93±135.3	325.04±149.0	**<0.05**	431.00±137.1	371.74±185.0	**<0.05**

Values shown in boldface are statistically significant.

the change pattern between the two groups over time starting at treatment baseline and found that only serum 25(OH)D showed a significant difference between group A and group B (Table 5).

Table 5. Comparison of the changes before and after treatment between group A and group B.

	Changed pattern after intervention of group A (*n*=45)	Changed pattern after intervention of group B (*n*=47)	*P* value
Ca (mmol/L)	0.09±0.1	0.08±0.1	>0.05
P (mmol/L)	0.02±0.1	0.04±0.2	>0.05
AKP (mmol/L)	5.49±15.1	7.47±15.0	>0.05
25(OH)D (ng/mL)	4.00±6.0	-1.09±5.1	**<0.01**
PTH (pg/mL)	-13.35±13.6	-8.97±10.3	>0.05
β-CTX (ng/L)	-48.89±129.5	-59.26±150.3	>0.05

Values shown in boldface are statistically significant.

Withdrawal from the study and adverse events

Eight participants (5 participants in the group A and 3 participants in the group B) discontinued the study. In the group A, two participants withdrew without providing a reason, two participants were lost during follow-up, and one participant withdrew because of cholelithiasis and shingles that, according to the clinical judgment, were attributed to a severe adverse event but were not related to the use of study medication. In the group B, three participants withdrew without providing a reason. After the 3-month treatment, the concentration of serum Ca, P, and the total AKP activities in the two groups remained within normal ranges.

Discussion

Many studies have shown that 40% to 100% of elderly people in the US and Europe suffer from vitamin D deficiencies[18, 19]. More than 50% of postmenopausal women had levels of 25-hydroxyvitamin D that were lower than 30 ng per milliliter[19]. Low levels of 25(OH)D are associated with a significant decrease in the absorption of intestinal calcium and induced secondary hyperparathyroidism[18, 20]. Secondary hyperparathyroidism may stimulate the transformation of preosteoclasts into mature osteoclasts, causing osteoporosis and increasing the risk of fracture[19]. Our results show that serum Ca levels increased and serum PTH levels decreased significantly after supplementation with cholecalciferol (800 IU/d) plus Caltrate D for three months. Kuwabara *et al*[21] discovered that the supplementation of 200 mg of calcium with 800 IU of vitamin D_3 daily for one month significantly lowered the serum PTH levels compared with the supplementation of only 200 mg of calcium daily. Seemans *et al*[17] identified that in the winter, the endpoint serum PTH level to be significantly lower in 3 cholecalciferol-supplemented groups (cholecalciferol 200 IU, 400 IU, and 600 IU) compared with the placebo group, though other bone turnover markers were not affected. An increased rate of bone turnover is associated with low bone mass[22] and an increased risk of bone fracture[23]. Higher levels of serum CTX indicate an increase in bone resorption and bone fragility[24]. Total AKP is primarily a nonspecific marker of bone formation. Our results show that after supplementing with 800 IU per day of cholecalciferol for three months, serum AKP levels increased significantly, and serum β-CTX levels decreased. These results indicate that 800 IU per day of cholecalciferol is effective for stimulating bone formation and reducing bone resorption. Hurst *et al*[16] has shown that vitamin D-deficient women who were administered 4000 IU of cholecalciferol daily for 6 months displayed a suppression of age-induced bone turnover and bone resorption. However, some studies have shown cholecalciferol supplementation have no effect on bone turnover markers[17, 21].

Oral vitamin D supplementation increases bone mineral density and appears to reduce the risk of hip and other nonvertebral fractures. Therefore, it is reasonable to supply 800–1000 IU/d of vitamin D to older individuals[25]. Heaney *et al*[11] found that after supplementing with 1000, 5000, and 10 000 IU of cholecalciferol, the serum 25(OH)D levels of every group plateaued after 3–4 months intervention. Therefore, Hanley *et al*[9] suggested measuring the serum 25(OH)D after 3–4 months of adequate intervention. In our study, the mean concentration of serum 25(OH)D increased from 16.01 to 20.02 ng/mL after 3 months of supplementation with cholecalciferol. However, 49% of this group was still vitamin D-deficient. The cholecalciferol group in our study was provided with 125 IU of Caltrate D. Therefore, the total cholecalciferol reached 925 IU, and the dose was not sufficient to achieve adequate 25(OH)D concentrations. Similarly, Pignotti *et al*[26] have shown that after supplementation with 400 IU of cholecalciferol and 1200 mg of calcium for 3 months in sunny Brazil, the concentration of serum 25(OH)D increased from 18.7 ng/mL to 23.8 ng/mL. However, 86.2% of the supplemented group did not reach optimal levels (30.0 ng/mL) of 25(OH)D. Kuwabara *et al*[21] discovered that after supplementation with 800 IU of cholecalciferol and 200 mg of calcium for 1 month, serum 25(OH)D levels in old men and women increased from 9.7 ng/mL to 19.3 ng/mL, although 60% of the subjects remained vitamin D-deficient. However, Chapuy *et al*[27] reported that after supplementation with 800 IU of cholecalciferol and 1200 mg of calcium for 6 months, serum 25(OH)D levels increased from 9.2 ng/mL to 30.0 ng/mL. The varied results of these different studies may be associated with the dose of cholecalciferol, the period of study, the intake of calcium and differences associated with the population. Hanley *et al*[9] systematically reviewed 168 potentially relevant vitamin D papers from 1996 to 2008 and concluded that vitamin D was necessary for the prevention of osteoporosis. They recommended an intake of cholecalciferol for high-risk and older adults ranging from 800 to 2000 IU daily. To achieve satisfactory vitamin D status (>30 ng/mL), many individuals may require higher doses. A similar suggestion was made at an expert roundtable discus-

sion. The participants concluded that the intake of vitamin D should be at least 800 IU daily[10]. In addition, this recommendation was independent of sun exposure, seasonal exposure and additional multivitamin use.

Calcitriol has been used as a therapy for osteoporosis for many years. One study verified that supplementation with calcitriol at 0.5 μg per day for six months may promote bone formation and decrease bone absorption[28]. Active vitamin D analogs have a larger impact in decreasing bone loss and fracture incidence than standard vitamin D in postmenopausal osteoporosis because vitamin D analogs display a greater effect in reducing numbers of falls[29]. Calcitriol plays an important role in skeletal system regulation and may have other bone-protective effects independent of its calcium absorption effects[30]. To prevent hypercalcinuria, patients with osteoporosis or osteopenia in China are frequently treated with 0.25 μg/d of calcitriol[13]. After 3 months of intervention in our study, no differences were identified in calcium metabolism and bone turnover between the group treated with 0.25 μg of calcitriol daily and the group treated with 800 IU of cholecalciferol daily. Serum calcium and AKP levels were significantly increased in both groups. The serum PTH and β-CTX levels were significantly decreased in both groups. However, the serum 25(OH)D level did not change significantly in the calcitriol group; it showed only a slight decreasing trend. Clements *et al*[31] discovered that after supplementation with 1 μg per day of calcitriol to treat postmenopausal osteoporosis, hypoparathyroidism and hypophosphatemic osteomalacia, the elimination half-time for 25(OH)D in the plasma could be significantly shortened by raising the circulating concentration of 1,25-dihydroxyvitamin D. One explanation for this result is that calcitriol is the activated form of cholecalciferol, and excessive calcitriol decreases serum 25(OH) in a negative feedback system. Halloran *et al*[32] discovered that rats chronically administered calcitriol displayed reduced serum concentrations of 25-OH-D_3 and 24,25$(OH)_2D_3$ in a dose- and time-dependent fashion. Calcitriol administration increased the metabolic clearance of 25-OH-D but not its production.

After 3 months of intervention, the concentration of serum Ca, P, and the total AKP activities in both groups remained within normal ranges. However, urinary calcium excretions were not observed in either group; this was a limitation of our study. In the United States, the previous NOF guidelines set the safe upper limit for vitamin D intake at 2000 IU per day. However, recent evidence has shown that higher intake is safe and that some older patients need at least this amount to maintain adequate 25(OH)D levels[8]. Doses of more than 50 000 IU of vitamin D_3 per day are associated with hypercalcemia and hyperphosphatemia[33]. However, Vieth *et al*[34] observed that doses of 10 000 IU of cholecalciferol daily for up to 5 months did not cause toxicity. In a randomized, double-blind trial that tested the efficacy and safety of zoledronic acid (5 mg) that was intravenously supplemented annually in preventing new fractures in women and men who had hip fractures[35], all the patients received oral calcium (1000–1500 mg) and vitamin D (800–1200 IU) daily. By the end of the study, none of the patients suffered from hypercalcemia. These results indicate that the current safe upper intake level of 2000 IU of vitamin D per day may be too conservative.

Our current study indicated that that cholecalciferol (800 IU/d) plus Caltrate D increased the mean serum 25(OH)D to 20 ng/mL in most but not all individuals. Both 800 IU/day of cholecalciferol and 0.25 μg/day of calcitriol plus Caltrate D effectively modified calcium and bone turnover markers in postmenopausal women in Shanghai with vitamin D insufficiency. The use cholecalciferol or calcitriol and the doses specified in the study for improving the bone health of postmenopausal women requires further investigation.

Acknowledgements

This study was supported by the National Natural Science Foundation of China (NSFC) (No 30800387, 30771019, 81070692, 81170803), Academic Leaders in Health Sciences in Shanghai (XBR2011014), STCSM10DZ1950100, Science and Technology commission of Shanghai municipality (11ZR1427300) and Shanghai Rising Star Project (No 11QA1404900).

Author contribution

Qi-ren HUANG designed this research; Hao ZHANG, Zhen-lin ZHANG, Jie-mei GU, Wei-wei HU, and Yu-juan LIU performed clinical research; Qi-ren HUANG, Jie-mei GU, Yun-qiu HU, and Yu-juan LIU recruited subjects; Hao ZHANG wrote the paper; and Qi-ren HUANG and Zhen-lin ZHANG revised the paper.

References

1 Holick MF. Vitamin D deficiency. N Engl J Med 2007; 357: 266–81.
2 Morales O, Samuelsson MK, Lindgren U, Haldosen LA. Effects of 1alpha,25-dihydroxyvitamin D3 and growth hormone on apoptosis and proliferation in UMR 106 osteoblast-like cells. Endocrinology 2004; 145: 87–94.
3 DeLuca HF. Overview of general physiologic features and functions of vitamin D. Am J Clin Nutr 2004; 80: 1689S–96S.
4 Thomas MK, Lloyd-Jones DM, Thadhani RI, Shaw AC, Deraska DJ, Kitch BT, *et al*. Hypovitaminosis D in medical inpatients. N Engl J Med 1998; 338: 777–83.
5 Dawson-Hughes B, Heaney RP, Holick MF, Lips P, Meunier PJ, Vieth R. Estimates of optimal vitamin D status. Osteoporos Int 2005; 16: 713–6.
6 Holick MF, Matsuoka LY, Wortsman J. Age, vitamin D, and solar ultraviolet. Lancet 1989; 2: 1104–5.
7 Weaver CM, Fleet JC. Vitamin D requirements: current and future. Am J Clin Nutr 2004; 80: 1735S–9S.
8 Foundation NO. Clinician's Guide to Prevention and Treatment of Osteoporosis. Washington, DC: National Osteoporosis Foundation; 2010. Report No: 0029–6643 (Print) 0029–6643 (Linking).
9 Hanley DA, Cranney A, Jones G, Whiting SJ, Leslie WD. Vitamin D in adult health and disease: a review and guideline statement from Osteoporosis Canada (summary). CMAJ 2010; 182: 1315–9.
10 Roux C, Bischoff-Ferrari HA, Papapoulos SE, de Papp AE, West JA, Bouillon R. New insights into the role of vitamin D and calcium in osteoporosis management: an expert roundtable discussion. Curr Med Res Opin 2008; 24: 1363–70.

11 Heaney RP, Davies KM, Chen TC, Holick MF, Barger-Lux MJ. Human serum 25-hydroxycholecalciferol response to extended oral dosing with cholecalciferol. Am J Clin Nutr 2003; 77: 204–10.
12 Lau KH, Baylink DJ. Vitamin D therapy of osteoporosis: plain vitamin D therapy versus active vitamin D analog (D-hormone) therapy. Calcif Tissue Int 1999; 65: 295–306.
13 Xia WB, Zhang ZL, Wang HF, Meng XW, Zhang Y, Zhu GY, *et al*. The efficacy and safety of calcitriol and/or Caltrate D in elderly Chinese women with low bone mass. Acta Pharmacol Sin 2009; 30: 372–8.
14 Holzherr ML, Retallack RW, Gutteridge DH, Price RI, Faulkner DL, Wilson SG, *et al*. Calcium absorption in postmenopausal osteoporosis: benefit of HRT plus calcitriol, but not HRT alone, in both malabsorbers and normal absorbers. Osteoporos Int 2000; 11: 43–51.
15 Richy F, Dukas L, Schacht E. Differential effects of D-hormone analogs and native vitamin D on the risk of falls: a comparative meta-analysis. Calcif Tissue Int 2008; 82: 102–7.
16 von Hurst PR, Stonehouse W, Kruger MC, Coad J. Vitamin D supplementation suppresses age-induced bone turnover in older women who are vitamin D deficient. J Steroid Biochem Mol Biol 2010; 121: 293–6.
17 Seamans KM, Hill TR, Wallace JM, Horigan G, Lucey AJ, Barnes MS, *et al*. Cholecalciferol supplementation throughout winter does not affect markers of bone turnover in healthy young and elderly adults. J Nutr 2010; 140: 454–60.
18 Holick MF, Siris ES, Binkley N, Beard MK, Khan A, Katzer JT, *et al*. Prevalence of vitamin D inadequacy among postmenopausal North American women receiving osteoporosis therapy. J Clin Endocrinol Metab 2005; 90: 3215–24.
19 Lips P, Hosking D, Lippuner K, Norquist JM, Wehren L, Maalouf G, *et al*. The prevalence of vitamin D inadequacy amongst women with osteoporosis: an international epidemiological investigation. J Intern Med 2006; 260: 245–54.
20 Heaney RP, Dowell MS, Hale CA, Bendich A. Calcium absorption varies within the reference range for serum 25-hydroxyvitamin D. J Am Coll Nutr 2003; 22: 142–6.
21 Kuwabara A, Tsugawa N, Tanaka K, Fujii M, Kawai N, Mukae S, *et al*. Improvement of vitamin D status in Japanese institutionalized elderly by supplementation with 800 IU of vitamin D(3). J Nutr Sci Vitaminol (Tokyo) 2009; 55: 453–8.
22 Ravn P, Fledelius C, Rosenquist C, Overgaard K, Christiansen C. High bone turnover is associated with low bone mass in both pre- and postmenopausal women. Bone 1996; 19: 291–8.
23 Seeman E, Delmas PD. Bone quality — the material and structural basis of bone strength and fragility. N Engl J Med 2006; 354: 2250–61.
24 Eastell R, Hannon RA. Biomarkers of bone health and osteoporosis risk. Proc Nutr Soc 2008; 67: 157–62.
25 Bischoff-Ferrari HA, Willett WC, Wong JB, Giovannucci E, Dietrich T, Dawson-Hughes B. Fracture prevention with vitamin D supplementation: a meta-analysis of randomized controlled trials. JAMA 2005; 293: 2257–64.
26 Pignotti GA, Genaro PS, Pinheiro MM, Szejnfeld VL, Martini LA. Is a lower dose of vitamin D supplementation enough to increase 25(OH)D status in a sunny country? Eur J Nutr 2010; 49: 277–83.
27 Chapuy MC, Pamphile R, Paris E, Kempf C, Schlichting M, Arnaud S, *et al*. Combined calcium and vitamin D3 supplementation in elderly women: confirmation of reversal of secondary hyperparathyroidism and hip fracture risk: the Decalyos II study. Osteoporos Int 2002; 13: 257–64.
28 Tsukamoto Y, Watanabe T, Nakagami T, Morishita K. Effect of treatment with oral calcitriol on calcium metabolism and fasting serum 25(OH)- or 1,25$(OH)_2$-vitamin D level in Japanese postmenopausal women. Endocr J 2003; 50: 681–7.
29 Schacht E, Richy F, Reginster JY. The therapeutic effects of alfacalcidol on bone strength, muscle metabolism and prevention of falls and fractures. J Musculoskelet Neuronal Interact 2005; 5: 273–84.
30 Richy F, Ethgen O, Bruyere O, Reginster JY. Efficacy of alphacalcidol and calcitriol in primary and corticosteroid-induced osteoporosis: a meta-analysis of their effects on bone mineral density and fracture rate. Osteoporos Int 2004; 15: 301–10.
31 Clements MR, Davies M, Hayes ME, Hickey CD, Lumb GA, Mawer EB, *et al*. The role of 1,25-dihydroxyvitamin D in the mechanism of acquired vitamin D deficiency. Clin Endocrinol (Oxf) 1992; 37: 17–27.
32 Halloran BP, Bikle DD, Levens MJ, Castro ME, Globus RK, Holton E. Chronic 1,25-dihydroxyvitamin D3 administration in the rat reduces the serum concentration of 25-hydroxyvitamin D by increasing metabolic clearance rate. J Clin Invest 1986; 78: 622–8.
33 Koutkia P, Chen TC, Holick MF. Vitamin D intoxication associated with an over-the-counter supplement. N Engl J Med 2001; 345: 66–7.
34 Vieth R. Why the optimal requirement for vitamin D3 is probably much higher than what is officially recommended for adults. J Steroid Biochem Mol Biol 2004; 89–90: 575–9.
35 Lyles KW, Colon-Emeric CS, Magaziner JS, Adachi JD, Pieper CF, Mautalen C, *et al*. Zoledronic acid and clinical fractures and mortality after hip fracture. N Engl J Med 2007; 357: 1799–809.

Acta Pharmacologica Sinica (2012) 33: 496–502
 1671-4083/11 $32.00
www.nature.com/aps

Original Article

Traditional Chinese medicine formula Qing Huo Yi Hao as superoxide anion scavenger in high glucose-treated endothelial cells

Qiong XU, Bin ZHANG, Xiao-mu LI, Xin GAO*

Department of Endocrinology and Metabolism, Zhongshan Hospital, Fudan University, Shanghai 200032, China

Aim: To investigate the effects of a traditional Chinese medicine formula Qing Huo Yi Hao (QHYH) and its components on hydroxyl radical ($HO^{\bullet}$) production *in vitro* and the activity of QHYH against free radicals in cultured endothelial cells induced by high glucose.
Methods: Hydroxyl radicals ($HO^{\bullet}$) were generated through Fenton reactions *in vitro*, and 5,5-dimethyl-1-pyrroline N-oxide (DMPO) was used as a spin trap to form DMPO/$HO^{\bullet}$ adducts detected using electron paramagnetic resonance (EPR). Immortalized mouse cerebral microvascular endothelial (bEnd.3) cells were treated with high glucose (35 mmol/L). The free radical scavenging ability of QHYH in the cells was evaluated using EPR. Superoxide dismutase (SOD) was used to identify the free radicals scavenged by QHYH in the cells.
Results: QHYH and its 8 components concentration-dependently reduced DMPO/$HO^{\bullet}$ signaling. The DMPO/$HO^{\bullet}$ adduct scavenging ability of QHYH was 82.2%, which was higher than each individual component. The free radical scavenging ability of 1% QHYH in high glucose-treated bEnd.3 cells was approximately 70%. In these cells, the free radicals were also specifically reduced by SOD (400 U/mL), implying that the free radicals were primarily superoxide anions.
Conclusion: The results demonstrate that the QHYH formula is potent antioxidant acting as scavenge of superoxide anions in high glucose-treated endothelial cells.

Keywords: TCM; Qing Huo Yi Hao; antioxidant; endothelial cell; high glucose; free radical; superoxide dismutase; electron paramagnetic resonance

Acta Pharmacologica Sinica (2012) 33: 496–502; doi: 10.1038/aps.2011.191; published online 19 Mar 2012

Introduction

Reactive oxygen species (ROS) is a collective term that broadly describes O_2-derived free radicals, such as superoxide anion ($O_2^{\bullet -}$), $HO^{\bullet}$, peroxyl ($RO_2^{\bullet}$), and alkoxyl ($RO^{\bullet}$) radicals, as well as O_2-derived non-radical species, such as hydrogen peroxide (H_2O_2)[1]. ROS are formed as by-products of aerobic respiration and various other metabolic processes in cells[2]. Enzymatic and non-enzymatic antioxidants also exist in cells that degrade and inactivate ROS to maintain them at a low or moderate level[3, 4]. ROS at physiological concentrations regulate many cellular processes, such as proliferation, differentiation, and cell death[5, 6]. However, an imbalance between ROS production and intracellular antioxidant defense could lead to ROS accumulation, which causes harmful effects collectively termed oxidative stress[7]. According to a large body of research, reactive stress is involved in the onset of aging and many diseases, including diabetes, cardiovascular disease, and neurodegenerative diseases (*eg*, Alzheimer's disease and Parkinson's disease)[8–11].

The prevalence of diabetes mellitus (DM) is increasing dramatically, especially in developing countries[12, 13]. Cardiovascular complications of diabetes are the leading cause of DM-related death[14]. The earliest pathophysiological stage of DM cardiovascular complications is endothelial dysfunction[15, 16]. Oxidative stress resulting from hyperglycemia, hyperlipidemia, and insulin resistance is the crucial factor involved in endothelial dysfunction[17, 18]. Therefore, using an antioxidant to reduce ROS could be effective for the prevention and treatment of cardiovascular complications from diabetes. However, many clinical trials investigating a possible role for antioxidants such as vitamin E, vitamin C and beta-carotene in the prevention of atherosclerosis or clinical events have failed[19, 20]. One reason for the failure of these trials is that antioxidants do not accumulate in the mitochondria, which is the major intracellular site of ROS production [21]. Therefore, developing a more potent mitochondria-targeting antioxidant is essential[22].

* To whom correspondence should be addressed.
E-mail gao.xin@zs-hospital.sh.cn
Received 2011-09-05 Accepted 2011-12-08

QHYH is a traditional Chinese medicine (TCM) formula, the principles of which are based on "clearing heat and detoxifying" and improving blood circulation and anti-inflammation. In our previous single-blind, randomized, controlled clinical trial, QHYH was demonstrated to reduce urinary albumin excretion ability (UAER), which is an important marker of systemic endothelial function[23], and to ameliorate microcirculation nail bed flow in type 2 diabetes[24]. These results suggested that QHYH could improve endothelial function. In addition, gene chip analysis showed that QHYH acted on high glucose-induced endothelial cells mainly through oxidative phosphorylation and glutathione pathways. Based on the results described above, we presumed that QHYH might be an antioxidant, which would explain its protective effects on high glucose-induced endothelial dysfunction. In this study, we determined the antioxidant effects of QHYH and each of its components *in vitro* by EPR. We further evaluated its antioxidant activity in high glucose-induced endothelial cells and identified the free radicals scavenged by QHYH in these cells.

Materials and methods

Chemicals

For the Fenton reaction, DMPO was purchased from Sigma-Aldrich (St Louis, MO, USA), and ammonium ferrous sulfate, diethylene triamine pentaacetic acid and hydrogen peroxide were obtained from Sangon Biotech Co, Ltd (Shanghai, China). N-Acetyl-*L*-cysteine (NAC) was used as a positive control and was purchased from Sigma-Aldrich (St Louis, MO, USA). SOD used for free radical identification was purchased from Haixing Co, Ltd (Beijing, China).

Cell cultures

Immortalized mouse cerebral microvascular endothelial (bEnd.3) cells, which were used for the antioxidant study of QHYH, were kindly provided by Hui-ming JIN (Department of Pathophysiology of Shanghai Medical College, Fudan University, Shanghai, China). The cells were cultured in normal glucose (5.6 mmol/L)-Dulbecco's modified Eagle's medium (DMEM) supplemented with 10% fetal bovine serum (FBS) and incubated in a humidified 95% air/5% CO_2 incubator at 37 ^{o}C.

Preparation of QHYH and its components

Aqueous extracts of QHYH and each of the formula components, named number (Num) 1 to Num 8 below, were prepared and provided by the TCM preparation room of ZhongShan Hospital. The components of QHYH are Ligusticum chuanxiong, Hirudo nipponica, Astragalus membranaceus, Pueraria lobata, Gardenia jasminoides, Artemisia capillaris, Pteris multifida and Pericarpium Citri (ratio 3:1.5:1.5:1.5:1.5:1:0.6:0.6, W/ W). A mixture of these components was boiled in water (ratio 1:5, W/ W) for 50 min to get the crucial solution, which was then extracted by 95% ethanol and left at room temperature for 48 h. After that, supernatant was collected and reserved for detection. A package of crude drug or its corresponding components is equivalent to 15 mL of aqueous extract, with concentrations of 2.0 g/mL, 1.0 g/mL, 1.0 g/mL, 1.0 g/mL, 1.0 g/mL, 0.66 g/mL, 0.4 g/mL, and 0.4 g/mL for each component from Num 1 to Num 8, respectively. Each ingredient was condensed to determine its concentration-dependent effects on free radical scavenging. The concentrations of these condensed components from Num 1 to Num 8 were 8.0 g/mL, 3.0 g/mL, 5.5 g/mL, 3.0 g/mL, 2.5 g/mL, 2.0 g/mL, 2.2 g/mL, and 0.8 g/mL, respectively.

An MTT cell proliferation assay was performed to determine the effects of QHYH, with concentrations ranging from 1/10 000 to 1 (*v/v*), on the viability of endothelial cells cultured in 5.6 mmol/L glucose DMEM. The results showed that QHYH with a concentration of 1/100 was the best condition for cell growth. Therefore, a working concentration of 1/100 QHYH aqueous extracts was chosen for the cell studies.

Determining the DMPO/HO$^{\bullet}$ adduct scavenging ability of QHYH and each of its components *in vitro*

To study the DMPO/HO$^{\bullet}$ adduct scavenging ability of QHYH *in vitro*, the HO$^{\bullet}$ free radicals were generated by the Fenton reaction system. This generating system was composed of 100 mmol/L H_2O_2 (5 μL), 0.3 mmol/L Fe^{2+}/0.15 mmol/L DTPA (5 μL) and phosphate-buffered saline (5 μL). To form DMPO/HO$^{\bullet}$ radicals that were detected by EPR (EMX-8/2.7, Bruker BioSpin GmbH), 100 mmol/L DMPO (5 μL) was used as a spin trap.

To determine the scavenging capacity of DMPO/HO$^{\bullet}$ spin adducts, 30-μL aqueous extracts of QHYH or each of its components were directly added to the Fenton reaction system. The mixture was then transferred into a flat quartz cell, and the EPR spectra was measured after Fe^{2+}/DTPA had been added for 5 min. The EPR conditions used in this experiment were: microwave frequency=9.87 GHz, microwave power=20 mW, modulating frequency=100 kHz, modulating extent=0.1 mT and measurement time=1 min. Data acquisition and analysis were performed with Win EPR analyzing software (Bruker). The scavenging ability of the samples on the DMPO/HO$^{\bullet}$ adducts was calculated using the formula $(h_0-h_1)/h_0\times100\%$, where h_1 and h_0 were the peak heights of the second low-field line of the DMPO/HO$^{\bullet}$ spin adduct with and without samples, respectively. To study the dose-dependent effects of the components of QHYH on free radical reduction, the following concentrations of the condensed components were used: 3.1%, 6.25%, 12.5%, 25%, 50%, and 100%.

Determining the effects of high glucose on free radical generation in bEnd.3 cells

To evaluate the antioxidant effects of QHYH on high glucose-induced bEnd.3 cells, free radicals generated from high glucose-treated bEnd.3 cells were initially evaluated. The cells were incubated with different glucose concentrations from 25 mmol/L to 40 mmol/L to find an optimum glucose concentration that would induce the strongest free radical signals. Next, bEnd.3 cells were incubated with glucose for 0.5 h to 24 h to obtain an optimal glucose incubation time. After incubation, the cells were digested with 0.25% pancreatin and centrifuged

at 300×*g* for 5 min. DMEM without fetal bovine serum was added to adjust the cell concentration to 5×10^6/mL. Forty-five-microliter cell samples were mixed with 100 mmol/L DMPO (5 μL). The mixture was then transferred to a flat quartz cell, and the EPR spectra were immediately collected using the conditions mentioned above. The EPR signal intensity was quantified by the second peak-to-peak height in the direction of the magnetic field.

To validate specific effects of high glucose on free radical generation in bEnd.3 cells, EPR spectra were collected in the following groups cultured for 1 h, which is the optimum condition for free radical generation: (1) normal glucose-treated cell group: bEnd.3 cells cultured with 5.6 mmol/L glucose-DMEM; (2) high glucose-treated cell group: bEnd.3 cells cultured with 35 mmol/L glucose-DMEM; (3) high-glucose group: 35 mmol/L glucose-DMEM without cells; (4) mannitol group (osmotic control): bEnd.3 cells cultured with normal glucose-DMEM containing 29.4 mmol/L mannitol. After incubation, the free radicals in these cells were determined by the same methods used for the detection of high glucose effects.

Determining the antioxidant effects of QHYH on high glucose-induced bEnd.3 cells

QHYH with a working concentration of 1/100 was incubated with high glucose-induced bEnd.3 cells at the optimum conditions to determine its antioxidant effects. NAC (10 mmol/L) was used as the positive control. After incubating for 1 h, the free radicals were determined by the same methods used for the detection of the high glucose effects.

Identifying the free radicals scavenged by QHYH in high glucose-induced bEnd.3 cells

To identify the free radicals scavenged by QHYH in high glucose-induced bEnd.3 cells, 400 U/mL SOD were added to the cells. After incubation for 1 h, the EPR spectra were collected from this group.

Statistical analysis

Numerical data are expressed as the mean±SEM. Statistical evaluation was performed using a Student's *t*-test. Differences were considered statistically significant when $P<0.05$.

Results

Hydroxyl radical scavenging activity of QHYH and its components

A strong free radical signal was detected in the DMPO/HO$^\bullet$ adduct generating system (Figure 1). To evaluate the free radical scavenging ability of QHYH, aqueous extracts of QHYH at various concentrations [12.5%, 25%, 50%, 75%, and 100% (*v*/*v*)] were added to this DMPO/HO$^\bullet$ adduct generating system. Compared to the hydroxyl radical model, the DMPO/HO$^\bullet$ adduct signals decreased significantly in a concentration-dependent manner (Figure 1). Quantitatively, 30 μL of QHYH (100% QHYH in Figure 1) with the same concentration as that of the crude drug scavenged approximately 82.2% of the DMPO/HO$^\bullet$ generated in this reaction (Figure 2). The DMPO/HO$^\bullet$ adduct scavenging ability of each QHYH component was also determined. All of the QHYH components except Num 3 reduced the DMPO/HO$^\bullet$ adducts. The DMPO/HO$^\bullet$ scavenging abilities of Num 1 to Num 8 ranged from 25% to 46.2%; however, the scavenging ability of Num

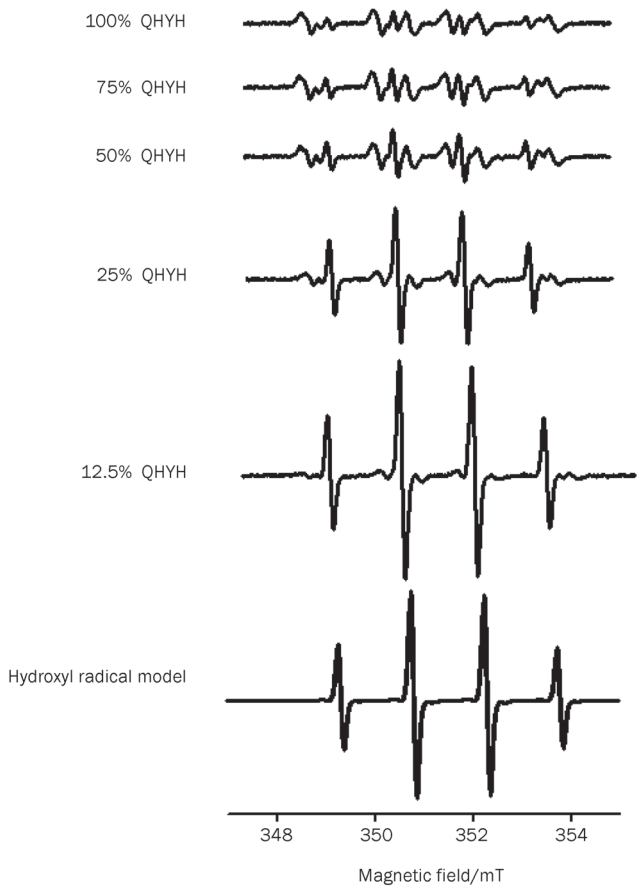

Figure 1. EPR spectra of DMPO/HO$^\bullet$ adducts before and after QHYH sample.

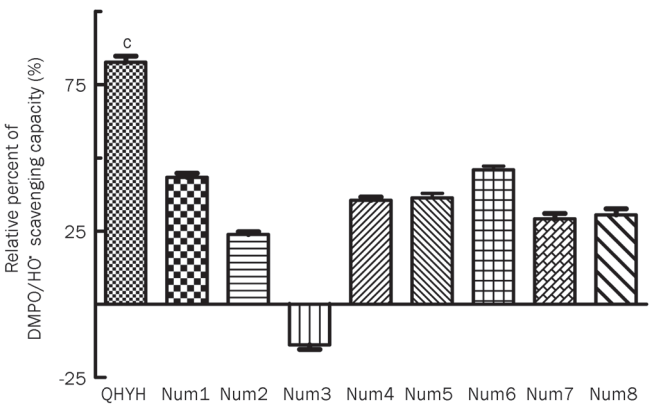

Figure 2. Hydroxyl radical scavenging ability of QHYH and its components. Aqueous extracts of QHYH or its components (30 μL) were added to the DMPO/HO$^\bullet$ adduct generating system. The scavenging ability on DMPO/HO$^\bullet$ adduct was calculated by $(h_0-h_1)/h_0\times100\%$, which was presented as mean±SEM (n=3). $^cP<0.01$ *vs* components from Num1 to Num8.

3 was -16.7% (Figure 2), suggesting that Num 3 at the dose in the TCM prescription may be a pro-oxidant. After the QHYH components, including Num 3, were condensed and added to the Fenton reaction at increasing concentrations, the DMPO/$HO^{\bullet}$ adducts were scavenged in a concentration-dependent manner (Table 1). The results imply that Num 3 may be both an antioxidant and a pro-oxidant depending on its concentration.

The effects of high glucose on free radical generation in bEnd.3 cells

When bEnd.3 cells were induced with glucose for 1 h, the EPR signal intensity was enhanced as the glucose level increased from 25 to 35 mmol/L (Figure 3). However, the EPR signal intensity induced by 40 mmol/L glucose was weaker than that induced by 35 mmol/L. This may be attributed to the alcohol groups in glucose that can decrease the free radical signals. Therefore, 35 mmol/L glucose was chosen as the optimum glucose concentration to induce ROS generation in bEnd.3 cells. Culturing time with high glucose was also various to determine its effects on ROS generation. The results showed that the EPR signal intensity in bEnd.3cells cultured with 35 mmol/L glucose for 1 h was stronger than that in cells induced by this glucose concentration cultured for 30 min, 2 h, 6 h, and 24 h (Figure 4). Thus, the optimum incubation condition for ROS generation in bEnd.3 cells was induction with 35 mmol/L glucose for 1 h.

Figure 3. EPR signal intensity of bEnd.3 cells cultured in different glucose concentration. The x-axis is the glucose concentrations that are 5.6 mmol/L, 25 mmol/L, 30 mmol/L, 35 mmol/L, and 40 mmol/L. The y-axis is EPR signal intensity that was quantified by the second peak-peak height in the direction of magnetic field.

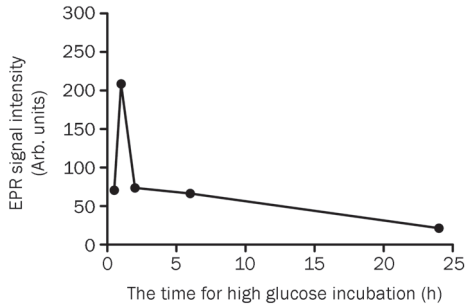

Figure 4. EPR signal intensity of bEnd.3 cells cultured in 35 mmol/L glucose DMEM for 30 min, 1 h, 2 h, 6 h, and 24 h. The x-axis is time of high glucose incubation. The y-axis is EPR signal intensity that was quantified by the second peak-peak height in the direction of magnetic field.

The EPR spectra of the normal glucose-treated cell group, the high glucose-treated cell group, the high-glucose group without cells and the mannitol group were collected to confirm the specific effects of high glucose on free radical generation in bEnd.3 cells. As an osmotic stress control, 29.4 mmol/L mannitol was used. The EPR spectra showed that no obvious signal was detected in the mannitol group compared to the high glucose-treated cell group (Figure 5), indicating that the ROS produced in the high glucose-treated cell group were not generated by osmotic stress. Similarly, there was no obvious signal detected in the normal glucose-treated cell group or the high-glucose group without cells compared to the high glucose-treated cell group (Figure 5).

Antioxidant effects of QHYH on high glucose-treated bEnd.3 cells

To evaluate the antioxidant effects of QHYH on high glucose-treated bEnd.3 cells, 1/100 QHYH was added to the bEnd.3 cells, which were then co-incubated with 35 mmol/L glucose for 1 h. After incubation, DMPO was added and EPR spec-

Table 1. Concentration-dependent property of QHYH's components on $HO^{\bullet}$ scavenging. QHYH's components were condensed to evaluate concentration-dependent effects on $HO^{\bullet}$ scavenging. The concentrations of the condensed components were 8.0 g/mL, 3.0 g/mL, 5.5 g/mL, 3.0 g/mL, 2.5 g/mL, 2.0 g/mL, 2.2 g/mL, and 0.8 g/mL individually. The scavenging abilities are presented as mean±SEM (*n*=3).

	Scavenging ability of $HO^{\bullet}$ (%)							
Content (%)	Num1 (8.0 g/mL)	Num2 (3.0 g/mL)	Num3 (5.5 g/mL)	Num4 (3.0 g/mL)	Num5 (2.5 g/mL)	Num6 (2.0 g/mL)	Num7 (2.2 g/mL)	Num8 (0.8 g/mL)
3.10	33.52±0.01	29.38±0.23	17.30±7.80	43.11±0.05	67.46±0.08	51.76±0.06	18.62±0.17	12.15±0.72
6.25	53.63±0.91	61.43±0.05	30.57±7.25	62.20±0.10	84.42±0.02	72.67±0.11	43.40±0.13	39.88±0.10
12.50	69.61±0.15	75.70±0.20	55.58±0.01	85.50±1.66	91.77±0.06	86.28±1.44	80.12±0.05	59.47±0.13
25.00	83±0.10	96.36±0.28	82.98±1.78	94.78±0.21	96.87±0.21	94.90±0.20	86.75±0.08	78.69±0.16
50.00	93.46±0.12	97.76±0.23	92.35±0.13	98.42±0.23	98.87±0.18	97.25±0.20	97.78±0.01	94.12±0.17
100.00	98.02±0.40	99.10±0.16	96.74±0.44	99.08±0.32	99.21±0.28	99.30±0.20	98.81±0.04	97.84±0.13

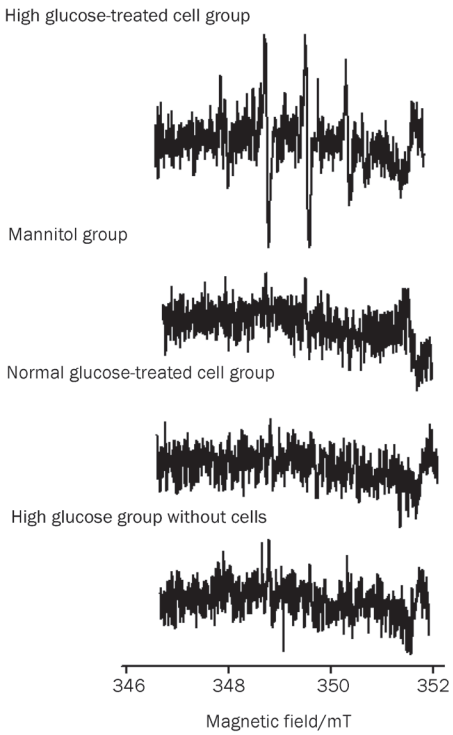

Figure 5. EPR spectra of high glucose-treated cell group (35 mmol/L), mannitol group (29.4 mmol/L), normal glucose-treated cell group (5.6 mmol/L), and high glucose group without cells (35 mmol/L).

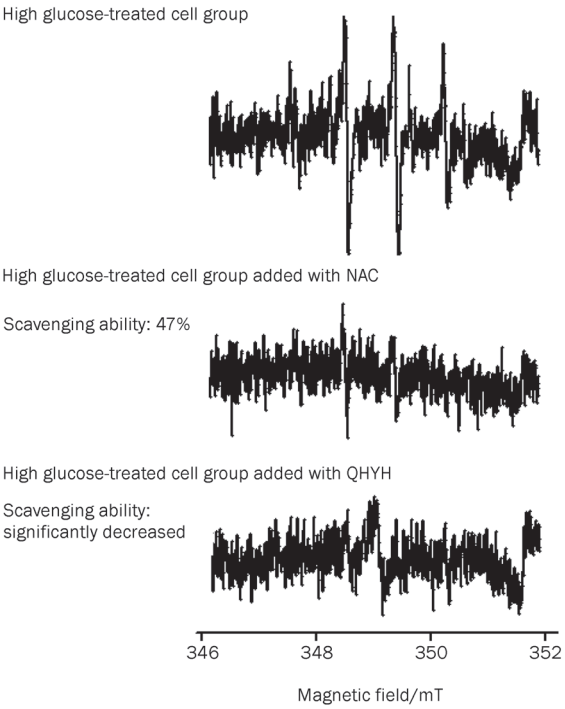

Figure 6. EPR spectra of high glucose-treated bEnd.3 cells before or after addition of QHYH. Cells cultured in high glucose (35 mmol/L) were treated with 1/100 QHYH for 1 h. Free radicals in the groups were then assessed by EPR using DMPO as a spin trap. NAC was used as a positive control.

tra were collected. Compared to the high glucose-treated cell group, the free radical signals in the QHYH group were remarkably reduced. The free radical scavenging ability of the QHYH group was approximately 70%, which was higher than that of the NAC group (Figure 6).

Identifying the free radicals scavenged by QHYH in high glucose-treated bEnd.3 cells

The free radicals scavenged by QHYH in the high glucose-treated cell group were identified by SOD. bEnd.3 cells treated with high glucose concentrations were co-incubated with 400 U/mL SOD, and the EPR spectra of this group were collected. As shown in Figure 7, the ROS signals were significantly reduced in the SOD group compared with the high glucose-treated cell group, which were decreased by approximately 60%. These results indicated that the ROS generated in bEnd.3 cells induced with 35 mmol/L glucose was $O_2^{\bullet -}$.

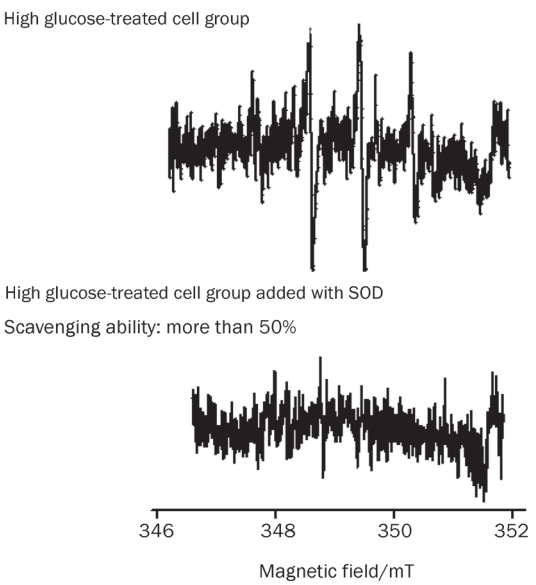

Figure 7. EPR spectra of high glucose-treated cell group (35 mmol/L) and high glucose-treated cell group added with 400 U/mL SOD.

Discussion

In this study, we found that QHYH and its components reduced the DMPO/$HO^{\bullet}$ adduct signal in a concentration-dependent manner, as measured by EPR *in vitro*, and, moreover, that QHYH decreased the free radicals generated in high glucose-induced bEnd.3 cells. The free radicals scavenged by QHYH in these cells were identified as superoxide anions.

EPR is the only approach (other than enzymatic detection) that can provide direct evidence of the presence of a free radical[25]. Using spin traps, EPR allows the detection of free radicals with short life spans, such as $HO^{\bullet}/O_2^{\bullet -}$ [26]. In addition, because every free radical has its own typical EPR spectrum, EPR is a unique technique to identify the nature of free radi-

cals. In our study, EPR was applied to evaluate the antioxidant effects of QHYH. The $HO^{\bullet}$ free radical was generated through a Fenton reaction (Fe^{2+}/H_2O_2). A DMPO spin trap was used to form DMPO/$HO^{\bullet}$ adducts with longer half-lives that were detectable with EPR[26, 27]. The DMPO/$HO^{\bullet}$ scavenging ability of QHYH was 82.2%, and it reduced DMPO/$HO^{\bullet}$ in a concentration-dependent manner (Figure 1 and 2). Most of the QHYH components also reduced free radicals in a concentration-dependent manner, except for the component Num 3 (Figure 2 and Table 1). However, when Num 3 was condensed, it showed antioxidant effects with concentrations ranging from 3.1% to 100% (Table 1). These results indicate that Num 3 produces pro-oxidant and antioxidant effects at different concentrations, which is similar to the properties of other natural materials, such as curcumin, tea extracts and guava extracts[28, 29]. Because the mechanism underlying this activity of Num 3 is not clear, more studies are required to determine it. Nonetheless, the scavenging free radical ability of the QHYH formula was higher than each of its individual components (Figure 2). These results demonstrate that the antioxidant effect of QHYH is more potent than that of any of its components, which explains the rationale for using TCM as a prescribed formula but not as a single drug.

It is worth noting that the main peaks in Figure 1 were reduced as the QHYH concentration increased, and a new small radical signal emerged (Figure 1), suggesting that the new signal may be the result of the reaction between DMPO and the radicals produced in the reaction between QHYH and $HO^{\bullet}$. Although the exact nature of the new signal is not known, it does not affect the determination of the antioxidant ability of QHYH.

ROS accumulation induced by hyperglycemia is the main factor contributing to endothelial dysfunction in type 2 diabetes mellitus[17, 18]. Free radical signals were most prominent in bEnd.3 cells cultured with 35 mmol/L glucose for 1 h compared to bEnd.3 cells in other culturing conditions (Figure 3 and Figure 4). No obvious free radical signal was detected in the high-glucose group without cells, the normal glucose-treated cell group or the osmotic control (mannitol) group (Figure 5). These results demonstrate that the free radicals were generated in the high glucose-treated endothelial cells rather than being affected by osmotic pressure. To determine the antioxidant effects of QHYH, its extracts at a concentration of 1/100 (*v/v*) were added to bEnd.3 cells treated under high-glucose conditions. The results showed that free radicals were reduced, and the scavenging ability of QHYH was higher than that of 10 mmol/L NAC (Figure 6). This indicates that QHYH is able to protect endothelial cells against high glucose-induced oxidative stress.

In this study, we observed that the free radicals generated in bEnd.3 cells treated under high-glucose conditions decreased dramatically when SOD was added (Figure 7). Because SOD catalyzes the reduction of the superoxide anion ($2O_2^{\bullet-}+2H^+ \rightarrow O_2+H_2O_2$) extremely rapidly[30, 31], the results demonstrate that the free radical induced by high glucose is $O_2^{\bullet-}$. Combined with the results described above, these findings show that QHYH exerts its antioxidant effects by scavenging $O_2^{\bullet-}$, which is mainly generated during the transfer of electrons through the respiratory chain[32, 33]. These results indicate that the site of action of QHYH is the mitochondria. In our previous report, we isolated several monomers from QHYH and found that tetramethylpyrazine, one of the strongest antioxidant compounds[34], can up-regulate mitochondrial biogenesis and reduce mitochondrial ROS production in palmitate-induced muscle cells[35]. All of these results indicate that QHYH may be a mitochondria-targeted antioxidant.

In this study, we demonstrated that the antioxidant activity of QHYH and its constituents *in vitro* using EPR, and we confirmed the ability of QHYH to specifically scavenge superoxide anions in high glucose-induced bEnd.3 cells. Our results suggest that QHYH is a potent antioxidant that protects endothelial cells against oxidative stress. Therefore, QHYH could be a promising antioxidant drug for the prevention and treatment of diabetic complications.

Acknowledgements

This work was supported by grants from the National Natural Science Foundation of China (No 30871196 to Xin GAO) and the National Basic Research Program of China (No 2011CB504004 to Xin GAO).

The authors thank Xiang-lin SHI and Shi-ming CHEN (The Institute for Nutritional Sciences, Chinese Academy of Sciences, China) for technical assistance.

Author contribution

Qiong XU analyzed the data and wrote the paper; Bing ZHANG performed the research; Xiao-mu LI helped to design the study and analyze the data. Xin GAO designed the study and analyzed the data.

References

1 Halliwell B, Cross CE. Oxygen-derived species: their relation to human disease and environmental stress. Environ Health Perspect 1994; 102: 5–12.
2 Halliwell B. Reactive oxygen species in living systems: source, biochemistry, and role in human disease. Am J Med 1991; 91: 14S–22S.
3 Holmgren A, Johansson C, Berndt C, Lonn ME, Hudemann C, Lillig CH. Thiol redox control via thioredoxin and glutaredoxin systems. Biochem Soc Trans 2005; 33: 1375–7.
4 Kirkman HN, Gaetani GF. Mammalian catalase: a venerable enzyme with new mysteries. Trends Biochem Sci 2007; 32: 44–50.
5 Shi M, Yang H, Motley ED, Guo Z. Overexpression of Cu/Zn-superoxide dismutase and/or catalase in mice inhibits aorta smooth muscle cell proliferation. Am J Hypertens 2004; 17: 450–6.
6 Covarrubias L, Hernandez-Garcia D, Schnabel D, Salas-Vidal E, Castro-Obregon S. Function of reactive oxygen species during animal development: passive or active? Dev Biol 2008; 320: 1–11.
7 Ridnour LA, Isenberg JS, Espey MG, Thomas DD, Roberts DD, Wink DA. Nitric oxide regulates angiogenesis through a functional switch involving thrombospondin-1. Proc Natl Acad Sci U S A 2005; 102: 13147–52.
8 Reddy VP, Zhu X, Perry G, Smith MA. Oxidative stress in diabetes and Alzheimer's disease. J Alzheimers Dis 2009; 16: 763–74.
9 Shenouda SM, Widlansky ME, Chen K, Xu G, Holbrook M, Tabit CE,

et al. Altered mitochondrial dynamics contributes to endothelial dysfunction in diabetes mellitus. Circulation 2011; 124: 444–53.
10 Chrissobolis S, Miller AA, Drummond GR, Kemp-Harper BK, Sobey CG. Oxidative stress and endothelial dysfunction in cerebrovascular disease. Front Biosci 2011; 16: 1733–45.
11 Vendelbo MH, Nair KS. Mitochondrial longevity pathways. Biochim Biophys Acta 2011; 1813: 634–44.
12 Bonow RO, Gheorghiade M. The diabetes epidemic: a national and global crisis. Am J Med 2004; 116: 2S–10S.
13 King H, Aubert RE, Herman WH. Global burden of diabetes, 1995-2025: prevalence, numerical estimates, and projections. Diabetes Care 1998; 21: 1414–31.
14 Xu J, Zou MH. Molecular insights and therapeutic targets for diabetic endothelial dysfunction. Circulation 2009; 120: 1266–86.
15 Huang PL. eNOS, metabolic syndrome and cardiovascular disease. Trends Endocrinol Metab 2009; 20: 295–302.
16 Versari D, Daghini E, Virdis A, Ghiadoni L, Taddei S. Endothelial dysfunction as a target for prevention of cardiovascular disease. Diabetes Care 2009; 32: S314–21.
17 Giacco F, Brownlee M. Oxidative stress and diabetic complications. Circ Res 2010; 107: 1058–70.
18 Thomas SR, Witting PK, Drummond GR. Redox control of endothelial function and dysfunction: molecular mechanisms and therapeutic opportunities. Antioxid Redox Signal 2008; 10: 1713–65.
19 Fearon IM, Faux SP. Oxidative stress and cardiovascular disease: novel tools give (free) radical insight. J Mol Cell Cardiol 2009; 47: 372–81.
20 Ceriello A. Hypothesis: the “metabolic memory”, the new challenge of diabetes. Diabetes Res Clin Pract 2009; 86: S2–6.
21 Victor VM, Apostolova N, Herance R, Hernandez-Mijares A, Rocha M. Oxidative stress and mitochondrial dysfunction in atherosclerosis: mitochondria-targeted antioxidants as potential therapy. Curr Med Chem 2009; 16: 4654–67.
22 Rocha M, Apostolova N, Hernandez-Mijares A, Herance R, Victor VM. Oxidative Stress and Endothelial Dysfunction in Cardiovascular Disease: Mitochondria-Targeted Therapeutics. Curr Med Chem 2010; 15: 3827–41.
23 Tsioufis C, Dimitriadis K, Antoniadis D, Stefanadis C, Kallikazaros I. Inter-relationships of microalbuminuria with the other surrogates of the atherosclerotic cardiovascular disease in hypertensive subjects. Am J Hypertens 2004; 17: 470–6.
24 Yu DQ, Li XM, Li X, Teng Y, Zhang JZ, Zhao NQ, *et al*. Effect and security of traditional Chinese medicine prescription on urine albumin excreting rate of type 2 diabetes. Shanghai Med J 2004; 27: 466–69.
25 Izuta H, Narahara Y, Shimazawa M, Mishima S, Kondo S, Hara H. 1,1-diphenyl-2-picrylhydrazyl radical scavenging activity of bee products and their constituents determined by ESR. Biol Pharm Bull 2009; 32: 1947–51.
26 Yu LL, Cheng Z. Application of electron spin resonance (ESR) spectrometry in nutraceutical and food research. Mol Nutr Food Res 2008; 52: 62–78.
27 Rohn S, Kroh LW. Electron spin resonance — a spectroscopic method for determining the antioxidative activity. Mol Nutr Food Res 2005; 49: 898–907.
28 Qian H, Nihorimbere V. Antioxidant power of phytochemicals from Psidium guajava leaf. J Zhejiang Univ Sci 2004; 5: 676–83.
29 Shishodia S, Sethi G, Aggarwal BB. Curcumin: getting back to the roots. Ann N Y Acad Sci 2005; 1056: 206–17.
30 Marklund S, Marklund G. Involvement of the superoxide anion radical in the autoxidation of pyrogallol and a convenient assay for superoxide dismutase. Eur J Biochem 1974; 47: 469–74.
31 McCord JM, Fridovich I. Superoxide dismutase. An enzymic function for erythrocuprein (hemocuprein). J Biol Chem 1969; 244: 6049-55.
32 Quan S, Kaminski PM, Yang L, Morita T, Inaba M, Ikehara S, *et al*. Heme oxygenase-1 prevents superoxide anion-associated endothelial cell sloughing in diabetic rats. Biochem Biophys Res Commun 2004; 315: 509–16.
33 Quagliaro L, Piconi L, Assaloni R, Da Ros R, Szabo C, Ceriello A. Primary role of superoxide anion generation in the cascade of events leading to endothelial dysfunction and damage in high glucose treated HUVEC. Nutr Metab Cardiovasc Dis 2007; 17: 257–67.
34 Kang Y, Hu M, Zhu Y, Gao X, Wang MW. Antioxidative effect of the herbal remedy Qin Huo Yi Hao and its active component tetramethylpyrazine on high glucose-treated endothelial cells. Life Sci 2009; 84: 428–36.
35 Gao X, Zhao XL, Zhu YH, Li XM, Xu Q, Lin HD, *et al*. Tetramethylpyrazine protects palmitate-induced oxidative damage and mitochondrial dysfunction in C2C12 myotubes. Life Sci 2011; 88: 803–9.

Acta Pharmacologica Sinica (2012) 33: 503–512
 1671-4083/12 $32.00
www.nature.com/aps

Original Article

Simultaneous TLR2 inhibition and TLR9 activation synergistically suppress tumor metastasis in mice

Jun YAN[#], Fang HUA[#], Han-zhi LIU, Hong-zheng YANG, Zhuo-wei HU[1, *]

Molecular Immunology and Pharmacology Laboratory State Key Laboratory of Bioactive Substance and Function of Natural Medicines; Institute of Meteria Medica, Chinese Academy of Medical Sciences & Peking Union Medical College, Beijing 100050, China

Aim: To develop a rational immunotherapy against tumor metastasis by combining a Toll-like-receptor 2 (TLR2)-neutralizing antibody with a TLR9 agonist CpG ODN, and then investigate the mechanism of action for this combinational regimen.
Methods: After mouse melanoma B16-F10 cell inoculation, female C57BL/6 mice were treated with either CpG ODN (0.5 mg/kg) or the anti-TLR2 antibody (200 μg/kg), or with a combination of the two agents. Pulmonary metastases were evaluated by counting metastatic nodes on the lung surface using anatomical microscopy. Flow cytometry was used to evaluate the cytotoxicity of the immune cells in tumor-draining lymph nodes, the cell population in the spleen, and the infiltration of immune cells within the lungs. Cytokine and enzyme expression in the lung tissue was evaluated using ELISA or immunostaining.
Results: Anti-metastatic effects were detected in mice treated with either CpG ODN or the anti-TLR2 antibody alone. However, treatment with CpG ODN plus the anti-TLR2 antibody synergistically suppressed the metastasis as compared with treatment with either single agent. The combinational treatment resulted in enhanced infiltration of natural killer cells and cytotoxic T cells, reduced recruitment of type 2 macrophages and Tregs, and decreased expression of immunosuppressive factors including TGF-β1, cyclooxygenase-2 and indoleamine 2,3-dioxygenase, thus stimulated tumor cytotoxicity and suppressed metastasis. The anti-metastatic effect of the combinational regimen was further confirmed in spontaneous metastatic mouse model of Lewis lung carcinoma.
Conclusion: Our studies suggest that combining a TLR9 agonist with an anti-TLR2 antibody, which eliminates immunosuppressive factors from the tumor environment, is critical for an effective anti-metastatic immunotherapy.

Keywords: B16-F10 cells; tumor microenvironment; metastasis; Toll-like receptor 2; Toll-like receptor 9; Toll-like-receptor 2-neutralizing antibody; CpG; immunotherapy

Acta Pharmacologica Sinica (2012) 33: 503–512; doi: 10.1038/aps.2011.193; published online 19 Mar 2012

Introduction

During the last two decades, significant advances have been made in the field of cancer immunotherapy, and numerous strategies have been developed to provide a tumor-specific immune response[1]. However, the success of these strategies in clinical trials remains limited. Increasing evidence has shown that not only are there insufficient numbers of anti-tumor effector cells but that there are also too many immunosuppressive factors in tumor environment, which culminates in the failure to eradicate tumor cells[2, 3]. Thus, a rational anti-cancer immunotherapeutic strategy should include both anti-tumor immune elements and elements able to eliminate tumor-induced immunosuppressive factors [4].

Toll-like receptors (TLRs) recognize pathogen- or damage-associated molecular patterns (PAMPs or DAMPs) to initiate innate and adaptive immune responses against pathogens and cancer cells[5]. In addition to their importance in pathogen and transformed cell elimination, TLRs are of great importance in mediating chronic inflammation and immune tolerance[6]. TLR targeting has been promising as an effective regimen for disease treatment. The TLR9 agonist CpG ODN was shown to have encouraging anti-tumor activity mediated by simulation of anti-tumor immunity in a number of experimental models. TLR9 agonists induce the activation of plasmacytoid DCs and B cells and stimulate potent Th1-type immune responses. Therefore, TLR9 agonists have been used or are currently under development as monotherapies or in combination with other anti-cancer therapies[7]. However, there have been disappointing results from phase III trials combining TLR9 agonists with chemotherapeutic agents for treatment of non-small-cell lung cancer, with little evidence of tumor regression

# These authors contributed equally to this work.
* To whom correspondence should be addressed.
E-mail huzhuowei@imm.ac.cn
Received 2011-07-07 Accepted 2011-12-06

or remission compared with the control[7, 8]. A recent study has suggested that immune suppression induced by tumor cells inhibits the activation of the immune system by TLR9 agonists[9].

Recent data indicate that many endogenous molecules released by transformed or damaged cells act as alarm signals to stimulate TLRs and induce chronic inflammation to facilitate tumor growth and metastasis[10]. TLR2 has been identified as one of the important mediators inducing the immunosuppressive response[11]. Studies by Kim *et al* and our own group indicate that blocking TLR2 activity is a novel therapeutic strategy for anti-metastasis that combats the immunosuppressive microenvironment[12, 13]. These findings collectively suggest that a combination of a TLR2-neutralizing antibody with a TLR9 agonist CpG ODN may produce greater anti-metastatic activity than either treatment alone. In this study, we demonstrate that a TLR9 agonist CpG ODN, which can initiate anti-tumor immunity, combined with a TLR2-neutralizing antibody, which can eliminate inhibitory immune factors from tumor tissue, synergistically act to induce an intense anti-metastatic effect compared with either agent alone. Our studies suggest that combining an immune stimulatory agent with an agent that eliminates immunosuppressive factors from the tumor environment is a rational strategy for designing an effective immunotherapeutic regimen against tumor metastasis.

Materials and methods

Reagents

CpG ODN 1826 (5′-tcc atg acg ttc ctg acg tt-3′, phosphorothioate) and the CpG ODN 1826 control (5′-tcc atg agc ttc ctg agc tt-3′, phosphorothioate) were synthesized by Beijing SBS Corporation. FITC-, PE-, or PE-cy5-conjugated anti-CD3, CD4, CD8, CD25, Foxp3, F4/80, CD206, NK1.1, interferon (IFN)-γ, IL-4, IgG2b, and IgG2a mAb were purchased from eBioscience (San Diego, CA, USA). Anti-Indoleamine 2,3-Dioxygenase (IDO) and Cyclooxygenase-2 (COX2) antibodies were purchased from Santa Cruz Biotechnology, Inc (Santa Cruz, CA, USA). The neutralizing TLR2 mAb was from R&D System Inc (Minneapolis, MN, USA).

Cell culture

The mouse melanoma cell line B16F10 and the Lewis lung carcinoma cells were cultured in RPMI-1640 (Invitrogen Corporation, Carlsbad, CA, USA) supplemented with 2 g/L Na_2CO_3, 100 units/mL penicillin, 50 μg/mL gentamicin, and 10% FBS at 37 °C in 5% CO_2. These two cells were kindly donated by Prof Rui HAN of the Institute of Materia Medica, Chinese Academy of Medical Sciences & Peking Union Medical College, Beijing, China.

Preparation of animal models

Female C57BL/6 mice were purchased from Vital River Lab Animal Technology, Co Ltd (Beijing, China) and maintained under standard conditions in an animal facility at the Institute of Materia Medica. Animal care and experimentation were conducted in accordance with the guidelines of the Institutional Committee for the Ethics of Animal Care and Treatment in Biomedical Research of the Chinese Academy of Medical Sciences and Peking Union Medical College. All mice used in these studies weighed between 16 and 18 g.

To generate a mouse model of pulmonary metastasis, B16F10 cells were trypsinized and resuspended in a PBS solution at a density of 6.25×10^5 cells/mL. Then, 200 μL of the suspension was injected into the lateral tail vein of each mouse. The mice were euthanized with an overdose of anesthesia on the 21st day after inoculation, and a whole lung was extracted for calibrating the lung index by lung weight (mg) per body weight (g). An anatomical microscopic metastasis quantization was performed by counting the metastatic nodes on the surface of the whole lung. The lungs were then fixed with 4% paraformaldehyde to prepare for histological analysis.

B16F10 melanoma cells were inoculated on day 0. The TLR2-neutralizing (200 μg/kg), anti-IgG antibody (200 μg/kg), CpG (0.5 mg/kg) and CpG control (0.5 mg/kg) were injected on day 3. The treatment with CpG or CpG control was repeated every three days and the treatment with TLR2-neutralizing or anti-IgG antibody was repeated every seven days[12, 14]. The sham and control mice received a PBS vehicle treatment alone.

To determine the impact of the TLR2-neutralizing antibody plus CpG treatment on tumor cell growth and spontaneous metastasis, 2×10^6 Lewis lung carcinoma cells were resuspended in 100 μL PBS and subcutaneously injected into the right flank of mice to establish tumors. Tumor volume was calculated as $(\text{length}\times\text{width})^2/2$ every four days. When small lumps ranging in diameter from 1 to 2 mm were palpated on the 7th day, the mice were randomly divided into four equally sized groups. The dosage and frequency of the TLR2-neutralizing antibody, IgG, CpG, and CpG control were the same as the B16 experiment. Mice treated with cyclophosphamide (40 mg/kg, ip) every two days were used as a positive control. At 24 days post-tumor inoculation, the mice were sacrificed by excessive anesthesia. The primary tumors and the lungs were surgically removed and weighed. The lung metastatic nodes were counted using anatomical microscopy.

Immunohistochemistry

The left lower lobe of the lung was isolated, fixed, paraffin embedded and coronally sliced into 4-μm sections. The protocols for immunohistochemical staining for IDO and COX2 have been described previously[12] (the dilution was 1:250 for primary and secondary antibodies). The protein signal intensity was determined by Image-Pro Plus image analysis software. The reported final integrated optical densities (IOD) represent averages from 10 non-overlapping images of each lung specimen.

Cytotoxicity assay

Tumor draining lymph nodes (TDLNs) from B16 mice treated with the indicated agents were isolated and tested for cytotoxicity against B16F10 tumor cells using a standard flow

cytometry assay[15]. To determine the cytotoxicity of immune cells from TDLNs, B16F10 melanoma cells were labeled with 5 μmol/L of CFSE [5- or 6-(N-Succinimidyloxycarbonyl)-3′,6′-O,O′-diacetylfluorescein, Dojindo Mol Technol, Inc] and cultured with the TDLNs at 3 different effector to target (E:T) ratios (50:1, 25:1, and 12.5:1) in triplicate wells for 4 h. The cells were harvested and stained with propidium iodide (PI). Dead target cells were detected as PI^+CFSE^+ cells using flow cytometry. Cytotoxicity, defined as the percent cytotoxicity in each sample, was calculated based on each E:T ratio. The dose-response curves of percent-specific lysis versus E:T ratios for each TDLN sample were evaluated.

Intracellular cytokine staining

Spleens were collected from the mice treated with the previously described agents. The spleens were minced over a 70-μm cell strainer, and the red blood cells were lysed using lysis buffer (Biolegend, San Diego). The splenocytes were stimulated with phorbol myristate acetate (50 ng/mL) and ionomycin (1 mmol/L) for 6 h in the presence of monensin (3.4 ng/mL) prior to staining[16]. The cells were stained with FITC-, PE-, and/or PE-cy5-conjugated mAb against CD4, IFN-γ and IL-4 (Dilution was 1:50) (Th1 cells: $CD4^+IFN\text{-}\gamma^+$ cells; Th2 cells: $CD4^+IL\text{-}4^+$ cells). Samples were determined by using a FACS Canto analyzer, and data were analyzed using CellQuest software (Becton Dickinson, San Joes, USA).

Flow cytometry

The lungs were perfused through the right ventricle with PBS, and whole lungs were then harvested and dissected into approximately 1-mm pieces. Single-cell suspensions were prepared with 2 mL of dispase containing collagenase (2 μg/mL) and DNase (50 μg/mL) for 30 min[17]. After red blood cell lysis, the digested lungs were resuspended in PBS and sequentially filtered through 70-μm filters. Each single-cell suspension was divided into three parts to analyze the number of cytotoxic T lymphocytes (CTL: $CD3^+CD4^-CD8^+$), regulatory T cells (Treg: $CD4^+CD25^+Foxp3^+$), and the M1 ($CD11b^+F4/80^+CD206^-$) and M2 ($CD11b^+F4/80^+CD206^+$) cells in the lung. The cells were incubated with saturated concentrations of FITC-, PE-, and/or PE-cy5-conjugated mAb against CD3, CD4, CD8, CD25, Foxp3, CD11b, F4/80, or CD206 (diluted 1:50 or 1:100). Isotype-matched mAbs were used in the control samples. $CD4^+$ and $CD8^+$ cells were gated from $CD3^+$ cells. $CD4^+CD25^+$ Tregs were gated from $Foxp3^+$ cells. M1 and M2 cells were gated from $CD11b^+$ cells. The data were analyzed using CellQuest software.

ELISA for cytokines in lung tissue

The right lung lobes were lysed in PBS supplemented with a complete protease inhibitor cocktail. The lung tissue homogenate was diluted with lysis buffer to a final protein concentration of 500 μg of protein per mL. The concentrations of IFN-γ and TGF-β1 in the lung were detected using ELISA kits in accordance with the manufacturer's instructions.

Statistical analysis

Differences between groups were assessed by ANOVA. Survival curves were compared by the log-rank test. Our results are presented as the means±standard error (SEM). P values < 0.05 were considered statistically significant.

Results

TLR2-neutralizing antibody and CpG ODN act in synergy to suppress metastasis and improve the survival rates of mice

Our group and others have previously reported that blocking TLR2 activity attenuates pulmonary metastasis by inhibiting the immunosuppressive tissue environment[12, 13]. We wondered if a combination of a TLR2-neutralizing antibody with a TLR9 agonist CpG ODN would exert increased inhibition of tumor metastasis. Lung metastasis was evaluated in mice 3 weeks after tail vein injections with B16 melanoma cells. The number of metastatic nodules in the lungs of mice in the combination treatment group was notably reduced in comparison with the mice treated with the CpG ODN or the TLR2-neutralizing antibody alone upon both visual (Figure 1A) and numerical analysis (Figure 1B). As shown in Figure 1B, the number of metastatic nodes in the lungs of mice treated with the CpG ODN plus the TLR2-neutralizing antibody was markedly attenuated compared with that of the IgG plus CpG ODN control group, the CpG ODN group and the TLR2-neutralizing antibody group. The number of metastatic nodes in the lungs of mice treated with either the CpG ODN or the TLR2-neutralizing antibody was also found to be significantly lower than that of the PBS group and the IgG plus CpG ODN control group. Consistent with these data, the average weight indices of the lungs of PBS-treated mice were markedly increased (15.3‰±1.8‰ *vs* 7.4‰±0.2‰, P<0.01), whereas the application of CpG ODN resulted in markedly decreased lung weight indices (11.6‰±0.7‰ *vs* 15.3‰±1.8‰, P<0.05). Further, the application of the TLR2-neutralizing antibody alone (10.5‰±0.6‰) or in combination with CpG ODN (7.8‰±0.4‰) efficiently attenuated the lung weight indicesas compared with the PBS group, the IgG plus CpG control group and the CpG ODN group. The average lung index of the mice that received combination therapy was found to be significantly lower than that of the anti-TLR2 group.

To compare the anti-metastatic efficacy of the CpG ODN, the TLR2-neutralizing antibody, and the combination of the CpG ODN and the TLR2-neutralizing antibody, animals in the individually treated groups were monitored for survival time after inoculation with B16 melanoma cells. As shown in Figure 1D, 50% of B16-bearing mice treated with PBS or IgG plus the CpG ODN died by the 29th day after tumor cell inoculation, and all died by the 35th or 36th day. The treatment of B16-bearing mice treated with the TLR2-neutralizing antibody increased the animals' survival rates (50% survival on the 35th day, 0% survival on the 42th day). For the mice treated with the CpG ODN alone, the survival rates decreased to 50% on the 32th day and to 0% on the 40th day. However, the treatment of B16-bearing mice with the CpG ODN plus the

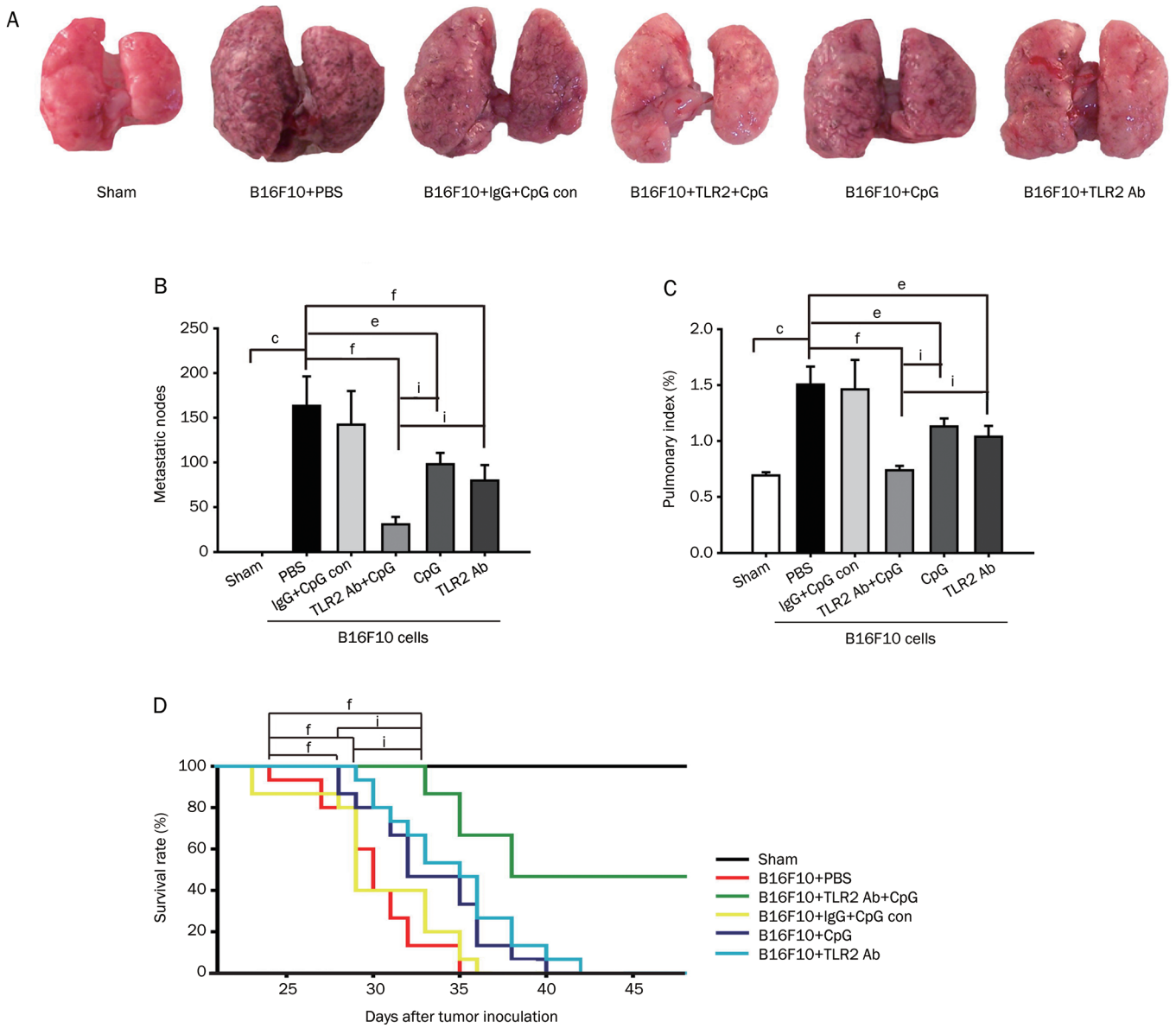

Figure 1. Blocking TLR2 and activating TLR9 markedly suppresses pulmonary metastasis of B16-F10 melanoma cells. (A) Representative lung samples. (B) The metastatic nodules were counted and data presented as the mean±SEM. *n*=15. (C) The pulmonary weight index of mice in the indicated treatment groups. Data are presented as mean±SEM. *n*=15 mice per group. (D) Kaplan-Meier graph representing the cumulative survival of mice in the indicated treatment groups. The data were analyzed using Kaplan-Meier survival analysis (*n*=15 per group). $^{c}P<0.01$ *vs* sham. $^{e}P<0.05$, $^{f}P<0.01$ *vs* PBS. $^{i}P<0.01$ *vs* anti-TLR2 plus CpG.

anti-TLR2 antibody markedly increased the survival rates and prolonged the survival time; 50% of the animals survived to the 38th day, and 45% of the mice in this group survived until the 48th day. Therefore, the combination of the TLR2-neutralizing antibody with the TLR9 agonist CpG ODN markedly improved the inhibition of pulmonary metastasis of B16F10 cells as compared with either individual treatment alone.

TLR2-neutralizing antibody and CpG ODN induce a synergistic cytotoxicity to B16 melanoma cells

To provide a biological explanation for the superior anti-metastatic effects of the combination regimen, we examined the cytotoxicity of immune cells in TDLNs from the mice treated with the single or combination regimens. Minimal cytotoxicity was detected in the PBS-treated, B16-bearing mice. The treatment of mice with the TLR2-neutralizing antibody or with the CpG ODN alone induced a moderate increase in the cytotoxicity of TDLN immune cells. A markedly enhanced cytotoxicity against B16F10 melanoma cells was detected in the TDLN immune cells of the mice treated with the combination regimen, indicating that the combination regimen induces synergistically enhanced tumor cytolysis activity (Figure 2A). We

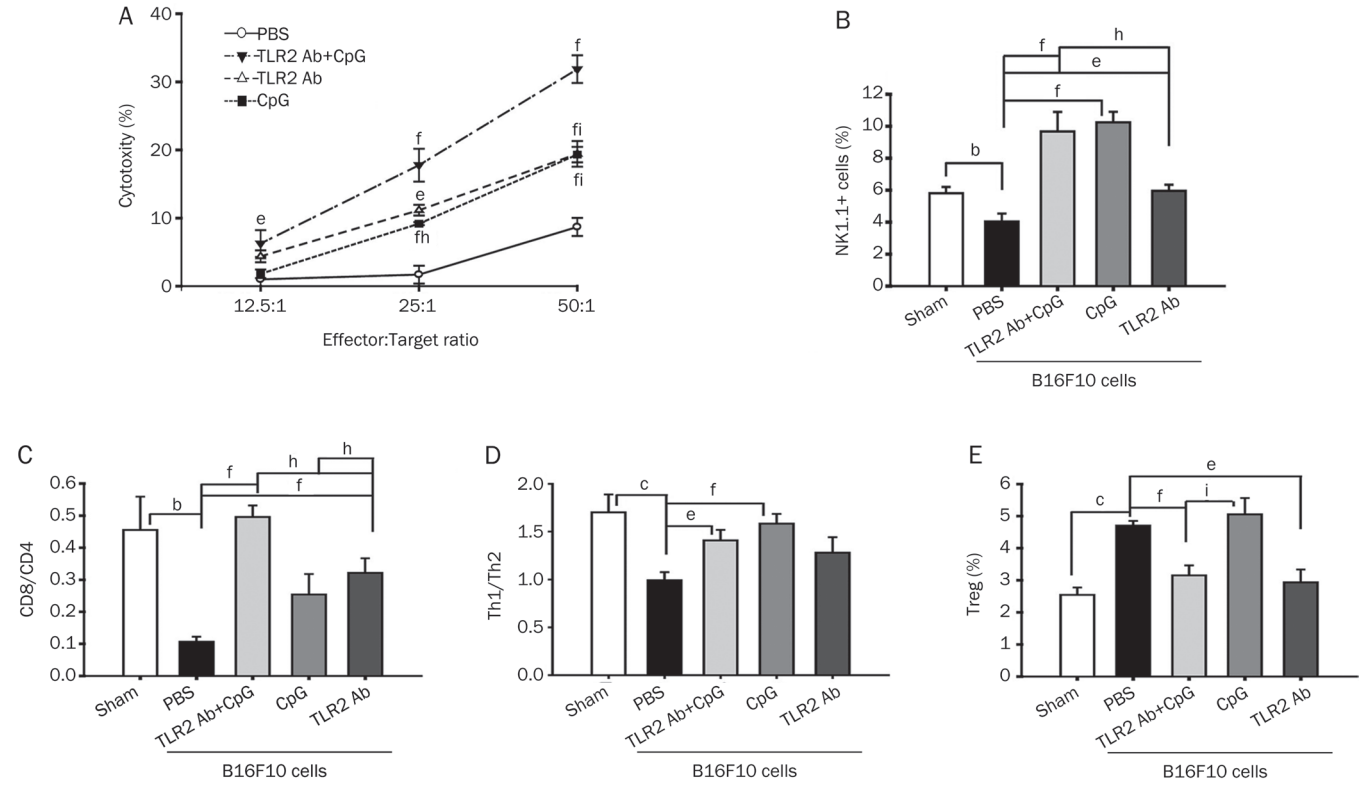

Figure 2. The combinational treatment increases the cytotoxicity of lymphocytes in TDLNs and increases the CD8/CD4 ratio in spleen. (A) Lymphocytes from B16 bearing mice showed the enhanced cytotoxicity after the combined treatment. Lymphocytes from TDLNs of mice with established B16 metastatic nodes were collected for evaluating the lystic activity to B16F10 cells *in vitro*. Data are presented as the mean ± SEM of 5 mice per group in triplicates. (B–E) The ratios of immune cells in spleen were regulated by the indicated immunotherapy. Splenocytes were isolated and collected for evaluating the amount of $NK1.1^+$ cells (B), the ratio of $CD3^+/CD8^+$ and $CD3^+/CD4^+$ T cells (C), the ratio of $CD4^+/IFN\text{-}\gamma^+$ and $CD4^+/IL\text{-}4^+$ T cells (D), and the percentage of $CD4^+/CD25^+$ regulatory T cells (E). Data are presented as the mean±SEM. of 5 mice per group in triplicates. $^bP<0.05$, $^cP<0.01$ *vs* sham. $^eP<0.05$, $^fP<0.01$ *vs* PBS. $^iP<0.01$ *vs* anti-TLR2 plus CpG.

then examined which immune cells induced the cytotoxicity in these animals. Inoculation of tumor cells resulted in decreases in the numbers of NK cells, the ratios of $CD8^+/CD4^+$ and the ratios of Th1/Th2 T cells in the mouse spleens. In comparison to the PBS treatment, the combination regimen and the CpG ODN treatment alone resulted in a 2- or 3-fold increase in the percentage of NK cells and $CD8^+$ T cells in the spleen, respectively. However, compared to the PBS treatment, the treatment of mice with the TLR2-neutralizing antibody alone resulted in only a moderate increase in the percentage of NK cells (6.0%±0.4% *vs* 9.7%±1.2%, $P<0.05$) and $CD8^+$ T cells (6.1%±1.0% *vs* 9.6%±0.9%, $P<0.05$) in the spleen (Figure 2B, 2C). However, treatment with the TLR2-neutralizing antibody alone or the combination regimen suppressed the proportion of tumor cell-induced $CD4^+$ T cells, while treatment with the CpG ODN alone enhanced the proportion of tumor cell-induced $CD4^+$ T cells (54.3%±7.9% *vs* 32.7%±2.6%, $P<0.05$). Therefore, the combination regimen synergistically increased the ratio of CD8/CD4 T cells in the spleen (Figure 2C).

Why did the CpG ODN treatment alone fail to induce an identical degree of tumor cell cytotoxicity as the combination treatment? We suspected that some fraction of the $CD4^+$ T cells induced by the CpG ODN suppressed the cytotoxicity of the NK cells and the $CD8^+$ T cells. Indeed, the CpG ODN treatment and the combination treatment decreased the frequency of Th2 cells induced by splenic tumor cells (Figure 2D). Treg cells represent a fraction of $CD4^+$ T cells that play a significant role in suppressing anti-tumor immunity. Inoculation of tumor cells resulted in a significant increase in the numbers of Tregs in the spleen. The anti-TLR2 antibody treatment alone and the combination therapy both suppressed the numbers of Tregs. However, the number of splenic Tregs in CpG ODN-treated mice was much higher than that of the anti-TLR2 antibody-treated or the combination regimen-treated mice (Figure 2E). These data indicate that the combination regimen produced greater tumor cell cytotoxicity compared with that of either single agent alone by inducing more NK and $CD8^+$ T cells while simultaneously reducing the numbers of Th2 cells and Tregs in the spleen.

Treatment with TLR2-neutralizing antibody plus CpG ODN enhances the antitumor immunity and reduces immune suppression in the tumor microenvironment

To find whether the differential immune responses induced by

the combination regimen or by either agent alone was responsible for the differences in metastasis suppression, we examined the lung infiltration of immune cells in animals treated with different agents. A suppressed immune response was observed in the lung tissues of the PBS-treated B16-bearing mice, with decreased infiltration of $CD3^+CD8^+$ T cells and M1 cells and increased infiltration of M2 cells and Treg cells (Figure 3A–3D). There was an increase in the lung infiltration of M1 cells, a decrease in the infiltration of M2 cells and no change in the infiltration of CTL (2.47%±0.68% *vs* 1.73%±0.28%, $P>0.05$) and Treg cells (3.35%±0.51% *vs* 4.25%±0.19%, $P>0.05$) in the CpG ODN treated mice compared to the PBS-treated mice. Treatment with the TLR2-neutralizing antibody alone or in combination with the CpG ODN significantly increased the lung infiltration of CTL and M1 cells (Figure 3A, 3B) and markedly decreased the infiltration of Treg and M2 cells (Figure 3C, 3D) as compared with the PBS treatment.

A number of studies indicate that IFN-γ can induce antitumor activity through STAT1 activation and autophagy induction[14, 18, 19]. By contrast, TGF-β1, IDO and COX2 are immunosuppressive factors that can promote tumor progression through the activation of Treg cells and suppression of T cell proliferation and responses[20]. As shown in Figure 4, there was a significant decrease in the expression of IFN-γ and a significant increase in the expression of TGF-β1, IDO and COX2 in the lung tissues of PBS-treated B16-bearing mice compared to normal mice. Treatment of mice with the CpG ODN plus the TLR2-neutralizing antibody (98.5±22.6 pg/mL), the CpG ODN alone (159.6±33.1 pg/mL) or the TLR2-neutralizing antibody alone (80.2±9.5 pg/mL) resulted in a significant increase in the expression of IFN-γ compared to PBS treatment (41.6±5.1 pg/mL) (Figure 4A). The treatment of mice with CpG ODN or the TLR2-neutralizing antibody alone did not result in any change in the expression of TGF-β1. However, the CpG ODN plus anti-TLR2 combination treatment (262.4±63.6 pg/mL) significantly reduced the expression of TGF-β1 in the lung tissues compared with the PBS treatment (668.2±112 pg/mL) and CpG ODN treatment (596.3±72.3 pg/mL) (Figure 4B). Furthermore, the expression of IDO and COX2 in the lung tissues from mice treated with the CpG ODN plus the anti-TLR2 antibody was markedly decreased compared with the PBS-treated, CpG ODN-treated and anti-TLR2-treated mice (Figure 4C and 4D). These data suggest that the combination regimen produces a synergistic anti-metastatic effect compared to treatment with the CpG ODN or the anti-TLR2 antibody alone by increasing anti-tumor factors and reducing pro-tumor factors in lung tissues.

Treatment with the TLR2-neutralizing antibody plus CpG ODN suppresses the spontaneous metastasis of Lewis lung carcinoma

To verify the antitumor effect of the TLR2-neutralizing antibody plus the CpG ODN, we examined whether this regimen could suppress the growth and spontaneous metastasis of Lewis lung carcinoma cells. Lewis lung carcinoma cells were transplanted into the right flanks of the mice. The chemotherapeutic agent CTX, used as positive control, inhibited the growth (1.5±0.2 *vs* 5.3±0.6 g, $P<0.001$) and spontaneous metastasis (5.6±1.7 *vs* 24.6±3.5, $P<0.001$) of the Lewis lung carcinoma cells (Figure 5A). As shown in Figure 5B, the average weight of the primary tumor 24 days post-inoculation was 5.3±0.6 g in the PBS-treated mice, 5.5±0.5 g in the isotype IgG plus CpG ODN control-treated mice, and 4.7±0.5 g in the mice treated with the TLR2-neutralizing antibody plus the CpG ODN ($P>0.05$) (Figure 5B). However, the number of metastatic

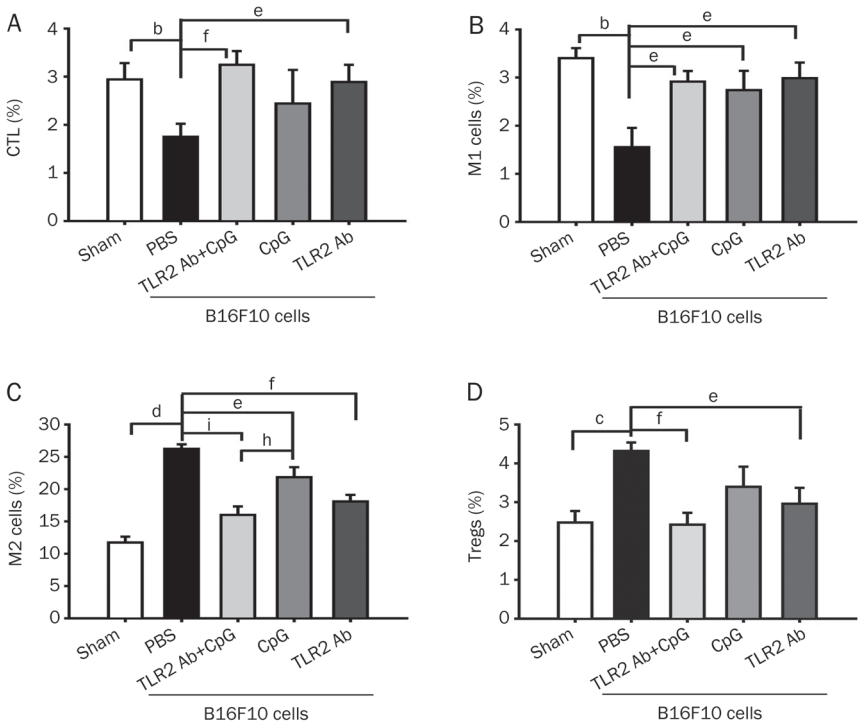

Figure 3. The combined therapy increases the infiltration of CTL and M1 cells and decreases the recruitment of M2 and Treg cells in lung tissues. Lung single-cell suspensions were obtained as indicated in the Methods. The number of CTL (A), M1 (B), M2 (C), and Treg (D) cells was analyzed by FCM. Data are presented as mean±SEM (n=5 mice per group). $^bP<0.05$, $^cP<0.01$ *vs* sham. $^eP<0.05$, $^fP<0.01$ *vs* PBS. $^hP<0.05$, $^iP<0.01$ *vs* anti-TLR2 plus CpG.

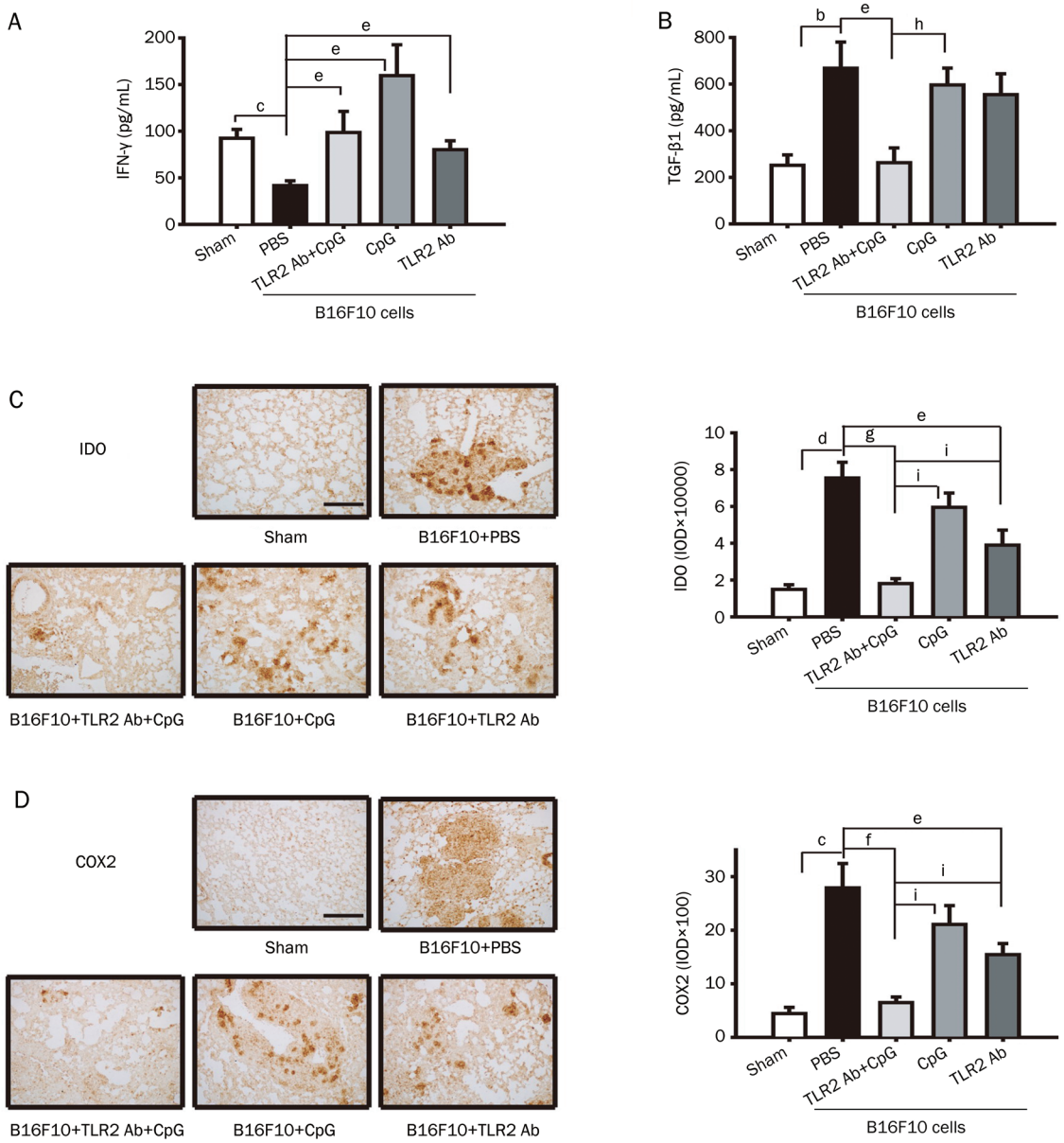

Figure 4. The combined treatment augments the expression of IFN-γ and attenuates the expression of TGF-β1, IDO, and COX2 in the lung tissues. Mice were sacrificed 3 weeks after B16 melanoma cells injection. (A–B) The expression of antitumor cytokines IFNγ and immunosuppressive factor TGF-β was detected in lung homogenates from mice using ELISA kits. Data are the mean±SEM. *n*=5. (C–D) The expression of IDO and COX2 was determined by immunohistochemistry. The IOD was analyzed by Image-Pro Plus image analysis software. The final IOD represents averages from 12 non-overlapping images of each lung specimen. Data are mean±SEM (*n*=6). $^{c}P<0.01$ *vs* sham. $^{e}P<0.05$, $^{f}P<0.01$ *vs* PBS. $^{h}P<0.05$, $^{i}P<0.01$ *vs* anti-TLR2 plus CpG.

nodes in the lungs of the mice treated with the TLR2-neutralizing antibody plus CpG ODN was markedly decreased by 53.3%±11.3% as compared with the PBS-treated and isotype IgG plus CpG ODN control-treated mice (Figure 5C). The lung index was also reduced in the combination-treated mice (Figure 5D). These results suggest that combining the TLR2-neutralizing antibody with the CpG ODN is not sufficient to attenuate the growth of established tumor but is efficient in the attenuation of tumor metastasis.

Discussion

The major finding of this study is that a rational combination of a TLR2-neutralizating antibody, which eliminates the inhibitory immune factors from tumor tissue, and the TLR9 agonist CpG ODN, which can increase the anti-tumor stimulatory factors, is more effective in inhibiting experimental and spontaneous metastasis than either agent alone. Indeed, the synergistic anti-metastatic effects of the two agents are the result of enhanced immune cytotoxicity against the tumor cells. This

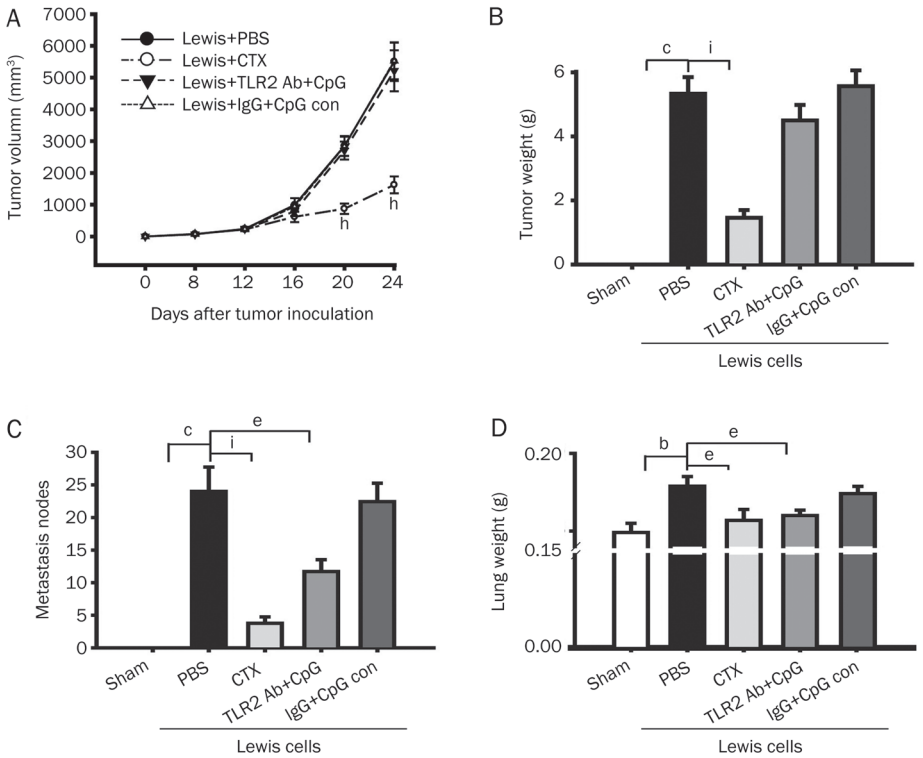

Figure 5. The combined therapy does not suppress the growth of primary tumor but attenuates the second pulmonary metastasis. (A) Primary tumor growth was monitored by counting the *size* of the external tumor lump every 4th day. (B) The tumor weight was monitored after mice were sacrificed. (C) The metastatic nodules were counted and data presented as the mean±SEM (n=15). (D) The pulmonary weight of mice in the indicated treatment groups. [b]P<0.05, [c]P<0.01 *vs* sham. [e]P<0.05, [f]P<0.01 *vs* PBS. [h]P<0.01, [i]P<0.01 *vs* anti-TLR2 plus CpG.

is reflected by numerous systemic and local changes in the immune responses: increases in the frequency of anti-tumor effector cell infiltration (such as NK, CTL, and M1 cells); decreases in the frequency of pro-tumor suppressor cell infiltration (such as Tregs, M2 cells); the enhanced expression of IFN-γ; and the downregulation of immunosuppressive factors including TGF-β1, IDO, and COX2. Treatment with either agent alone also induced a similar pattern of changes in the immune response, but the magnitudes observed were significantly less than those of the combination regimen. However, the combination regimen does not suppress tumor growth. This result may be due to the following: 1) the importance of TLR2 and TLR9 on host immune cells and tumor cells for positively modulating metastatic behavior compared to their minimal influence on primary subcutaneously implanted tumor growth[12, 13, 21, 22]; 2) the failure of the combination regimen to promote sufficient immune cell infiltration into the primary tumor to produce a potent cytotoxic suppression of tumor growth due to the anatomical site of administration[23]; 3) the inability of the therapeutic administration of the combination regimen to overcome the immunosuppressive barrier after the suitable microenvironment for tumor growth has been established[14].

The TLR9 agonist CpG ODN is a promising anti-cancer immunotherapy based on its ability to safely stimulate Th1-dominant innate and adaptive immunity in humans[7]. Nevertheless, tumors employ multiple means of suppressing or evading antitumor immunity[24] and cannot be overcome by the CpG ODN treatment alone. For example, the CpG ODN is a potent inducer of IL-10 from DCs and has been found to protect Streptozocin-induced autoimmune diabetes by the induction of IDO and Tregs[25]. Indeed, administration of the CpG ODN in the current study increased the frequency of NK and CTL cell infiltration, IFNγ secretion, and M1 cell differentiation but did not suppress the number of Tregs in the spleen. Further, the TLR9 agonist CpG ODN increased the expression of TGF-β1, IDO, and COX-2 and promoted the infiltration of Treg cells into the tumor microenvironment after tumor inoculation. The Tregs, other immune-suppressive cells, cytokines and enzymes subsequently counteract the initiation and perpetuation of antitumor cytotoxicity either by direct cell contact or by secreting suppressive cytokines. Thus, the cytotoxicity of the immune cells from CpG ODN-treated B16-bearing mice is diminished even though the numbers of NK and CTL cells are increased in the spleen. Xiong Z *et al* recently demonstrated that CpG ODN immunotherapy in a breast cancer model prevents but fails to entirely eradicate established brain metastases despite a significant increase in brain-infiltrating T and natural killer cells in treated mice relative to saline controls[26]. These findings indicate that CpG ODN treatment alone can stimulate anti-tumor effectors but fails to reverse the immunosuppressive responses in the tumor microenvironment. Therefore, the anti-metastatic activity of CpG ODN monotherapy is limited.

TLR2 is an unique member of the TLR family because it triggers an immunosuppressive response *in vivo*[27]. Activation of TLR2 promotes IL-10 production by innate immune cells *in vitro* and results in the proliferation of Tregs *in vitro* and *in vivo*[28]. Treg numbers in the circulation of TLR2-deficient mice are reduced compared with their WT littermate controls[10].

Furthermore, the activation of the TLR2 signal may be crucial for tumor cells to escape killing by the host[29]. Huang *et al* recently found that activation of TLR2 on cancer cells by Listeria monocytogenes promotes tumor growth[30], while Kim *et al* reported that activation of TLR2 by an extracellular matrix proteoglycan versican of Lewis lung carcinoma stimulates pro-tumor inflammation and metastasis[13]. We recently demonstrated that the level of TLR2 expressed on B16F10 melanoma cells determines their invasive activity in response to the endogenous factors released from tumor cells[12]. However, contradictory observations by others indicate that TLR2 activation is able to induce inflammatory cytokines and activate NK cells *in vitro* and *in vivo* and protect mice from tumor development and progression[31, 32]. In the current study, we find that blocking TLR2 effectively reverses the immunosuppressive characteristics of the microenvironment by suppressing the expression of TGF-β1, IDO, and COX2 and attenuating the infiltration of M2 and Tregs cells. This scenario is an example of how immunotherapy is able to break self-tolerance by depleting immunosuppressive factors in the tumor microenvironment to generate effective anti-tumor immunity.

In summary, our studies indicate that developing an optimal immunotherapeutic strategy in which combining an immune stimulator with an agent eliminating inhibitory immune factors is critical for obtaining a desired therapeutic effect against tumor metastasis. Our studies provide novel insights into the development of the rational immunotherapeutic strategies against cancer.

Acknowledgements

This study was supported by grants from the Creation of Major New Drugs (2009ZX09301-003-13; 2009ZX09301-003-9-1), the National Natural Science Foundation of China (30973557), and the PhD. Programs Foundation of the Ministry of Education of China (20070023035).

Author contribution

Jun YAN and Fang HUA designed and performed most of the experiments, analyzed and interpreted the data and contributed to writing the manuscript; Hong-zheng YANG and Hanzhi LIU performed and analyzed individual experiments; and Zhuo-wei HU conceived the project, designed and interpreted experiments and modified and edited the manuscript.

References

1 King J, Waxman J, Stauss H. Advances in tumour immunotherapy. QIM 2008; 101: 675–83.
2 Lasaro MO, Ertl HC. Targeting inhibitory pathways in cancer immunotherapy. Curr Opin Immunol 2010; 22: 385–90.
3 Curiel TJ. Tregs and rethinking cancer immunotherapy. J Clin Invest 2007; 117: 1167–74.
4 Rüttinger D, Winter H, van den Engel NK, Hatz R, Jauch KW, Fox BA, *et al*. Immunotherapy of cancer: key findings and commentary on the Third Tegernsee Conference. The Oncologist 2010; 15: 112–8.
5 Kawai T, Akira S. The role of pattern-recognition receptors in innate immunity: update on Toll-like receptors. Nat immunol 2010; 11: 373–84.
6 de Visser KE, Eichten A, Coussens LM. Paradoxical roles of the immune system during cancer development. Nat Rev Cancer 2006; 6: 24–37.
7 Krieg AM. Development of TLR9 agonists for cancer therapy. J Clin Invest 2007; 117: 1184–94.
8 Schmidt C. Clinical setbacks for toll-like receptor 9 agonists in cancer. Nat Biotechnol 2007; 25: 825–6.
9 Kopfstein L, Christofori G. Metastasis: cell-autonomous mechanisms versus contributions by the tumor microenvironment. Cell Mol Life Sci 2006; 63: 449–68.
10 Huang B, Zhao J, Unkeless JC, Feng ZH, Xiong H. TLR signaling by tumor and immune cells: a double-edged sword. Oncogene 2008; 27: 218–24.
11 Zanin-Zhorov A, Cahalon L, Tal G, Margalit R, Lider O, Cohen IR. Heat shock protein 60 enhances $CD4^+$ $CD25^+$ regulatory T cell function via innate TLR2 signaling. J Clin Invest 2006; 116: 2022–32.
12 Yang HZ, Cui B, Liu HZ, Mi S, Yan J, Yan HM, *et al*. Blocking TLR2 activity attenuates pulmonary metastases of tumor. PloS One 2009; 4: e6520.
13 Kim S, Takahashi H, Lin WW, Descargues P, Grivennikov S, Kim Y, *et al*. Carcinoma-produced factors activate myeloid cells through TLR2 to stimulate metastasis. Nature 2009; 457: 102–6.
14 Yan J, Wang ZY, Yang HZ, Liu HZ, Mi S, Lv XX, *et al*. Timing is critical for an effective anti-metastatic immunotherapy: the decisive role of IFNgamma/STAT1-mediated activation of autophagy. PloS One 2011; 6: e24705.
15 Russell JH, Ley TJ. Lymphocyte-mediated cytotoxicity. Annu Rev Immunol 2002; 20: 323–70.
16 Molavi O, Ma Z, Hamdy S, Lai R, Lavasanifar A, Samuel J. Synergistic antitumor effects of CpG oligodeoxynucleotide and STAT3 inhibitory agent JSI-124 in a mouse melanoma tumor model. Immunol Cell Biol 2008; 86: 506–14.
17 Huffnagle GB, Lipscomb MF, Lovchik JA, Hoag KA, Street NE. The role of $CD4^+$ and $CD8^+$ T cells in the protective inflammatory response to a pulmonary cryptococcal infection. J Leukoc Biol 1994; 55: 35–42.
18 Martini M, Testi MG, Pasetto M, Picchio MC, Innamorati G, Mazzocco M. IFN-gamma-mediated upmodulation of MHC class I expression activates tumor-specific immune response in a mouse model of prostate cancer. Vaccine 2010; 28: 3548–57.
19 Dunn GP, Koebel CM, Schreiber RD. Interferons, immunity and cancer immunoediting. Nat Rev 2006; 6: 836–48.
20 Muller AJ, Scherle PA. Targeting the mechanisms of tumoral immune tolerance with small-molecule inhibitors. Nat Rev Cancer 2006; 6: 613–25.
21 Xie W, Wang Y, Huang Y, Yang H, Wang J, Hu Z. Toll-like receptor 2 mediates invasion via activating NF-kappaB in MDA-MB-231 breast cancer cells. Biochem Biophys Res Commun 2009; 379: 1027–32.
22 Wang C, Cao S, Yan Y, Ying Q, Jiang T, Xu K, *et al*. TLR9 expression in glioma tissues correlated to glioma progression and the prognosis of GBM patients. BMC Cancer 2010; 10: 415.
23 Nierkens S, den Brok MH, Roelofsen T, Wagenaars JA, Figdor CG, Ruers TJ, *et al*. Route of administration of the TLR9 agonist CpG critically determines the efficacy of cancer immunotherapy in mice. PloS One 2009; 4: e8368.
24 Yu H, Kortylewski M, Pardoll D. Crosstalk between cancer and immune cells: role of STAT3 in the tumour microenvironment. Nat Rev Immunol 2007; 7: 41–51.
25 Fallarino F, Volpi C, Zelante T, Vacca C, Calvitti M, Fioretti MC, *et al*. IDO mediates TLR9-driven protection from experimental autoimmune diabetes. J Immunol 2009; 183: 6303–12.
26 Xiong Z, Gharagozlou S, Vengco I, Chen W, Ohlfest JR. Effective CpG

immunotherapy of breast carcinoma prevents but fails to eradicate established brain metastasis. Clin Cancer Res 2008; 14: 5484–93.

27 Netea MG, Van der Meer JW, Kullberg BJ. Toll-like receptors as an escape mechanism from the host defense. Trends Microbiol 2004; 12: 484–8.

28 Yamazaki S, Okada K, Maruyama A, Matsumoto M, Yagita H, Seya T. TLR2-dependent induction of IL-10 and Foxp3$^+$ CD25$^+$ CD4$^+$ regulatory T cells prevents effective anti-tumor immunity induced by Pam2 lipopeptides *in vivo*. PloS One 2011; 6: e18833.

29 Rüttinger D, Winter H, van den Engel NK, Hatz R, Jauch KW, Fox BA, *et al*. Immunotherapy of cancer: key findings and commentary on the third Tegernsee conference. Oncologist 2010; 15: 112–8.

30 Xiong Z, Gharagozlou S, Vengco I, Chen W, Ohlfest JR. Effective CpG immunotherapy of breast carcinoma prevents but fails to eradicate established brain metastasis. Clin Cancer Res 2008; 14: 5484–93.

31 Huang B, Zhao J, Shen S, Li H, He KL, Shen GX, *et al*. Listeria monocytogenes promotes tumor growth via tumor cell toll-like receptor 2 signaling. Cancer Res 2007; 67: 4346–52.

32 Lu H, Yang Y, Gad E, Wenner CA, Chang A, Larson ER, *et al*. Polysaccharide krestin is a novel TLR2 agonist that mediates inhibition of tumor growth via stimulation of CD8 T cells and NK cells. Clin Cancer Res 2010; 17: 67–76.

33 Lowe EL, Crother TR, Rabizadeh S, Hu B, Wang H, Chen S, *et al*. Toll-like receptor 2 signaling protects mice from tumor development in a mouse model of colitis-induced cancer. PloS One 2010; 5: e13027.

Acta Pharmacologica Sinica (2012) 33: 513–522
 1671-4083/12 $32.00
www.nature.com/aps

Original Article

Lentivirus-mediated RNA silencing of c-Met markedly suppresses peritoneal dissemination of gastric cancer *in vitro* and *in vivo*

Xiao-lei WANG[1, *], Xi-mei CHEN[1], Jian-ping FANG[2], Chang-qin YANG[1]

[1]*Department of Gastroenterology, Institute of Digestive Disease, Tongji Hospital affiliated to Tongji University, Shanghai 200065, China;*
[2]*Department of Pathology, Tongji Hospital affiliated to Tongji University, Shanghai 200065, China*

Aim: To investigate the expression of c-Met in peritoneal free cancer cells isolated from human gastric cancer ascites, and its relationship to peritoneal dissemination of gastric cancer.
Methods: Peritoneal free cancer cells (PFCCs) were isolated from ascites specimens of gastric cancer patients. c-Met expression in PFCCs was detected with immunocytochemistry. In human gastric cancer cell line SGC7901, c-Met expression was detected using RT-PCR and Western blot, and was suppressed with lentivirus-mediated RNAi. The proliferation of SGC7901 cells was measured using MTT assay, and the invasion ability was detected with invasion assay. The adhesion of SGC7901 cells to peritoneum was observed in human peritoneal mesothelial cells (HPMCs) monolayer *in vitro* and in mice *in vivo*.
Results: PFCCs were isolated from ascites of 6 out of 10 gastric cancer patients. c-Met expression in PFCCs was detected in 5 of the 6 gastric cancer patients. In SGC7901 cells, Lentivirus-mediated RNAi significantly reduced both c-Met mRNA and protein expression, which resulted in suppressing the cell proliferation, invasion and adhesion to peritoneum. The expression of α3β1 integrin and E-cadherin was significantly inhibited in SGC7901 cells transfected with Lenti-miRNAc-Met. In the peritoneal dissemination model of gastric cancer, intraperitoneal injection of Lenti-miRNAc-Met markedly suppressed the tumor progression of SGC7901 cells.
Conclusion: c-Met is expressed in PFCCs from the ascites of gastric cancer patients. Down-regulation of c-Met expression markedly suppresses the multistep process of peritoneal dissemination, thus may be a potential target for the treatment of gastric cancer.

Keywords: gastric cancer; peritoneal free cancer cell; ascites; peritoneal dissemination; c-Met; lentivirus; RNA interference

Acta Pharmacologica Sinica (2012) 33: 513–522; doi: 10.1038/aps.2011.205; published online 12 Mar 2012

Introduction

Peritoneal metastasis frequently occurs in patients with gastric cancer and is associated with a poor prognosis. Despite advances in chemotherapy, including neoadjuvant intraperitoneal systemic chemotherapy for peritoneal dissemination of gastrointestinal cancers, the results are unsatisfactory, and a standard and effective treatment has not been developed.

The establishment of peritoneal dissemination is a multistep process that includes the detachment of cancer cells from primary cancer, the adhesion and interaction of peritoneal free cancer cells (PFCCs) and mesothelial cells on the peritoneal surface, the penetration of free cancer cells into the submesothelial space, the attachment of cancer cells to the exposed submesothelial basement membrane, and the invasion of the peritoneal-blood barrier finally[1]. Many molecules are involved in this process. For example, E-cadherin is the key molecule for detachment[2]. CD44 is considered important for the adhesion and interaction between cancer cells and mesothelial cells[3]. Integrins, a family of adhesion receptors consisting of 18 α and 8 β subunits that form 24 distinct integrins, mediate cell-cell and cell-extracellular matrix (ECM) connections and are involved in the penetration of cancer cells into the submesothelial basement membrane[4, 5].

Recently, c-Met, a receptor tyrosine kinase, and its ligand, hepatocyte growth factor (HGF), have become leading candidates for molecular targeted cancer therapies[6] with the potential to block peritoneal metastasis. c-Met and HGF participate in most stages of malignant progression, including adhesion, degradation of ECM, promotion of cell mobility and the interaction between cancer cells and peritoneal mesothelial cells. Thus, integrins are involved with adhesion, invasion, dissemination and metastasis[6]. Many human cancers, includ-

* To whom correspondence should be addressed.
E-mail xlwang2006@163.com
Received 2011-09-28 Accepted 2011-12-19

ing ovarian cancer[7], gastric cancer[8], esophageal adenocarcinoma[9], and colorectal cancer[10], have c-Met overexpression in the primary cancer tissues, which is also associated with poor outcome. Moreover, an effective therapy which targeted c-Met *in vivo* demonstrated the ability to inhibit peritoneal dissemination and invasion in ovarian cancer xenografts[11]. The measurement of c-Met expression level in tissues is crucial to predict the treatment response to inhibitors. PFCCs are considered to play a key role in the process of peritoneal metastasis in gastric cancer, and the molecules expressed on the surface of PFCCs usually provide important clues for targeted therapy[12]. However, only approximately 10% of the malignant cells in the peritoneal cavity or ascites are detected by conventional methods. According to previous reports, immunomagnetic separation can efficiently improve the detection of rare free malignant cells in fluid and blood specimens[13, 14] and, thus, has the ability to study c-Met expression on PFCCs.

RNAi has been widely used as a powerful tool in gene function studies and as a potential treatment model for human cancers. miRNAs are members of a class of small regulatory RNAs and are targets of novel anticancer gene therapy by antisense molecules that can inhibit mRNA activity by mRNA cleavage or translational repression[15]. In this paper, we present a preliminary study on c-Met expression in PFCCs from gastric cancer patients and demonstrate a successful long-term efficient lentiviral miRNA (lenti-miRNA) system for silencing c-Met expression in the SGC7901 human gastric cancer cell line. We also evaluate c-Met as a therapeutic target in the treatment of gastric cancer peritoneal dissemination.

Materials and methods

Immunomagnetic isolation of PFCCs in ascites from gastric cancer patients

PFCCs from ascites of gastric cancer patients were isolated by the magnetic activated cell sorting (MACS) method. Briefly, ascites specimens were collected sterilely at the time of initial diagnosis, as confirmed by biopsy pathology, from 10 primary gastric cancer patients (Table 1). Samples and clinical data were collected after informed consent was obtained. The ascites samples were centrifuged into pellets and resuspended in 10 mL of phosphate-buffered saline (PBS) supplemented with 0.5% bovine serum albumin (BSA). The red blood cells (RBCs) were lysed with fresh lysing buffer with a volume ratio of 1:5. The manufacturer's instructions (Miltenyi Biotec, Germany) for MACS were followed for cancer cell enrichment. Mononuclear cells (MNCs) were recovered by centrifugation (200×*g*, 10 min) through a Ficoll density gradient according to the manufacture's protocol. Next, 20 μL FcR blocking reagent (Miltenyi Biotec) was added to block unspecific binding of MNCs to the microbeads. Anti-EpCAM conjugated with phycoerythrin (PE) monoclonal antibody (mAb) (Miltenyi Biotec) was incubated with the cells at a dilution of 1:10. Human peritoneal mesothelial cells (HPMCs) were labeled by anti-CD45 conjugated with fluorescein isothiocyanate (FITC) (Beijing CellChip Biotechnology Co, Ltd, China). The cells were incubated with 20 μL anti-PE microbeads for 15 min on ice and then resuspended in 80 μL MACS buffer. The magnetically labeled cells were washed with 1.5 mL MACS buffer and passed through a magnetic separation column (Miltenyi Biotec). The column was removed from the separator, and the positive fraction was eluted with the plunger supplied.

Table 1. PFCCs isolated by MACS and the c-Met/CK20 expression in the ascites of ten gastric cancer patients.

Patient No	Histological type	PFCCs	c-Met expression	CK20 expression
1	Adenocarcinoma	Positive	Positive	Positive
2	Signet-ring cell carcinoma	Negative	–	Negative
3	Adenocarcinoma	Negative	–	Negative
4	Adenocarcinoma	Negative	–	Negative
5	Adenocarcinoma	Positive	Positive	Positive
6	Signet-ring cell carcinoma	Negative	–	Negative
7	Adenocarcinoma	Positive	Positive	Positive
8	Signet-ring cell carcinoma	Positive	Negative	Positive
9	Adenocarcinoma	Positive	Positive	Positive
10	Adenocarcinoma	Positive	Positive	Positive

Immunocytochemistry (ICC)

Each isolated cell sample underwent routine hematoxylin-eosin (HE) staining to observe cell morphology under a light microscope. Expressions of CK20 and c-Met were evaluated by immunocytochemical staining using streptavidin-biotin-peroxidase method in a cellular smear. First, cells were fixed in 4% paraformaldehyde. Next, primary anti-human CK20 (1:100) and c-Met (1:100) antibodies were incubated with the cells for 2 h at room temperature. The procedure was performed according to the manufacturer's instructions utilizing the horseradish peroxidase (HRP) immunohistochemistry (IHC) kit (Chemicon International Inc, Temecula, CA, USA). Cytoplasmic and/or cytomembrane immunostaining was considered positive. Negative control samples were processed similarly in the absence of primary antibody. The standard for assessment of malignancy was according to cytomorphology. The malignant cells were verified via light microscope criteria based on HE staining, including cellular pleomorphism, an altered nucleus and hyperchromasia.

Cell line and cell culture

The human gastric cancer cell line SGC7901 was obtained from Type Culture Collection of the Chinese Academy of Sciences (Institute of Biochemistry and Cell Biology, Shanghai, China). The tumor cells were cultured in RPMI-1640 media (PAA Laboratories GmbH, Austria) supplemented with 10% fetal calf serum (FCS) and penicillin (100 U/mL)/streptomycin (100 μg/mL) in an atmosphere of 37 °C in 5% CO_2.

HPMCs were obtained following informed consent from the omental tissue of patients who underwent abdominal surgery for benign conditions. The HPMCs were isolated according to methods previously reported[11]. Briefly, the resected omental

tissue was incubated in the presence of 0.25% trypsin/0.01% EDTA at 37 °C for 20 min. The detached HPMCs were then cultured in RPMI-1640 media (PAA Laboratories GmbH, Austria) supplemented with 20% FCS, penicillin (100 U/mL)/streptomycin (100 μg/mL), 0.4 mg/L hydrocortisone and 5 mg/L insulin in fibronectin-coated tissue culture flasks at 37 °C in a humid atmosphere of 5% CO_2. Cells were used for experiments following 3 rounds of passage.

Recombinant plasmid construction, lentivirus production and transduction

All the procedures were performed according to the BLOCK- iT™ Pol II miR RNAi Expression Vector Kit and the Lentiviral Pol II miR RNAi Expression System (Invitrogen, Carlsbad, CA, USA). Four pairs of miR-155-based c-Met targeting sequences (64 bp) and a negative control sequence were designed using the Invitrogen RNAi Designer (www.invitrogen.com/rnaiexpress). The engineered pre-miRNA sequence structure was based on the murine miR-155 sequence, and synthesized double oligonucleotides were cloned into the pcDNA6.2-GW/EmGFP/miR plasmid (Invitrogen) to produce the recombinant plasmids containing either the c-Met miRNA insert (pCMV-c-Met miRNA-825, pCMV-c-Met miRNA-1872, pCMV-c-Met miRNA-3409, and pCMV-c-Met miRNA-4339) or the negative control (pCMV-c-Met miRNA-neg). Each purified expression plasmid was transfected into the SGC7901 cells. RT-PCR and Western blot analysis were performed to assess the efficiency of c-Met knockdown at 48 h post-transfection.

The lentiviral miRNA system based on the above vectors was generated. The third generation self-inactivating lentivirus vector, pLenti6/V5-DEST containing a CMV-driven EGFP reporter and a SV40 promoter upstream of the cloning sites for high-level expression of miRNA was used. The constructed functional pre-miRNA expression cassette targeting c-Met was transferred into the destination vector (pLenti6/V5-DEST) to generate the lentiviral expression vector (Lenti-c-MetmiRNA) or the negative control vector (Lenti-c-MetmiRNA-neg). The recombinant lentivirus and the control lentivirus were produced by co-transfecting 293FT cells with the transfer vector and the 3 packaging vectors. The virus-containing supernatant was harvested 72 h post-transfection. The prepared SGC7901 cells were transduced with the lentiviral expression vectors (Lenti-c-MetmiRNA or Lenti-c-MetmiRNA-neg). At 48 h after transduction, the knockdown of c-Met was evaluated by Western blot analysis. Stable cell lines were obtained after selection by long-term culture in medium containing 4 μg/mL blasticidin for 12 d.

Proliferation assay

Cell proliferation was evaluated by 3-(4,5-dimethylthiazol-2-yl)-2,5-diphenyltetrazolium bromide (MTT, Sigma, USA) assay. Cells were seeded at a density of 5×10^3 in 96-well plates in Dulbecco's modified Eagle's medium (DMEM) containing 10% FCS in a final volume of 100 μL. After incubation for 18 h, the cells grew to approximately 85% confluency, and then were transduced with the lentivirus (50 μL/well). At 24, 48, 60, and 96 h post-transduction, an MTT assay was performed. Cells were incubated in the presence of MTT (20 μL/well of 5 g/L solution in sterile PBS) for 4 h at 37 °C. The assay was read by determination of the reaction product at 490 nm by using a microplate reader (Multiskan MK3, Thermo Labsystems, Finland).

Invasive assay

The ability of cells to invade through ECM was assessed using the Chemicon QCM 96-well Invasion Assay Kit (ECM555, CHEMICON, International, CA, USA). Cells (3×10^6) were harvested with trypsin/EDTA, and suspended in PRMI-1640 media with 0.5% FBS. The invasive assay was performed according to the manufacturer's instructions. Briefly, the invasive gastric cancer cells, which migrated through the ECM layer and attached to the bottom of the polycarbonate membrane, were dissociated from the membrane after incubation with the Cell Detachment Solution for 30 min at 37 °C. Next, 50 μL of lysis buffer/CyQuant GR Dye Solution (1:75) was added to each well and incubated for 15 min at room temperature. Finally, 150 μL of the mixture was transferred to a new 96-well plate, and the fluorescence value was detected with a fluorescence plate reader using 480 nm/520 nm filter set. As a negative control, Cell Detachment Solution in the absence of SGC7901 cells was used.

Adhesion of gastric cancer cells to a HPMCs monolayer *in vitro*

Tumor cells were fluorescently labeled with 5 μmol/mL BCECF/AM (Biotium, Hayward, CA, USA). HPMCs (1.5×10^4 cells/well) were cultured in 96-well plates, which were precoated with 0.1% gelatin, until confluent. SGC7901 cells (3×10^4) were resuspended in 200 μL medium and added to each well. The plates were incubated for 60 min at 37 °C. The number of adhesive cells was quantified by measuring the fluorescence intensity on a Perkin Elmer plate reader (CA, USA) with 488 nm excitation and 535 nm emission filters.

Adhesion of gastric cancer cells to mice peritoneum *in vivo*

Six-week-old BALB/c athymic female nude mice (Shanghai Laboratory Animal Center, Shanghai, China) were used in this study. The mice were divided into three groups (10 mice per group): SGC7901, Lenti-miRNAc-Met and Lenti-miRNAc-Met-neg. Cultured tumor cells, fluorescently labeled as above, were injected at a concentration of 2×10^6/mL into the mice peritoneal cavity in a final volume of 1 mL. After 4 h, mice were sacrificed, and the full peritoneum was cut into 1 cm^2 pieces and placed in a 24-well culture plate in DMEM containing 10% FCS. Adherent cells were lysed with 1% NP-40, and the fluorescence intensity was measured. All animal experiments were conducted in accordance with the Guidelines for the Care and Use of Laboratory Animals of Tongji University.

Reverse transcription-PCR (RT-PCR)

Total RNA was extracted with TRIzol Reagent (Invitrogen). PCR was performed using the RT-PCR Kit (Toyobo, Japan)

with 5 μg total RNA to synthesize cDNA. The primers of c-Met were 5′-CCTGCGAAGTGAAGGGTCTCC-3′ (forward primer) and 5′-CTGGCAGCTTTGCACCTGTTT-3′ (reverse primer). GAPDH was used as an internal control. The primers of human GAPDH were 5′-ACCACAGTCCATGCCATCAC-3′ (forward primer) and 5′-TCCACCACCCTGTTGCTGTA-3′ (reverse primer). PCR was performed in 30 μL of reaction mixture. Thermal cycle conditions were conducted with preamplification denaturation at 95 °C for 3 min, followed by 30 cycles of denaturation at 95 °C for 20 s, annealing at 62 °C for 20 s, and extension at 72 °C for 30 s, with a final extension at 72 °C for 3 min. For the semi-quantification, an image of the gel was captured, and the intensity of the bands was quantified by gel analysis system (Bio-Rad, USA).

Western blot analysis

SGC7901 cells (5×10^6) were collected and lysed in cold PBS with 0.5% NP-40 and a protease inhibitor cocktail (Novogen, Australia). Whole-cell proteins were extracted using the Whole Cell Extraction Kit (Chemicon). Protein concentrations were determined according to the manufacturer's instructions of the BCA (bicinchoninic acid) Protein Assay Kit (Pierce, Rockford, USA). Samples were equalized, and 40 mg of total protein for each sample was loaded into separate lanes on a 12% SDS-PAGE and transferred onto a nitrocellulose membrane (Invitrogen). Western blot analysis was performed using primary antibody for c-Met (1:100 dilution, Santa Cruz Biotechnology, CA, USA). Protein expression was quantified by densitometry and normalized to β-actin (1:100, Santa Cruz) expression using enhanced chemiluminescence (Pierce, Rockford, IL, USA).

Adhesion molecule expression as detected by flow cytometry (FCM)

Tumor cells (3×10^6) were incubated with primary antibodies (Integrin β1 1.5 μg, E-cadherin 1.5 μg, CD44 0.75 μg, Biolegend, San Diego, CA, USA) for 30 min at 4 °C. PE-labeled secondary antibody was added and incubated for 30 min. Additionally, the primary antibody PE-α3-integrin (BioLegend, San Diego, CA, USA) was incubated with tumor cells for 30 min. Next, cells were resuspended in 500 μL of 1% BSA/PBS. Fluorescence expressions on cells surface were quantitatively analyzed with a FACSCalibur (Becton-Dickinson, San Jose, USA). Cells incubated in the absence of primary antibody were set as a blank, and those incubated in the isotype-specific hamster IgG1-PE were set as a negative control to eliminate nonspecific staining.

In vivo studies of peritoneal dissemination model in nude mice

BALB/c female nude mice (5–6 weeks of age) were purchased from the Shanghai Laboratory Animal Center (Shanghai, China). Thirty mice were allocated to three groups (10 mice per group): SGC7901 (group A), Lenti-miRNAc-Met-neg (group B) and Lenti-miRNAc-Met (group C). Suspensions of tumor cells (1×10^7 cells) in 1 mL RPMI-1640 media were injected into the peritoneal cavity of the mice for incubation. On d 30, all thirty mice were sacrificed.

To evaluate further the treatment effect of Lenti-miRNAc-Met, another 45 nude mice were allocated to three groups as above (15 mice per group). In the PBS group, 4 mL PBS was injected into the peritoneal cavity of each mouse. In the Lenti-miRNAc-Met-neg group, 5×10^7 copies/4 mL of Lenti-miRNAc-Met-neg was injected in each mouse intraperitoneally (ip). In the Lenti-miRNAc-Met group, 5×10^7 copies/4 mL of Lenti-miRNAc-Met was injected in each mouse ip. Three days postinoculation, 1×10^7 SGC7901 cells in 1 mL PBS were injected into each mouse ip. On d 30, 10 mice from each group were sacrificed. The remaining five mice in each group were used to evaluate the survival up to d 120. The macroscopic nodules on peritoneal surface were counted, and tumor size of large nodules that exceeded 1.0 cm in diameter was calculated by assuming a spherical shape. The fused nodules were counted as a single nodule. All animal experiments were conducted in accordance with the Guidelines for the Care and Use of Laboratory Animals of Tongji University.

Statistical analysis

Statistical analysis was performed using the Statistics Package for the Social Science software (version 11.5; SPSS Inc, Chicago, IL, USA). The comparison between different groups was analyzed by the Independent Samples *t* Test or the Mann-Whitney Test. Survival curves were obtained using the Kaplan-Meier method and compared by the log-rank test. All the statistical analysis was two sides with significance defined as $P<0.05$.

Results

Expression of c-Met in the PFCCs

PFCCs were found utilizing MACS in the ascites of 6 out of 10 gastric cancer patients. PFCCs had an increased nucleus: cytoplasm ratio with nuclear hyperchromasia observed by light microscope (Figure 1Aa). CK20-positive expression verified their epithelial origin, notably from gastrointestinal tract (Figure 1Ab). c-Met expression was detected in the PFCCs of 5 patients (Figure 1Ac).

Lentivirus-mediated RNAi significantly inhibited c-Met expression in SGC7901 cells

Four recombinant expression plasmids targeting c-Met were constructed. The mRNA and protein expression levels of c-Met in SGC7901 cells were examined by RT-PCR and Western blot analysis at 48 h post-transfection. As shown in Figure 1B and 1C, when compared with the parental SGC7901 cells, the negative control did not affect the expression levels of c-Met, whereas pCMV-c-MetmiRNA-825 resulted in the decrease of both c-Met mRNA and protein levels. Specifically, c-Met mRNA expression was reduced by 80%–83%, while c-Met protein expression was reduced by 88%–90% in pCMV-c-MetmiRNA-825 transfected cells.

The recombinant expression plasmid pCMV-c-Met-miRNA-825 was inserted into pLenti6/V5-DEST destination vector to develop a Lenti-miRNA expression vector. We infected SGC7901 cells with the lentivirus carrying pCMV-

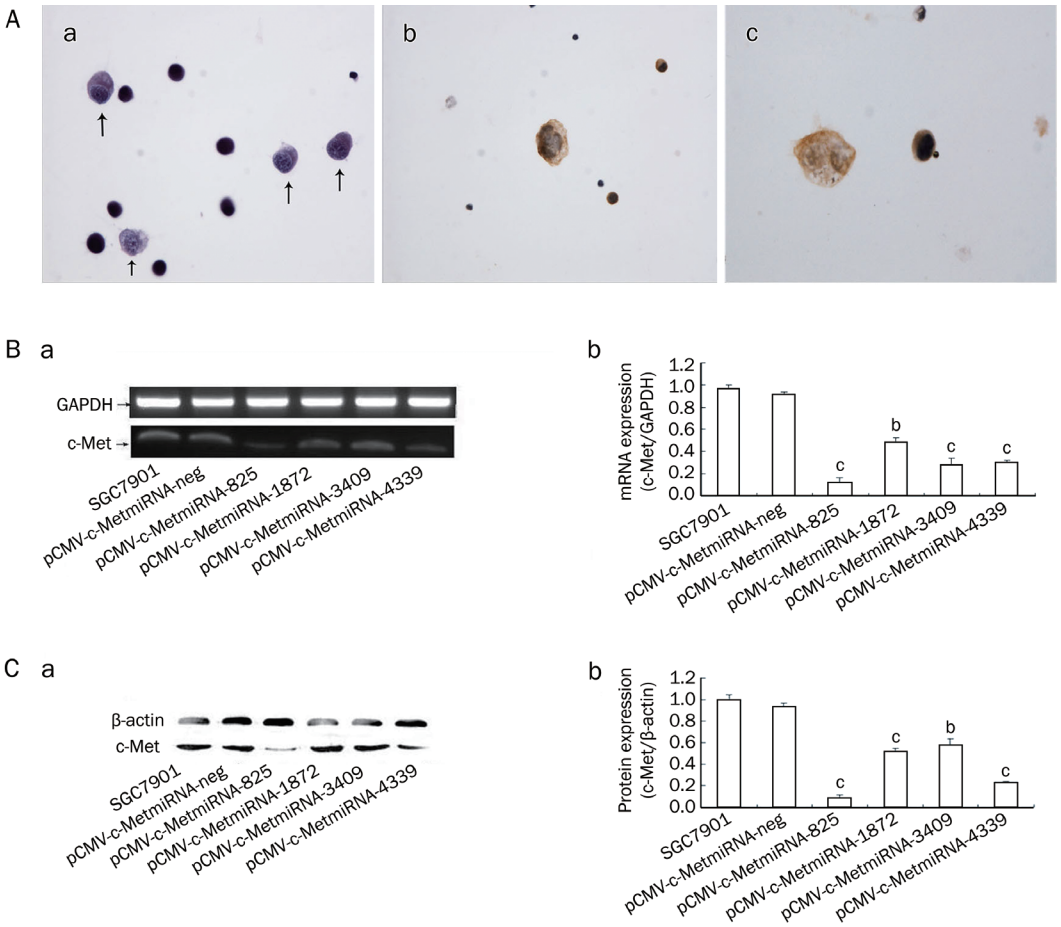

Figure 1. Expression of c-Met in the PFCCs and SGC7901 cells. (A) Free malignant cells detected by MACS from the ascites of gastric cancer patients. (a) HE staining (arrows, magnification 200×). (b) CK20 expression in the free gastric cancer cells (immunocytochemical staining, magnification 200×). (c) c-Met expression in the free gastric cancer cells (immunocytochemical staining, magnification 200×). (B) Expression of c-Met mRNA in SGC7901 cells transduced with pCMV-c-MetmiRNA expression plasmids at 48 h. (a) RT-PCR assay. (b) c-Met mRNA in pCMV-c-MetmiRNA-825 transduced cells was significantly reduced by 87.6% when compared with parental SGC7901 cells ($^bP<0.05$, $^cP<0.01$). (C) Expression of c-Met protein in SGC7901 cells transduced with different pCMV-c-MetmiRNA expression plasmids at 48 h. (a) Western blot assay. (b) c-Met protein in pCMV-c-MetmiRNA-825 transduced cells was significantly reduced by 90% when compared with the parental SGC7901 cells ($^bP<0.05$, $^cP<0.01$).

c-MetmiRNA-825 or pCMV-c-MetmiRNA-neg. c-Met protein expression decreased by 91.5% in Lenti-miRNAc-Met transfected cells as compared with the parental SGC7901 cells ($P<0.05$, Figure 2A, 2B) 48 h post-transfection. A stable SGC7901 cell line transduced with lentivirus was successfully generated by blasticidin (4 μg/mL) selection. After continuous culture for 30 d, the lentivirus-transduced cells had a stable inhibition of c-Met expression (EGFP positive expression in cells was 78.6%, Figure 2C).

Knockdown of c-Met suppressed cell proliferation *in vitro*

The effect of knockdown of c-Met expression via Lenti-miRNAc-Met on gastric cancer cell proliferation was determined by MTT assay. As shown in Figure 3, cell proliferation was inhibited in a time-dependent manner in SGC7901 cells transfected with Lenti-miRNAc-Met for 24–96 h post-transduction when compared with the parental cells and negative-control groups.

Knockdown of c-Met suppressed cell invasion *in vitro*

To verify the effect of knockdown of c-Met expression via Lenti-miRNAc-Met on migration ability of SGC7901 cells, an invasion assay was performed. Migration was determined in accordance with the fluorescence value, which represented the invading SGC7901 cells that migrated through the ECM layer. Figure 4 demonstrated that the fluorescence value of the cells transduced with Lenti-miRNAc-Met (23191.21±5183.91) was much lower than the parental cells (45496.13±9408.99) or the negative control cells (42821.36±9513.45), indicating the invasive capacity of the Lenti-miRNAc-Met transduced cells markedly decreased. This result suggested that Lenti-miRNAc-Met attenuated the metastatic potential of gastric cancer cells *in vitro*.

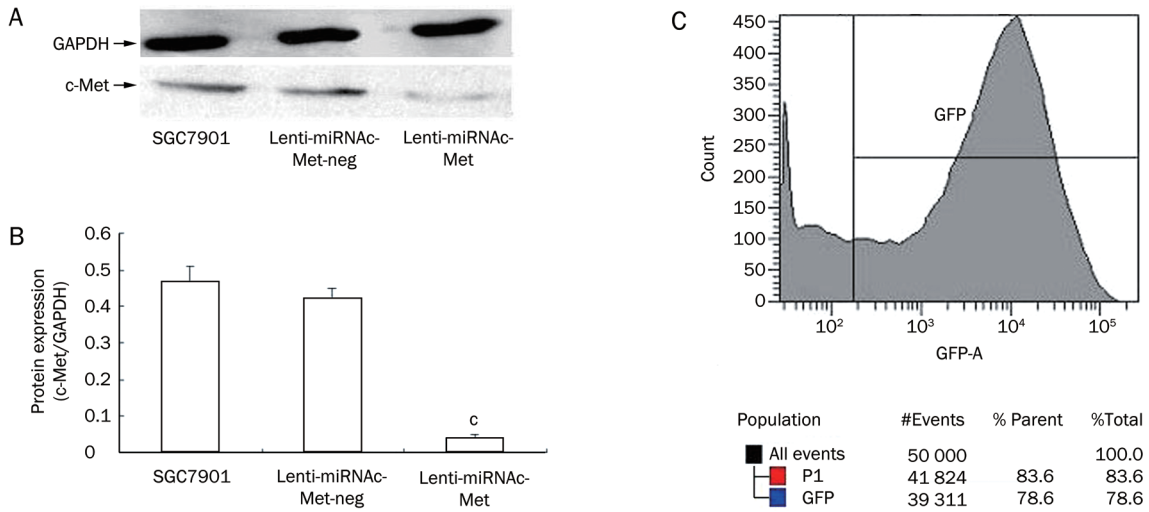

Figure 2. Lentivirus-mediated RNAi suppressed c-Met protein expression in SGC7901 cells. (A) Western blot assay. (B) c-Met protein in Lenti-miRNAc-Met transduced cells was significantly reduced by 91.5% when compared with the parental SGC7901 cells ($^cP<0.01$). (C) The transduction efficiency after continuous culture in the lentivirus-miRNAc-Met stably transduced cell line was 78.6% as measured by FCM.

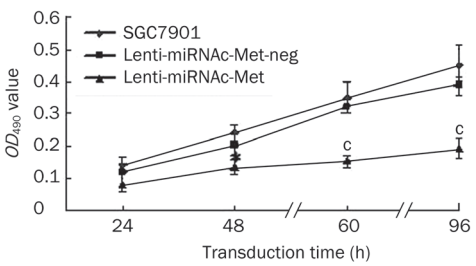

Figure 3. Cell growth was significantly inhibited in SGC7901 cells after transduction with Lenti-miRNAc-Met at various times as measured by MTT assay ($^cP<0.01$).

Knockdown of c-Met suppressed cell adhesion to HPMCs *in vitro* and mouse peritoneum *in vivo* by downregulation of integrin α3β1 and E-cadherin

Cancer cell adhesion to peritoneum is a crucial process and the initial step during peritoneal metastasis. To determine the effect of knockdown of c-Met expression via Lenti-miRNAc-Met on adhesion, fluorescently labeled SGC7901 cells were tested via an adhesion assay. *In vitro*, the adhesion of the Lenti-miRNAc-Met transduced SGC7901 cells to the monolayer of HPMCs was decreased by 64% (Figure 5A1, $P<0.01$), and *in vivo*, adhesion to the full-thickness mice peritoneum decreased by 69% (Figure 5A2, $P<0.01$), both compared with

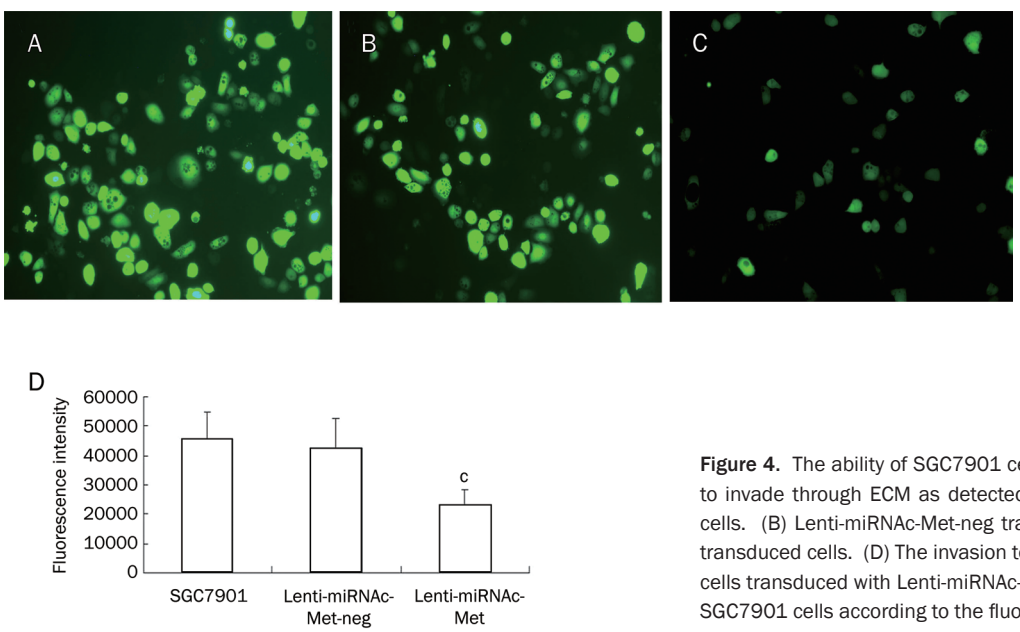

Figure 4. The ability of SGC7901 cells transduced with Lenti-miRNAc-Met to invade through ECM as detected by an invasion assay. (A) SGC7901 cells. (B) Lenti-miRNAc-Met-neg transduced cells. (C) Lenti-miRNAc-Met transduced cells. (D) The invasion to ECM was significantly inhibited in the cells transduced with Lenti-miRNAc-Met when compared with the parental SGC7901 cells according to the fluorescence assay ($^cP<0.01$).

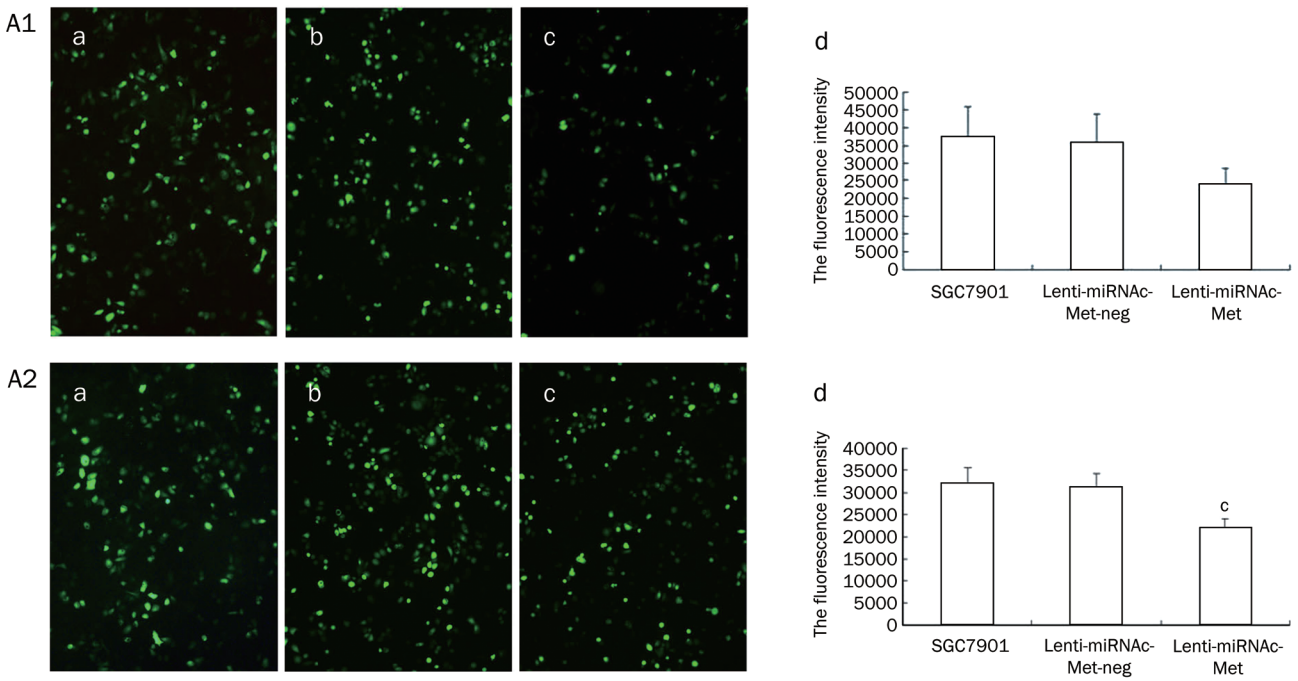

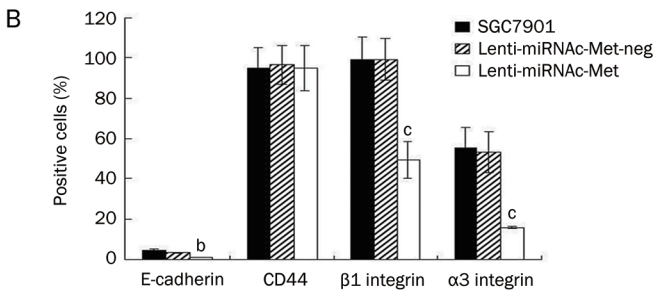

Figure 5. Adhesion of SGC7901 cells transduced with Lenti-miRNAc-Met detected by the fluorescence value assay (A) and their expressions of adhesion molecules detected by FCM (B) ($^bP<0.05$, $^cP<0.01$). (A1) Adhesion of SGC7901 cells transduced with Lenti-miRNAc-Met to HPMCs monolayer *in vitro* was significantly inhibited when compared with parental SGC7901 cells. (A2) Adhesion of SGC7901 cells transduced with Lenti-miRNAc-Met to mice peritoneum *in vivo* was significantly inhibited when compared with parental SGC7901 cells. (B) The adhesion molecules expressions in SGC7901 cells. Groups: (a) SGC7901 cells; (b) Lenti-miRNAc-Met-neg transduced cells; (c) Lenti-miRNAc-Met transduced cells.

the parental cells. No statistical significance was observed between the SCG7901 cells and the negative control ($P>0.05$).

To investigate the mechanism of adhesion to the peritoneum, adhesion molecule expression was examined by FCM. As shown in Figure 5B, the expressions of E-cadherin, integrin β1 and integrin α3 were significantly reduced in Lenti-miRNAc-Met transduced SGC7901 cells after 48 h, compared with the SGC7901 cells (Figure 5B, $P<0.01$). However, CD44 expression was not significantly inhibited (Figure 5B, $P>0.05$).

Knockdown of c-Met inhibited tumorigenicity of SGC7901 cells *in vivo*

To observe the inhibition of peritoneal dissemination of SGC7901 cells *in vivo* after knockdown of c-Met, we inoculated nude mice ip with 1×10^7 parental, Lenti-miRNAc-Met-neg transduced or Lenti-miRNAc-Met transduced SGC7901 cells. At 30 d postinoculation, numerous tumor nodules of peritoneal dissemination were observed on the peritoneal surface around the radix of mesentery and blood vessels in SGC7901 group and the negative control group, whereas tumor nodules were significantly suppressed in mice in the Lenti-miRNAc-Met inoculated group ($P<0.05$, Figure 6). The size of large nodules that exceeded 1.0 cm in diameter was also significantly reduced compared with SGC7901 and the negative control inoculated animals ($P<0.05$, Figure 6A3).

Treatment of peritoneal dissemination by Lenti-miRNAc-Met in nude mice

To further study the efficacy of Lenti-miRNAc-Met as a therapeutic target for peritoneal dissemination in gastric cancer, three days after we injected Lenti-miRNAc-Met and the control lentivirus, we established a peritoneal dissemination model by intraperitoneal incubation with 1×10^7 SGC7901 cells in nude mice. Peritoneal dissemination was significantly inhibited in the group treated with Lenti-miRNAc-Met as compared with the control group treated with Lenti-miRNAc-Met-neg or PBS ($P<0.05$, Figure 6B). The mice treated with Lenti-miRNAc-Met-neg or PBS died within 75 d. However, the mice treated with Lenti-miRNAc-Met had prolonged lives up to 116 d ($P<0.05$, Figure 6B2).

Discussion

The biological function of PFCCs can be considered a decisive factor in tumor peritoneal dissemination and the basis for ther-

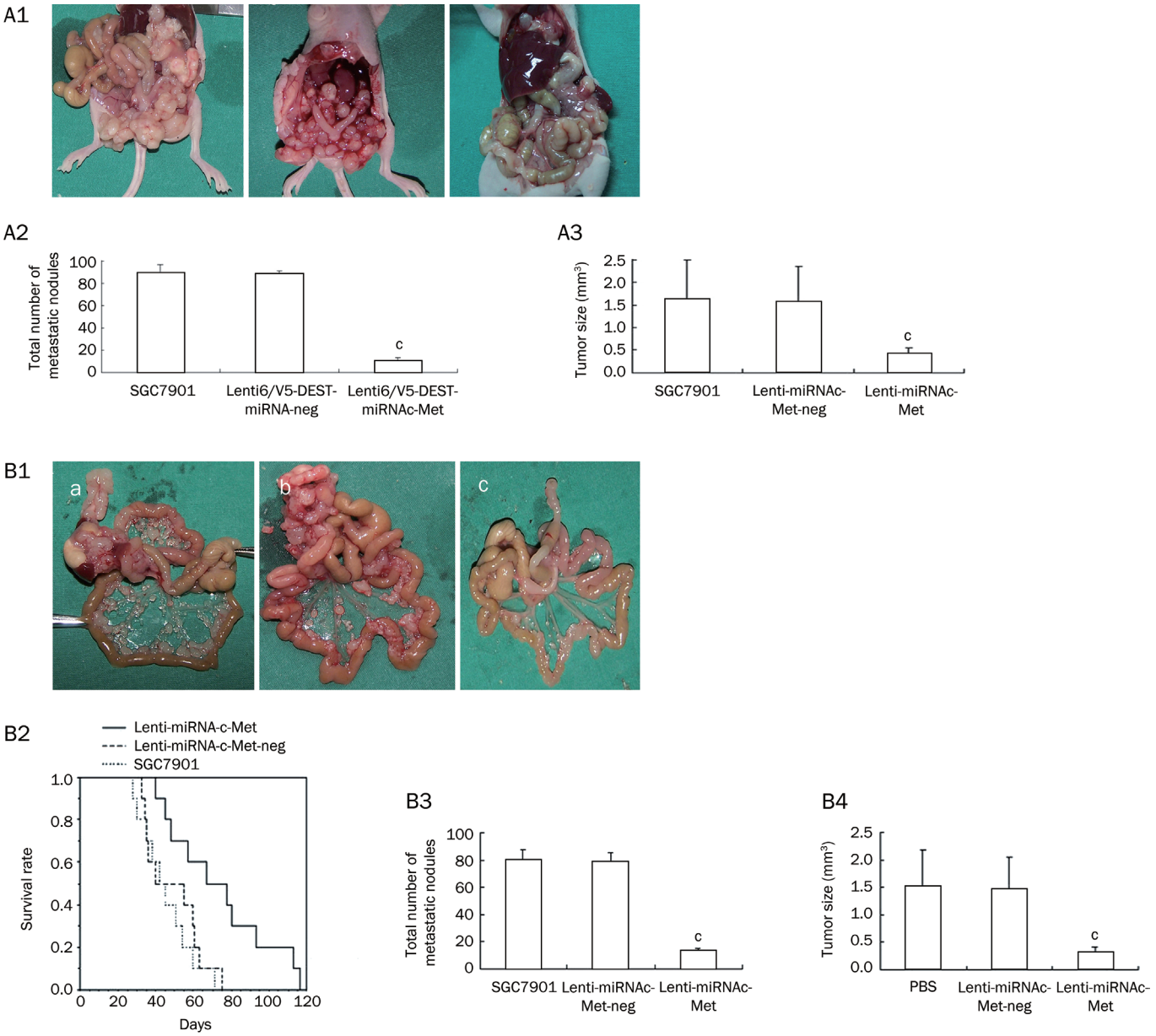

Figure 6. Lentivirus-mediated RNAi silencing of c-Met effectively suppresses peritoneal dissemination of gastric cancer *in vitro* and *in vivo*. Groups: (a) SGC7901; (b) Lenti-miRNAc-Met-neg; (c) Lenti-miRNAc-Met. (A) Tumor growth in the abdominal cavities of mice was inhibited by suppression of c-Met using Lenti-miRNAc-Met. (A1) Tumor nodules on peritoneal surface and around the radix of mesentery. (A2) The total number of tumor nodules was significantly reduced in Lenti-miRNAc-Met transduced cells when compared with the parental SGC7901 cells ($^cP<0.01$). (A3) The tumor size was significantly reduced in Lenti-miRNAc-Met transduced cells when compared with the parental SGC7901 cells ($^cP<0.01$). (B) Intraperitoneal injection of Lenti-miRNAc-Met significantly suppressed tumor growth in a nude mouse peritoneal dissemination model of gastric cancer. (B1) Tumor nodules on peritoneal surface and around the radix of mesentery were significantly reduced in the Lenti-miRNAc-Met group (c), when compared with the PBS group (a) and the Lenti-miRNAc-Met-neg group (b). (B2) The survival rate of the mice treated with Lenti-miRNAc-Met was higher than those of the mice treated with Lenti-miRNAc-Met-neg or PBS. (B3) The total number of tumor metastatic nodules was significantly reduced in mice treated with Lenti-miRNAc-Met when compared with Lenti-miRNAc-Met-neg or PBS ($^cP<0.01$). (B4) The tumor size was significantly reduced in mice treated with Lenti-miRNAc-Met when compared with Lenti-miRNAc-Met-neg or PBS ($^cP<0.01$).

apeutic strategy. Isolation of PFCCs is helpful to understand their biological characteristics. However, early detection of rare free cancer cells in the abdominal cavity is difficult with conventional methods. In this study, we successfully isolated PFCCs using the MACS method in the ascites from 6 out of 10 gastric cancer patients, and moreover, c-Met expression was detected in the PFCCs of 5 patients.

The general indication for treatment with kinase and sig-

naling pathway inhibitors is based on the level of expression and mutation status in cancer cells. For example, the effect of targeting human epidermal growth factor receptor-2 (HER-2) therapy in breast cancer depends on the level of HER-2 expression in breast cancer cells. Gastric cancer as a common cancer leading to peritoneal dissemination, the peritoneum is a common site for distant metastasis. Though the previous study has shown the effect of targeting c-Met therapy in ovarian cancer *in vivo*[11], the potential therapeutic efficacy of c-Met for gastric cancer has not been studied. Therefore, the expression of c-Met in PFCCs from gastric cancer ascites suggests that it may have the possibility to develop a treatment targeting c-Met for peritoneal dissemination in gastric cancer patients.

Due to that peritoneal dissemination is characterized by the adhesion and invasion of tumor cells into the peritoneum[11], it is an important process that cancer cells detaching from the primary cancer and successfully adhering to mesothelial cells in the dissemination and formation of metastases in gastric cancer. In this study, using lentivirus mediated RNAi technique, the expression of c-Met in both mRNA (80%–83%) and protein levels (88%–90%) were effectively knocked down by artificial engineered pre-miRNA sequences specifically targeting c-Met in human SGC7901 gastric cancer cell line. Moreover, we established the stably transduced Lenti-miRNAc-Met SGC7901 cell line and the control stably transduced cell line. After knockdown of c-Met expression, the adhesion of SGC7901 gastric cancer cells to monolayer HPMC *in vitro* and to mice peritoneum *in vivo* were significantly suppressed, compared with the control virus.

Many adhesion molecules are involved in this regulation as the previous reported. We further investigated the mechanism of adhesion. The findings showed that E-cadherin and α3β1 integrin expression were reduced in the Lenti-miRNAc-Met transduced SGC7901 cells, as compared with the negative control and parental cells. However, no close relationship between c-Met and CD44 in our study was found although some CD44 isoforms can promote or increase c-Met activation[16]. E-cadherin is also involved in the multistep process of peritoneal dissemination in epithelial ovarian carcinoma[2]. c-Met can remove E-cadherin from cell-cell adhesion sites and regulate the activity of integrins[17]. In gastric cancer, modulation of E-cadherin by hepatocyte growth factor/c-Met induces aggressiveness of gastric carcinoma[18]. CD44 can cause very strong cell adhesion to peritoneal mesothelium and an unfavourable prognosis in ovarian cancer[3], but we did not find the similar result in gastric cancer in this study. α3β1 integrin plays an essential role in mediating the initial attachment of cancer cells to the peritoneum in the peritoneal implantation of NUCC-4 human gastric cancer cells in athymic mice[8]. Therefore, c-Met can regulate these molecules in the peritoneal dissemination of gastric cancer. However, in ovarian cancer, targeting c-Met *in vivo* inhibited peritoneal dissemination and invasion through an α5β1 integrin-dependent mechanism[11]. So, in human cancers, various integrin combinations of α and β subunits produce polymorphisms with different ligands specificity and function. The molecules involved in peritoneal dissemination may also be different.

After adhesion to peritoneum, cancer cells invade the ECM of the peritoneum and form the metastasis site. c-Met plays an important role in the process of epithelial-mesenchymal interaction, regulation of cell migration, invasion, cell proliferation and survival. Our results indicated the Lenti-miRNAc-Met transduced SGC7901 cells survival and their ability to invade the ECM were significantly inhibited *in vitro*.

The biological function of HGF-MET axis affects tumor growth and development of metastasis[19]. The advantage of stable and long-term gene silencing offered by the lentivirus vector system makes it a powerful tool for gene therapy. Based on the peritoneal metastasis model established by SGC7901 gastric cancer cells[20], we found that tumor growth (including the number of macroscopic nodules on peritoneal surface and tumor size of large nodules) in mice which received intraperitoneal injections of SGC7901 cells transduced with Lenti-miRNAc-Met was strongly suppressed compared with the Lenti-miRNAc-Met-neg control and parental SGC7901 cell groups. The intraperitoneal administration of Lenti-miRNAc-Met dramatically suppressed the growth of gastric cancer cells on the surface of peritoneum and improved the survival of the mice. Combining these findings *in vitro* and *in vivo*, we confirmed the role of c-Met in the growth, proliferation, invasion to ECM, adhesion to peritoneum and peritoneal dissemination in gastric cancer.

In summary, our findings indicate that c-Met is expressed in PFCCs, and it plays an important role in the process of gastric cancer peritoneal dissemination, including tumor growth, adhesion to peritoneum and invasion to ECM. E-cadherin and α3β1 integrin are involved in the regulation of adhesion of SGC7901 cells to mesothelial cells. Therefore, Lentivirus-mediated RNAi targeting c-Met may be a useful tool for gene therapy targeting gastric cancer peritoneal dissemination.

Acknowledgements

This work was supported in part by the Natural Science Foundation of Shanghai (No 05ZR14130).

Author contribution

Xiao-lei WANG was the guarantor of integrity of the entire study, responsible for study design, data analysis and manuscript preparation. Xi-mei CHEN provided final approval of the version to be submitted. Jian-ping FANG participated in the immunocytochemical staining experiments. Chang-qin YANG revised the article for important intellectual content.

References

1 Yonemura Y, Endo Y, Obata T, Sasaki T. Recent advances in the treatment of peritoneal dissemination of gastrointestinal cancers by nucleoside antimetabolites. Cancer Sci 2007; 98: 11–8.

2 Terauchi M, Kajiyama H, Yamashita M, Kato M, Tsukamoto H, Umezu T, *et al*. Possible involvement of TWIST in enhanced peritoneal metastasis of epithelial ovarian carcinoma. Clin Exp Metastasis 2007; 24: 329–39.

3 Li CZ, Liu B, Wen ZQ, Li HY. Inhibition of CD44 expression by small

interfering RNA to suppress the growth and metastasis of ovarian cancer cells *in vitro* and *in vivo*. Folia Biol (Praha) 2008; 54: 180–6.
4 Hynes RO. Integrins: bidirectional, allosteric signaling machines. Cell 2002; 110: 673–87.
5 Jin H, Varner J. Integrins: roles in cancer development and as treatment targets. Br J Cancer 2004; 90: 561–5.
6 Knudsen BS, Vande Woude G. Showering c-MET-dependent cancers with drugs. Curr Opin Genet Dev 2008; 18: 87–96.
7 Ayhan A, Ertunc D, Tok EC, Ayhan A. Expression of the c-Met in advanced epithelial ovarian cancer and its prognostic significance. Int J Gynecol Cancer 2005; 15: 618–23.
8 Drebber U, Baldus SE, Nolden B, Grass G, Bollschweiler E, Dienes HP, *et al*. The overexpression of c-met as a prognostic indicator for gastric carcinoma compared to p53 and p21 nuclear accumulation. Oncol Rep 2008; 19: 1477–83.
9 Tuynman JB, Lagarde SM, Ten Kate FJ, Richel DJ, van Lanschot JJ. Met expression is an independent prognostic risk factor in patients with oesophageal adenocarcinoma. Br J Cancer 2008; 98: 1102–8.
10 Zeng ZS, Weiser MR, Kuntz E, Chen CT, Khan SA, Forslund A, *et al*. c-Met gene amplification is associated with advanced stage colorectal cancer and liver metastases. Cancer Lett 2008; 265: 258–69.
11 Sawada K, Radjabi AR, Shinomiya N, Kistner E, Kenny H, Becker AR, *et al*. c-Met overexpression is a prognostic factor in ovarian cancer and an effective target for inhibition of peritoneal dissemination and invasion. Cancer Res 2007; 67: 1670–9.
12 Yonemura Y, Endo Y, Obata T, Sasaki T. Recent advances in the treatment of peritoneal dissemination of gastrointestinal cancers by nucleoside antimetabolites. Cancer Sci 2007; 98: 11–8.
13 Barker SD, Casado E, Gomez-Navarro J, Xiang J, Arafat W, Mahasreshti P, *et al*. An immunomagnetic-based method for the purification of ovarian cancer cells from patient-derived ascites. Gynecol Oncol 2001; 82: 57–63.
14 Clement JH, Schwalbe M, Buske N, Wagner K, Schnabelrauch M, Görnert P, *et al*. Differential interaction of magnetic nanoparticles with tumor cells and peripheral blood cells. J Cancer Res Clin Oncol 2006; 132: 287–92.
15 Ross JS, Carlson JA, Brock G. miRNA: The new gene silencer. Am J Clin Pathol 2007; 128: 830–6.
16 Orian-Rousseau V, Chen L, Sleeman JP, Herrlich P, Ponta H. CD44 is required for two consecutive steps in HGF/c-Met signaling. Genes Dev 2002; 16: 3074–86.
17 Garmy-Susini B, Varner JA. Roles of integrins in tumor angiogenesis and lymphangiogenesis. Lymphat Res Biol 2008; 6: 155–63.
18 Han SU, Lee HY, Lee JH, Kim WH, Nam H, Kim H, *et al*. Modulation of E-cadherin by hepatocyte growth factor induces aggressiveness of gastric carcinoma. Ann Surg 2005; 242: 676–83.
19 Lesko E, Majka M. The biological role of HGF-MET axis in tumor growth and development of metastasis. Front Biosci 2008; 13: 1271–80.
20 Li Z, Zhan W, Wang Z, Zhu B, He Y, Peng J, *et al*. Inhibition of PRL-3 gene expression in gastric cancer cell line SGC7901 via microRNA suppressed reduces peritoneal metastasis. Biochem Biophys Res Commun 2006; 348: 229–37.

Acta Pharmacologica Sinica (2012) 33: 523–530
 1671-4083/12 $32.00
www.nature.com/aps

Original Article

Piperine suppresses tumor growth and metastasis *in vitro* and *in vivo* in a 4T1 murine breast cancer model

Li-hua LAI[1, #], Qi-hong FU[2, #], Yang LIU[1], Kai JIANG[1], Qing-ming GUO[1], Qing-yun CHEN[1], Bin YAN[3], Qing-qing WANG[1, *], Jian-gen SHEN[1, *]

[1]*Institute of Immunology, Zhejiang University School of Medicine, Hangzhou 310058, China;* [2]*Clinical Medicine College, Hangzhou Normal University, Hangzhou 310036, China;* [3]*Ningbo First Hospital, Ningbo 315000, China*

Aim: To investigate the effects of piperine, a major pungent alkaloid present in *Piper nigrum* and *Piper longum*, on the tumor growth and metastasis of mouse 4T1 mammary carcinoma *in vitro* and *in vivo*, and elucidate the underlying mechanisms.
Methods: Growth of 4T1 cells was assessed using MTT assay. Apoptosis and cell cycle of 4T1 cells were evaluated with flow cytometry, and the related proteins were examined using Western blotting. Real-time quantitative PCR was applied to detect the expression of matrix metalloproteinases (MMPs). A highly malignant, spontaneously metastasizing 4T1 mouse mammary carcinoma model was used to evaluate the *in vivo* antitumor activity. Piperine was injected into tumors every 3 d for 3 times.
Results: Piperine (35–280 μmol/L) inhibited the growth of 4T1 cells in time- and dose-dependent manners (the IC_{50} values were 105±1.08 and 78.52±1.06 μmol/L, respectively, at 48 and 72 h). Treatment of 4T1 cells with piperine (70–280 μmol/L) dose-dependently induced apoptosis of 4T1 cells, accompanying activation of caspase 3. The cells treated with piperine (140 and 280 μmol/L) significantly increased the percentage of cells in G_2/M phase with a reduction in the expression of cyclin B1. Piperine (140 and 280 μmol/L) significantly decreased the expression of MMP-9 and MMP-13, and inhibited 4T1 cell migration *in vitro*. Injection of piperine (2.5 and 5 mg/kg) dose-dependently suppressed the primary 4T1 tumor growth and injection of piperine (5 mg/kg) significantly inhibited the lung metastasis.
Conclusion: These results demonstrated that piperine is an effective antitumor compound *in vitro* and *in vivo*, and has the potential to be developed as a new anticancer drug.

Keywords: anticancer drug; piperine; 4T1 breast cancer; apoptosis; cell cycle; metastasis; MMP-9; MMP-13

Acta Pharmacologica Sinica (2012) 33: 523–530; doi: 10.1038/aps.2011.209; published online 5 Mar 2012

Introduction

Piperine (Figure 1) is a major pungent alkaloid present in black pepper (*Piper nigrum*) and long pepper (*Piper longum*). It exhibits a wide variety of biological effects. Piperine could inhibit both the drug transporter P-glycoprotein and the major drug-metabolizing enzyme CYP3A4[1, 2], so it has been used as a bioavailability enhancer with various structurally and therapeutically diverse drugs[3]. Piperine also had anti-inflammatory, anti-nociceptive, and anti-arthritic effects by inhibiting the expression of interleukin 6 (IL-6), matrix metalloproteinases 13 (MMP-13) and prostaglandin E2 (PGE2) in an arthritis animal model[4] or by inhibiting tumor necrosis factor-α (TNF-α) induced activation of NF-κB via blocking IκBα kinase activation[5]. Additionally, piperine also possessed anti-depression like activity, cognitive enhancing effect[6], a blood pressure-lowering effect[7], anti-oxidative, anti-apoptotic and chemo-protective ability in blastogenesis[8]. More of the diverse physiological effects of piperine have been reported in recent decades[9].

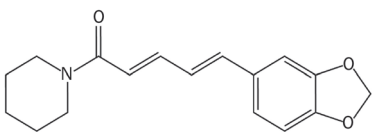

Figure 1. Chemical structure of piperine {1-[5-(1,3-benzodioxol-5-yl)-oxo-2,4-pentadienyl]piperidine}.

Concerning the antitumor effects, piperine has been reported to inhibit lung metastasis induced by B16F-10 mela-

# These two authors contribute equally to this work.
* To whom correspondence should be addressed.
E-mail wqq@zju.edu.cn (Qing-qing WANG);
sjg7217143@sina.com (Jian-gen SHEN)
Received 2011-07-15 Accepted 2011-12-26

noma cells[10], and the anti-invasive effects of piperine on fibrosarcoma cells also have been demonstrated[11]. The therapeutic properties of piperine with other antitumor drugs were tested in various cell types[12, 13]. But there is little known about the anticancer activities of piperine on mammary cancer cells and the underlying mechanism.

The 4T1 tumors closely mimics human breast cancer in its anatomical site, immunogenicity and growth characteristics[14]. After sc inoculation in the abdominal mammary fat pad, the primary tumor grows into a nodule with the histology of a high-grade breast cancer and sheds spontaneous systemic metastases. Metastatic growth in the lungs is usually the main cause of death of mice. The pattern and histological appearance of such metastases are similar to what is seen in humans, therefore, this model is suitable for testing the effects of experimental therapies on metastatic disease. In the present study, we observed the effects of piperine on the tumor growth and metastasis of 4T1 breast cancer *in vitro* and *in vivo*. And the possible mechanism for the inhibitory effect of piperine on tumor cell growth and migration were investigated. The antitumor efficacy makes piperine a potential candidate for future cancer therapy.

Materials and methods

Materials

Piperine (molecular weight, 285.35) was purchased from Fluka (St Louis, MO, USA). A 50 mg/mL stock solution of piperine was prepared in DMSO and then further diluted in cell culture medium or PBS. 3-(4,5-dimethylthiazol-2-yl)-2,5-diphenyltetrazolium bromide (MTT) was purchased from Sigma (St Louis, MO, USA). Annexin-V FITC Apoptosis Detection Kit was purchased from R&D systerms (Minneapolis, MN, USA). Reverse transcription enzymes and SYBR Green detection chemistry were obtained from Takara Bio Inc (Japan). Anti-Bcl-2 (sc-7382), anti-Bax (sc-526), anti-cyclin D1 (sc-8396), anti-cyclin B1 (sc-595), anti-β-actin (sc-4778) and IgG-HRP were obtained from Santa Cruz Biotechnology (Santa Cruz, CA, USA). Anti-caspase 3 (1087-1) was purchased from Epitomics (Epitomics, CA, USA). All chemicals and reagents were of analytical grade.

Cell lines

4T1 mouse mammary carcinoma cells were a kind gift from Prof Yang-xin FU (Chicago University, Chicago, IL, USA). NIH3T3 (murine fibroblast cell line) cells were obtained from American Type Culture Collection (ATCC, Manassas, VT, USA). Cells were cultured in RPMI-1640 supplemented with 10% fetal bovine serum (FBS). Cultures were maintained in a humidified atmosphere with 5% CO_2 at 37 °C.

Animals

Female BALB/c mice syngeneic to 4T1 cells, aged 5–6 weeks, were purchased from Joint Ventures Sipper BK Experimental Animal Co (Shanghai, China) and housed in a room maintained at constant temperature and humidity under 12-h light and darkness cycle and fed with regular autoclave chow diet with water. All animal usage was conducted according to protocols approved by the Zhejiang University Institutional Animal Care and Use Committee.

MTT assay

The effect of piperine on the growth of 4T1 and NIH3T3 cells was examined using a MTT assay. Cells were subcultured in 96-well plates at a density of 10^3 cells per well with or without piperine (35, 70, 100, 140, and 280 μmol/L) for 24 h, 48 h, or 72 h in a final volume of 200 μL. Then, the medium was removed and 20 μL of MTT (5 mg/mL in PBS) was added to the fresh medium. After 2 h incubation at 37 °C, 100 μL DMSO was added to each well and plates were agitated for 1 min. Spectrophotometric absorbance at 570 nm was measured. The percentage of viability was calculated as the following formula: (viable cells)%=(*OD* of drug-treated sample/*OD* of untreated sample)×100.

Apoptosis detection assay

After the treatment with piperine 0, 70, 140, and 280 μmol/L for 24 h, harvested cells were suspended in 100 μL binding buffer (1×) including 1 μL Annexin V-FITC and 10 μL PI for 15 min in dark at room temperature and then 400 μL binding buffer (1×) was added to each sample. The FITC and PI fluorescence were measured through FL-1 filter (530 nm) and FL-2 filter (585 nm) respectively, and 10 000 events were acquired.

Cell cycle analysis

After the treatment with piperine 0, 70, 140, and 280 μmol/L for 24 h, 4T1 cells were collected, washed with cold PBS, fixed in cold 70% ethanol and stored at -20 °C overnight. Cells were then washed again with PBS before staining (100 μg/mL of RNase A, 25 μg/mL of propidium iodide and 0.1% of Triton X-100 in PBS), and incubated at 37 °C for 30 min. Cell cycle analysis was performed on flow cytometer.

Western blot analysis

4T1 cells were lysed in lysis buffer (Cell Signaling Technology, Danvers, MA, USA) for 30 min on ice after the treatment with piperine 0, 70, 140, and 280 μmol/L for 24 h. Lysates were then centrifuged at 14 000×*g* for 10 min to remove insoluble material. Then a BCA kit (Pierce Biotechnology, Rockford, IL, USA) was used to determine the concentration of lysates. Cell extracts were separated by 10% sodium dodecylsulfate–polyacrylamide gel electrophoresis and transferred to a polyvinylidene difluoride membrane, blocked with 5% nonfat milk. The blot was probed with each antibody against Bcl-2, Bax, cyclin D1, cyclin B1, caspase 3, and β-actin. Then the blot was washed, exposed to horseradish peroxidase conjugated secondary antibodies for 1 h at room temperature. Signals were detected as we previously described[15].

Wound healing assay

To study the effects of piperine on cell migration *in vitro*, a wound healing assay was performed following standard methods[16]. 4T1 cells were seeded in 6-well plates and grown

until 90% confluent. Cells were then serum starved for 24 h, and a linear wound was created in the confluent monolayer using a 200 μL pipette tip. Cells were then washed with PBS and diluted in RPMI-1640 containing 1% FBS with piperine at a concentration of 70 or 140 μmol/L. Images of the wound surfaces were recorded after 24 h.

RNA isolation and real-time quantitative PCR analysis

Total RNA from cells was extracted using TRIzol reagent in accordance with the manufacturer's instructions. Real-time quantitative PCR, using SYBR Green detection chemistry, was performed on a 7500 Real-Time PCR System (Applied Biosystems). Quantitative measurements were determined using the ΔΔCt method and expression of GAPDH was used as the internal control. The sequences of the primers are as shown in Table 1.

Evaluation of antitumor activity of piperine in 4T1 mammary carcinoma models

4T1 harvested from subconfluent cultures were washed once in serum-free medium and resuspended in PBS. Cells (5×10^5) in 0.1 mL PBS were implanted subcutaneously into the female BALB/c mice in the abdominal mammary fat pad. After 3 d of implantation, piperines (0, 2.5, and 5 mg/kg) were dissolved in 0.2% DMSO and injected into tumors every three days for three times. The tumor volume was measured every two or three days using the formula $V=0.5236\times d_1^2\times d_2$, where d_1 is the shortest diameter, and d_2 is the longest diameter. Tumor tissues for histology examination were collected on d 20, fixed in 10% formalin, and embedded in paraffin. Sections (5 μm thick) were prepared for hematoxylin–eosin staining.

Examination of lung metastases by colonogenic assay

Cells (5×10^5) in 0.1 mL PBS were implanted subcutaneously into the female BALB/c mice. After 3 d of implantation, piperine (0 and 5 mg/kg) were dissolved in 0.2% DMSO and injected into tumors every three days for three times. Five days after the last therapy, primary 4T1 tumors were eliminated from the experiments. For surgical excision of primary 4T1 tumors, mice were anesthetized, and tumors were resected with sterilized instruments. Wounds were closed with metallic clips. Mice in which primary tumors recurred at the site of the surgical excision were eliminated from the experiments. A colonogenic assay was used to evaluate metastases by 4T1 tumors as we previously described[15]. Briefly, lungs were collected and chopped before being dissociated in RPMI-1640 supplemented with 10% FBS containing 1.5 mg/mL collagenase type D (Sigma, St Louis, MO, USA) for 30 min in 37 °C shaking incubator at 178 r/min speed. Lungs were then plated at various dilutions in the RPMI-1640 supplemented with 10% FBS and 60 μmol/L 6-thioguanine. Individual colonies representing micrometastases were counted after 5–10 d.

Statistical analysis

All experiments were repeated two or three times. Data was described as the mean±SD, and statistical analysis was carried out using Student's *t*-test or the log-rank test (for survival analysis). The difference was considered statistically significant when the *P*-value was less than 0.05.

Results

Piperine inhibited the growth of 4T1 cells *in vitro*

Inhibitory effects of piperine on the growth of 4T1 cells were examined using the MTT assay. We also tested the effects of piperine on murine NIH3T3 fibroblast cell growth. Compared to the untreated cells (taken as 100% viable), different concentrations of piperine showed a time- and dose-dependent inhibition on 4T1 cell growth in the concentration range of 35~280 μmol/L (Figure 2A). Exposure of 4T1 cells to piperine at 140 μmol/L and 280 μmol/L for 24 h caused a marked decrease in the viability from 100% to 78% and 48% of untreated control levels, respectively. And 48 h of piperine treatment at 140 μmol/L and 280 μmol/L caused a decrease in the viability from 100% to 33% and 18%, respectively. The IC_{50} values for piperine were 105±1.08 μmol/L for 48 h, and 78.52±1.06 μmol/L for 72 h treatment (Figure 2C), suggesting a dose-dependent inhibition of growth, while piperine was not so toxic to NIH3T3 cells (Figure 2B), for the IC_{50} values was 232±1.15 μmol/L for 48 h treatment (Figure 2C).

Piperine induced apoptosis of 4T1 cells and increased the caspase 3 activity

In order to evaluate the mechanism of growth inhibition of 4T1 cells by piperine, apoptosis of 4T1 cells treated with various concentrations of piperine (0, 140, and 280 μmol/L) for 24 h was analyzed by Annexin V-FITC/PI double-labeled flow cytometry. The apoptosis rate was the sum of early apoptosis and late apoptosis. There was little binding of Annexin-V in untreated and 70 μmol/L piperine treated 4T1 cells (Figure 3A). But after treatment with piperine at 140 and 280 μmol/L for 24 h, the apoptosis rate was about 24.2%, 23.6%, respectively (Figure 3B).

Apoptosis is characterized by changes in the expression and activity of several apoptotic markers. The control and regula-

Table 1. Primer sequences used in real time PCR.

Gene	Forward (5′→3′)	Reverse (5′→3′)	Size (bp)
MMP-9	TGAGTTCCAGGGCACACCA	TGTCTGGAGATTCGACTTGAAGTC	91
MMP-13	GCCCATGAGCTTGGCCACTCC	GGGTCTTCATCGCCTGGACCATAA	158
MMP-14	TTCAGCCCCGAAGCCTGGCT	GAGGGCGCCTCATGGCCATC	178
GAPDH	TCTCCACTTTGCCACTGCAA	GAACGGATTTGGCCGTATTG	65

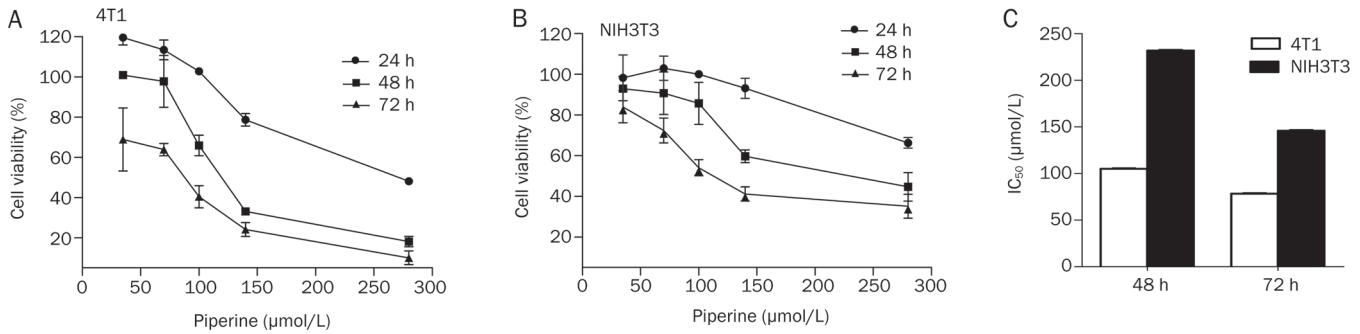

Figure 2. Inhibition of growth by piperine in 4T1 and NIH3T3 cells. 4T1 (A) and NIH3T3 (B) cells were treated with 0, 35, 70, 100, 140, and 280 μmol/L piperine for 24 h, 48 h, and 72 h. Cell viability was monitored by MTT assay. The percentage of viability was calculated as the following formula: (viable cells)%=(*OD* of drug-treated sample/*OD* of untreated sample)×100. Mean±SD. *n*=3. (C) The IC_{50} values for piperine on 4T1 and NIH3T3 cells.

tion of the apoptotic mitochondrial events occur through the members of the Bcl-2 family of proteins which can be pro-apoptotic (Bcl-10, Bax, *etc*) or anti-apoptotic (Bcl-2, Bcl-xL, *etc*). The expression levels of Bax and Bcl-2 are detected by Western blot. The results showed no change in the expression of Bcl-2 and Bax in 4T1 cells after piperine treatment (Figure 3C). Caspases are responsible for cell apoptosis. Therefore we determined the effect of piperine on the expression of caspases by Western blot analysis. The results indicated that caspase 3 activity was up-regulated after piperine treatment (Figure 3C).

Piperine caused the accumulation of the cells in G_2/M phase

After incubation with various concentrations of piperine (0, 70, 140, and 280 μmol/L) for 24 h, cell cycle distributions were analyzed by FCM. We found that with the dose of piperine increased, the percentage of cells in G_2/M phase was increased, and there were slight changes in G_0/G_1 phase cell population (Figure 4A). After incubation with 140 and 280 μmol/L piperine for 24 h, percentage of cells in G_2/M phase was increased to 7.3%, 15.5%, respectively (Figure 4B).

Piperine down-regulated the expression of cyclin B1

Given that cyclins are required for the cell cycle progression, the protein levels of cyclin D1 and cyclin B1 in 4T1 cells were detected by Western blot. The result showed that piperine treatment down-regulated the expression of cyclin B1 in a dose-dependent manner, with maximum suppression observed at 280 μmol/L (Figure 4C), while there was no change of cyclin D1 expression after piperine treatment with various concentrations.

Piperine inhibited the migration ability of 4T1 cells *in vitro*

We investigated the effects of piperine on the migration properties of 4T1 cells *in vitro* by wound healing assay. Cells were treated by piperine at a concentration of 0, 70, and 140 μmol/L, and the results showed that piperine inhibited the migration of 4T1 cells in a dose-dependent manner (Figure 5A).

Piperine decreased the mRNA expression of MMP-9 and 13

Matrix metalloproteinases (MMPs), comprise a family of zinc-containing endopeptidases that share common structural domains. These proteins have the capacity to degrade extracellular matrix (ECM) components, as well as alter their biological functions. Therefore, we examined the mRNA expression of MMP-9, 13, and 14 in 4T1 cells by real-time quantitative PCR after piperine treatment. The mRNA expression of MMP-9 and 13 in 4T1 cells, but not MMP-14, were decreased in a dose-dependent manner (Figure 5B).

Piperine suppressed 4T1 tumor growth *in vivo*

To test the antitumor effect of piperine, female BALB/c mice were inoculated sc with 5×10^5 4T1 cells. Piperines (0, 2.5, and 5 mg/kg) were injected intratumorally every three days for three times. The result showed that piperine exhibited a significant inhibition of tumor growth especially at a high dose (5 mg/kg) (Figure 6A). To determine whether the regulation of apoptotic proteins and cell cycle-related regulatory proteins was also involved in the inhibition of tumor growth by piperine *in vivo*, the tumors were harvested from each group and the expression level of these proteins were analyzed by Western blot. As shown in Figure 6B, the level of active caspase 3 was increased and cyclin B1 was reduced in tumors from the mice received piperine therapy, which was similar to the effect of piperine *in vitro*. Histopathological analysis of the tumor tissues excised from the control mice showed groups of large, round and polygonal cells, with pleomorphic shapes, hyperchromatic nuclei and binucleation. Several degrees of cellular and nuclear pleomorphism were seen. In the tumors excised from the mice treated with piperine, extensive areas of coagulative necrosis were observed (Figure 6C).

Piperine also inhibited the lung metastasis of 4T1 tumors

4T1 cells can metastasize to various organs, such as lung, as early as d 10 after inoculation of 1×10^5 4T1 tumor cells[17]. To study the potential inhibitory effect of piperine on metastasis, we used a colonogenic assay to evaluate the metastases in the lung. We detected less metastasis in the lungs of the mice that had been given 5 mg/kg piperine treatment compared to the lungs of the control mice (Figure 7). The results indicated that piperine not only suppressed the local primary tumor growth,

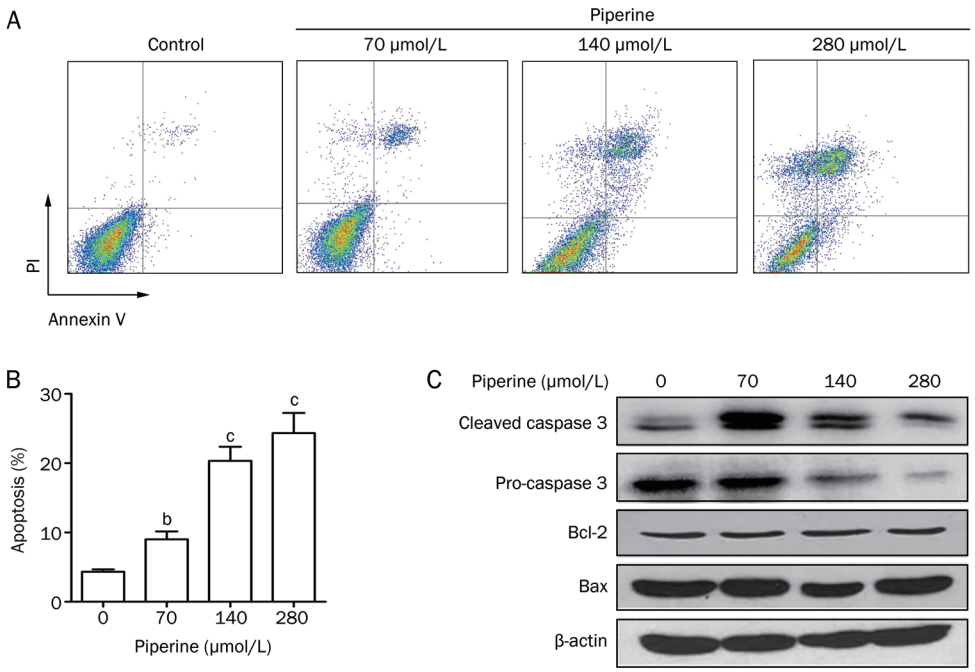

Figure 3. Piperine induced the apoptosis in 4T1 cells with the up-regulation of caspase 3. (A) 4T1 cells were treated with piperine (0, 70, 140, and 280 μmol/L) for 24 h. The induction of apoptosis was detected by Annexin V-FITC/PI double staining assay. (B) The apoptotic cell death was quantified as Annexin V$^+$ (both PI-negative and PI-positive) cells. Mean±SD. n=3. ^bP<0.05, ^cP<0.01. (C) Western blot analysis of caspase 3, Bcl-2, and Bax in 4T1 cells treated with or without piperine. Similar results were obtained in four independent experiments.

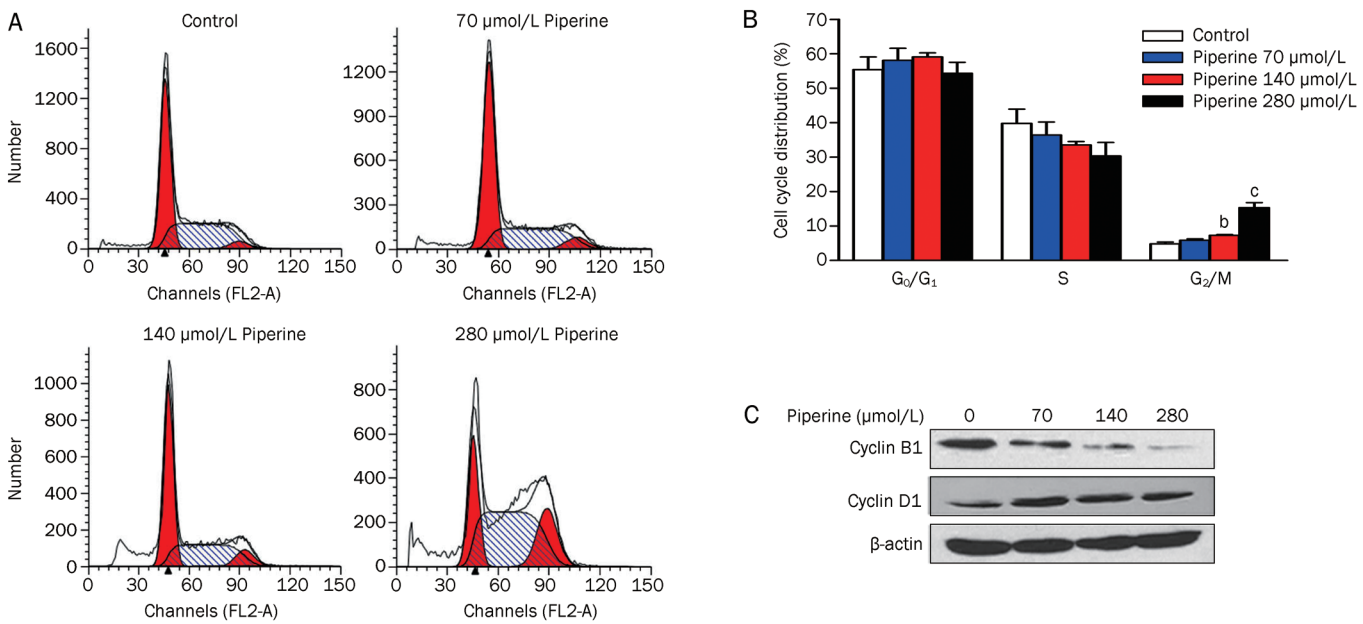

Figure 4. Piperine caused the accumulation of the cells in the G_2/M phase possibly by reducing the expression of cyclin B1. (A) 4T1 cells were treated with piperine 0, 70, 140, 280 μmol/L for 24 h. Then the cells were washed, fixed, stained with propidiumiodide, and analyzed for DNA content by flow cytometry. One representative result was shown. (B) The percentage of cells in different phases of cell cycle after piperine treatment. Mean±SD. n=4. ^bP<0.05, ^cP<0.01. (C) Western blot analysis of cyclin D1 and cyclin B1 expression in 4T1 cells treated with or without piperine. One representative result of three independent experiments was shown.

but also effectively controlled the occurrence of spontaneous metastases.

Discussion

Piperine is a potent anticancer compound that has been

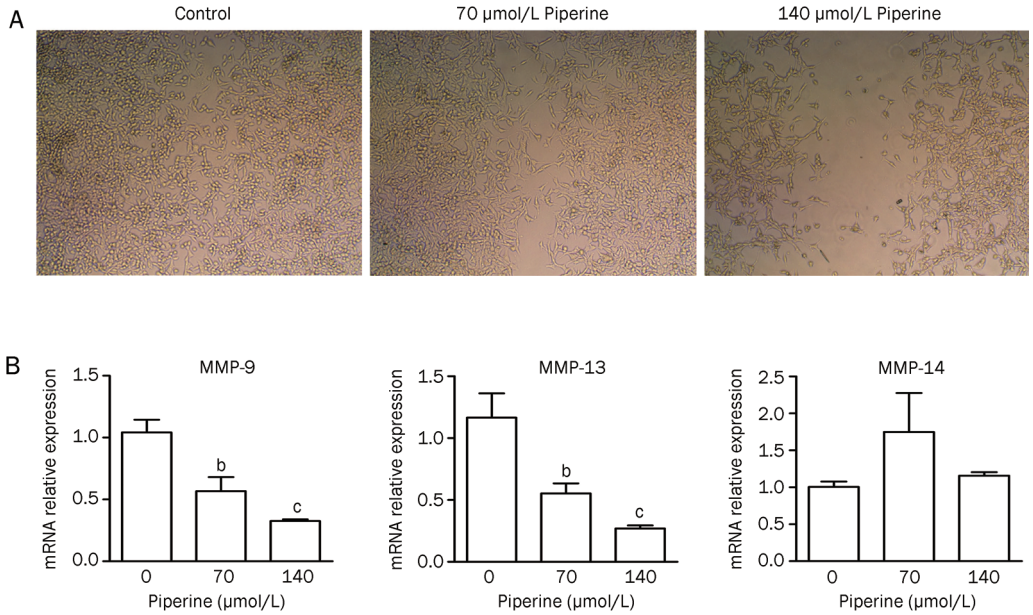

Figure 5. Piperine inhibited 4T1 cell migration *in vitro* and down-regulated the expression of MMP-9 and 13. (A) Cell migration was evaluated by wound healing assay after 24 h incubation with 0, 70, 140 μmol/L piperine. (B) The mRNA expression of MMP-9, 13 and 14 in 4T1 cells treated by piperine at different concentrations (0, 70, and 140 μmol/L) for 24 h was detected by real-time PCR and normalized to the expression of GAPDH in each sample. Mean±SD. n=4. ^{b}P<0.05, ^{c}P<0.01.

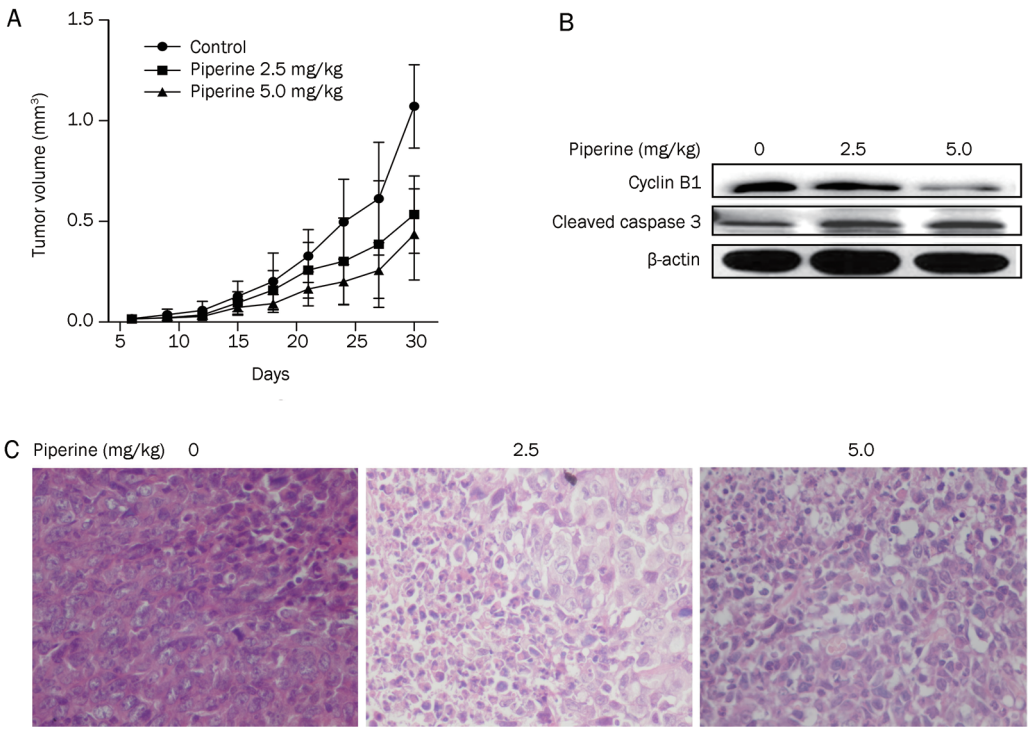

Figure 6. Piperine suppressed 4T1 tumor growth *in vivo*. (A) 5×10^5 cells in 0.1 mL PBS were implanted subcutaneously into the BALB/c mice. After 3 d of implantation, piperine (0, 2.5, and 5 mg/kg) were dissolved in 0.2% DMSO and injected into tumors every three days for three times. The tumor volume was measured every two or three days using the formula $V=0.5236\times d_1^2\times d_2$, where d_1 is the shortest diameter, and d_2 is the longest diameter (n=5). Data are the mean±SD of one representative experiment. Similar results were obtained in at least three independent experiments. (B) Western blot analysis of cleaved caspase 3 and cyclin B1 expression in tumor tissues that were collected on d 20. One representative result of three independent experiments was shown. (C) Hematoxylin-eosin staining of tumor mass after various therapies. Tumor tissues from different groups were collected on d 20, fixed in 10% formalin, and embedded in paraffin. Sections (5 μm thick) were prepared for HE staining.

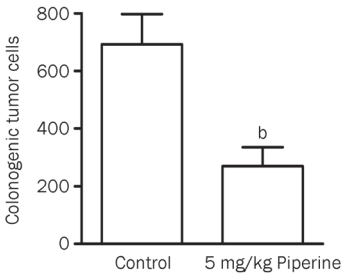

Figure 7. Piperine inhibited the metastasis of 4T1 tumors *in vivo*. 4T1 cells were implanted subcutaneously into the female BALB/c mice. After 3 days of implantation, piperine (0 and 5 mg/kg) was dissolved in 0.2% DMSO and intratumorally injected every three days for three times. Primary tumor was surgically removed on d 15 and mice were sacrificed on d 30 post-tumor inoculation for analysis of lung metastases by colonogenic assay. Mean±SD. n=3. ^bP<0.05.

demonstrated in various cell types. However, the antitumor activity and action mechanism of piperine on mammary cancer cells still remain unknown. Our results firstly indicated that piperine possessed significant cytoxicity against 4T1 cells both *in vitro* and *in vivo*. It was shown piperine induced the apoptosis of 4T1 cells in a dose-dependent manner. We investigated the effect of piperine on the expression levels of the Bcl-2 family, the pro-apoptotic Bax and the anti-apoptotic Bcl-2, which regulate mitochondrial apoptosis. When Bax is overexpressed in cells, apoptotic death in response to death signals is accelerated, while Bcl-2 is overexpressed, it heterodimerized with Bax and the cell death is repressed. Following the exposure to piperine, we found no change of Bax and Bcl-2 at protein level in the 4T1 cells, indicating that the apoptosis induced by piperine is not dependent of the Bcl-2 pathway. We found that the up-regulation of caspase 3 activity may lead to the apoptosis in 4T1 cells. Members of the cyclin family of proteins are key regulators of the cell cycle. Cyclins bind and activate members of the cyclin-dependent kinase (Cdk) family to control cell cycle progression. During the G_1 phase, cyclins D1, D2, and D3 form complexes with cdk4 or cdk6, and cyclin E with cdk2, to modulate the expression of proliferative genes. Cyclin A associates with cdk2 during the S phase, and with cdc2 (cdk1) at the S-G_2 boundary and into G_2. Progression through G_2, culminating in mitosis, further requires that cdc2 form complexes with cyclins B1 and B2[18]. We found that piperine treatment down-regulated the expression of cyclin B1 in 4T1 cells with a dose-dependent manner, while there was no change of cyclin D1 expression after piperine treatment. It is consistent with the observation that the percentage of 4T1 cells in G_2/M phase was increased after piperine treatment, while no significant change in G_0/G_1 phase cell population.

The results of the present study provide the potential application of piperine in tumor therapy. Bhat BG *et al* reported the metabolism of piperine including absorption, tissue distribution and excretion of urinary conjugates in rats[19]. Upon administration of piperine to male albino rats by gavage or intraperitoneally, about 97% was absorbed irrespective of the mode of dosing. Examination of the passage of piperine through the gut indicated that the highest concentration in the stomach and small intestine was attained at about 6 h[19].

The anticancer activity of piperine *in vivo* was probably partly due to its direct antiproliferative effect on 4T1 cells possibly by increasing the caspase 3 activity and down-regulated the expression of cyclin B1. In this study, we also provided the evidence that piperine can suppress the metastasis of 4T1 tumor *in vitro* and *in vivo*. It is well known the process of tumor cell metastasis requires the degradation of ECM molecules in the basement membrane, which is the largest barrier between cancer cells and the bloodstream. The key proteases that are involved in ECM degradation contain MMPs. Our results showed that Piperine significantly reduced the mRNA expression of MMP-9 and MMP-13. It had been reported that suppression of the expression of MMP-9 in tumor cells by piperine is through the inhibition of PKCα and ERK phosphorylation and reduction of NF-κB and AP-1 activation[11]. MMP-13 was shown to be expressed in more invasive breast carcinoma cells[20], and some evidence demonstrated that increased tumor-derived MMP-13 expression independently predicts poor prognoses[21]. In breast cancer, MMP-9 seems to be expressed in cancer tissue. Malignant breast tumors have increased MMP-9 activity compared to the benign tumors[22]. Nevertheless, MMP-9 expression has also been described as a positive prognostic marker in node-negative breast cancer[23]. In another study, positive stromal MMP-9 expression predicts poor survival in the hormone-responsive small tumors, whereas MMP-9 expression in carcinoma cells favors survival[24]. Thus, MMP-9 expression is associated with both inhibition and stimulation of tumor growth and progression. So, the exact mechanism of the inhibitory effect of piperine on tumor metastasis *in vivo* needs to be further elucidated. It have been supposed that the inhibition effects of piperine on oxygenase, p450 isoenzyme and cycloxygenase-1 expression may contribute to the antimetastatic qualities[25].

According to some authors, the antitumor activity of piperine may be related to its immunomodulatory properties, which involves the activation of cellular and humoral immune responses[26, 27]. It was proved to be a potent inhibitor of NF-κB, c-Fos, CREB, ATF-2, and proinflammatory cytokine gene expression in B16F-10 melanoma cells[10]. Other researches documented the chemopreventive efficacy of Piperine is probably due to their antilipidperoxidative and antioxidant potential as well as its modulating effect on the carcinogen detoxification process[28, 29]. Piperine is also known to enhance the bioavailability of some drugs by inhibiting drug metabolism or by increasing absorption[12, 30, 31]. Piperine with other antitumor drugs such as 5-FU[12], piplartine[13] augmented the antitumor activity and also decreased the side effects.

In conclusion, piperine can inhibit tumor growth by inducing cell apoptosis and cell cycle blockage. Also it can suppress 4T1 tumor growth and metastasis *in vivo*. Further studies will need to be carried out to determine the exact mechanisms of the antitumor action of piperine, and to investigate how it can

be used in cancer therapy alone or combination with other antitumor drugs.

Acknowledgements

This work was supported by grants from the National Natural Science Foundation of China (30872377), Education of Zhejiang Province (Y200803762), Zhejiang Provincial Natural Science Foundation (R2100528), Ningbo Municipal Bureau of Science and Technology (2010A610058) and also sponsored by Zhejiang Provincial Program for the Cultivation of High-level Innovative Health Talents.

Author contribution

Jian-gen SHEN, Qing-qing WANG, and Li-hua LAI designed research; Li-hua LAI, Qi-hong FU, Yang LIU, Kai JIANG, Qing-ming GUO, Qing-yun CHEN, and Bin YAN performed research; Li-hua LAI and Qi-hong FU analyzed data; Li-hua LAI and Qing-qing WANG wrote the paper.

References

1 Bhardwaj RK, Glaeser H, Becquemont L, Klotz U, Gupta SK, Fromm MF. Piperine, a major constituent of black pepper, inhibits human P-glycoprotein and CYP3A4. J Pharmacol Exp Ther 2002; 302: 645–50.
2 Volak LP, Ghirmai S, Cashman JR, Court MH. Curcuminoids inhibit multiple human cytochromes P450, UDP-glucuronosyltransferase, and sulfotransferase enzymes, whereas piperine is a relatively selective CYP3A4 inhibitor. Drug Metab Dispos 2008; 36: 1594–605.
3 Bhutani MK, Bishnoi M, Kulkarni SK. Anti-depressant like effect of curcumin and its combination with piperine in unpredictable chronic stress-induced behavioral, biochemical and neurochemical changes. Pharmacol Biochem Behav 2009; 92: 39–43.
4 Bang JS, Oh DH, Choi HM, Sur BJ, Lim SJ, Kim JY, *et al*. Anti-inflammatory and anti-arthritic effects of piperine in human interleukin-1beta-stimulated fibroblast-like synoviocytes and in rat arthritis models. Arthritis Res Ther 2009; 11: R49.
5 Kumar S, Singhal V, Roshan R, Sharma A, Rembhotkar GW, Ghosh B. Piperine inhibits TNF-alpha induced adhesion of neutrophils to endothelial monolayer through suppression of NF-kappaB and IkappaB kinase activation. Eur J Pharmacol 2007; 575: 177–86.
6 Wattanathorn J, Chonpathompikunlert P, Muchimapura S, Priprem A, Tankamnerdthai O. Piperine, the potential functional food for mood and cognitive disorders. Food Chem Toxicol 2008; 46: 3106–10.
7 Taqvi SI, Shah AJ, Gilani AH. Blood pressure lowering and vasomodulator effects of piperine. J Cardiovasc Pharmacol 2008; 52: 452–8.
8 Pathak N, Khandelwal S. Cytoprotective and immunomodulating properties of piperine on murine splenocytes: an *in vitro* study. Eur J Pharmacol 2007; 576: 160–70.
9 Srinivasan K. Black pepper and its pungent principle-piperine: a review of diverse physiological effects. Crit Rev Food Sci Nutr 2007; 47: 735–48.
10 Pradeep CR, Kuttan G. Effect of piperine on the inhibition of lung metastasis induced B16F-10 melanoma cells in mice. Clin Exp Metastasis 2002; 19: 703–8.
11 Hwang YP, Yun HJ, Kim HG, Han EH, Choi JH, Chung YC, *et al*. Suppression of phorbol-12-myristate-13-acetate-induced tumor cell invasion by piperine via the inhibition of PKCalpha/ERK1/2-dependent matrix metalloproteinase-9 expression. Toxicol Lett 2011; 203: 9–19.
12 Bezerra DP, de Castro FO, Alves AP, Pessoa C, de Moraes MO, Silveira ER, *et al*. *In vitro* and *in vivo* antitumor effect of 5-FU combined with piplartine and piperine. J Appl Toxicol 2008; 28: 156–63.
13 Bezerra DP, Castro FO, Alves AP, Pessoa C, Moraes MO, Silveira ER, *et al*. *In vivo* growth-inhibition of Sarcoma 180 by piplartine and piperine, two alkaloid amides from Piper. Braz J Med Biol Res 2006; 39: 801–7.
14 Pulaski BA, Ostrand-Rosenberg S. Reduction of established spontaneous mammary carcinoma metastases following immunotherapy with major histocompatibility complex class II and B7.1 cell-based tumor vaccines. Cancer Res 1998; 58: 1486–93.
15 Hong X, Liu Y, Hu G, Zhao D, Shen J, Shen F, *et al*. EBAG9 inducing hyporesponsiveness of T cells promotes tumor growth and metastasis in 4T1 murine mammary carcinoma. Cancer Sci 2009; 100: 961–9.
16 Valster A, Tran NL, Nakada M, Berens ME, Chan AY, Symons M. Cell migration and invasion assays. Methods 2005; 37: 208–15.
17 Yu P, Lee Y, Wang Y, Liu X, Auh S, Gajewski TF, *et al*. Targeting the primary tumor to generate CTL for the effective eradication of spontaneous metastases. J Immunol 2007; 179: 1960–8.
18 Koepp DM, Harper JW, Elledge SJ. How the cyclin became a cyclin: regulated proteolysis in the cell cycle. Cell 1999; 97: 431–4.
19 Bhat BG, Chandrasekhara N. Studies on the metabolism of piperine: absorption, tissue distribution and excretion of urinary conjugates in rats. Toxicology 1986; 40: 83–92.
20 Balduyck M, Zerimech F, Gouyer V, Lemaire R, Hemon B, Grard G, *et al*. Specific expression of matrix metalloproteinases 1, 3, 9 and 13 associated with invasiveness of breast cancer cells *in vitro*. Clin Exp Metastasis 2000; 18: 171–8.
21 Zhang B, Cao X, Liu Y, Cao W, Zhang F, Zhang S, *et al*. Tumor-derived matrix metalloproteinase-13 (MMP-13) correlates with poor prognoses of invasive breast cancer. BMC Cancer 2008; 8: 83.
22 Hanemaaijer R, Verheijen JH, Maguire TM, Visser H, Toet K, McDermott E, *et al*. Increased gelatinase-A and gelatinase-B activities in malignant *vs* benign breast tumors. Int J Cancer 2000; 86: 204–7.
23 Scorilas A, Karameris A, Arnogiannaki N, Ardavanis A, Bassilopoulos P, Trangas T, *et al*. Overexpression of matrix-metalloproteinase-9 in human breast cancer: a potential favourable indicator in node-negative patients. Br J Cancer 2001; 84: 1488–96.
24 Pellikainen JM, Ropponen KM, Kataja VV, Kellokoski JK, Eskelinen MJ, Kosma VM. Expression of matrix metalloproteinase (MMP)-2 and MMP-9 in breast cancer with a special reference to activator protein-2, HER2, and prognosis. Clin Cancer Res 2004; 10: 7621–8.
25 Stohr JR, Xiao PG, Bauer R. Constituents of Chinese Piper species and their inhibitory activity on prostaglandin and leukotriene biosynthesis *in vitro*. J Ethnopharmacol 2001; 75: 133–9.
26 Sunila ES, Kuttan G. Immunomodulatory and antitumor activity of *Piper longum* Linn and piperine. J Ethnopharmacol 2004; 90: 339–46.
27 Pathak N, Khandelwal S. Modulation of cadmium induced alterations in murine thymocytes by piperine: oxidative stress, apoptosis, phenotyping and blastogenesis. Biochem Pharmacol 2006; 72: 486–97.
28 Manoharan S, Balakrishnan S, Menon VP, Alias LM, Reena AR. Chemopreventive efficacy of curcumin and piperine during 7,12-dimethylbenz[a]anthracene-induced hamster buccal pouch carcinogenesis. Singapore Med J 2009; 50: 139–46.
29 Selvendiran K, Banu SM, Sakthisekaran D. Oral supplementation of piperine leads to altered phase II enzymes and reduced DNA damage and DNA-protein cross links in Benzo(a)pyrene induced experimental lung carcinogenesis. Mol Cell Biochem 2005; 268: 141–7.
30 Zhao JQ, Du GZ, Xiong YC, Wen YF, Bhadauria M, Nirala SK. Attenuation of beryllium induced hepatorenal dysfunction and oxidative stress in rodents by combined effect of gallic acid and piperine. Arch Pharm Res 2007; 30: 1575–83.
31 Suresh D, Srinivasan K. Studies on the *in vitro* absorption of spice principles — curcumin, capsaicin and piperine in rat intestines. Food Chem Toxicol 2007; 45: 1437–42.

Acta Pharmacologica Sinica (2012) 33: 531–541
 1671-4083/12 $32.00
www.nature.com/aps

Original Article

Gambogic acid inhibits TNF-α-induced invasion of human prostate cancer PC3 cells *in vitro* through PI3K/Akt and NF-κB signaling pathways

Lei LÜ[1], Dong TANG[1], Liang WANG[1], Lu-qi HUANG[2], Guo-song JIANG[1], Xing-yuan XIAO[1], Fu-qing ZENG[1, *]

[1]*Department of Urology, Union Hospital, Tongji Medical College, Huazhong University of Science and Technology, Wuhan 430022, China;* [2]*Department of Neurology, Jingzhou Central People's Hospital, Jingzhou 434020, China*

Aim: To investigate the mechanisms underlying the inhibitory effect of gambogic acid (GA) on TNF-α-induced metastasis of human prostate cancer PC3 cells *in vitro*.
Methods: TNF-α-mediated migration and invasion of PC3 cells was examined using migration and invasion assays, respectively. NF-κB transcriptional activity and nuclear translocation were analyzed with luciferase reporter gene assays, immunofluorescence assays and Western blots. The ability of p65 to bind the promoter of Snail, an important mesenchymal molecular marker, was detected using a chromatin immunoprecipitation (ChIP) assay. After treatment with Snail-specific siRNA, the expression of invasiveness-associated genes was measured using quantitative real-time PCR and Western blot.
Results: GA significantly inhibited the viability of PC3 cells at 1–5 μmol/L, but did not produce cytotoxic effect at the concentrations below 0.5 μmol/L. GA (0.125–0.5 μmol/L) dose-dependently inhibited the migration and invasion of PC3 cells induced by TNF-α (10 ng/mL). Moreover, the TNF-α-mediated activation of phosphatidylinositol-3-OH kinase/protein kinase B (PI3K/Akt) and NF-κB pathways was suppressed by GA (0.5 μmol/L). Furthermore, this anti-invasion effect of GA was associated with regulation of Snail. Snail expression was significantly down-regulated by treatment with GA (0.5 μmol/L) in the TNF-α-stimulated PC3 cells.
Conclusion: GA inhibits TNF-α-induced invasion of PC3 cells via inactivation of the PI3K/Akt and NF-κB signaling pathways, which may offer a novel approach for the treatment of human prostate cancer.

Keywords: gambogic acid; human prostate cancer; tumor metastasis; tumor invasion; tumor necrosis factor-α (TNF-α); PI3K/Akt signaling pathway; NF-κB signaling pathway; Snail

Acta Pharmacologica Sinica (2012) 33: 531–541; doi: 10.1038/aps.2011.180; published online 19 Mar 2012

Introduction

TNF-α is a potent pro-inflammatory cytokine involved in the regulation of multiple physiological and pathological processes, including inflammatory reaction, immunity, cachexia and tumor progression[1]. As a multifunctional cytokine, TNF-α is a double-edged sword in the treatment of malignant disease. High doses of human recombinant TNF-α were found to exert a powerful anti-cancer effect by inducing cell apoptosis and inhibiting tumor blood vessel formation. However, in low doses and with chronic stimulation, TNF-α could induce angiogenesis, proliferation, invasion and metastasis of tumor cells[2].

As an endogenous tumor-promoting factor TNF-α plays an important role in promoting invasion in many cancer types including prostate cancer. Some crosstalk between pathways that are activated by TNF-α, such as NF-κB and PI3K/Akt[3, 4], is correlated with TNF-α-mediated tumor cell migration and invasion. For example, sustained activation of NF-κB by TNF-α has been reported to be involved in the regulation of tumor cell invasion via up-regulated expression of macrophage migration inhibitory factor (MIF), enhanced matrix metalloproteinases (MMPs) production and stabilized Snail[5, 6]. In addition, TNF-α also induces a cell-invasion signal through the PI3K/Akt pathway. Activation of Akt by TNF-α could enhance the transcription of Zeb2 and suppress the expression of E-cadherin[7]. Considering the critical role of TNF-α in tumor invasion, inhibiting the TNF-α signaling pathway may provide an important base for new targeting therapies in the intervention of human prostate cancer.

Gambogic acid (GA) is a compound extracted from natural resin gamboges, which has been widely used in traditional Chinese medicine[8]. It has been shown that GA exhibited anti-

* To whom correspondence should be addressed.
E-mail Fuqing_Zeng@163.com
Received 2011-09-01 Accepted 2011-11-28

proliferative and pro-apoptotic effects on breast, oral, stomach and liver cancer cells[9–13]. Although it is clear that GA inhibited the growth of different tumor cell lines by promoting apoptosis and repressing proliferation, the relationship between GA and tumor metastasis remains unclear.

The aim of this study is to evaluate whether GA can inhibit the TNF-α-mediated invasion in human prostate cancer PC3 cells and to further explore its functional mechanism.

Materials and methods

Cell culture

Human prostate cancer PC3 cells were cultured in RPMI-1640 medium supplemented with 10% fetal bovine serum (FBS), 100 U/mL penicillin and 100 μg/mL streptomycin. The cells were incubated in 5% CO_2 at 37 °C.

Antibodies and reagents

GA was purchased from Sigma-Aldrich (St Louis, MO, USA), dissolved in DMSO at a concentration of 25 mmol/L, aliquoted and stored at -20 °C. Recombinant TNF-α was obtained from R&D systems (Minneapolis, MN, USA). Polyclonal antibodies directed against MMP-9, fibronectin and GAPDH were purchased from Santa Cruz Biotechnology (Santa Cruz, CA, USA). Anti-Snail, anti-E-cadherin and anti-NF-κB p65 were purchased from Abcam (Abcam, USA). Anti-Akt, anti-phosphor-Akt (Ser^{473}), anti-GSK-3β and anti-phosphor-GSK-3β (Ser^{9}) were obtained from Cell Signaling Technology (Beverly, MA, USA). PI3K inhibitor LY294002 (5 μmol/L) was purchased from Sigma-Aldrich (St Louis, MO, USA).

Cell viability assay

The impact of GA on cell viability was assessed by the MTT assay (Beyotime Institute Biotechnology, China). Briefly, PC3 cells at 5×10^3 per well were seeded in 96-well plates and treated with different concentrations of GA for 24 h. The relative level of cell viability in each group of cells compared to control unmanipulated cells was calculated, and the unmanipulated control cells were designated as 100%.

Migration and invasion assays

Cell invasion assays were performed in a Boyden chemotaxis chamber (matrigel-coated polycarbonate membrane, Costar, USA) according to the manufacturer's protocol. Briefly, PC3 cells (5×10^4) were suspended in serum-free RPMI-1640 medium and were placed into the upper chamber in the presence of various concentrations of GA. In the lower chamber, serum-free RPMI-1640 containing 10 ng/mL TNF-α served as a chemoattractant. After incubation for 24 h, the cells in the upper chamber were carefully wiped with cotton swabs, and the cells at the bottom of the membrane were fixed and stained with 0.1% crystal violet. Then, the stained cells that invaded the lower surface of the membrane were counted under the microscope. Migration assays were carried out using the same procedure, except that the polycarbonate membrane was not coated with matrigel, and the incubation time was 12 h.

Western blot analysis

Briefly, cells were harvested and lysed with RIPA buffer containing protease inhibitor (Pierce, USA). After quantification of the protein concentrations using the BCA protein assay reagent kit (Pierce, USA), an equal amount of proteins (30 μg) was resolved by 10% SDS-PAGE and transferred to nitrocellulose membranes. Subsequently, the membranes were blocked with 5% skim milk and incubated with the antibodies as described above. Protein bands were visualized using the super signal kit, according to the manufacturer's instructions (Pierce, USA).

Immunofluorescence assay

The cells were fixed with 4% paraformaldehyde for 10 min and permeabilized with 0.5% Triton X-100 for 10 min at room temperature. Then, the cells were washed with PBS for three times, blocked with 10% goat serum for 1 h at room temperature and incubated with primary anti-NF-κB p65 antibody overnight at 4 °C. Then, the cells were incubated with rabbit IgG antibody labeled with Cy3 and viewed under a fluorescence microscope.

Quantitative real-time PCR (qRT-PCR)

Total RNA was extracted using the TRIzol Reagent kit (Invitrogen, USA) and reverse transcription was performed according to the manufacturer's protocol. The relative levels of target gene mRNA transcripts to that of the control were determined by quantitative real-time polymerase chain reaction (qRT-PCR), using cDNA as a template, the specific primers and the SYBR premix system. The sequences of the specific primers used in the present study were as followed: Snail (NM_005985), forward primer 5′-CTTCCAGCAGCCCTACGA-3′, reverse primer 5′-AGCCTTTCCCACTGTCCTC-3′; MMP-9 (NM_004994), forward primer 5′-CGCTGGGCTTAGATCATTC-3′, reverse primer 5′-CAGGGCGAGGACCATAGA-3′; E-cadherin (NM_004360), forward primer 5′-ATCTTCAATCCCACCACG-3′, reverse primer 5′-TGTAGAATGTACTGCTGCTT-3′; fibronectin (NM_212482), forward primer 5′-ATGGAGGAAGCCGAGGTT-3′, reverse primer 5′-AGCGGTTTGCGATGGTAC-3′; and GAPDH (NM_002046) forward primer 5′-TGAAGGTCGGAGTCAACGG-3′, reverse primer 5′-CCTGGAAGATGGTGATGGG-3′. The level of GAPDH mRNA transcript was used to normalize all reported gene expression levels, and the data were analyzed using the $2^{-\Delta\Delta Ct}$ method.

Transfection and luciferase reporter gene assay

Briefly, PC3 cells at 1×10^6 cells per well were plated in 6-well plates and grown to approximately 70% confluence. Then, the cells were transiently co-transfected with pGL6-NF-κB-TA-luc (Beyotime Institute Biotechnology, China) and pRL-TK (Promega) for normalizing transfection efficiency. Six hours after transfection, the cells were pretreated with 10 ng/mL TNF-α for 12 h and subsequently incubated with or without GA for an additional 12 h, then harvested with passive lysis buffer

(Promega). The NF-κB transcriptional activity was assayed by using the dual luciferase system (Promega). The results were normalized to the luciferase activity of the internal control.

Chromatin immunoprecipitation (ChIP) assay

ChIP assay was performed using the ChIP Assay kit (Beyotime Institute Biotechnology, China) according to the manufacturer's protocol. To confirm the ability of p65 to bind to the Snail promoter, an anti-NF-κB p65-specific antibody was used to immunoprecipitate regions of the Snail promoter bound by anti-NF-κB p65 in this study. NF-κB p65-immunoprecipitated DNA was amplified with PCR using specific primers to analyze the NF-κB p65 binding site of the putative Snail promoter. The Snail promoter-specific primers were described as follows: forward primer 5′-GCCTCGCTTCGCTCGACGTC-3′ and reverse primer 5′-AGGCCACTCCCCGAGCAGGT-3′.

RNA interference

The mRNA sequence of Snail was obtained from GenBank (NM_005985), and the targeting sequences were designed using an RNAi algorithm available online. The siRNA sequences for Snail as follows: Snail siRNA-1, 5′-GCCCUCCGACCCCAAUCGGtt-3′ (sense), 5′-CCGAUUGGGGUCGGAGGGCtt-3′ (antisense); Snail siRNA-2, 5′-UCGGAAGCCUAACUACAGCtt-3′ (sense), 5′-GCUGUAGUUAGGCUUCCGAtt-3′ (antisense); and Snail siRNA-3, 5′-UUGCCUGGGCCUCCCUUCGtt-3′ (sense), 5′-CGAAGGGAGGCCCAGGCAAtt-3′ (antisense). Snail-specific siRNAs and a nonsense siRNA (control siRNA) were obtained from Ribobio (Guangzhou, China). PC3 cells were transfected using Translipid reagent (TransGen, China) according to the manufacturer's protocol.

Statistical analysis

The results are presented as the mean±SD of at least three independent experiments. Statistical analysis was performed using one-way ANOVA or Student-Newman-Keuls (SNK)-*q* Test. Differences were considered statistically significant when P values <0.05.

Results

Cytotoxicity of GA on PC3 cells

A series of concentrations of GA were tested on cell viability using an MTT assay. The results showed that GA with concentrations over 0.5 μmol/L markedly inhibited cell viability of PC3 cells. However, low concentrations of GA (<0.5 μmol/L) did not produce obvious cytotoxic effect on PC3 cells (Figure 1A). Therefore, a concentration of ~0.5 μmol/L GA was chosen for the subsequent experiments.

Inhibition of TNF-α-induced cell migration and invasion by GA

To investigate whether GA exerts a regulatory effect on cell migration and invasion, TNF-α (10 ng/mL) was applied to the lower chamber as a chemoattractive agent to induce *in vitro* migration and invasion of PC3 cells. Compared to the control, TNF-α could significantly induce migration and invasion of PC3 cells. Interestingly, administration of GA (0.5 μmol/L) caused an inhibition of PC3 cell migration and invasion induced by TNF-α. Further studies found that GA inhibited TNF-α-induced cell migration and invasion in a dose-dependent manner (Figure 1B).

Involvement of the PI3K/Akt signaling pathway in GA-induced inhibition of cell invasion by TNF-α

Previous studies have reported that the PI3K/Akt/GSK-3β pathway was involved in cell migration and invasion[14, 15]. Akt and GSK-3β are both the critical components of signal transduction following PI3K activation[16]. We therefore asked whether the PI3K/Akt/GSK-3β pathway is associated with the TNF-α-induced cell invasion of PC3 cells. Following TNF-α treatment, PC3 cells showed a striking phosphorylation of Akt, whereas total Akt level remains unaltered. This increased phosphorylation of Akt reached its peak at 2 h after the TNF-α (10 ng/mL) application and returned back to the basal level

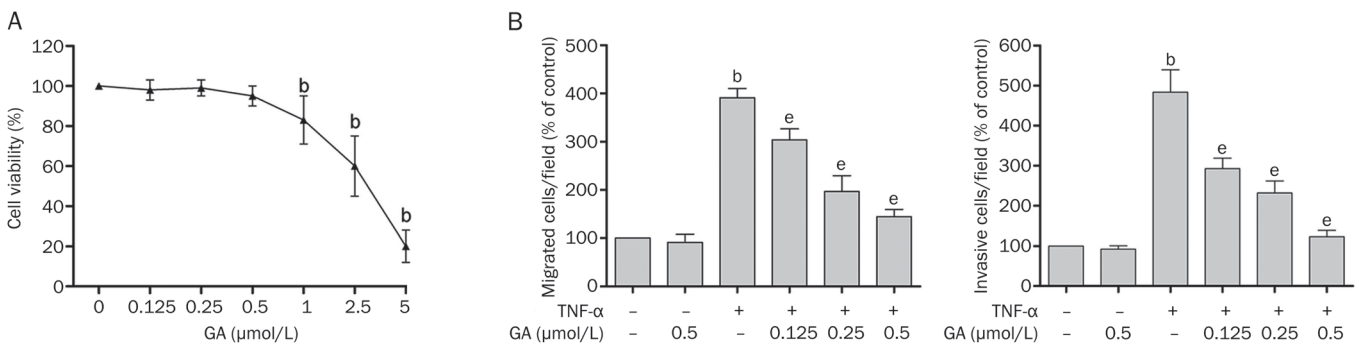

Figure 1. GA inhibits TNF-α-induced invasion of PC3 cells. (A) The effect of GA on the viability of PC3 cells. Cells were treated with GA at the indicated concentrations for 24 h. Viability of PC3 cells was determined by an MTT assay. (B) Inhibitory effect of GA on TNF-α-induced migration and invasion of PC3 cells. PC3 cells (5×10^4) were seeded into the upper compartment and treated with GA at the indicated concentrations. TNF-α (10 ng/mL) was applied to the lower chamber as a chemoattractive agent. Then, the cells were incubated for 12 h (migration assay) or 24 h (invasion assay). The migrating or invading cells were counted under the microscope. Data are presented as the mean±SD of each group of cells from three independent experiments. $^bP<0.05$ *vs* control group; $^eP<0.05$ *vs* TNF-α alone treatment group. Imaged at 200× magnification.

between 6–12 h after the application. In parallel, GSK-3β displayed dramatic phosphorylation with a similar magnitude and time course with Akt. In the presence of GA, the TNF-α-induced increase in Akt phosphorylation was largely reduced, while increased GSK-3β phosphorylation was not affected (Figure 2A and 2B). To further determine whether the inhibition of the TNF-α-induced invasion by GA is mediated by Akt signaling pathway, we evaluated the effect of the PI3K/Akt pathway inhibitor on *in vitro* migration and invasion. We found that treatment with LY294002 strongly suppressed PC3 cell migration and invasion induced by TNF-α, which is identical to the effect of GA (Figure 3). This result suggested that the PI3K/Akt signaling pathway may be involved in the anti-invasion effect of GA in PC3 cells.

Suppression of TNF-α-induced NF-κB transcriptional activity and NF-κB nuclear translocation by GA

We then addressed whether GA influences TNF-α-induced NF-κB transcriptional activity in PC3 cells using an NF-κB-mediated luciferase reporter gene assay. Our results demonstrated that TNF-α strongly induced luciferase activity of endogenous NF-κB compared to the basal activity in non-stimulated control cells. However, delivery of GA dose-dependently reduced TNF-α-mediated NF-κB transcriptional activity (Figure 4A). Under inflammatory stimulation, dissociation of IκB from the IκB/NF-κB complex leads to NF-κB p65 subunit translocation into the nucleus where it binds to specific promoter sites on target genes[17]. To investigate whether the anti-invasion effect of GA is mediated by inhibition of

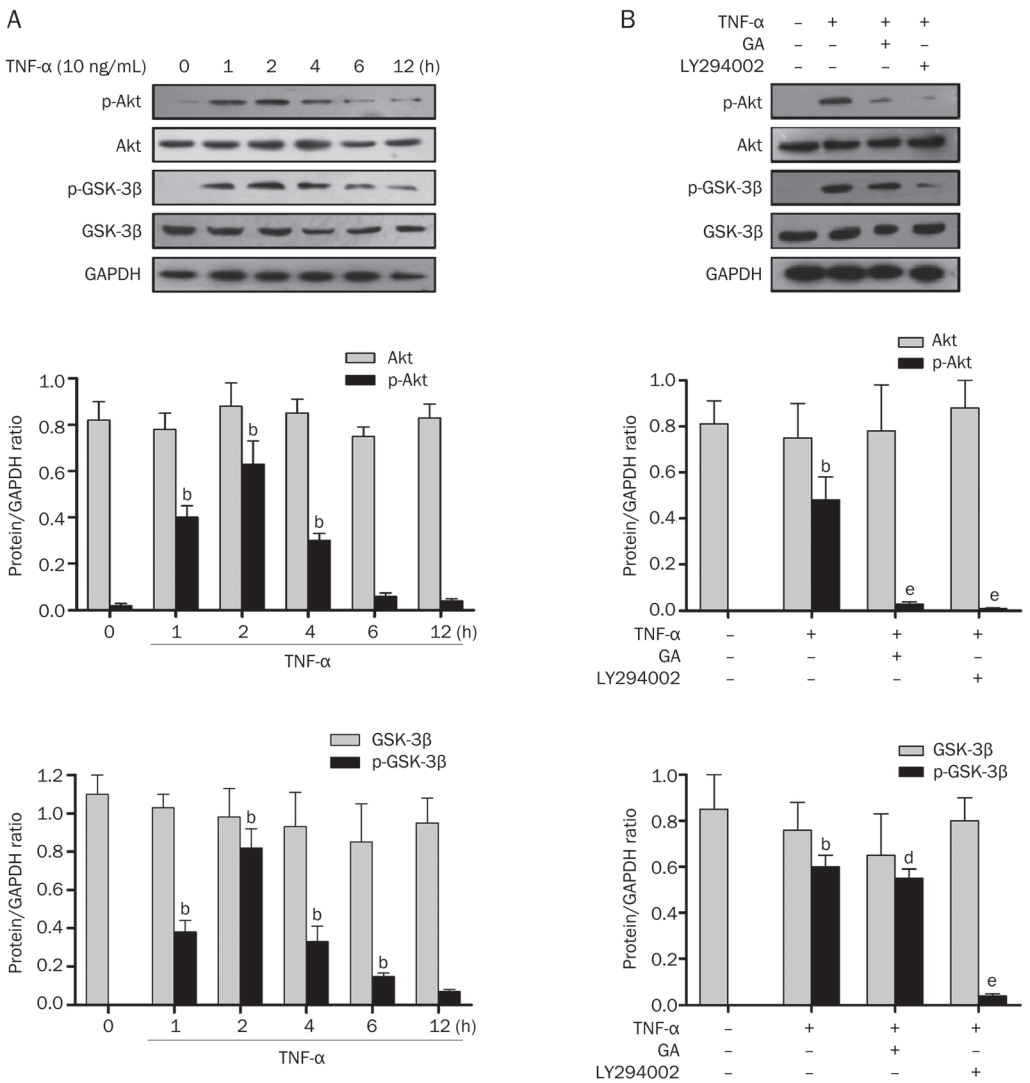

Figure 2. Effect of Gambogic acid (GA) on TNF-α-mediated activation of PI3K/Akt/GSK-3β pathway. (A) PC3 cells were treated with TNF-α (10 ng/mL) for indicated time. The active phosphorylated forms of Akt and GSK-3β or Akt, GSK-3β and GAPDH were analyzed by Western blot analysis. (B) Cells were pretreated with GA (0.5 μmol/L) or the specific PI3K inhibitor LY294002 (5 μmol/L) for 2 h and then treated with TNF-α (10 ng/mL) for an additional 2 h. The active phosphorylated forms of Akt and GSK-3β were determined using Western blot analysis. Data are representative images or expressed as the mean±SD of each group of cells from three independent experiments. $^{b}P<0.05$ *vs* control group; $^{d}P>0.05$, $^{e}P<0.05$ *vs* TNF-α alone treatment group.

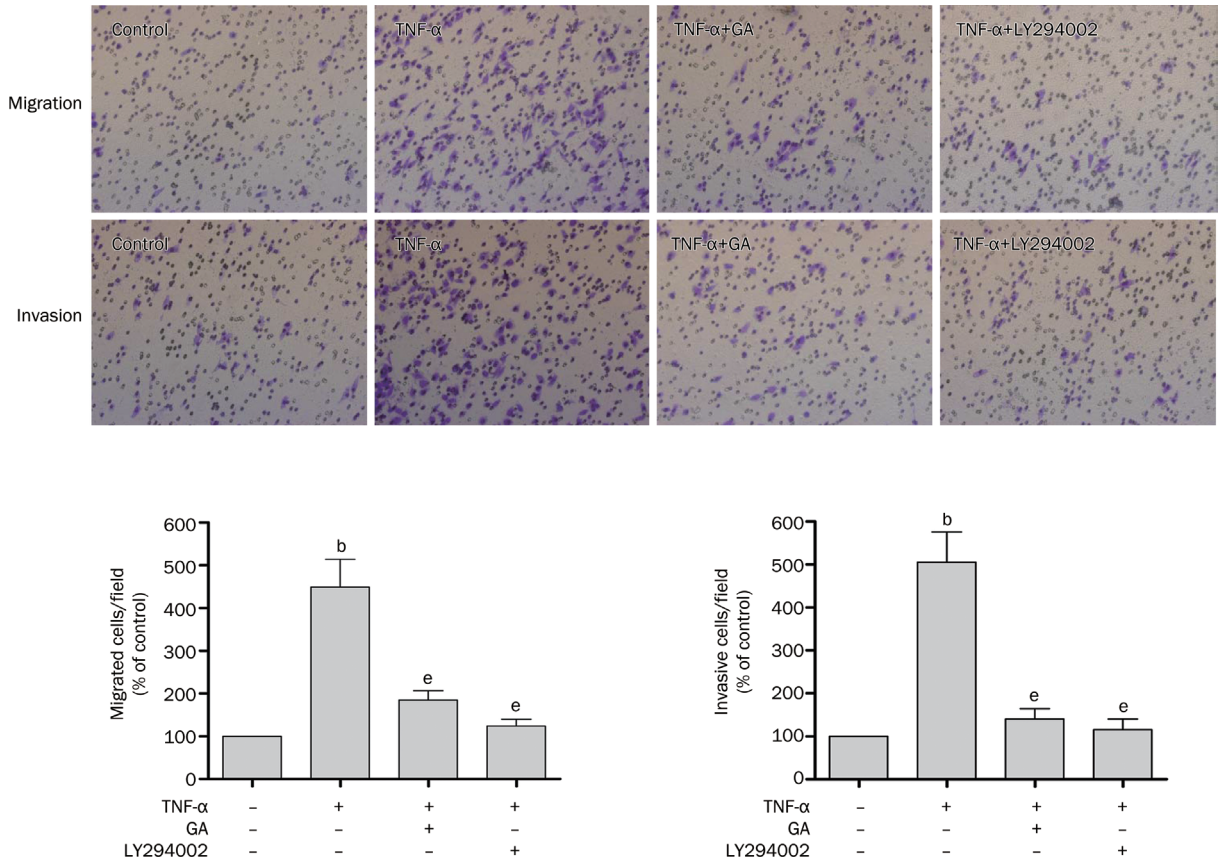

Figure 3. Effect of LY294002 on TNF-α-induced migration and invasion. PC3 cells (5×10^4) were cultured in the upper compartment and incubated with GA (0.5 μmol/L) or LY294002 (5 μmol/L) for 12 h (migration assay) or 24 h (invasion assay). The TNF-α-induced migrating or invading cells were counted in a blind manner. Data are representative images or expressed as the mean±SD of each group of cells from three independent experiments. $^bP<0.05$ *vs* control group; $^eP<0.05$ *vs* TNF-α alone treatment group. Imaged at 200× magnification.

TNF-α-induced NF-κB activation, we evaluated the nuclear translocation of NF-κB p65 using Western blot and immunofluorescence analyses. Western blot and immunofluorescence analyses revealed that TNF-α induced an obvious increase in NF-κB p65 nuclear translocation in comparison to the control group. However, this increased NF-κB nuclear translocation was significantly suppressed by the treatment with GA (Figure 4B and 4C).

GA represses the TNF-α-induced physical interaction between the p65 subunit of NF-κB and Snail in PC3 cells

Snail, an important mesenchymal molecular marker, is known to increase tumor cell invasion and contributes to the induction of the epithelial to mesenchymal transition (EMT)[18]. To investigate whether TNF-α-stimulation could affect the expression of Snail, we determined the expression levels of Snail mRNA and protein using qRT-PCR and Western blot analysis, respectively. Upon TNF-α-stimulation, both Snail mRNA and protein displayed an up-regulated expression in PC3 cells compared to the control group. However, administration of GA was found to markedly reduce the increase of Snail mRNA and protein levels induced by TNF-α (Figure 5A and 5B). It was recently reported that transcription of Snail was regulated by the NF-κB pathway[6]. As a critical subunit of NF-κB, p65 can bind the human Snail promoter and increase Snail transcription[19]. To further determine the mechanisms underlying the regulatory effect of GA on TNF-α-induced cell invasion, we examined the DNA binding activity of NF-κB using a ChIP assay. Our data revealed that TNF-α-stimulation significantly increased p65 binding to the Snail promoter. However, the TNF-α-mediated NF-κB DNA binding activity was inhibited by treatment with GA (Figure 5D).

Knockdown of Snail by RNAi inhibits TNF-α-induced cell invasion

Because the expression level of Snail was up-regulated by TNF-α-stimulation, we investigated the effect of silencing Snail on TNF-α-induced cell invasion. It has been previously shown that Snail overexpression could induce tumor progression via regulation of invasion, migration and EMT in a variety of cancer cell lines[20], which can be attenuated by a knockdown of Snail. We therefore assessed the role of Snail on TNF-α-induced cell invasion with RNA interference. As expected, transfection with specific Snail siRNA-1 dramatically inhibited TNF-α-mediated cell invasion consistent with the decreased expression levels of Snail (Figure 6). When compared to the GA treatment group, the Snail siRNA-1

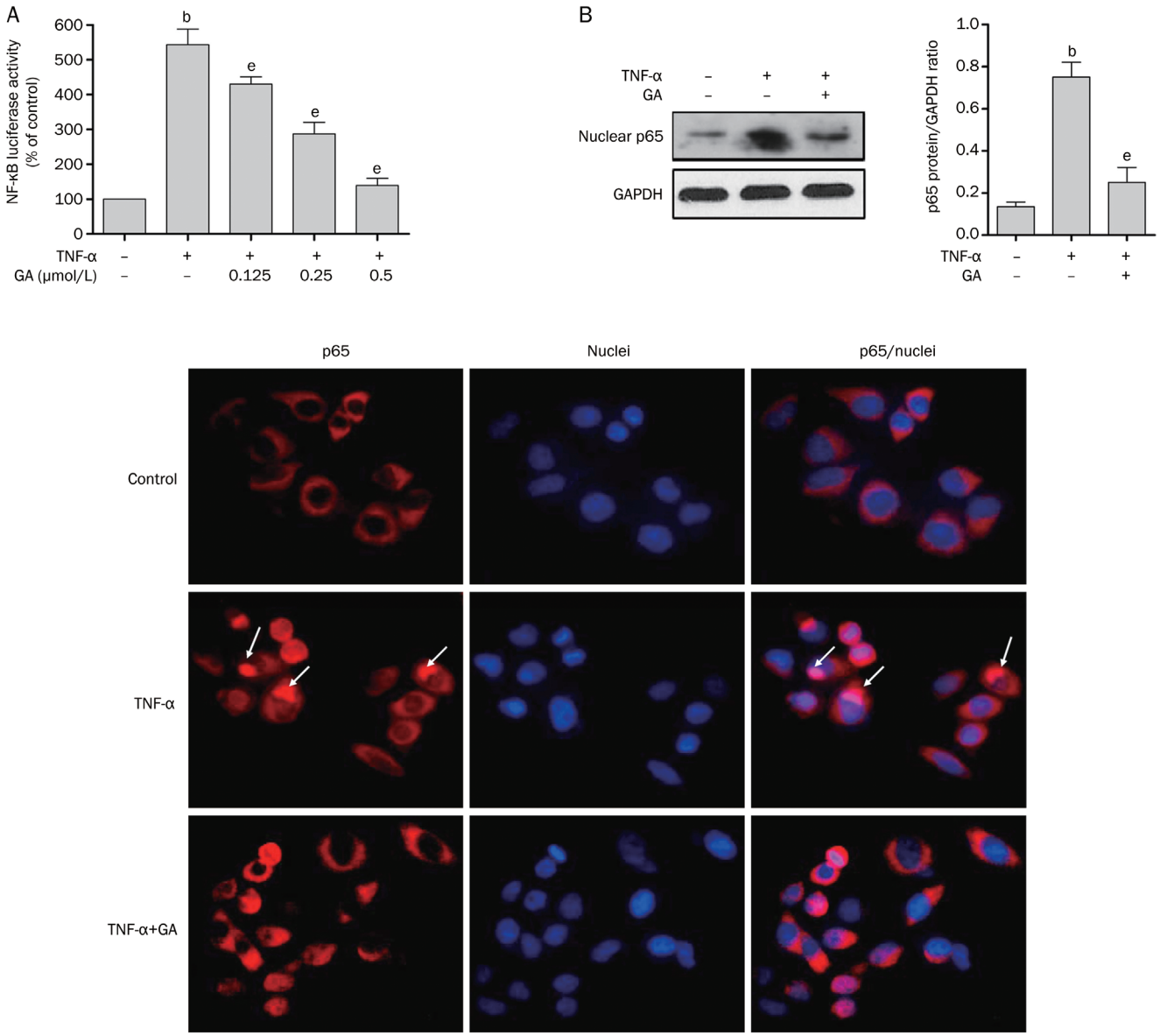

Figure 4. Effect of GA on TNF-α-induced activation of NF-κB. (A) PC3 cells were transiently co-transfected with pGL6-NF-κB-TA-luc and pRL-TK. After 6 h, the cells were incubated with TNF-α (10 ng/mL) for 12 h. Then, the cells were treated with or without GA for additional 12 h. The transcriptional activity of NF-κB was determined by luciferase reporter gene assay and normalized to the internal control. (B) PC3 cells were pretreated with TNF-α (10 ng/mL) for 12 h and incubated with or without GA (0.5 μmol/L) for additional 12 h. Cells were then harvested and cellular nuclear protein extracted using Nuclear and Cytoplasmic Extraction Reagents kit according to the manuscript's instructions. Overall, 30 μg of the nuclear proteins was resolved by SDS-PAGE on 10% polyacrylamide gels and transferred to nitrocellulose membranes. The blots were probed with anti-NF-κB p65 or anti-GAPDH antibodies. (C) The nuclear translocation was analyzed by immunofluorescence assay. Data are representative images or expressed as the mean±SD of each group of cells from three independent experiments. $^{b}P<0.05$ *vs* control group; $^{e}P<0.05$ *vs* TNF-α alone treatment group. Imaged at 200× magnification.

group exhibited a similar effect to GA in inhibiting the expression levels of Snail, cell invasion and migration stimulated by TNF-α (Figure 6C–6E). These data further supported that the regulation of Snail appears to be responsible for the inhibition of TNF-α-induced cell invasion by GA.

Modulation of TNF-α-induced invasiveness-associated genes expression by GA

Considering that Snail regulates the expression of invasiveness-associated genes, such as E-cadherin, MMP-9, and fibronectin[21, 22], we determined whether GA could regulate the expression of invasiveness-associated genes in TNF-α-stimulated PC3 cells. It was demonstrated that TNF-α-treated PC3 cells exhibited up-regulated mRNA and protein expression levels of both MMP-9 and fibronectin. In contrast, the expression of E-cadherin was down-regulated by TNF-α. However, incubation of cells with GA or Snail siRNA effectively blocked the TNF-α-induced upregulation of MMP-9 and

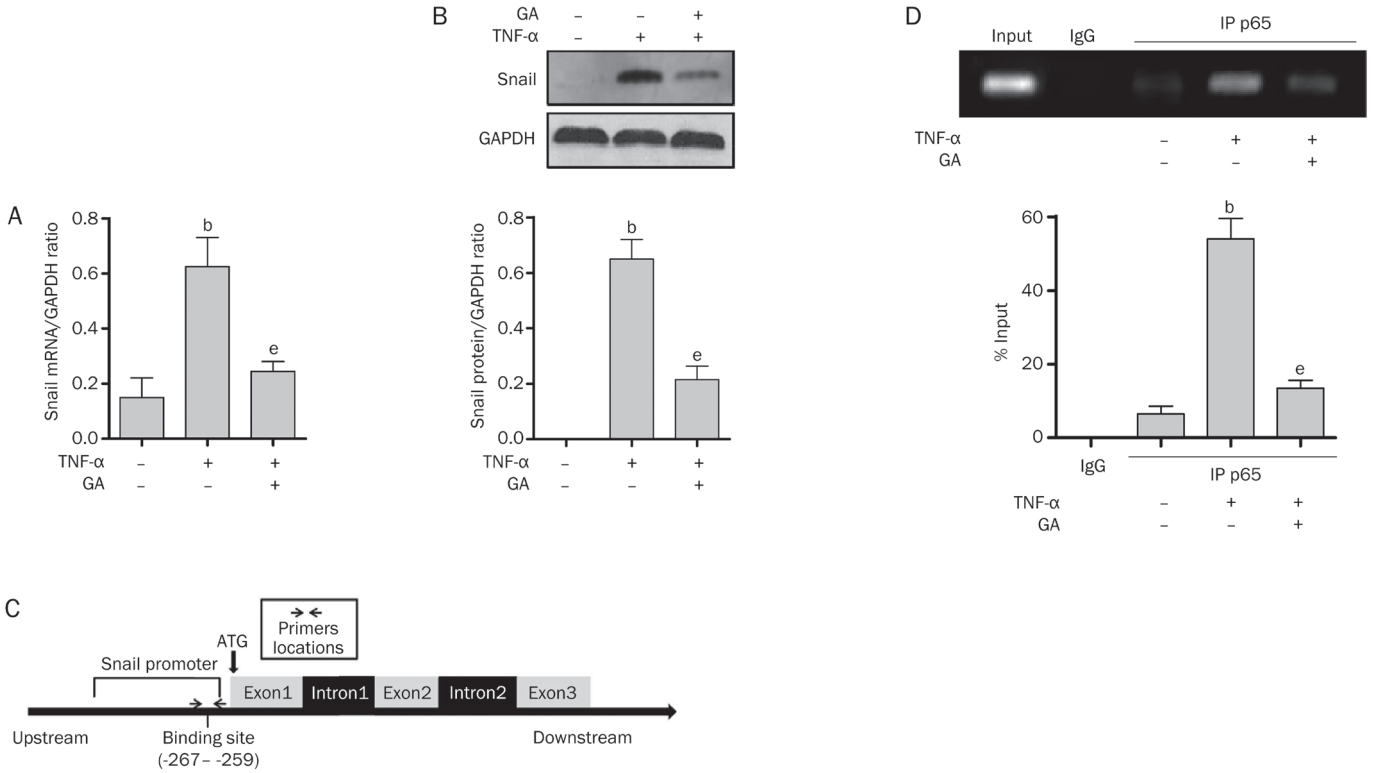

Figure 5. Effect of GA on TNF-α-induced physical interaction between p65 and Snail. (A, B) Cells were treated with TNF-α (10 ng/mL) for 12 h, and the expression of Snail mRNA and protein was determined by qRT-PCR and western blot analysis, respectively. (C) Schematic diagram showing positions of putative Snail promoter and NF-κB p65 binding site. The upstream DNA sequence of the Snail gene and putative Snail promoter sequence were analyzed using the Promoter Retrieval online database (http://rulai.cshl.edu/cgi-bin/TRED). The binding site of the putative Snail promoter was obtained by gene regulation available online (http://www.gene-regulation.com). (D) Cells were pretreated with TNF-α (10 ng/mL) for 12 h and then incubated with or without GA (0.5 μmol/L) for an additional 12 h. The ability of p65 to bind to the Snail promoter was detected using a ChIP assay. ChIP was performed using antibodies against p65 and IgG. NF-kB p65-immunoprecipitated DNA was amplified with PCR. Data are representative images or expressed as the mean±SD of each group of cells from three independent experiments. $^{b}P<0.05$ *vs* control group; $^{e}P<0.05$ *vs* TNF-α alone treatment group.

fibronectin and downregulation of E-cadherin (Figure 7A and 7B).

Discussion

Prostate cancer is the most common urological neoplasm and the major cause of cancer-related death in aging men[23]. An important factor for the mortality rate of prostate cancer is the invasiveness of the constituent tumor cells causing metastasis[24]. Prostate cancer usually progresses through hormone-dependent to hormone-independent stages, leading to a low efficacy for anti-androgen therapies and increasing the probability of metastasis[25]. Despite numerous efforts that have focused on investigating the processes of tumor invasion and metastasis for the development of new therapies, the precise mechanisms causing the directional migration and invasion of tumor cells into selective organs is poorly understood. Thus, development of effective anti-metastatic therapies for prostate cancer will be of great significance.

Inflammation has been confirmed to play a crucial role in cancer progression including prostate cancer[26]. It is assumed that inflammation could promote survival or induce the death of tumor cells through various signaling pathways[27]. In some cancers, inflammation was identified as a tumor promoting factor, which might increase the risk of tumor metastasis[28]. TNF-α has been demonstrated to be an important inflammatory cytokine produced by immune cells under inflammation. Although some studies reported its capacity to induce tumor necrosis[29, 30], accumulating evidence has shown that TNF-α could induce tumor cell invasion and migration as an endogenous tumor promoter[31–34]. Overproduction of TNF-α disrupted cell adhesion and increased the metastatic potential of tumor cells. In addition, it is worthwhile to mention that TNF-α might increase the risk of cancer development and spreading in the specific tumor microenvironment[35]. GA, a major active ingredient of gamboges, has been recently demonstrated to possess potent anti-cancer activity in several tumor cell lines[9–13]. Previous reports have shown that GA could induce cell apoptosis and repress proliferation via several mechanisms, such as inhibiting the NF-κB signaling pathway, regulating the expression of Bcl-2 and Bax and disturbing CDK7-mediated phosphorylation of CDC2/p34[9, 10, 12]. As an NF-κB inhibitor, GA could enhance the pro-apoptotic

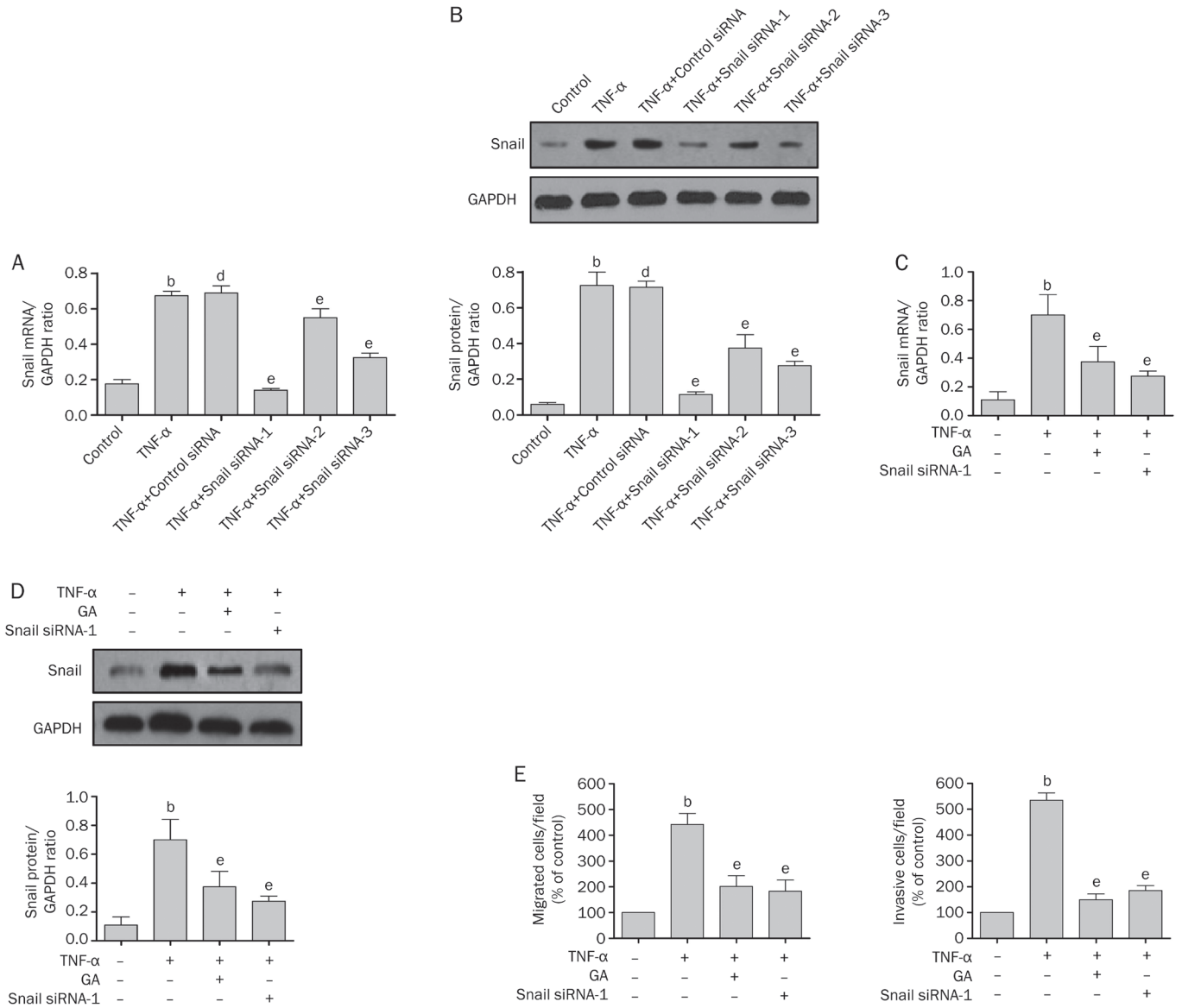

Figure 6. Effect of Snail silencing on the TNF-α-induced migration and invasion of PC3 cells. (A, B) PC3 cells were pretreated with TNF-α (10 ng/mL) for 12 h and then transfected with control siRNA or Snail siRNAs for 24 h. The mRNA and protein expression levels of Snail were determined by qRT-PCR and Western blot analysis, respectively. (C, D) PC3 cells were treated with the Snail-specific siRNA-1 for 24 h or GA for 12 h, and the TNF-α-induced mRNA and protein expression levels of Snail were measured by qRT-PCR and Western blot analysis, respectively. (E) Cells were treated with the Snail-specific siRNA-1 for 24 h or GA for 12 h, and TNF-α-induced migration and invasion were measured by migration and invasion assays. Data are representative or expressed as the mean±SD of each group of cells from three independent experiments. $^{b}P<0.05$ *vs* control group; $^{d}P>0.05$ *vs* TNF-α alone treatment group; $^{e}P<0.05$ *vs* TNF-α alone treatment group.

and anti-proliferative effects of TNF-α[36]. However, it is still unclear whether GA has anti-invasion properties under the chronic inflammatory condition induced by TNF-α in prostate cancer.

In the present study, we have demonstrated that TNF-α-induced migration and invasion of PC3 cells were significantly suppressed by GA. Moreover, TNF-α-induced cell invasion was associated with activation of the PI3K/Akt and NF-κB, and such activation was inhibited by treatment with GA. Furthermore, GA inhibited the TNF-α-induced cell invasion and migration by regulating the expression of Snail.

Akt is a critical component of signal transduction following PI3K activation, which has been linked to cell survival and development[16, 37]. An accumulating body of evidence revealed that the PI3K/Akt signaling pathway was involved in morphological changes, migration and invasion induced by TNF-α in various cell types. Activated Akt-phosphorylated substrates can directly or indirectly affect downstream transcription factor activity, including NF-κB[38]. Thus, Akt activity may be essential for TNF-α-induced oncogenic transformation

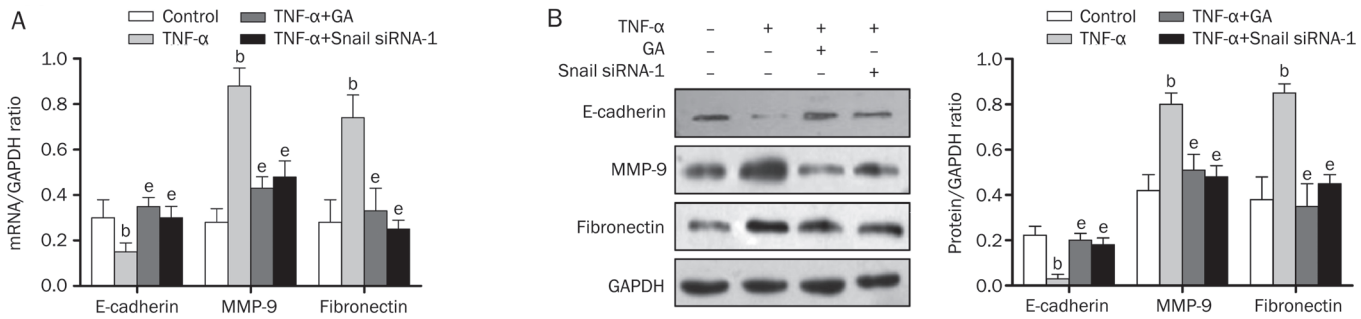

Figure 7. GA regulates the expression of invasiveness-associated genes in TNF-α-stimulated PC3 cells. (A, B) Cells were incubated with TNF-α (10 ng/mL) for 12 h and then treated with GA for 12 h or the Snail-specific siRNA-1 for 24 h. The mRNA and protein expression levels of E-cadherin, MMP-9, and fibronectin were assessed by qRT-PCR and Western blot analysis, respectively. Data are representative images or expressed as the mean±SD of each group of cells from three independent experiments. $^{b}P<0.05$ *vs* control group; $^{e}P<0.05$ *vs* TNF-α alone treatment group.

in cancer cells, and the treatment of prostate cancer cells with Akt inhibitors blocks the progression of tumorigenesis[37, 39, 40]. Our results further supported that TNF-α-induced invasion is mediated by Akt. More importantly, GA greatly reduced the phosphorylation and activation of Akt in PC3 cells. GSK-3β is the downstream target of the PI3K signaling pathway, which has also been shown to regulate cell survival, proliferation and differentiation[41]. In the present study, we found that TNF-α induced the phosphorylation of GSK-3β. However, GA does not affect TNF-α-activated GSK-3β in PC3 cells, indicating that GA-mediated inhibition of migration and invasion is independent of GSK-3β phosphorylation.

NF-κB plays a critical role in TNF-α-induced tumor development. It has been previously reported that the NF-κB signaling pathway is activated upon TNF-α-induced tumor cell migration and invasion via G protein coupled receptors. Several studies have shown that constitutive activation of NF-κB is associated with TNF-α-induced cell migration and invasion[6, 33, 40]. In the present study, utilizing western blot, immunofluorescence and luciferase reporter gene assays, we further confirmed that TNF-α can indeed increase NF-κB transcriptional activity. However, administration of GA can markedly inhibit TNF-α-induced NF-κB transcriptional activity in PC3 cells.

Several zinc-finger transcriptional repressors, including Snail, Slug, Twist, Zeb1, and Zeb2, have been shown to repress transcription of E-cadherin[18, 34, 42]. Snail was first identified as the most important transcriptional repressor of E-cadherin[43]. Snail can down-regulate expression of E-cadherin, inducing EMT and promoting cell migration and invasion[22, 44]. Overexpression of Snail was detected in various tumor cell lines, including breast, pancreatic and gastric cancers[45-47]. It was recently reported that Akt could up-regulate Snail expression and induce invasion[40, 48]. In addition, TNF-α-induced cell migration and invasion were associated with NF-κB-mediated stabilization of Snail[3, 6]. Because NF-κB may bind to the human Snail promoter causing increased Snail expression[19], we tested whether the regulation of Snail expression might be involved in the TNF-α-mediated migration and invasion of PC3 cells. A ChIP assay revealed that the NF-κB p65 subunit was constitutively bound to the Snail promoter, and this binding was increased upon NF-κB activation by TNF-α. The opposite effect was observed after GA addition. Given that Snail is the critical regulator of cell migration and invasion, we further investigated the impact of Snail knockdown on TNF-α-induced migration and invasion of PC3 cells. We surprisingly found that knockdown of Snail expression inhibited TNF-α-induced migration and invasion of PC3 cells. These data further supported that GA can down-regulate Snail expression, leading to an inhibition of TNF-α-induced tumor migration and invasion by PC3 cells. We subsequently examined the expression of Snail-regulated genes, such as E-cadherin, MMP-9 and fibronectin, which are associated with cell migration and invasion. As expected, both Snail siRNA and GA down-regulated MMP9 and fibronectin and upregulated E-cadherin expression in TNF-α-stimulated PC3 cells.

In summary, we showed that GA could inhibit TNF-α-induced migration and invasion. This inhibitory effect of GA is likely mediated by regulation of the PI3K/Akt and NF-κB signaling pathways resulting in a down-regulation of Snail. This finding may provide a new development of therapies for the inhibition TNF-α-induced migration and invasion of prostate cancer. Further studies *in vivo* are needed to determine the full potential of GA in prevention of cancer.

Acknowledgements

This study was supported by the grants from the National Natural Science Foundation of China (No 30972980 and 81001132).

Author contribution

Lei LÜ, Liang WANG, and Fu-qing ZENG designed the research; Lei LÜ, Dong TANG, Guo-song JIANG, and Xing-yuan XIAO performed the research; Lei LÜ, Lu-qi HUANG, and Fu-qing ZENG analyzed the data and wrote the paper.

References

1 Wajant H, Pfizenmaier K, Scheurich P. Tumor necrosis factor signaling. Cell Death Differ 2003; 10: 45–65.
2 Wang X, Lin Y. Tumor necrosis factor and cancer, buddies or foes?

Acta Pharmacol Sin 2008; 29: 1275–88.
3 Wu Y, Zhou BP. TNF-alpha/NF-kappaB/Snail pathway in cancer cell migration and invasion. Br J Cancer 2010; 102: 639–44.
4 Sandra F, Matsuki NA, Takeuchi H, Ikebe T, Kanematsu T, Ohishi M, *et al*. TNF inhibited the apoptosis by activation of Akt serine/threonine kinase in the human head and neck squamous cell carcinoma. Cell Signal 2002; 14: 771–8.
5 Hagemann T, Wilson J, Kulbe H, Li NF, Leinster DA, Charles K, *et al*. Macrophages induce invasiveness of epithelial cancer cells via NF-kappa B and JNK. J Immunol 2005; 175: 1197–205.
6 Wu Y, Deng J, Rychahou PG, Qiu S, Evers BM, Zhou BP. Stabilization of snail by NF-kappaB is required for inflammation-induced cell migration and invasion. Cancer Cell 2009; 15: 416–28.
7 Choi KW, Park HJ, Jung DH, Kim TW, Park YM, Kim BO, *et al*. Inhibition of TNF-alpha-induced adhesion molecule expression by diosgenin in mouse vascular smooth muscle cells via downregulation of the MAPK, Akt and NF-kappaB signaling pathways. Vascul Pharmacol 2010; 53: 273–80.
8 Liesenklas W, Auterhoff H. The constitution of gambogic acid and its isomerization. 4. Chemistry of gum-resin. Arch Pharm Ber Dtsch Pharm Ges 1966; 299: 797–8.
9 Zhao L, Guo QL, You QD, Wu ZQ, Gu HY. Gambogic acid induces apoptosis and regulates expressions of Bax and Bcl-2 protein in human gastric carcinoma MGC-803 cells. Biol Pharm Bull 2004; 27: 998–1003.
10 Yu J, Guo QL, You QD, Zhao L, Gu HY, Yang Y, *et al*. Gambogic acid-induced G_2/M phase cell-cycle arrest via disturbing CDK7-mediated phosphorylation of CDC2/p34 in human gastric carcinoma BGC-823 cells. Carcinogenesis 2007; 28: 632–8.
11 Rong JJ, Hu R, Qi Q, Gu HY, Zhao Q, Wang J, *et al*. Gambogic acid down-regulates MDM2 oncogene and induces p21 (Waf1/CIP1) expression independent of p53. Cancer Lett 2009; 284: 102–12.
12 He D, Xu Q, Yan M, Zhang P, Zhou X, Zhang Z, *et al*. The NF-kappa B inhibitor, celastrol, could enhance the anti-cancer effect of gambogic acid on oral squamous cell carcinoma. BMC Cancer 2009; 9: 343.
13 Guo QL, Lin SS, You QD, Gu HY, Yu J, Zhao L, *et al*. Inhibition of human telomerase reverse transcriptase gene expression by gambogic acid in human hepatoma SMMC-7721 cells. Life Sci 2006; 78: 1238–45.
14 Lee YC, Lin HH, Hsu CH, Wang CJ, Chiang TA, Chen JH. Inhibitory effects of andrographolide on migration and invasion in human non-small cell lung cancer A549 cells via down-regulation of PI3K/Akt signaling pathway. Eur J Pharmacol 2010; 632: 23–32.
15 Jin L, Hu X, Feng L. NT3 inhibits FGF2-induced neural progenitor cell proliferation via the PI3K/GSK3 pathway. J Neurochem 2005; 93: 1251–61.
16 Cantley LC. The phosphoinositide 3-kinase pathway. Science 2002; 296: 1655–7.
17 Ghosh S, Karin M. Missing pieces in the NF-kappaB puzzle. Cell 2002; 109: 81–96.
18 Hemavathy K, Ashraf SI, Ip YT. Snail/slug family of repressors: slowly going into the fast lane of development and cancer. Gene 2000; 257: 1–12.
19 Barbera MJ, Puig I, Dominguez D, Julien-Grille S, Guaita-Esteruelas S, Peiro S, *et al*. Regulation of Snail transcription during epithelial to mesenchymal transition of tumor cells. Oncogene 2004; 23: 7345–54.
20 Kudo-Saito C, Shirako H, Takeuchi T, Kawakami Y. Cancer metastasis is accelerated through immunosuppression during Snail-induced EMT of cancer cells. Cancer Cell 2009; 15: 195–206.
21 Haraguchi M, Okubo T, Miyashita Y, Miyamoto Y, Hayashi M, Crotti TN, *et al*. Snail regulates cell-matrix adhesion by regulation of the expression of integrins and basement membrane proteins. J Biol Chem 2008; 283: 23514–23.
22 Blechschmidt K, Sassen S, Schmalfeldt B, Schuster T, Hofler H, Becker KF. The E-cadherin repressor Snail is associated with lower overall survival of ovarian cancer patients. Br J Cancer 2008; 98: 489–95.
23 Greenlee RT, Murray T, Bolden S, Wingo PA. Cancer statistics, 2000. CA Cancer J Clin 2000; 50: 7–33.
24 Bostwick DG, Burke HB, Djakiew D, Euling S, Ho SM, Landolph J, *et al*. Human prostate cancer risk factors. Cancer 2004; 101: 2371–490.
25 Wegiel B, Bjartell A, Tuomela J, Dizeyi N, Tinzl M, Helczynski L, *et al*. Multiple cellular mechanisms to cyclin A1 in prostate cancer invasion and metastasis. J Natl Cancer Inst 2008; 100: 1022–36.
26 Sugar LM. Inflammation and prostate cancer. Can J Urol 2006; 13: 46–7.
27 Yamamoto Y, Gaynor RB. Therapeutic potential of inhibition of the NF-kappaB pathway in the treatment of inflammation and cancer. J Clin Invest 2001; 107: 135–42.
28 Wu Y, Zhou BP. Inflammation: a driving force speeds cancer metastasis. Cell Cycle 2009; 8: 3267–73.
29 Kim SJ, Kelly WK, Fu A, Haines K, Hoffman A, Zheng T, *et al*. Genome-wide methylation analysis identifies involvement of TNF-alpha mediated cancer pathways in prostate cancer. Cancer Lett 2011; 302: 47–53.
30 Danforth KN, Rodriguez C, Hayes RB, Sakoda LC, Huang WY, Yu K, *et al*. TNF polymorphisms and prostate cancer risk. Prostate 2008; 68: 400–7.
31 Qin Z, Kruger-Krasagakes S, Kunzendorf U, Hock H, Diamantstein T, Blankenstein T. Expression of tumor necrosis factor by different tumor cell lines results either in tumor suppression or augmented metastasis. J Exp Med 1993; 178: 355–60.
32 Orosz P, Echtenacher B, Falk W, Ruschoff J, Weber D, Mannel DN. Enhancement of experimental metastasis by tumor necrosis factor. J Exp Med 1993; 177: 1391–8.
33 Bates RC, Mercurio AM. Tumor necrosis factor-alpha stimulates the epithelial-to-mesenchymal transition of human colonic organoids. Mol Biol Cell 2003; 14: 1790–800.
34 Chua HL, Bhat-Nakshatri P, Clare SE, Morimiya A, Badve S, Nakshatri H. NF-kappaB represses E-cadherin expression and enhances epithelial to mesenchymal transition of mammary epithelial cells: potential involvement of ZEB-1 and ZEB-2. Oncogene 2007; 26: 711–24.
35 Balkwill F. Tumor necrosis factor or tumor promoting factor? Cytokine Growth Factor Rev 2002; 13: 135–41.
36 Pandey MK, Sung B, Ahn KS, Kunnumakkara AB, Chaturvedi MM, Aggarwal BB. Gambogic acid, a novel ligand for transferrin receptor, potentiates TNF-induced apoptosis through modulation of the nuclear factor-kappa B signaling pathway. Blood 2007; 110: 3517–25.
37 Vivanco I, Sawyers CL. The phosphatidylinositol 3-kinase AKT pathway in human cancer. Nat Rev Cancer 2002; 2: 489–501.
38 Ozes ON, Mayo LD, Gustin JA, Pfeffer SR, Pfeffer LM, Donner DB. NF-kappaB activation by tumour necrosis factor requires the Akt serine-threonine kinase. Nature 1999; 401: 82–5.
39 Prawettongsopon C, Asawakarn S, Suthiphongchai T. Suppression of prometastatic phenotype of highly metastatic androgen-independent rat prostate cancer MLL cell line by PI3K inhibitor LY294002. Oncol Res 2009; 17: 301–9.
40 Julien S, Puig I, Caretti E, Bonaventure J, Nelles L, van Roy F, *et al*. Activation of NF-kappaB by Akt upregulates Snail expression and induces epithelium mesenchyme transition. Oncogene 2007; 26: 7445–56.
41 Ougolkov AV, Billadeau DD. Targeting GSK-3: a promising approach for cancer therapy? Future Oncol 2006; 2: 91–100.

42 Bolos V, Peinado H, Perez-Moreno MA, Fraga MF, Esteller M, Cano A. The transcription factor Slug represses E-cadherin expression and induces epithelial to mesenchymal transitions: a comparison with Snail and E47 repressors. J Cell Sci 2003; 116 : 499–511.

43 Nieto MA. The snail superfamily of zinc-finger transcription factors. Nat Rev Mol Cell Biol 2002; 3: 155–66.

44 Miyoshi A, Kitajima Y, Sumi K, Sato K, Hagiwara A, Koga Y, *et al*. Snail and SIP1 increase cancer invasion by upregulating MMP family in hepatocellular carcinoma cells. Br J Cancer 2004; 90: 1265–73.

45 Rosivatz E, Becker I, Specht K, Fricke E, Luber B, Busch R, *et al*. Differential expression of the epithelial-mesenchymal transition regulators snail, SIP1, and twist in gastric cancer. Am J Pathol 2002; 161: 1881–91.

46 Martin TA, Goyal A, Watkins G, Jiang WG. Expression of the transcription factors snail, slug, and twist and their clinical significance in human breast cancer. Ann Surg Oncol 2005; 12: 488–96.

47 Yin T, Wang C, Liu T, Zhao G, Zha Y, Yang M. Expression of snail in pancreatic cancer promotes metastasis and chemoresistance. J Surg Res 2007; 141: 196–203.

48 Cho HJ, Baek KE, Saika S, Jeong MJ, Yoo J. Snail is required for transforming growth factor-beta-induced epithelial-mesenchymal transition by activating PI3 kinase/Akt signal pathway. Biochem Biophys Res Commun 2007; 353: 337–43.

Acta Pharmacologica Sinica (2012) 33: 542–550
 1671-4083/12 $32.00
www.nature.com/aps

Original Article

Perifosine induces protective autophagy and upregulation of ATG5 in human chronic myelogenous leukemia cells *in vitro*

Yin TONG, Yan-yan LIU, Liang-shun YOU, Wen-bin QIAN*

Institute of Hematology, The First Affiliated Hospital, College of Medicine, Zhejiang University, Hangzhou 310003, China

Aim: The efficacy of the Akt inhibitor perifosine against chronic myeloid leukemia (CML) cells and its mechanisms of action are unknown. In this study, the cytotoxic effects of perifosine on CML and acute myeloid leukemia (AML) cell lines were compared to elucidate the mechanisms underlying the differences.

Methods: Human AML cell lines Kasumi-1 and HL-60, and the CML cell line K562 were used. Cell viability was quantitated using MTT assay. Apoptosis was determined using Annexin V-FITC/propidium iodide and Hoechst staining, which were followed by flow cytometry and fluorescence microscopy analysis, respectively. Caspase pathway activation and the expression of autophagy-related genes were examined using Western blot. Autophagy was studied using electron microscopy, the acridine orange staining method, and GFP-LC3 was examined with fluorescence microscopy.

Results: In contrast to AML cell lines, the CML cell lines K562 and K562/G (an imatinib-insensitive CML cell line) were resistant to perifosine (2.5–20 μmol/L) in respect to inhibiting cell growth and inducing apoptosis. Perifosine (2.5, 5, and 10 μmol/L) inhibited Akt and its phosphorylation in AML cells, but not in CML cells. Treatment with perifosine (20 μmol/L) resulted in autophagy in CML cells as shown by the increased formation of acidic vesicular organelles and the accumulation of LC3-II. Treatment of CML cells with perifosine (5, 10, and 20 μmol/L) dose-dependently upregulated AGT5, but not Beclin 1 at the protein level. Furthermore, inhibition of autophagy by chloroquine (40 nmol/L) significantly suppressed the cell growth and induced apoptosis in CML cells treated with perifosine (20 μmol/L) .

Conclusion: Our results show that CML cell lines were resistant to the Akt inhibitor perifosine *in vitro*, which is due to perifosine-induced protective autophagy and upregulation of ATG5.

Keywords: Akt inhibitor; perifosine; chronic myeloid leukemia; acute myeloid leukemia; autophagy; apoptosis; beclin 1; ATG5

Acta Pharmacologica Sinica (2012) 33: 542–550; doi: 10.1038/aps.2011.192; published online 12 Mar 2012

Introduction

A hallmark of chronic myeloid leukemia (CML) is expression of the BCR/ABL oncoprotein that results from a reciprocal translocation involving chromosomes 9 and 22. This fusion protein has been exploited as a therapeutic target for the treatment of CML because it plays critical and essential roles in leukemogenesis[1, 2]. The chimeric BCR/ABL protein possesses cellular transforming ability that is ascribed to its elevated tyrosine kinase (TK) activity compared with that of native c-ABL[3]. Inhibition of BCR/ABL with imatinib mesylate (imatinib), a selective inhibitor of ABL kinase activity, results in long-term remission in CML patients; therefore, imatinib is the first-line therapy for newly diagnosed CML patients[4]. However, early relapses occur, and imatinib resistance due primarily to BCR/ABL kinase mutations has been documented[5]. Some resistant cells exhibit genomic amplification of non-mutated BCR/ABL and possess a BCR/ABL independence pathway[6]. Several signaling pathways are affected by constitutively active BCR/ABL, including increased proliferation through RAS/MAPK activation[7], increased transcriptional activity via STAT recruitment[8], and decreased apoptosis through the activation of PI3K/Akt[9].

PI3K/Akt signaling is activated in numerous cancers types and is a crucial event in tumorigenesis[10]. Activation of receptor TKs by BCR/ABL results in activation of the PI3K/Akt pathway[11]. Numerous molecules downstream of Akt have been linked to the leukemogenic effects of BCR/ABL, including the proapoptotic protein BAD, MDM2, mammalian target of rapamycin (mTOR), and the FoxO (forkhead) family of

* To whom correspondence should be addressed.
E-mail qianwenb@yahoo.com.cn
Received 2011-10-13 Accepted 2011-12-09

transcription factors[12, 13]. Activation of Akt may endow CML progenitor cells with the ability to self-renew through deregulation of GSK3β, a critical negative regulator of the Wnt/β-catenin pathway[14]. Additionally, it was recently reported that imatinib treatment activated the PI3K/Akt/mTOR pathway and that this activation was important in mediating cell survival early in the development of imatinib resistance before the emergence of overt resistance[15].

Perifosine is a lipid-based Akt inhibitor that exhibits antitumor activity in a broad range of tumor types. *In vitro*, perifosine inhibits the translocation of Akt to the cell membrane and suppresses the growth of various types of solid tumor and leukemia cells[16–18]. Perifosine induces apoptosis in acute myeloid leukemia (AML) cell lines and reduces the clonogenic activity of AML progenitors, but not of normal $CD34^+$ cells, thereby sensitizing blast cells to etoposide[19]. Recent preclinical studies showed that perifosine has synergistic effects with chemotherapeutic agents, such as etoposide in leukemia cells[19] and doxorubicin in multiple myeloma cells[20]. Based on these data, Phase II clinical trials of perifosine alone or in combination with dexamethasone for patients with relapsed or refractory multiple myeloma have shown promising antitumor activity[21]. However, it has been reported that human CML cell lines are unexpectedly resistant to GSK690693 (another Akt inhibitor); the underlying mechanism for this is unclear[22]. The present study followed up on this interesting observation by investigating the cytotoxic effects of perifosine on human AML cell lines and the CML cell lines K562 and K562/G (a cell line resistant to imatinib). We demonstrated perifosine-induced modulation of different apoptotic and autophagic molecules in an attempt to understand its mechanisms of action. Our data showed that perifosine induced apoptosis and inhibited Akt activation in AML cells, but not in CML cells. Interestingly, treatment of CML cells with perifosine induced autophagy and resulted in the upregulation of ATG5. We also observed that inhibition of the perifosine-mediated autophagic response with the lysosomotropic agent chloroquine led to accelerated apoptotic cell death. These findings support the notion that perifosine-induced autophagy is cytoprotective in CML cells.

Materials and methods

Cell lines and cell culture

The human AML cell lines Kasumi-1 and HL-60 and the CML cell line K562 were obtained from American Type Culture Collection (ATCC, Rockville, MD, USA). K562/G cells were kindly provided by the Institute of Hematology, Chinese Academy of Medical Sciences (Tianjin, China). The K562/G cell line is resistant to imatinib (50% inhibition at 48 h in K562 and K562/G was 71.8 and 261.0 nmol/L, respectively) but does not contain mutations within the TK domain. K562 cells expressing GFP-LC3 were established previously in our laboratory[23]. Cell lines were maintained in RPMI-1640 medium with 10% fetal bovine serum (Hyclone, Utah, USA) at 37 °C in a 5% CO_2 humid atmosphere.

Cellular proliferation assay

Colorimetric assays were performed to evaluate drug activity. Leukemia cell lines were seeded into 96-well plates at a density of 1×10^5/mL in triplicate and then treated with 1.25–20 μmol/L perifosine (Binxinbio, Tianjin, China) alone or in combination with chloroquine (CQ, Sigma, St Louis, MO, USA) for 24 h or 48 h, respectively. At the end of the drug exposure, 20 μL of 3-(4,5-dimethylthiazol-2-yl)-2,5-diphenyltetrazolium bromide (MTT, Sigma) solution (5 mg/mL) was added into each well and incubated for an additional 4 h at 37 °C, at which time the supernatants were removed and 200 μL DMSO was used to dissolve the formazan crystals. The absorbance was read at 570 nm with a microplate reader (Bio-RAD, Berkeley, USA).

Western blot analysis

Cells were harvested and extracted with lysis buffer (Cell Signaling, Danvers, USA). The cell lysate was collected by centrifugation at 12000×*g* for 5 min at 4 °C and protein concentration was determined by the BCA method. Samples containing 50 μg protein lysate were separated on 12% SDS-PAGE gels before transfer to a polyvinylidene difluoride membrane (Millipore, Billerica, MA, USA). The membranes were blocked with TBST containing 5% fat-free milk before overnight incubation with the indicated primary antibodies at 4 °C. The primary antibodies used in this study were as follows: Beclin-1 (Novus Biologicals, Colorado, USA), light chain 3 (LC3, Novus Biologicals), ATG-5 (Sigma), ATG7 (Sigma), JNK (Biovision, CA, USA), and phosphorylated-JNK (p-JNK). Antibodies to BCR/ABL, Akt, phosphorylated-Akt (p-Akt, Ser473), caspase-3, caspase-9, and polyadenosine-5-diphosphate-ribose polymerase (PARP) were purchased from Cell Signaling. The β-actin antibody was obtained from Santa Cruz Biotechnology (Santa Cruz, CA, USA). After incubation with the appropriate secondary antibodies (Multisciences Biotech, Hangzhou, China), antibody binding was detected by enhanced chemiluminescence (ECL) according to the manufacturer's recommendation.

Detection of acidic vesicular organelles

Autophagy is the process of sequestering cytoplasmic proteins into the cellular lytic compartment and is characterized by the development of acidic vesicular organelles (AVOs). Acridine orange (AO) is a widely used method to visualize AVOs. In AO-stained cells, the cytoplasm and nucleolus fluoresce bright green and dim red, respectively, whereas acidic compartments fluoresce bright red. To detect the formation of AVOs, perifosine-treated cells were washed twice with PBS, fixed with 4% paraformaldehyde, stained with AO (Molecular Probes, CA, USA) at 1 μg/mL for 15 min, washed with PBS to remove unbound dye, and subsequently examined under a fluorescence microscope (Olympus, Tokyo, Japan).

Transmission electron microscopy (TEM)

TEM was performed as previously described[23]. Briefly, cells

were harvested, washed twice with PBS, and fixed with ice-cold 2.5% glutaraldehyde overnight. After washing with PBS, the cells were fixed in OsO_4 and embedded in Spurr's resin. Ultrathin sections (0.12 μm) were cut and double stained with uranyl acetate and lead citrate. Representative areas were chosen and viewed with a Philips TECNA10 transmission electron microscope.

Assessment of apoptosis

Apoptosis was measured using an annexin V-FITC and propidium iodide (PI) apoptosis detection kit (Biouniquer, Suzhou, China) according to the manufacturer's instructions. Prepared cells were analyzed with a FACScan flow cytometer and CELLQuest software (Becton Dickinson, Franklin Lakes, NJ, USA). Chromatin condensation and nuclear fragmentation in leukemia cells were detected by Hoechst staining. Briefly, cells were harvested, plated on glass slides for fixation with 4% paraformaldehyde, and stained with 5 μg/mL Hoechst 33258 (Sigma) for 15 min in the dark at room temperature. Apoptotic cells were observed under a fluorescence microscope (Olympus).

Statistical analysis

All assays were performed in triplicate, and the results were presented as the mean±SD. Data were analyzed by the Student's *t*-test and ANOVA for statistical significance. *P* values <0.05 were considered significant.

Results

Perifosine reduces cell viability and induces apoptosis of AML, but not CML, cell lines

To compare the cytotoxic effects of perifosine on AML and CML cell lines, Kasumi-1, HL-60, K562, and K562/G cells were cultured with the indicated concentrations of perifosine for 24 h or 48 h, respectively. Cell viability was evaluated using an MTT assay. As shown in Figure 1, perifosine inhibited the growth of Kasumi-1 and HL-60 cells with 50% inhibition (IC_{50}) at 48 h of 4.24 and 3.62 μmol/L, respectively. In contrast, 20 μmol/L perifosine did not significantly reduce the viability of the CML cell lines (K562 and K562/G) at 48 h, suggesting that they were resistant to perifosine. In order to characterize the cytotoxicity of perifosine on leukemia cells, we analyzed the induction of apoptosis in AML and CML cells cultured with 10 μmol/L perifosine for 24 h. Upon perifosine treatment, 27.5% and 24.6% of the AML cells were apoptotic, respectively, whereas little apoptosis was observed in the K562 and K562/G cells (Figure 2A). These results were confirmed by fluorescent microscopy analysis of Hoechst staining (Figure 2B). Furthermore, Western blotting analysis demonstrated that dose-dependent cleavage of caspase-9, caspase-3, and PARP was induced by perifosine in the AML cell lines. Neither cleavage of PARP nor activation of caspase-3 or -9 was detected in the CML cell lines (Figure 2C). These data indicated that CML cells were resistant to perifosine-induced apoptosis.

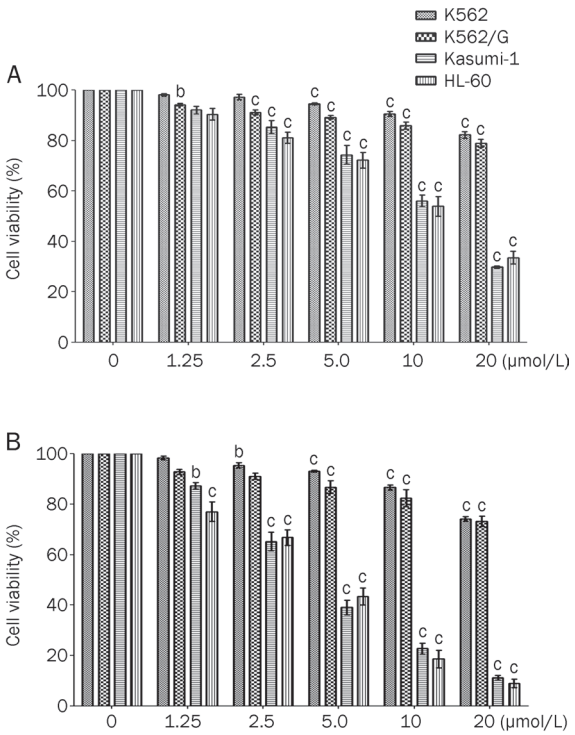

Figure 1. AML cell lines are much sensitive to perifosine than CML cells. Exponentially growing cells were plated into 96-well plates, and then treated with the indicated concentrations of perifosine for 24 h (A) and 48 h (B), respectively. Growth inhibition in leukemia cell lines by perifosine was assessed by a MTT assay. Data represent mean±SD of three independent experiments. $^{b}P<0.05$, $^{c}P<0.01$ compared with untreatment (analyzed by ANOVA and Turkey-Kramer test).

Different effects of perifosine on the phosphorylation of Akt and JNK in leukemia cells

Because the degree of Akt downregulation is correlated with cell sensitivity to perifosine-induced apoptosis[24], we examined if perifosine could modulate the expression and phosphorylation of Akt (Ser473) in leukemia cell lines (Figure 3A). Kasumi-1 and HL-60 cells exhibited a dose-dependent decrease in Akt and p-Akt levels when exposed to perifosine for 24 h. As expected, downregulation of Akt was not observed in CML cell lines that are resistant to perifosine. Perifosine has been reported to trigger JNK activation followed by caspase-8, caspase-9, and PARP cleavage in multiple myeloma and AML cells[20, 25]. We also observed that perifosine strongly induced the phosphorylation of JNK1/2 in AML, but not CML, cells in a dose-dependent manner (Figure 3B). Collectively, these results suggested that the failure of perifosine to inhibit Akt and induce phosphorylation of JNK might play a role in mediating the drug resistance of CML cells.

Perifosine induces autophagy in CML cells, but not in AML cells

Autophagy is frequently activated in response to stress and some therapeutic agents and is protective against cell

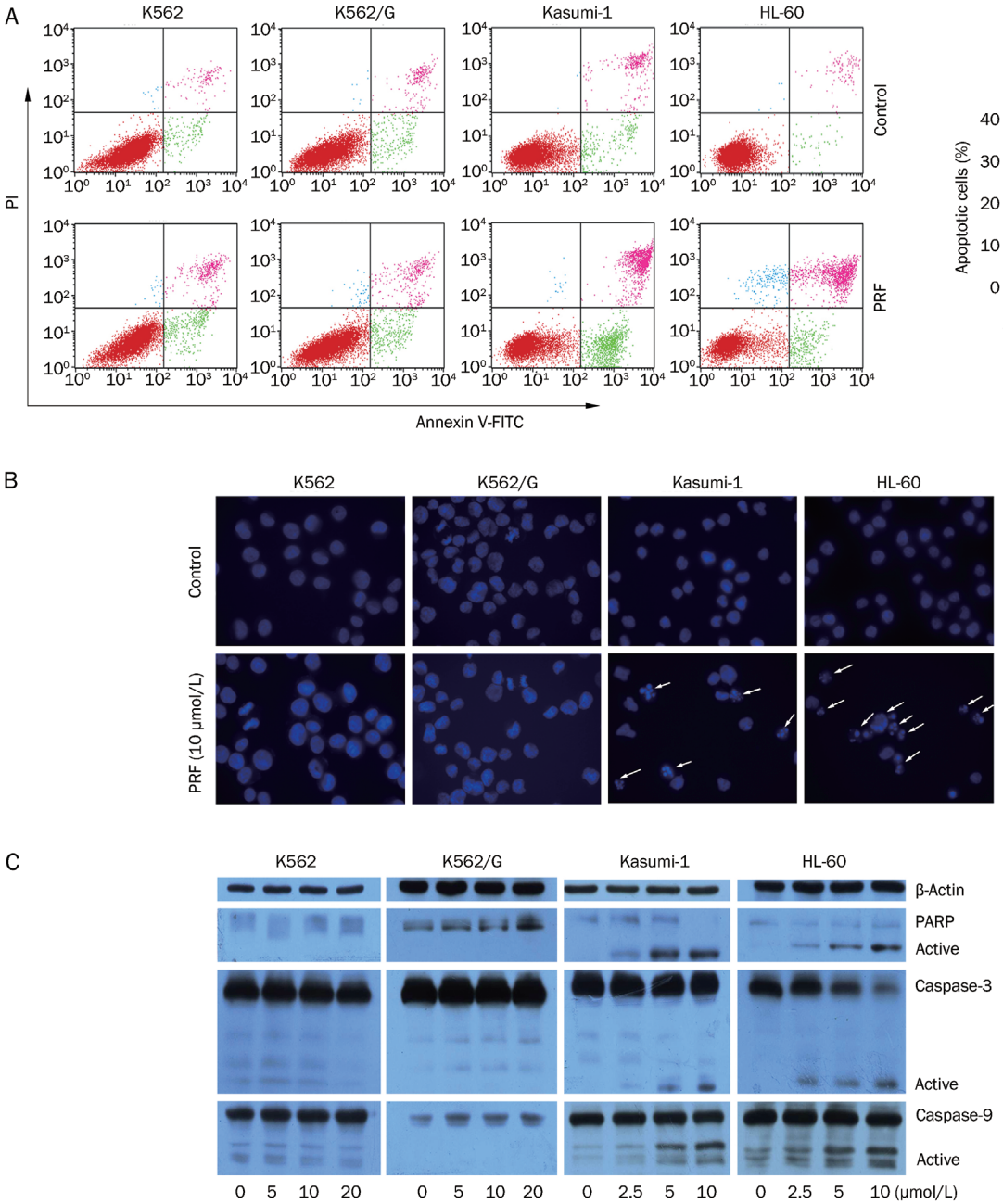

Figure 2. Apoptosis induced by perifosine in AML cells but not in CML cells. (A) After treatment with perifosine (PRF) at 10 μmol/L for 24 h, leukemia cell lines were harvested and detected by annexin V/propidium (PI)-staining method. The inserted panel shows data from three separate experiments (B) CML and AML cells were stained with Hoechst 33258 from one day after perifosine (10 μmol/L) treatment, and then observed under a fluorescence microscope. Arrows represent the apoptotic nuclei. (C) After incubation of leukemia cell lines for 24 h with the indicated concentrations of perifosine, whole cell extracts were analyzed by Western blot analysis using anti-caspase-3, -9, and PARP antibodies. β-Actin was used as a loading control. The results are representatives of three separate experiments.

death[26–28]. Given these observations, we investigated if perifosine could induce autophagy in K562 cells. An increase in AO-positive acidic vesicular organelles occurs in conjunction with the induction of autophagy in leukemia[23, 27]. As shown in Figure 4A, AO staining of AVOs was detected in K562 cells treated with perifosine, but not in those cells treated with PBS as a control. Fusing GFP with LC3 provides a fluorescent marker for autophagy, so we transfected this construct into K562 cells. The cells were treated with the indicated dose of perifosine for 24 h and autophagosome formation was visualized by fluorescent microscopy. Perifosine treatment at 20 and 40 μmol/L resulted in 33.3% and 47.1%, respectively, of cells that contained LC3-positive vesicles (Figure 4B). Transmission electron microscopy revealed the formation of autophagic

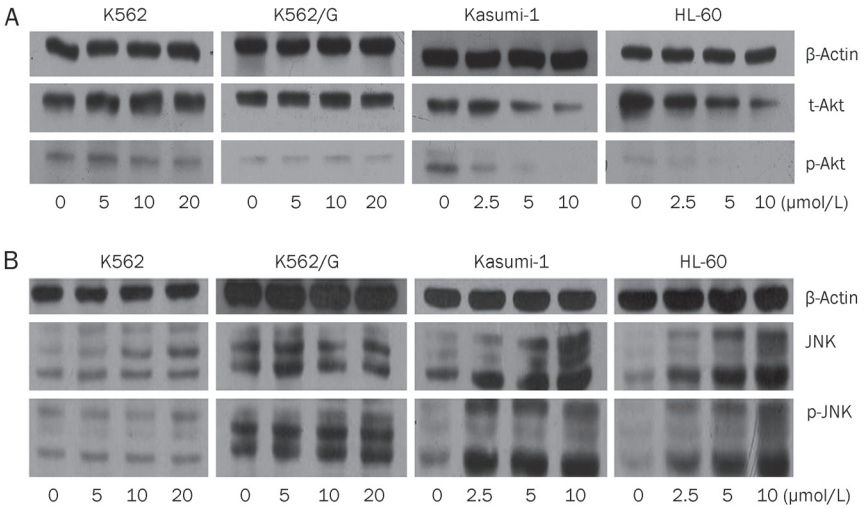

Figure 3. Perifosine's effect on phosphorylation and protein expression of Akt and JNK. (A) Leukemia cells were exposed to the indicated concentrations of perifosine for 24 h and then analyzed for expression of total and phosphorylated Akt (Ser473). (B) CML and AML cell lines were treated with varying doses of perifosine for 24 h, after which cells were harvested, and extracted proteins were immunoblotted for the expression of total and phosphorylated JNK, and β-actin. These experiments were repeated once with identical results.

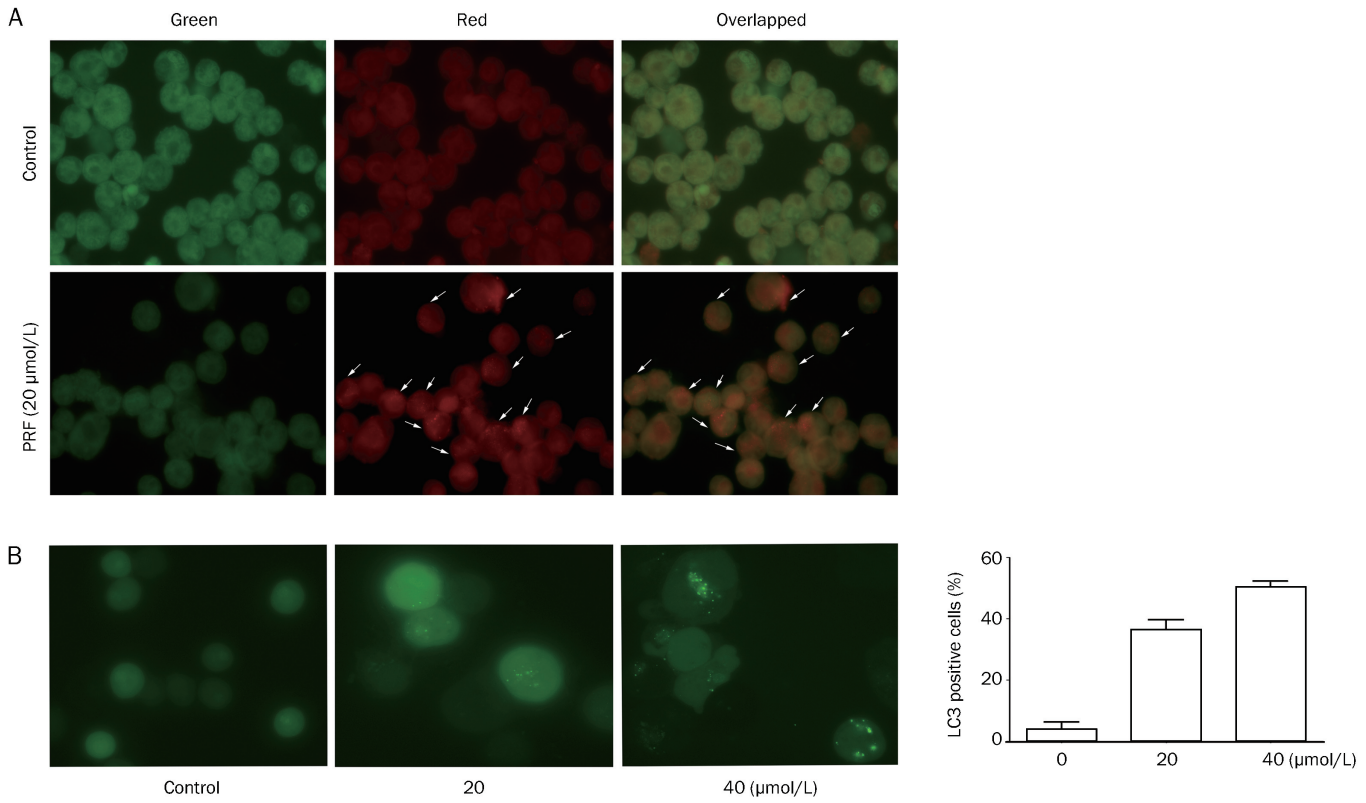

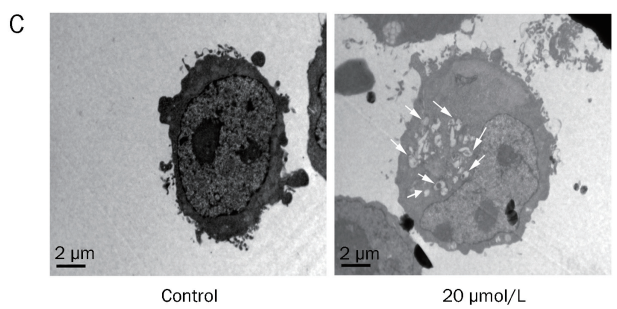

Figure 4. Induction of autophagy by perifosine(PRF) in K562 cells. (A) K562 cells were treated with or without 20 μmol/L perifosine for 48 h, and then stained with acridine orange (1 μg/mL), and then visualized under green and red filter microscope; note the presence of numerous autophagical vacuoles (white arrows). All digital micrographs were taken at the same exposure setting and images were overlapped. (B) K562 cells that were transfected with GFP-LC3 were incubated for 24 h without or with perifosine at 20 and 40 μmol/L, respectively, and then examined by a fluorescence microscopy. The cells with LC3-positive vesicles were calculated using ImageJ software, and data from three independent experiments were shown (right panel). (C) Representative TEM photomicrographs (×3700) of the K562 cells treated without or with 20 μmol/L perifosine for 48 h. Arrows, autophagic vacuoles. Scale bars, 2 μm.

vesicles after treatment with perifosine in K562 cells (Figure 4C). These findings suggested that perifosine induced autophagy in K562 cells.

We next examined by Western blot if perifosine could induce the expression of autophagy-related genes. As shown in Figure 5, a dose-dependent increase in the expression of AGT5 was observed in K562 cells treated with perifosine. Meanwhile, a progressive increase in autophagic activity (defined by LC3-I to LC3-II conversion) was detected after exposure to perifosine for 24 h. However, upregulation of ATG7 and Beclin-1, which are required for autophagy[29], did not occur. Kasumi-1 cells failed to show this autophagic response or changes in autophagy-related gene expression.

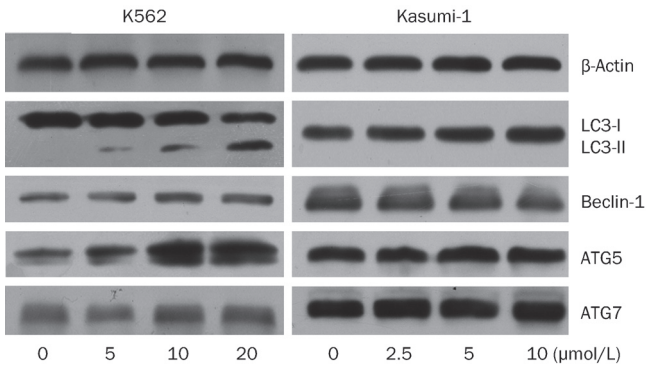

Figure 5. Effects of perifosine on expression of autophagy-related genes. After treatment with the indicated doses of perifosine for 24 h, K562 and Kasumi-1 cells were harvested. Whole cell lysates were subjected to Western blotting for protein expression of Beclin-1, ATG5, ATG7, and LC3. Anti-β-actin antibody was used as a control for protein loading.

Inhibition of autophagy potentiates perifosine-mediated apoptosis in K562 cells

To examine the significance of perifosine-induced autophagy in CML cells, we inhibited autophagy in K562 and K562/G cells using CQ and analyzed the effect on perifosine-induced cell death. As shown in Figure 6A, cell death, as measured using an MTT assay, significantly increased when perifosine was combined with CQ (from 21.5% to 46.8%; P=0.004). Western blotting showed an enhanced accumulation of LC3-II in CQ- and perifosine-treated K562 cells (Figure 6B) because CQ prevents autophagosome-lysosome fusion and thereby blocks autophagic degradation[30]. Furthermore, inhibition of autophagy upon co-treatment with perifosine and CQ promoted the apoptosis of K562 cells as evidenced by increased PARP cleavage and caspase-3 activation (Figure 6C). Treatment with perifosine and CQ showed no detectable modulation of the protein level of BCR/ABL (Figure 6C). Similar results were also observed in K562/G cells, an imatinib-resistant cell line (Figure 6). These data indicate that perifosine-induced autophagy plays a prosurvival role in protecting leukemia cells.

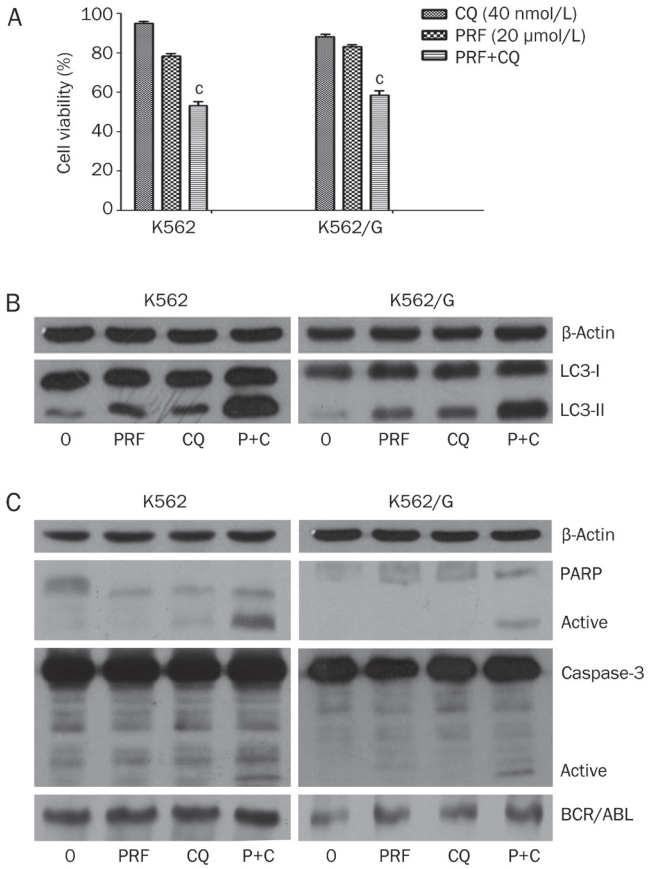

Figure 6. Inhibition of autophagy results in enhanced suppression of cell growth and apoptosis in CML cell lines. (A) K562 and K562/G cells were treated for 48 h with perifosine (PRF, 20 μmol/L), chloroquine (CQ, 40 nmol/L) or two agents combination, respectively. Viability of cells growth was examined by a MTT assay. Mean±SD. n=3. (B) Western blotting analysis was performed for the expression of LC3 and β-actin. (C) The levels of BCR/ABL fusion protein, cleavage of PARP, and activation of caspase-3 were analyzed using western blotting. Anti-β-actin was used as a control for protein loading. ^cP<0.01 *vs* perifosine.

Discussion

Akt kinase is reported to be constitutively active in the chronic phase of CML, during blast crisis of CML, and in the K562 cell line[11, 31]. Activation of Akt may endow CML progenitor cells with the ability to self-renew and could play an important role in mediating imatinib resistance[14, 15]. Thus, the Akt pathway is an attractive target for the treatment of CML. However, the present study demonstrated that the Akt kinase inhibitor perifosine has activity against AML cells, but not CML cells. This is consistent with a previous report showing that CML cell lines were resistant to GSK690693, another Akt kinase inhibitor[22], although the mechanism of this resistance is unknown. Some studies suggest that the downregulation of Akt phosphorylation is associated with perifosine-induced apoptosis and inhibition of tumor growth[19, 20, 22, 32]. Similarly, our *in vitro* experiments showed that perifosine inhibited cell growth and Akt phosphorylation and induced apoptosis in AML

cells. Inhibition of Akt kinase activity was not observed in the perifosine-insensitive CML cell lines K562 and K562/G, suggesting that the lack of sensitivity was likely due to a failure to inhibit Akt phosphorylation. In contrast to our findings, acute lymphoblastic leukemia cells in which the lack of sensitivity is not related to the inability of perifosine to inhibit Akt signaling have been reported[22]. Therefore, multiple mechanisms of resistance might exist.

Autophagy is a highly conserved catabolic program for the degradation and recycling of cellular components, including long-lived proteins and organelles, and has been recognized as an important regulatory mechanism in cell fate decisions. This process is activated in cancer cells in response to stress or therapeutic agents[23, 26, 27, 33]. An emerging role for autophagy has been demonstrated in response to tyrosine kinase inhibitors (TKI) such as imatinib and INNO-406 in CML cells, including the stem cells[34–36]. This autophagic response to therapeutic agents in CML cells is dependent on Beclin 1. In the present study, we observed an accumulation of the autophagic protein marker LC3-II and a substantial increase in the formation of AVOs in K562 cells treated with perifosine. Electron microscopy revealed a massive accumulation of autophagic vacuoles after perifosine treatment. Our findings support the previous report in which autophagy was observed in lung cancer cells treated with perifosine[37]. The same study showed that perifosine inhibited the Akt and mTOR axes, which may contribute to perifosine-induced autophagy. Another study reported that Akt inactivation with small molecule inhibitors did not significantly induce apoptosis but instead increased autophagy[38]. In our study, perifosine did not inhibit either the Akt or mTOR axes in CML cells (data not shown), suggesting that alternative signaling pathways are involved in autophagy. Interestingly, we found that treatment with perifosine markedly increased ATG5 protein expression, but not that of Beclin 1. Recent publications suggest that non-canonical autophagy is Beclin 1-independent, and this process is emerging as a key regulator of the cell death pathway[39–42]. Prior studies have shown that the formation of autophagosomes during Beclin 1-independent autophagy is dependent on the ATG12-ATG5 conjugation system, and that ATG5 is necessary for gossypol-mediated autophagy in cancer cells[43–45]. However, in this study we could not successfully transfect ATG5 siRNA into K562 cells using Lipofectamine. Further investigations are needed to elucidate the molecular mechanism by which perifosine-induced non-canonical autophagy in CML cells is associated with the upregulation of ATG5.

It is well established that autophagy functions in a prosurvival role in cancer cells and that the inhibition of autophagy increases the effectiveness of anticancer drugs[26, 36]. TKIs, the histone deacetylase inhibitor SAHA, and OSI-027 (a drug primarily targeting mTOR) have been reported to initiate protective autophagy in CML cells; disrupting this drug-induced autophagy using CQ, 3-MA, NH_4Cl, or bafilomycin A_1 significantly augments an agent's antileukemic activity[13, 28, 34]. Consistent with these findings, we showed that the combined use of the Akt inhibitor perifosine with CQ resulted in an enhanced inhibition of cell growth and induction of apoptosis, even though CML cells are resistant to perifosine alone. Moreover, this therapeutic strategy also effectively killed imatinib-resistant cells (K562/G), indicating that autophagy inhibitors such as CQ, in combination with Akt inhibitors, could be beneficial in overcoming drug resistance. Importantly, it has been shown that the combination of TKIs with inhibitors of autophagy sensitizes the $CD34^+CD38^-$ subpopulation to TKIs. In a long-term culture-initiating assay that assessed leukemia stem cell functionality, the inhibition of autophagy resulted in a significant elimination of CML stem cells[36]. These promising results led to a phase II clinical trial that will evaluate the efficacy of imatinib combined with hydroxychloroquine (a lysosomotropic agent) in reducing the population of CML stem cells.

In conclusion, we show for the first time that the Akt inhibitor perifosine induces autophagy in CML cells, which along with the upregulation of ATG5, may contribute to the drug-induced autophagic response. Moreover, the inhibition of perifosine-induced autophagy led to enhanced cell death in CML cells, suggesting that the inhibition of autophagy may improve the therapeutic effects of Akt inhibitors in the treatment of CML.

Acknowledgements

This work was supported by the Zhejiang Provincial Natural Science Foundation of China (R2090392) and Science and the Technology Foundation of Zhejiang Province (2011c23089). We are grateful to Prof Tamotsu YOSHIMORI, PhD, for providing the EGFP-LC3 plasmid and to Li WANG (Zhejiang University) for her help with TEM.

Author contribution

Wen-bin QIAN designed the research; Yin TONG, Yan-yan LIU, and Liang-shun YOU performed the experiments; Wen-bin QIAN and Yin TONG analyzed the data and wrote the paper.

References

1 Druker BJ. Translation of the Philadelphia chromosome into therapy for CML. Blood 2008; 112: 4808–17.
2 Groffen J, Stephenson JR, Heisterkamp N, de Klein A, Bartram CR, Grosveld G. Philadelphia chromosomal breakpoints are clustered within a limited region, bcr, on chromosome 22. Cell 1984; 36: 93–9.
3 Daley GQ, Van Etten RA, Baltimore D. Induction of chronic myelogenous leukemia in mice by the P210 bcr/abl gene of the Philadelphia chromosome. Science 1990; 247: 824–30.
4 Deininger M, Buchdunger E, Druker BJ. The development of imatinib as a therapeutic agent for chronic myeloid leukemia. Blood 2005; 105: 2640–53.
5 Gorre ME, Mohammed M, Ellwood K, Hsu N, Paquette R, Rao PN, *et al*. Clinical resistance to STI-571 cancer therapy caused by BCR-ABL gene mutation or amplification. Science 2001; 293: 876–80.
6 Koptyra M, Falinski R, Nowicki MO, Stoklosa T, Majsterek I, Nieborowska-Skorska M, *et al*. BCR/ABL kinase induces self-mutagenesis via reactive oxygen species to encode imatinib resistance. Blood 2006;

108: 319–27.
7 Puil L, Liu J, Gish G, Mbamalu G, Bowtell D, Pelicci PG, *et al*. Bcr-Abl oncoproteins bind directly to activators of the Ras signalling pathway. EMBO J 1994; 13: 764–73
8 Warsch W, Kollmann K, Eckelhart E, Fajmann S, Cerny-Reiterer S, Hölbl A, *et al*. High STAT5 levels mediate imatinib resistance and indicate disease progression in chronic myeloid leukemia. Blood 2011; 117: 3409–20.
9 Skorski T, Kanakaraj P, Nieborowska-Skorska M, Ratajczak MZ, Wen SC, Zon G, *et al*. Phosphatidylinositol-3 kinase activity is regulated by BCR/ABL and is required for the growth of Philadelphia chromosome-positive cells. Blood 1995; 86: 726–36.
10 Vivanco I, Sawyers CL. The phosphatidylinositol 3-Kinase AKT pathway in human cancer. Nat Rev Cancer 2002; 2: 489–501.
11 Quintás-Cardama A, Cortes J. Molecular biology of bcr-abl1-positive chronic myeloid leukemia. Blood 2009; 113: 1619–30.
12 Ruiter GA, Zerp SF, Bartelink H, van Blitterswijk WJ, Verheij M. Anticancer alkyl-lysophospholipids inhibit the phosphatidylinositol 3-kinase-Akt/PKB survival pathway. Anticancer Drugs 2003; 14: 167–73.
13 Helgason GV, Karvela M, Holyoake TL. Kill one bird with two stones: potential efficacy of BCR-ABL and autophagy inhibition in CML. Blood 2011; 118: 2035–43.
14 Jamieson CH. Chronic myeloid leukemia stem cells. Hematology Am Soc Hematol Educ Program 2008: 436–42.
15 Burchert A, Wang Y, Cai D, von Bubnoff N, Paschka P, Müller-Brüsselbach S, *et al*. Compensatory PI3-kinase/Akt/mTor activation regulates imatinib resistance development. Leukemia 2005; 19: 1774–82.
16 Vink SR, Schellens JH, van Blitterswijk WJ, Verheij M. Tumor and normal tissue pharmacokinetics of perifosine, an oral anti-cancer alkylphospholipid. Invest New Drugs 2005; 23: 279–86.
17 LoPiccolo J, Blumenthal GM, Bernstein WB, Dennis PA. Targeting the PI3K/Akt/mTOR pathway: effective combinations and clinical considerations. Drug Resist Updat 2008; 11: 32–50.
18 Nyåkern M, Cappellini A, Mantovani I, Martelli AM. Synergistic induction of apoptosis in human leukemia T cells by the Akt inhibitor perifosine and etoposide through activation of intrinsic and Fas-mediated extrinsic cell death pathways. Mol Cancer Ther 2006; 5: 1559–70.
19 Papa V, Tazzari PL, Chiarini F, Cappellini A, Ricci F, Billi AM, *et al*. Proapoptotic activity and chemosensitizing effect of the novel Akt inhibitor perifosine in acute myelogenous leukemia cells. Leukemia 2008; 22: 147–60.
20 Hideshima T, Catley L, Yasui H, Ishitsuka K, Raje N, Mitsiades C, *et al*. Perifosine, an oral bioactive novel alkylphospholipid, inhibits Akt and induces *in vitro* and *in vivo* cytotoxicity in human multiple myeloma cells. Blood 2006; 107: 4053–62.
21 Richardson P, Lonial S, Jakubowiak A, Krishnan A, Wolf J, Densmore J, *et al*. Multi-center phase II study of Perifosine (KRX-0401) alone and in combination with dexamethasone (Dex) for patients with relapsed or relapsed/refractory multiple myeloma (MM): promising activity as combination therapy with manageable toxicity. Blood 2007; 110: 1164.
22 Levy DS, JA Kahana JA, Kumar R. AKT inhibitor, GSK690693, induces growth inhibition and apoptosis in acute lymphoblastic leukemia cell lines. Blood 2009; 113: 1723–29.
23 Yang C, Tong Y, Ni W, Liu J, Xu W, Li L, *et al*. Inhibition of autophagy induced by overexpression of MDA/Interleukin-24 using a PI3K inhibitor results in significant enhanced antileukmia activity *in vivo*. Cancer Gene Ther 2010; 17: 109–19.
24 Elrod HA, Lin YD, Yue P, Wang X, Lonial S, Khuri FR, *et al*. The alkylphospholipid perifosine induces apoptosis of human lung cancer cells requiring inhibition of Akt and activation of the extrinsic apoptotic pathway. Mol Cancer Ther 2007; 6: 2029–38.
25 Rahmani M, Reese E, Dai Y, Bauer C, Payne SG, Dent P, *et al*. Coadministration of histone deacetylase inhibitors and perifosine synergistically induces apoptosis in human leukemia cells through Akt and ERK1/2 inactivation and the generation of ceramide and reactive oxygen species. Cancer Res 2005; 65: 2422–32.
26 Mathew R, Karantza-Wadsworth V, White E. Role of autophagy in cancer. Nat Rev Cancer 2007; 7: 961–7.
27 Qian W, Liu J, Jin J, Ni W, Xu W. Arsenic trioxide induces not only apoptosis but also autophagic cell death in leukemia cell lines via up-regulation of Beclin-1. Leuk Res 2007; 31: 329–39.
28 Carew JS, Nawrocki ST, Kahue CN, Zhang H, Yang C, Chung L, *et al.* Targeting autophagy augments the anticancer activity of the histone deacetylase inhibitor SAHA to overcome Bcr-Abl-mediated drug resistance. Blood 2007; 110: 313–22.
29. Yu L, Alva A, Su H, Dutt P, Freundt E, Welsh S, *et al*. Regulation of an ATG7-beclin 1 program of autophagic cell death by caspase-8. Science 2004; 304: 1500–2.
30 Levine B, Kroemer G. Autophagy in the pathogenesis of disease. Cell 2008; 132: 27–42.
31 Kawauchi K, Ogasawara T, Yasuyama M, Ohkawa S. Involvement of Akt kinase in the action of STI571 on chronic myelogenous leukemia cells. Blood Cells Mol Dis 2003; 31: 11–7.
32 Li Z, Tan F, Liewehr DJ, Steinberg SM, Thiele CJ. *In vitro* and *in vivo* inhibition of neuroblastoma tumor cell growth by AKT inhibitor perifosine. J Natl Cancer Inst 2010; 102: 758–70.
33 Han J, Hou W, Goldstein LA, Lu C, Stolz DB, Yin XM, *et al*. Involvement of protective autophagy in TRAIL resistance of apoptosis-defective tumor cells. J Biol Chem 2008; 283: 19665–77.
34 Ertmer A, Huber V, Gilch S, Yoshimori T, Erfle V, Duyster J, *et al*. The anticancer drug imatinib induces cellular autophagy. Leukemia 2007; 21: 936–42.
35 Kamitsuji Y, Kuroda J, Kimura S, Toyokuni S, Watanabe K, Ashihara E, *et al*. The Bcr-Abl kinase inhibitor INNO-406 induces autophagy and different modes of cell death execution in Bcr-Abl-positive leukemias. Cell Death Differ 2008; 15: 1712–22.
36 Bellodi C, Lidonnici MR, Hamilton A, Helgason GV, Soliera AR, Ronchetti M, *et al*. Targeting autophagy potentiates tyrosine kinase inhibitor-induced cell death in Philadelphia chromosome-positive cells, including primary CML stem cells. J Clin Invest 2009; 119: 1109–23.
37 Fu L, Kim YA, Wang X, Wu X, Yue P, Lonial S, *et al*. Perifosine inhibits mammalian target of rapamycin signaling through facilitating degradation of major components in the mTOR axis and induces autophagy. Cancer Res 2009; 69: 8967–76.
38 Degtyarev M, De Mazière A, Orr C, Lin J, Lee BB, Tien JY, *et al*. Akt inhibition promotes autophagy and sensitizes PTEN-null tumors to lysosomotropic agents. J Cell Biol 2008; 183: 101–16.
39 Chu CT, Zhu J, Dagda R. Beclin 1-independent pathway of damage-induced mitophagy and autophagic stress: implications for neurodegeneration and cell death. Autophagy 2007; 3: 663–6.
40 Scarlatti F, Maffei R, Beau I, Ghidoni R, Codogno P. Non-canonical autophagy: an exception or an underestimated form of autophagy? Autophagy 2008; 4: 1083–5.
41 Scarlatti F, Maffei R, Beau I, Codogno P, Ghidoni R. Role of non-canonical Beclin 1-independent autophagy in cell death induced by resveratrol in human breast cancer cells. Cell Death Differ 2008; 15: 1318–29.
42 Smith DM, Patel S, Raffoul F, Haller E, Mills GB, Nanjundan M. Arsenic trioxide induces a beclin-1-independent autophagic pathway

via modulation of SnoN/SkiL expression in ovarian carcinoma cells. Cell Death Differ 2010; 17: 1867–81.

43 Nishida Y, Arakawa S, Fujitani K, Yamaguchi H, Mizuta T, Kanaseki T, *et al*. Discovery of Atg5/Atg7-independent alternative macroautophagy. Nature 2009; 461: 654–8.

44 Gao P, Bauvy C, Souquère S, Tonelli G, Liu L, Zhu Y, *et al*. The Bcl-2 homology domain 3 mimetic gossypol induces both Beclin 1-dependent and Beclin 1-independent cytoprotective autophagy in cancer cells. J Biol Chem 2010; 285: 25570–81.

45 Xia HG, Zhang L, Chen G, Zhang T, Liu J, Jin M, *et al*. Control of basal autophagy by calpain1 mediated cleavage of ATG5. Autophagy 2010; 6: 61–6.

Acta Pharmacologica Sinica (2012) 33: 551–557
 1671-4083/12 $32.00
www.nature.com/aps

Original Article

Imatinib induces H2AX phosphorylation and apoptosis in chronic myelogenous leukemia cells *in vitro* via caspase-3/Mst1 pathway

Yan-jun ZHANG[1, 2], Cheng-rong LU[1, *], Yan CAO[1, 2], Yuan LUO[1], Rong-feng BAO[1], Shu YAN[1, 3], Mei XUE[4], Feng ZHU[5], Zhe WANG[1], Lian-ning DUAN[1, *]

[1]Aviation Medicine Research Lab and [4]Department of Hematology, General Hospital of Air Force, Beijing 100142, China; [2]Graduate Student Ministry of Education, Hebei North University, Zhangjiakou 075000, China; [3]Department of Post-Graduate, China Medical University, Shenyang 110001, China; [5]Hormel Institute, University of Minnesota, Austin, MN 55912, USA

Aim: Histone H2AX is a novel tumor suppressor and its phosphorylation at the C terminus (Ser139 and Tyr142) is required for tumor cell apoptosis. The aim of the present study was to elucidate the mechanisms underlying imatinib-induced C-terminal phosphorylation of H2AX in chronic myelogenous leukemia cells *in vitro*.
Methods: BCR–ABL-positive K562 cells were used. Microscopy, Western blotting and flow cytometry were used to study the signaling pathways that regulate imatinib-induced H2AX phosphorylation and the apoptotic mechanisms.
Results: Treatment of K562 cells with imatinib (1–8 μmol/L) induced phosphorylation of H2AX at Ser139 and Tyr142 in time- and dose-dependent manners. In contrast, imatinib at the same concentrations did not affect H2AX acetylation at Lys 5, and the acetylated H2AX maintained a higher level in the cells. Meanwhile, imatinib (1–8 μmol/L) activated caspase-3 and its downstream mammalian STE20-like kinase 1 (Mst1), and induced apoptosis of K562 cells. The caspase-3 inhibitor Z-VAD (40 μmol/L) reduced imatinib-induced H2AX phosphorylation at Ser139 and Tyr142 and blocked imatinib-induced apoptosis of K562 cells. Imatinib (4 μmol/L) induced expression of Williams–Beuren syndrome transcription factor (WSTF), but not wild-type p53-induced phosphatase 1 (Wip1) in K562 cells.
Conclusion: The caspase-3/Mst1 pathway is required for H2AX C-terminal phosphorylation at Ser139 and Tyr142 and subsequent apoptosis in Bcr-Abl-positive K562 cells induced by imatinib.

Keywords: chronic myelogenous leukemia; imatinib; H2AX; phosphorylation; acetylation; apoptosis; caspase-3; mammalian STE20-like kinase 1 (Mst1); Z-VAD; Williams–Beuren syndrome transcription factor

Acta Pharmacologica Sinica (2012) 33: 551–557; doi: 10.1038/aps.2012.9; published online 5 Mar 2012

Introduction

Chronic myelogenous leukemia (CML) is a myeloproliferative disorder of the hematopoietic stem cells, caused by a t(9; 22) (q34; q11) translocation that generates a BCR–ABL fusion gene encoding a BCR–ABL fusion oncoprotein[1–3]. BCR–ABL fusion protein possesses constitutively active tyrosine kinase activity, which plays an essential role in the initiation of CML. Multiple signaling pathways including Ras, Stat 5, Erk/MAPK, Jak2, PI3K, and others are activated by BCR–ABL, leading to excessive and uncontrolled proliferation of differentiated myeloid cells[4]. Clinically, CML has been successfully treated with imatinib mesylate, a selective small-molecule protein kinase inhibitor that specifically targets the oncogenic BCR–ABL fusion protein kinase, although the regulation mechanism involved in imatinib-induced CML cell apoptosis is only partially understood[5, 6]. However, new difficulties have challenged clinicians. It has also been found that many CML patients have resistance to imatinib treatment because of a high frequency of BCR–ABL fusion gene mutations[5–7]. Thus, identifying the signaling pathways or biochemical mediators of imatinib-induced CML cell death may help to develop innovative strategies to overcome imatinib resistance.

Histone variant H2AX is a major regulator of the cellular response to DNA damage and is associated with cell death[8, 9]. Increasing evidence has demonstrated that the function of H2AX is mainly regulated by its C-terminal phosphorylation

* To whom correspondence should be addressed.
E-mail luchengrong@263.net (Cheng-rong LU);
duanlianning@hotmail.com (Lian-ning DUAN)
Received 2011-11-29 Accepted 2012-01-12

at Ser139[10, 11]. The phosphorylated form of H2AX at Ser139 has also been referred to as γH2AX[12]. We have previously reported that γH2AX is required for DNA degradation mediated by caspase-activated DNase (CAD) in apoptotic cells[9]. Recently C-terminal Tyr142 of H2AX has been found to be a phosphorylation site[13, 14]. Tyr142 phosphorylation is not a prerequisite for Ser139 phosphorylation but cooperates to regulate DNA damage repair or apoptosis. *In vitro* and *in vivo* experiments have both already provided compelling evidence that H2AX phosphorylation is related to tumor development[15–17]. It has been reported that deletion of H2AX attenuates the apoptotic response of gastrointestinal stromal tumors (GISTs) to imatinib and induces blast crisis of CML in a transgenic mouse model[16, 18]. Taken together, these published data indicate that H2AX plays an important role in regulation of tumor cell apoptosis and acts as a novel human tumor suppressor protein. However, it is still unknown how H2AX phosphorylation at Ser139 and Tyr142 is regulated in CML cells. Therefore, identification of the signaling pathways involved in imatinib-induced H2AX phosphorylation and apoptosis may provide new molecular targets for imatinib-resistant CML or other cancer therapy.

In this study, we used imatinib to induce apoptosis of BCR–ABL-positive K562 cells and investigated the signaling pathways involved in regulation of H2AX phosphorylation (Ser139/Tyr142). We demonstrated that imatinib induced strong phosphorylation of H2AX (Ser139/Tyr142) in a time- and dose-dependent manner. However, H2AX acetylation (Lys 5) was not induced by imatinib. Caspase-3 and its downstream Mst1 could be activated by imatinib during apoptosis, coinciding with H2AX phosphorylation at Ser139 and Tyr142. Inhibition of the caspase-3/Mst1 pathway with caspase-3 inhibitor Z-VAD reduced H2AX phosphorylation at Ser139 and Tyr142 and blocked K562 cell apoptosis. In addition, we found that expression of WSTF, which is reported to regulate H2AX phosphorylation at Tyr142, was increased by imatinib. However, expression of Wip1, which has been shown to dephosphorylate H2AX at Ser139, was not affected by imatinib. Overall, these data show that the caspase-3/Mst1 pathway is required for imatinib-induced H2AX C-terminal phosphorylation (Ser139 and Tyr142) and subsequent apoptosis of Bcr−Abl-positive K562 cells.

Materials and methods

Reagents

Imatinib mesylate and caspase-3 inhibitor Z-VAD were purchased from Axon Medchem (Groningen, Netherlands) and Calbiochem (La Jolla, CA, USA), respectively. The antibodies against γH2AX, phosphorylated H2AX (Y142), acetylated H2AX (Lys 5) (aH2AX), H2AX, Mst1, active Mst1, and WSTF were obtained from Millipore (Billerica, MA, USA). The antibody to detect β-actin was from Sigma-Aldrich (St Louis, MO, USA). The antibodies against caspase-3, activated caspase-3 (cleaved caspase-3 fragment) and Wip1 were obtained from Santa Cruz Biotechnology (Santa Cruz, CA, USA).

Cell culture and chemical drug treatments

K562 cells were cultured in RPMI-1640 medium supplemented with 10% fetal bovine serum (FBS) in a 37 °C 5% CO_2 incubator. Before each experiment, K562 cells (5×10^6) were seeded in 10-cm dishes and treated for various times with culture medium supplemented with imatinib mesylate or with Z-VAD 1 h before treatment with imatinib mesylate.

Observation of apoptotic cell morphology

K562 cells after treatment with imatinib mesylate at different concentrations for various times were observed by inverted microscopy (Olympus, Tokyo, Japan). To detect chromatin condensation, K562 cells after imatinib mesylate treatment were stained with DAPI (Cell Apoptosis DAPI Detection Kit; KeyGen Biotech, Nanjing, China). All samples were viewed with a fluorescence microscope (Olympus).

Total cellular protein or histone extraction and Western blot analysis

Cellular proteins were extracted after drug treatments by disrupting the cells in lysis buffer (50 mmol/L Tris–HCl, pH 7.4, 1% NP-40, 0.25% sodium deoxycholate, 150 mmol/L NaCl, 1 mmol/L EGTA, 1 mmol/L Na_3VO_4, 1 mmol/L NaF, 1 mg/mL aprotinin, 1 mg/mL leupeptin, 1 mg/mL pepstatin, and 1 mmol/L PMSF). To extract the histones after drug treatment, cells were lysed in NETN buffer (150 mmol/L NaCl, 1 mmol/L EDTA, 20 mmol/L Tris, pH 8, and 0.5% NP-40) and centrifuged for 5 min. The histones were extracted from the pellets with 0.1 mol/L HCl[10]. The protein samples were resolved by SDS-PAGE and transferred to polyvinylidene difluoride membranes. The membranes were blocked at room temperature for 1 h with 5% nonfat milk in Tris-buffered saline containing Tween 20 (TBST). Primary antibodies were incubated with membranes at 4 °C overnight. Membranes were incubated with the appropriate secondary antibody in TBST for 1 h at room temperature. Proteins were detected by enhanced chemiluminescence (Amersham Biosciences, Bucks, UK).

Flow cytometry

Imatinib-induced apoptosis of K562 cells was examined using a PE Annexin V Apoptosis Detection Kit (BD Biosciences, San Jose, CA, USA) according to the protocol provided. Cells were washed once with RPMI-1640 medium containing serum, and incubated with Annexin V-conjugated PE. Apoptosis was analyzed by flow cytometer (FACS-Calibur; Becton Dickinson, San Jose, CA, USA).

Statistical analysis

Data are expressed as the mean±SD from three independent determinations, and significance was assessed using a *t* test and one-way ANOVA. Differences were considered significant at $P<0.01$.

Results

Imatinib induces H2AX C-terminal phosphorylation and apoptosis

Human K562 cells are BCR–ABL-positive CML cells[19]. Imatinib inhibits the kinase activity of BCR–ABL, leading to inhibition of K562 cell growth and apoptosis. Previous data have shown that H2AX C-terminal phosphorylation is required for tumor cell apoptosis[17, 20, 21]. Hence, we investigated whether imatinib could induce H2AX C-terminal phosphorylation in CML cells. Histones were extracted from K562 cells after imatinib treatment at the indicated time and dose and Western blot analysis was conducted. The data demonstrated that treatment with imatinib for 24 or 48 h induced H2AX C-terminal phosphorylation at Ser139 and Tyr142 in a dose-dependent manner (Figure 1A). At the same time, we also detected H2AX acetylation and found that imatinib did not induce H2AX acetylation (Lys 5) in K562 cells (Figure 1A). Our data showed that H2AX acetylation appeared not to affect H2AX phosphorylation (Ser139/Tyr142). However, the reason why K562 cells maintained such a high endogenous level of acetylated H2AX (Lys 5) and how acetylated H2AX (Lys 5) functioned is an interesting issue that requires further investigation (Figure 1A).

We also observed that K562 cell apoptosis (cell shrinking) was triggered by imatinib in a dose-dependent manner (Figure 1B), following a parallel response with H2AX phosphorylation (Ser139/Tyr142) (Figure 1A). These data suggested that H2AX C-terminal phosphorylation was related to apoptosis of CML cells, and supported the previous suggestion that H2AX C-terminal phosphorylation is involved in tumor cell apoptosis.

Imatinib triggers activation of caspase-3 and its downstream Mst1

Caspase-3 has been identified as a key mediator of apoptosis of mammalian cells, and its activation is believed to be a hall-

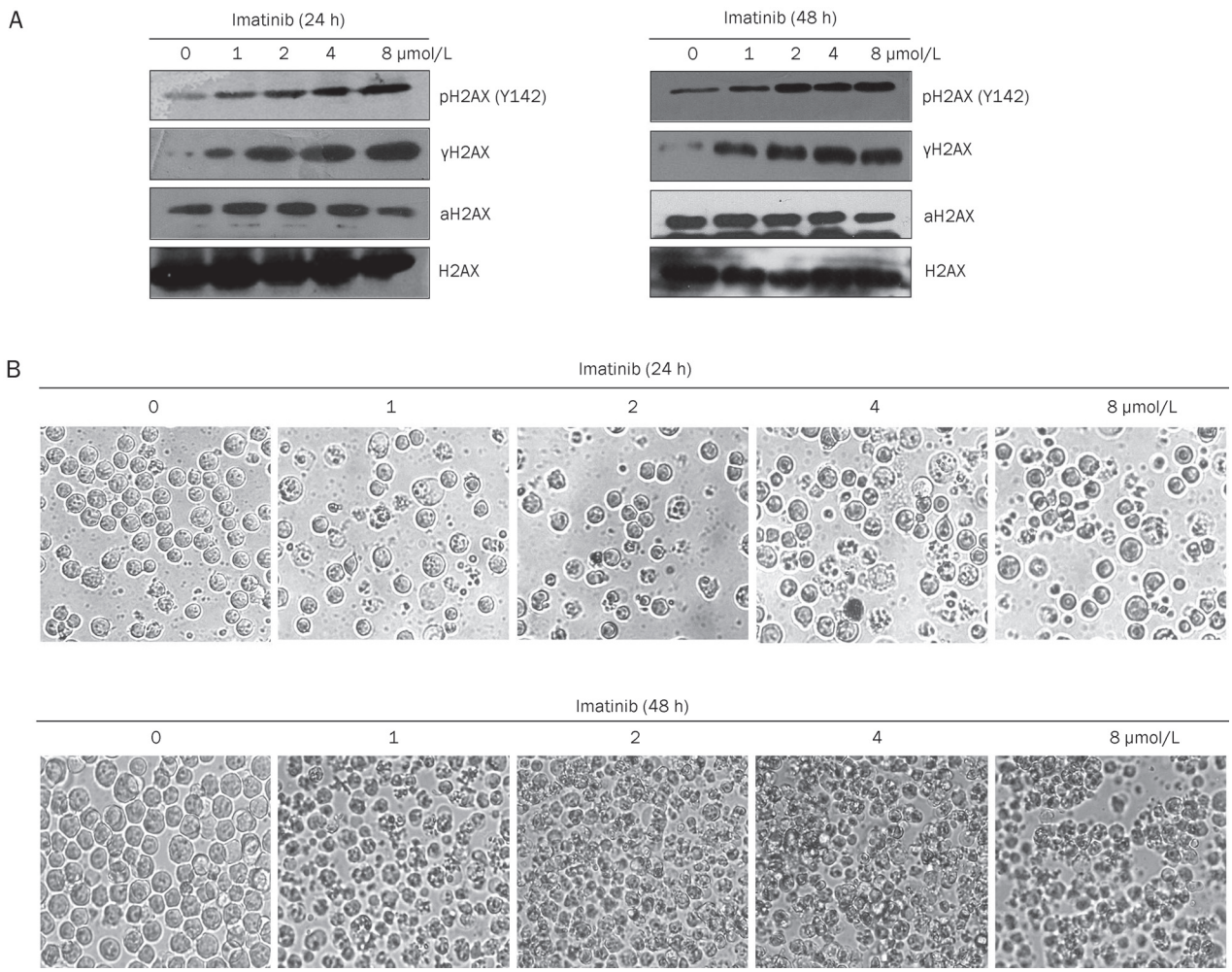

Figure 1. Imatinib induces H2AX phosphorylation at Ser139 and Tyr142 and apoptosis. (A) K562 cells were treated with different concentrations of imatinib as indicated for 24 h (left panel) and 48 h (right panel). Cells not treated with imatinib served as negative controls. The histones were extracted and resolved by 15% SDS-PAGE followed by Western blot analysis with antibodies against γH2AX (phosphorylated H2AX at Ser139), pH2AX (Y142) (phosphorylated H2AX at Tyr142), aH2AX (acetylated H2AX at Lys 5) and total H2AX. (B) As for (A), K562 cells after treatment with imatinib at the indicated time and dose were observed by microscopy (original magnification: ×400).

mark of apoptosis, and to regulate chromatin condensation by its downstream CAD[22]. Mst1, another caspase-3 downstream protein, has recently been reported to phosphorylate H2AX at Ser139 directly in HEK 293 cells, resulting in formation of γH2AX, which regulates apoptosis[23]. To investigate whether the caspase-3/Mst1 signaling pathway is involved in regulation of C-terminal phosphorylation of H2AX in CML cells, we studied the effect of imatinib on activation of the caspase-3/Mst1 pathway, using Western blot analysis. We indicated that caspase-3 and Mst1 were dramatically activated after 24 or 48 h imatinib treatment in a dose-dependent manner (Figure 2A). Caspase-3 (34 kDa) was cleaved to produce the active fragment (17 kDa). Simultaneously, Mst1 (54 kDa) was cleaved by activated caspase-3 to form the active Mst1 fragment (34 kDa). Together with these data, we demonstrated that caspase-3 and Mst1 activation were triggered by imatinib (Figure 2A), following a similar response as that for H2AX C-terminal phosphorylation induced by imatinib (Figure 1A). These results suggest that the caspase-3/Mst1 pathway contributes to C-terminal phosphorylation of H2AX. To confirm that imatinib induces apoptosis, we stained K562 cells with DAPI to observe chromatin condensation. The data clearly showed that imatinib induced strong apoptosis of K562 cells in a time-dependent manner (Figure 2B).

Caspase-3/Mst1 pathway is required for imatinib-induced H2AX phosphorylation and apoptosis

The data presented in Figures 1 and 2 indicated that imatinib might induce H2AX C-terminal phosphorylation (Ser139 and Tyr142) via the caspase-3/Mst1 pathway during K562 cell apoptosis. To confirm this, we used caspase-3 inhibitor Z-VAD to block caspase-3/Mst1 signaling in K562 cells and then detected H2AX C-terminal phosphorylation and apoptosis induced by imatinib. K562 cells treated with imatinib alone or together with Z-VAD were harvested for Western blotting and flow cytometry. Imatinib triggered caspase-3 and Mst1 activation in a time-dependent manner (Figure 3, bottom left). At the same time, phosphorylation of H2AX at Ser139/Tyr142 was induced (Figure 3, top left). To investigate the action of the caspase-3/Mst1 pathway in regulation of H2AX phosphorylation at Ser139/Tyr142 and apoptosis of K562 cells, Z-VAD was used to treat K562 cells with imatinib. We found that Z-VAD inhibited the cleavage of caspase-3 and Mst1 to form their active fragments. That is to say, Z-VAD inhibited imatinib-induced activity of caspase-3, leading to inhibition of Mst1 activity (Figure 3, bottom right). Simultaneously, imatinib-induced phosphorylation of Ser139 and Tyr142 in H2AX was inhibited by Z-VAD (Figure 3, top right).

Furthermore, we also detected the function of the caspase-3/

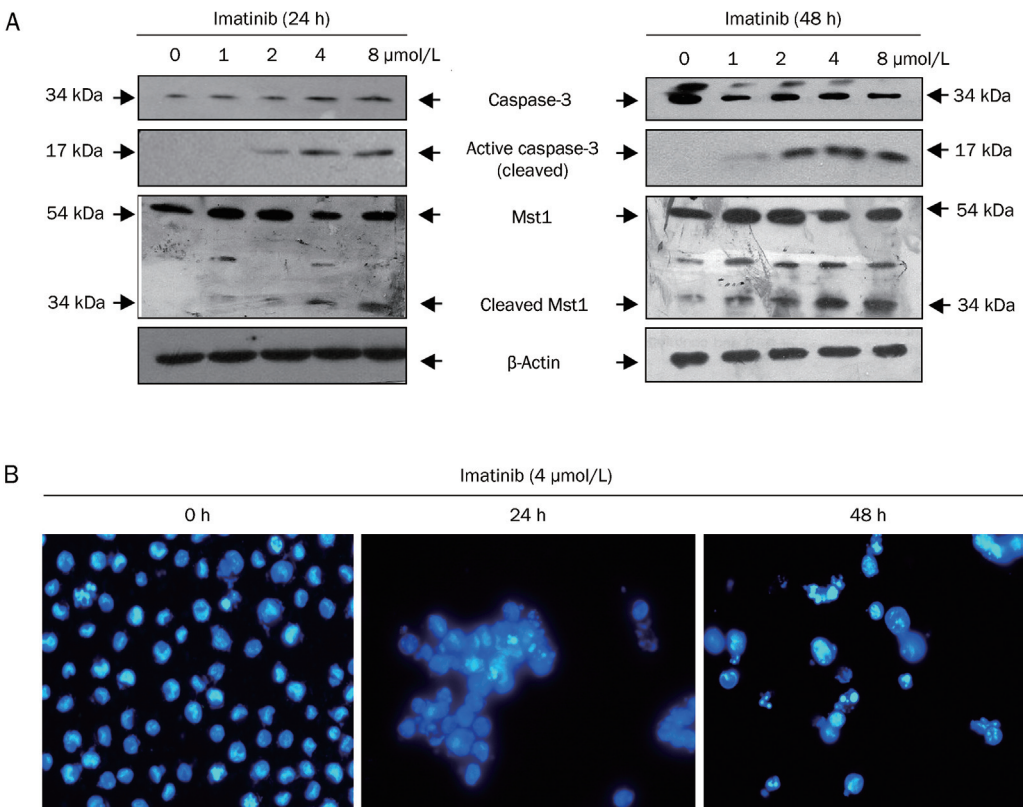

Figure 2. Imatinib induces caspase-3 and Mst1 activation and apoptosis. (A) K562 cells were treated with imatinib at the indicated concentrations for 24 h (left panel) or 48 h (right panel) and harvested for Western blot analysis to detect caspase-3 (full length, 34 kDa), cleavage of caspase-3 (17 kDa fragment), Mst1 (full length, 54 kDa), and cleaved Mst1 (34 kDa). β-Actin was also detected as a loading control. (B) K562 cells were treated with imatinib (4 μmol/L) for 0, 24, or 48 h and stained with DAPI for observation by immunofluorescence microscopy (original magnification: ×400).

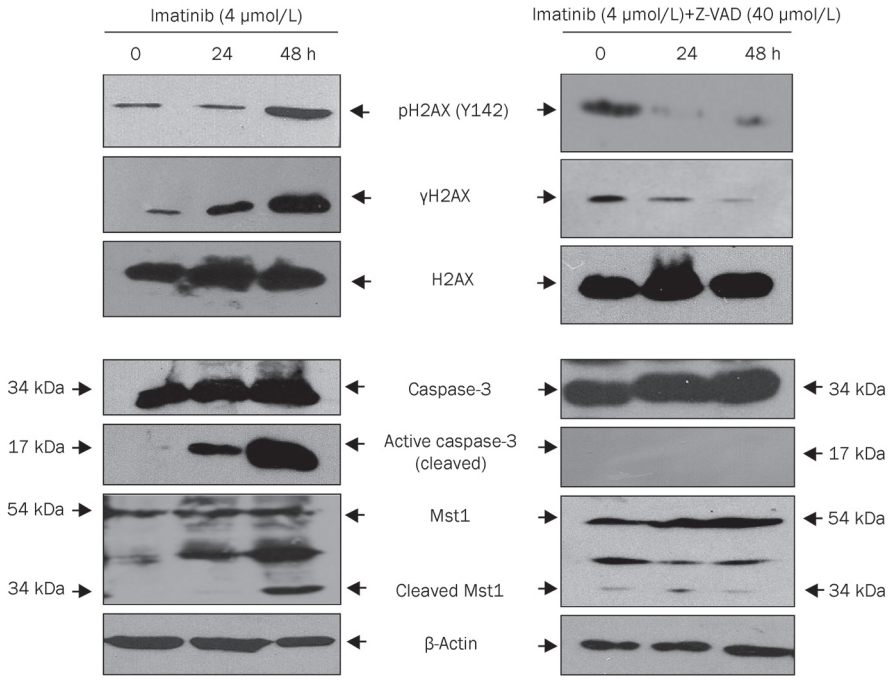

Figure 3. Caspase-3/Mst1 pathway is involved in imatinib-induced H2AX phosphorylation at Ser139 and Tyr142. K562 cells were treated with imatinib (left panels) and imatinib with Z-VAD (right panel) for the indicated time. The extracted whole proteins were resolved by 10% SDS-PAGE followed by Western blot analysis with antibodies against caspase-3 (full length, 34 kDa), cleaved caspase-3 (17 kDa fragment), Mst1 (full length, 54 kDa), and cleaved Mst1 (34 kDa) (bottom, left panel and right panel). The extracted histones were analyzed by Western blotting to detect phosphorylation of H2AX [pH2AX (Y142), γH2AX, and total H2AX] (top left and right panels).

Mst1 pathway in regulation of K562 cell apoptosis induced by imatinib. Flow cytometry showed that imatinib effectively induced apoptosis of K562 cells, characterized by the percentage of early apoptotic cells, in a time-dependent manner (Figure 4). Z-VAD strongly reduced imatinib-induced apoptosis of K562 cells (Figure 4).

Overall, these data provided strong evidence that H2AX phosphorylation (Ser139/Tyr142) and apoptosis of K562 cells induced by imatinib is regulated by the caspase-3/Mst1 signaling pathway.

Imatinib induces Tyr142 phosphorylation of H2AX by increasing WSTF but not Wip1 expression

Wip1 is a nuclear oncogenic type 2C protein phosphatase that is amplified in many human tumors, such as breast cancer, ovarian clear cell carcinoma, and medulloblastoma[24, 25]. Previous data have indicated that Wip1 directly dephosphorylates γH2AX (Ser139) and regulates DNA damage response. Hence, we investigated whether imatinib induced H2AX phosphorylation (Ser139) by inhibiting expression of Wip1. We showed that imatinib did not increase Wip1 expression in K562 cells (Figure 5A).

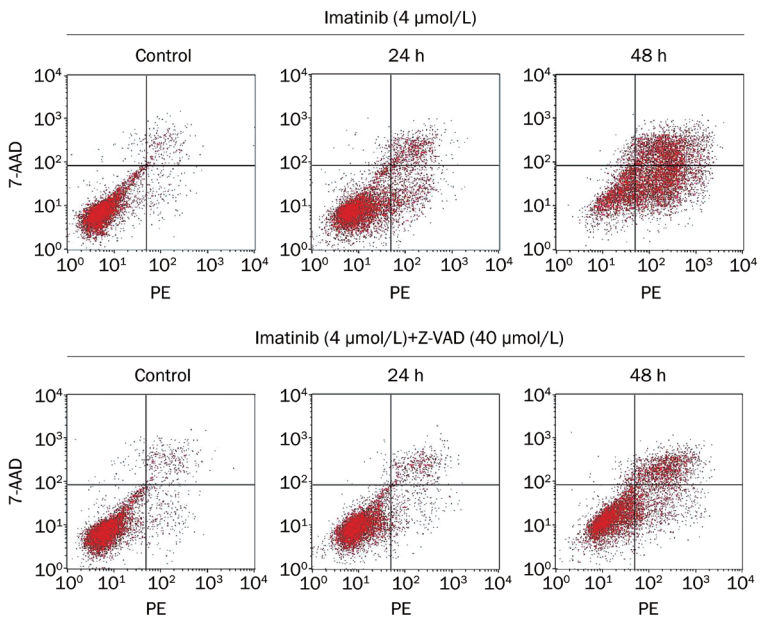

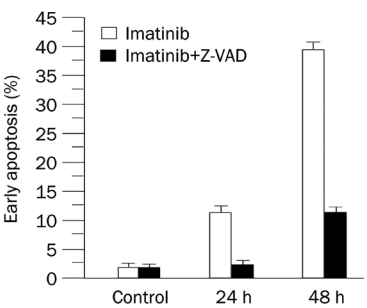

Figure 4. Caspase-3 is required for apoptosis of K562 cells. K562 cells were treated with 4 μmol/L imatinib (top left panels) and 4 μmol/L imatinib with 40 μmol/L Z-VAD (bottom left panels). Cells were harvested at the indicated time and subjected to flow cytometry after Annexin V-conjugated PE staining to assess early apoptosis (PE Annexin V positive and 7-AAD negative) (right bottom area). The mean±SD of three independent determinations are shown (right panel) (P<0.01).

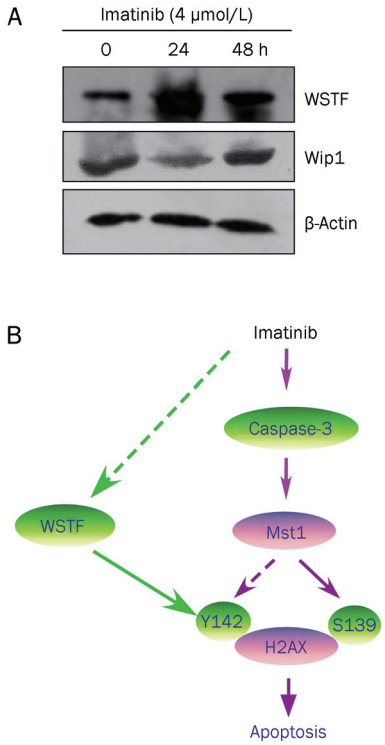

Figure 5. (A) WSTF regulates imatinib-induced Tyr142 phosphorylation of H2AX. K562 cells were treated with 4 μmol/L imatinib at the indicated time. The extracted whole proteins were subjected to Western blot analysis with antibodies against WSTF, Wip1, and β-actin. (B) A regulation model of H2AX phosphorylation (C-terminal) during imatinib-induced apoptosis. Once caspase-3 activation is triggered by imatinib and its down stream Mst1 will be cleaved and activated. Active Mst1 can regulate H2AX phosphorylation at Ser139 (S139) and Tyr142 (Y142), which is involved in apoptosis. Simultaneously, imatinib can also increases Tyr142 phosphorylation of H2AX by increasing WSTF protein level to regulate apoptosis. The dotted arrows indicate the regulation mechanisms that remain to be characterized further.

Another protein, WSTF, a component of the WICH complex (WSTF–ISWI ATP-dependent chromatin-remodeling complex) was found to regulate Tyr142 phosphorylation of H2AX[14]. We indicated that imatinib actually increased WSTF level in K562 cells (Figure 5A). This is a novel finding, suggesting that WSTF protein at least partially contributed to imatinib-induced H2AX phosphorylation (Tyr142) to regulate apoptosis. How imatinib regulates expression of WSTF or whether the caspase-3/Mst1 pathway is also involved in regulation of WSTF protein level requires further investigation.

Discussion

Histone H2AX is a variant of histone H2A that is ubiquitously expressed throughout the genome, and has been designated as the histone guardian of the genome[26]. Deficiency of histone H2AX decreases genomic stability and increases tumor susceptibility of normal cells and tissues, suggesting that it might act as a tumor suppressor[27, 28]. Increasing evidence, along with our present results show that the function of H2AX involved in regulation of apoptosis is mediated by its C-terminal phosphorylation. We previously have demonstrated that H2AX phosphorylation at Ser139 plays a key role in regulation of apoptosis[9, 10]. Mutation of Ser139 in H2AX to block Ser139 phosphorylation greatly inhibited apoptosis. Recently, Tyr142 in the C terminus of H2AX was found to be regulated by WSTF during apoptosis. Tyr142 phosphorylation has been confirmed as not essential for Ser139 phosphorylation, but it might cooperate to regulate DNA damage repair or apoptosis[14]. We found that WSTF protein level in K562 cells was increased by imatinib treatment, indicating that imatinib induced Tyr142 phosphorylation, partially dependent on WSTF. However, we excluded the possibility of Wip1 involved in imatinib-induced phosphorylation of H2AX at Ser139. To summarize our present results, we suggest a regulation model of H2AX C-terminal phosphorylation during imatinib-induced apoptosis. The model demonstrates that imatinib can induce both Ser139 and Tyr142 phosphorylation, and apoptosis in K562 cells through the caspase-3/Mst1 pathway (Figure 5B). Furthermore, the imatinib-induced increase in WSTF level was at least partially involved in phosphorylation of H2AX at Tyr142 (Figure 5B). Our previous work has shown that H2AX phosphorylated at Ser139 (γH2AX) regulates DNA fragmentation triggered by CAD in apoptotic cells[9]. However, how the Tyr142 phosphorylation of H2AX cooperates with Ser139 phosphorylation of H2AX to regulate apoptosis is currently unknown in detail.

Our data confirmed the importance of H2AX in apoptosis of CML cells. Interestingly, the H2AX gene maps to chromosome 11q23, a region which is frequently altered in mantle cell lymphoma and CML[2]. Furthermore, H2AX deficiency promotes B-cell tumorigenesis[29]. The data from the transgenic mouse model of CML further demonstrate that H2AX functions as a tumor suppressor, and low expression of H2AX promotes the blast crisis of CML[18]. H2AX dysfunction could make animals more sensitive to carcinogenic factors. Apparently, the function of H2AX as a tumor suppressor is related to its regulation of apoptosis. Carcinogenic factors usually induce DNA double-strand breaks (DSBs) in the genome, and cells themselves can trigger repair of these DSBs. Once DNA damage such as DSBs cannot be repaired, cells have to choose the apoptotic fate to protect the organism. If the apoptotic mechanism is prevented because of loss of H2AX function, the cells bearing an increasing number of DSBs possibly face a high risk of malignant mutations in the genome and therefore are easier to tumorigenesis.

CML is a clonal disease of hematopoietic stem cells that is characterized by BCR–ABL fusion protein, which has constitutive tyrosine kinase activity and is essential for the pathogenesis of the disease[3]. Imatinib, an ATP-competitive selective inhibitor of BCR–ABL, has emerged as the lead compound for clinical development against CML because of its unprecedented efficacy[1]. However, the mechanism of apoptosis induced by imatinib is not known well, which prevents effective treatment of CML, especially in patients who develop imatinib resistance. H2AX has been found to be expressed at

low levels in GISTs[16]. Low levels of γH2AX destroy the balance between growth and apoptosis of tumor cells, resulting in uncontrolled proliferation. Therefore, inhibition of H2AX phosphorylation is one possible reason why many patients with tumors develop resistance to radiotherapy and chemotherapy, including imatinib treatment. To the best of our knowledge, our study is the first to reveal the signal transduction pathway which regulates H2AX phosphorylation (Ser139/Tyr142), and to demonstrate the importance of H2AX phosphorylation in apoptosis of CML cells. Overall, these data provided mechanistic insights into imatinib-induced tumor cell apoptosis and suggested H2AX as a novel target in cancer therapy.

Acknowledgements

This work was supported by the National Natural Science Foundation of China (No 30770430 and 81070424).

Author contribution

Yan-jun ZHANG performed most of experiments and analyzed the results. Cheng-rong LU, Yan-jun ZHAG, and Lianning DUAN designed the study. Cheng-rong LU wrote the manuscript, which was revised by Feng ZHU and Lian-ning DUAN. Feng ZHU and Mei XUE also provided support and general guidance for this work. Yan CAO and Shu YAN performed flow cytometry analysis for apoptosis. Yuan LUO, Rong-feng BAO, and Zhe WANG performed morphological observation of apoptotic cells.

References

1 Brauer KM, Werth D, von Schwarzenberg K, Bringmann A, Kanz L, Grunebach F, *et al*. BCR-ABL activity is critical for the immunogenicity of chronic myelogenous leukemia cells. Cancer Res 2007; 67: 5489–97.
2 Goldman JM, Melo JV. Chronic myeloid leukemia — advances in biology and new approaches to treatment. N Engl J Med 2003; 349: 1451–64.
3 Goldman JM, Melo JV. Targeting the BCR-ABL tyrosine kinase in chronic myeloid leukemia. N Engl J Med 2001; 344: 1084–6.
4 Yoshida C, Yoshida F, Sears DE, Hart SM, Ikebe D, Muto A, *et al*. Bcr-Abl signaling through the PI-3/S6 kinase pathway inhibits nuclear translocation of the transcription factor Bach2, which represses the antiapoptotic factor heme oxygenase-1. Blood 2007; 109: 1211–9.
5 Strout MP, Schatz DG. Imatinib resistance and progression of CML to blast crisis: somatic hypermutation AIDing the way. Cancer Cell 2009; 16: 174–6.
6 Lu Z, Jin Y, Chen C, Li J, Cao Q, Pan J. Pristimerin induces apoptosis in imatinib-resistant chronic myelogenous leukemia cells harboring T315I mutation by blocking NF-kappaB signaling and depleting Bcr-Abl. Mol Cancer 2010; 9: 112.
7 Deguchi Y, Kimura S, Ashihara E, Niwa T, Hodohara K, Fujiyama Y, *et al*. Comparison of imatinib, dasatinib, nilotinib and INNO-406 in imatinib-resistant cell lines. Leuk Res 2008; 32: 980–3.
8 Rogakou EP, Pilch DR, Orr AH, Ivanova VS, Bonner WM. DNA double-stranded breaks induce histone H2AX phosphorylation on serine 139. J Biol Chem 1998; 273: 5858–68.
9 Lu C, Zhu F, Cho YY, Tang F, Zykova T, Ma WY, *et al*. Cell apoptosis: requirement of H2AX in DNA ladder formation, but not for the activation of caspase-3. Mol Cell 2006; 23: 121–32.
10 Lu C, Shi Y, Wang Z, Song Z, Zhu M, Cai Q, *et al*. Serum starvation induces H2AX phosphorylation to regulate apoptosis via p38 MAPK pathway. FEBS Lett 2008; 582: 2703–8.
11 Cheung P, Allis CD, Sassone-Corsi P. Signaling to chromatin through histone modifications. Cell 2000; 103: 263–71.
12 Burma S, Chen BP, Murphy M, Kurimasa A, Chen DJ. ATM phosphorylates histone H2AX in response to DNA double-strand breaks. J Biol Chem 2001; 276: 42462–7.
13 Cook PJ, Ju BG, Telese F, Wang X, Glass CK, Rosenfeld MG. Tyrosine dephosphorylation of H2AX modulates apoptosis and survival decisions. Nature 2009; 458: 591–6.
14 Xiao A, Li H, Shechter D, Ahn SH, Fabrizio LA, Erdjument-Bromage H, *et al*. WSTF regulates the H2AX DNA damage response via a novel tyrosine kinase activity. Nature 2009; 457: 57–62.
15 Novik KL, Spinelli JJ, Macarthur AC, Shumansky K, Sipahimalani P, Leach S, *et al*. Genetic variation in H2AFX contributes to risk of non-Hodgkin lymphoma. Cancer Epidemiol Biomarkers Prev 2007; 16: 1098–106.
16 Liu Y, Tseng M, Perdreau SA, Rossi F, Antonescu C, Besmer P, *et al*. Histone H2AX is a mediator of gastrointestinal stromal tumor cell apoptosis following treatment with imatinib mesylate. Cancer Res 2007; 67: 2685–92.
17 Bonner WM, Redon CE, Dickey JS, Nakamura AJ, Sedelnikova OA, Solier S, *et al*. γH2AX and cancer. Nat Rev Cancer 2008; 8: 957–67.
18 Nagamachi A, Yamasaki N, Miyazaki K, Oda H, Miyazaki M, Honda Z. *et al*. Haploinsufficiency and acquired loss of Bcl11b and H2AX induces blast crisis of chronic myelogenous leukemia in a transgenic mouse model. Cancer Sci 2009; 100: 1219–26.
19 Jacquel A, Herrant M, Legros L, Belhacene N, Luciano F, Pages G, *et al*. Imatinib induces mitochondria-dependent apoptosis of the Bcr-Abl-positive K562 cell line and its differentiation toward the erythroid lineage. FASEB J 2003; 17: 2160–2.
20 Cha H, Lowe JM, Li H, Lee JS, Belova GI, Bulavin DV, *et al*. Wip1 directly dephosphorylates gamma-H2AX and attenuates the DNA damage response. Cancer Res 2010; 70: 4112–22.
21 Liu Y, Parry JA, Chin A, Duensing S, Duensing A. Soluble histone H2AX is induced by DNA replication stress and sensitizes cells to undergo apoptosis. Mol Cancer 2008; 7: 61.
22 Li P, Nijhawan D, Wang X. Mitochondrial activation of apoptosis. Cell 2004; 116: S57–9.
23 Wen W, Zhu F, Zhang J, Keum YS, Zykova T, Yao K, *et al*. MST1 promotes apoptosis through phosphorylation of histone H2AX. J Biol Chem 2010; 285: 39108–16.
24 Macurek L, Lindqvist A, Voets O, Kool J, Vos HR, Medema RH. Wip1 phosphatase is associated with chromatin and dephosphorylates gammaH2AX to promote checkpoint inhibition. Oncogene 2010; 29: 2281–91.
25 Moon SH, Lin L, Zhang X, Nguyen TA, Darlington Y, Waldman AS, *et al*. Wildtype p53-induced phosphatase 1 dephosphorylates histone variant γ-H2AX and suppresses DNA double strand break repair. J Biol Chem 2010; 285: 12935–47.
26 Kouzarides T. Chromatin modifications and their function. Cell 2007; 128: 693–705.
27 Zhu F, Zykova TA, Peng C, Zhang J, Cho YY, Zheng D, *et al*. Phosphorylation of H2AX at Ser139 and a new phosphorylation site Ser16 by RSK2 decreases H2AX ubiquitination and inhibits cell transformation. Cancer Res 2011; 71: 393–403.
28 Wu CY, Kang HY, Yang WL, Wu J, Jeong YS, Wang J, *et al*. Critical role of monoubiquitination of histone H2AX protein in histone H2AX phosphorylation and DNA damage response. J Biol Chem 2011; 286: 30806–15.
29 Klemm L, Duy C, Iacobucci I, Kuchen S, von Levetzow G, Feldhahn N, *et al*. The B cell mutator AID promotes B lymphoid blast crisis and drug resistance in chronic myeloid leukemia. Cancer Cell 2009; 16: 232–45.

Acta Pharmacologica Sinica (2012) 33: 558–567
 1671-4083/12 $32.00
www.nature.com/aps

Original Article

Retinol induces morphological alterations and proliferative focus formation through free radical-mediated activation of multiple signaling pathways

Daniel Pens GELAIN*, Matheus Augusto de Bittencourt PASQUALI, Fernanda Freitas CAREGNATO, Mauro Antonio Alves CASTRO, José Claudio Fonseca MOREIRA

Center for Oxidative Stress Research, Department of Biochemistry, Federal University of Rio Grande do Sul – Porto Alegre, RS, Brazil

Aim: Toxicity of retinol (vitamin A) has been previously associated with apoptosis and/or cell malignant transformation. Thus, we investigated the pathways involved in the induction of proliferation, deformation and proliferative focus formation by retinol in cultured Sertoli cells of rats.

Methods: Sertoli cells were isolated from immature rats and cultured. The cells were subjected to a 24-h treatment with different concentrations of retinol. Parameters of oxidative stress and cytotoxicity were analyzed. The effects of the p38 inhibitor SB203580 (10 μmol/L), the JNK inhibitor SP600125 (10 μmol/L), the Akt inhibitor LY294002 (10 μmol/L), the ERK inhibitor U0126 (10 μmol/L) the pan-PKC inhibitor GÖ6983 (10 μmol/L) and the PKA inhibitor H89 (1 μmol/L) on morphological and proliferative/transformation-associated modifications were studied.

Results: Retinol (7 and 14 μmol/L) significantly increases the reactive species production in Sertoli cells. Inhibition of p38, JNK, ERK1/2, Akt, and PKA suppressed retinol-induced [^{3}H]dT incorporation into the cells, while PKC inhibition had no effect. ERK1/2 and p38 inhibition also blocked retinol-induced proliferative focus formation in the cells, while Akt and JNK inhibition partially decreased focus formation. ERK1/2 and p38 inhibition hindered transformation-associated deformation in retinol-treated cells, while other treatments had no effect.

Conclusion: Our results suggest that activation of multiple kinases is responsible for morphological and proliferative changes associated to malignancy development in Sertoli cells by retinol at the concentrations higher than physiological level.

Keywords: retinol; vitamin toxicity; Sertoli cell; oxidative stress; cell deformation; p38; JNK; Akt; ERK; PKC; PKA

Acta Pharmacologica Sinica (2012) 33: 558–567; doi: 10.1038/aps.2011.202; published online 19 Mar 2012

Introduction

Vitamin A (retinol) affects several biological processes through diverse mechanisms. Classically, it was believed that most actions of retinol were mediated only by different isomers of retinoic acid (RA), which is obtained from retinol enzymatic dehydrogenation[1]. RA modulates the transcription of several genes associated to cell cycle regulation through the action of the so-called retinoid receptors, which belong to the superfamily of steroid/thyroid receptors[2]. Gene transcription regulated by retinoid receptors influences cell death/survival, differentiation and growth, and is believed to exert an important role in neural development[3].

Besides this genomic action, there has been some recent attention to a potential role in redox modulation of oxidative balance at cellular and systemic levels by retinol[4]. Based on epidemiologic studies, retinol was suggested to be an important dietary antioxidant, preventing pathologies associated to oxidative stress such as cancer, atherosclerosis, neurodegenerative diseases and other age-related conditions[5]. On the other hand, extensive trials of retinol supplementation resulted in increased incidence of lung cancer and cardiovascular diseases[6, 7], and more recent works on the redox properties of retinol and other retinoids revealed a pro-oxidant action at specific concentrations and experimental conditions[8–10]. Besides, retinol and RA have been reported to regulate cellular processes not related to retinoid receptor-mediated gene transcription, in which has been denominated a "non-genomic" action[11, 12]. These actions were observed to influence synaptic transmission, catecholamine production and also cell cycle regulation through mitogen-activated protein kinase (MAPK),

* To whom correspondence should be addressed.
E-mail dgelain@yahoo.com.br
Received 2011-11-07 Accepted 2011-12-19

Akt and Protein Kinase C (PKC) activation[11, 13–15]. Since oxidative stress and protein kinase activation have been extensively associated with cancer induction, it has been speculated that non-genomic actions of vitamin A may account for many of these pro-neoplastic effects.

We have previously observed that retinol is able to enhance reactive species production and induce extensive oxidative damage in Sertoli cells, a physiological target of retinol[16–21]. In these cells, retinol and RA are endocrine factors that regulate diverse reproductive-related functions in a constitutive fashion. Although Sertoli cells are "professional" vitamin A targets, retinol is also able to induce cell cycle impairment and DNA damage via reactive species production at concentrations slightly above the reported physiological limit[19–21]. In this regard, primary Sertoli cell cultures constitute an excellent model to study the mechanisms and effects of vitamin A supplementation at cellular level.

Considering that the role of retinol in diet supplementations or in new therapies to treat or prevent malignant processes is still a matter of debate, here we investigated the effects of retinol on morphological parameters associated to pre-neoplasic morphological transformation and mitosis in Sertoli cell cultures, aiming to determine the role of the MAPKs ERK1/2, p38 and Jun-activated kinase (JNK), the protein kinase Akt, the cAMP-activated Protein Kinase (PKA) and PKC.

Material and methods

Chemicals and animals

Pregnant Wistar rats were housed individually in Plexiglas cages. Litters were restricted to eight pups each. Animals were maintained on a 12-h light/dark cycle at a constant temperature of 23 °C, with free access to commercial food and water. Male immature rats (15 days old) were killed by cervical dislocation. All experiments were conducted in accordance with the National Institute of Health Guide for the Care and Use of Laboratory Animals (NIH publication number 80–23 revised, 1996). Our research protocol was approved by the Ethical Committee for animal experimentation of the Federal University of Rio Grande do Sul. All-trans retinol alcohol, epinephrine, thiobarbituric acid, dinitrophenylhydrazine, Trolox, Tween-20, and β-mercaptoethanol were purchased from Sigma Chemical Co (St Louis, MO, USA). U0126 was from Promega Corporation (Madison, WI, USA), GÖ6983 and SB203580 were from Merck Biosciences (Darmstadt, Germany) and H89 was from Biomol Research Laboratories (Plymouth Meeting, PA, USA). Other kinase inhibitors were kind gifts from Professor Peter DUNKLEY (University of Newcastle, NSW, Australia). Rabbit polyclonal antibodies against phosphorylated forms of p38, JNK, ERK1/2 and Akt were obtained from Santa Cruz Biotechnology Inc (Santa Cruz, CA, USA), and monoclonal anti-β-actin was from Sigma. West Pico chemiluminescent kit was obtained from Pierce (Rockford, IL, USA). Concentrated stocks of solutions were prepared immediately before experiments by diluting retinol into ethanol and determining final stock concentration by UV absorption; solution was kept protected from light and temperature during all procedures. Appropriate solvent controls were performed for each condition. Treatments were initiated by adding concentrated solutions to reach final concentrations in the well. The final ethanol concentration did not exceed 0.2% in any experiment. Electrophoresis reagents and equipment were from BioRad (Hercules, CA, USA). Tissue culture reagents were from Gibco (Invitrogen Corporation, Carlsbad, CA, USA) and were of tissue culture grade.

Isolation and culture of Sertoli cells and assays

Sertoli cells were isolated as previously described[18]. Briefly, testes of 15-day-old rats were removed, decapsulated and digested enzymatically with trypsin and deoxyribonuclease for 30 min at 37 °C, and centrifuged at 750×*g* for 5 min. The pellet was mixed with soybean trypsin inhibitor, then centrifuged and incubated with collagenase and hyaluronidase for 30 min at 37 °C. After incubation, this fraction was centrifuged (10 min at 40×*g*). The pellet was taken to isolate Sertoli cells and supernatant was discarded. After counting, Sertoli cells were plated in multiwell plates (3×10^5 cells/cm^2) in Medium 199 pH 7.4 1% FBS, and maintained in humidified 5% CO_2 atmosphere at 37 °C for 24 h for attachment. The medium was then changed to serum-free medium and cells were maintained for more 24 h. Medium was then replaced by fresh medium containing treatments and cells were incubated for more 24 h. Morphology was examined at the end of the 24 h treatments.

Measurement of mitochondrial superoxide production

Mitochondrial superoxide production was assessed as previously described[18]. To isolate submitochondrial particles (SMP) from Sertoli cell cultures, cells were homogenized in an isolation buffer (230 mmol/L mannitol, 70 mmol/L sucrose, 10 mmol/L Tris-HCl, 1 mmol/L EDTA, pH 7.4). Homogenates were centrifuged (750×*g*, 10 min) to eliminate nuclei and cell debris and the pellet was washed to enrich supernatant; the supernatant was then centrifuged at 7000×*g* for 10 min. The pellet was washed and resuspended in the same buffer, and then SMP were obtained by freezing and thawing (three times) this fraction. The resulting SMP are washed twice with buffer consisting of 140 mmol/L KCl and 20 mmol/L Tris-HCl (pH 7.4) and resuspended in the same medium for determination of superoxide production, which was assessed by mixing SMP solution (0.3–0.1 mg protein/ml) to a reaction medium consisting of 230 mmol/L mannitol, 70 mmol/L sucrose, 20 mmol/L Tris-HCl (pH 7.4), plus 0.1 mmol/L catalase and 1 mmol/L epinephrine. Succinate (7 mmol/L) was used as substrate, and the superoxide-dependent oxidation of epinephrine to adrenochrome at 37 °C (Extinction molar coefficient at 480 nm and nm and 4020 mmol·L^{-1}·cm^{-1}) was followed by spectrophotometry detection. SOD was used at 0.1–0.3 mmol/L final concentration to assess assay specificity.

Thiobarbituric acid reactive species (TBARS)

As an index of lipid peroxidation, we quantified the formation of TBARS formed in an acid-heating reaction of cell

lipid extracts with thiobarbituric acid[22]. Briefly, the cell homogenates were mixed with 0.6 mL of 10% trichloroacetic acid (TCA) and 0.5 mL of 0.67% thiobarbituric acid, and then heated in a boiling water bath for 25 min. TBARS were determined by the absorbance in a spectrophotometer at 532 nm. Results were normalized against the content of cell protein and expressed as TBARS/mg of protein.

Measurement of protein carbonyls

The oxidative damage to proteins was measured by the quantification of carbonyl groups based on the reaction with dinitrophenylhidrazine (DNPH)[23]. Briefly, proteins were precipitated by the addition of 20% TCA, redissolved in DNPH and the absorbance was read in a spectrophotometer at 370 nm. Results were expressed as nmol carbonyl/mg of protein.

Proliferation focus assessment

Cell focus assay was carried as previously described[18]. Briefly, Sertoli cells were treated during 24 h with retinol in the presence or absence of different protein kinase inhibitors. The incubation medium was then replaced by Medium 199 (pH 7.4) supplemented with 10% FBS in all groups. Cells were maintained in humidified 5% CO_2 atmosphere at 37 °C for 14 d, with medium replacement every 3 d. Morphology was examined during this period and cell foci were scored at the end of the experiment under a light microscope (Nikon Eclipse TE 300). Photomicrography images were captured at the end of the 24 h-period of incubation with retinol and also at the end of the 14 d-period of proliferative focus induction.

Cell proliferation assay

As an index of cell proliferation we used the incorporation of [methyl-^{3}H] thymidine ([^{3}H]dT). Briefly, after the first 24 h of culture in Medium 199 at 1% FSB, the medium was replaced for serum-free Medium 199 supplemented with 2.5 μCi/mL of [^{3}H]dT (248 GBq/mmoL; Amersham International, Amersham, UK). After 24 h, the medium was replaced by the same medium containing retinol and different protein kinase inhibitors, and cells were incubated for more 24 h. Cells were then washed, harvested, suspended in nucleus isolation buffer (50 mmol/L $NaPO_4$, 2 mol/L NaCl, pH 7.4) and centrifuged (5 min, 14 000×*g*) to extract nuclear DNA. An aliquot was used to determine [^{3}H]dT incorporation into DNA in a Packard Tri-Carb Model 3320 scintillation counter, and another aliquot was utilized for protein quantification.

Deformation coefficient *D* measurement

The morphological relation between spreading and confluent cells was measured to assess modifications in cell plasticity. The increase in the difference between spread and confluent cells implies an increase of coefficient D[24]. Morphometrical measurements were obtained by analysis of the scanned phase-contrast photomicrographs of cells plated as dispersed and confluent densities. At least 35 cells from each experimental group in three independent experiments were measured to evaluate shape parameters of each cell. Data are reported as mean±SEM, with the level of significance set at $P<0.05$.

Immunoblot

To perform immunoblot experiments, Sertoli cell cultures were lysed in Laemmli-sample buffer (62.5 mmol/L Tris-HCl, pH 6.8, 1% (*w/v*) SDS, 10% (*v/v*) glycerol) and equal amounts of cell proteins (approximately 35 μg/lane) were fractionated by SDS-polyacrylamide gel electrophoresis (PAGE) and electroblotted onto polyvinyledilene difluoride (PVDF) membranes. Protein loading and electrobloting efficiency were verified by Ponceau S staining, and the membrane was then blocked in Tween-Tris buffered saline (TTBS; 100 mmol/L Tris-HCl, pH 7.5, containing 0.9% NaCl and 0.1% Tween-20) containing 5% albumin and incubated overnight with the primary antibody to be tested. The membrane was washed in TTBS and incubated with horseradish peroxidase coupled anti-IgG antibody, washed again and the immunoreactivity was detected by enhanced chemiluminescence. Densitometric analysis of the films was performed with GraphPad Software Inc; San Diego, CA, USA. Blots were developed to be linear in the range used for densitometry.

Data normalization and statistics

Data were normalized by protein content, which was measured by the Lowry method. Normalized data was analyzed with GraphPad software by one-way ANOVA with Duncan's *post-hoc* test. Differences were considered significant when $P<0.05$.

Results

Previously, we reported that retinol induced oxidative stress at 7 μmol/L during 24 h of incubation[17]. To confirm this observation, here we incubated Sertoli cells with retinol for 24 h to establish the concentrations at which retinol was able to induce oxidative stress. Cytosolic concentrations of retinol at physiological conditions have been reported to range between 0.2 to 5 μmol/L[25]; for this reason, we incubated Sertoli cells with concentrations ranging from physiological (2 and 5 μmol/L) to elevated levels (7 and 14 μmol/L). As previously observed[26], mitochondrial superoxide production (Figure 1A), carbonyl levels (Figure 1B) and lipid peroxidation (Figure 1C) were significantly increased by retinol at 7 μmol/L; retinol at 2 μmol/L or 5 μmol/L had no effect on these parameters. In previous reports, we also observed that retinol enhances intracellular free radical production at 7 and 14 μmol/L, but the concentration of 14 μmol/L also led to extensive cell death after 24 h of incubation[27]. Altogether, these results confirmed that retinol increases reactive species production at 7 μmol/L and 14 μmol/L, and increasing concentrations of retinol may induce cytotoxic effects probably due to uncontrolled oxidative damage to cells.

Retinol did not cause any detectable morphological changes in cell monolayers at 2 μmol/L and 5 μmol/L (Figure 2). On the other hand, retinol 7 μmol/L induced visible morphologic modifications in the cell. At the concentration of 14 μmol/L

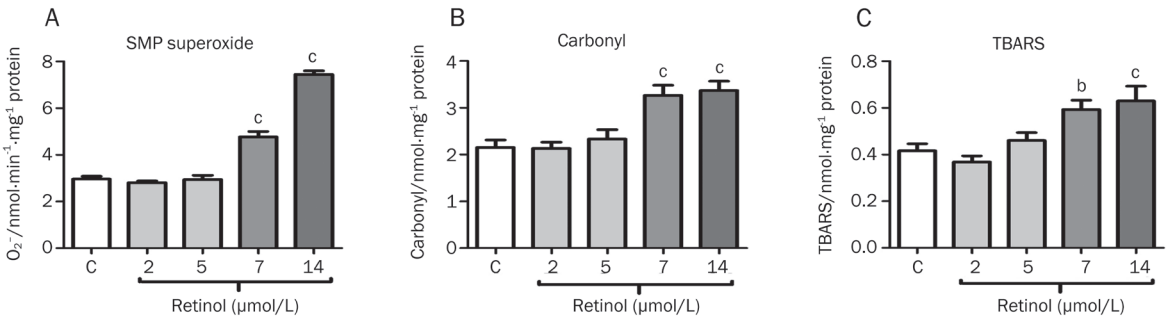

Figure 1. Sertoli cells were treated with retinol for 24 h and different parameters related to oxidative stress and cell damage were assessed. (A) Superoxide production by submitochondrial particles isolated from retinol-treated cells was measured, and oxidative damage was assessed by quantification of (B) carbonyl and (C) TBARS levels. C=control in all graphs. Bars represent mean±SEM from three independent experiments (triplicate); data were analyzed by one-way ANOVA with Duncan's *post hoc* test. $^{b}P<0.05$, $^{c}P<0.01$ *vs* control.

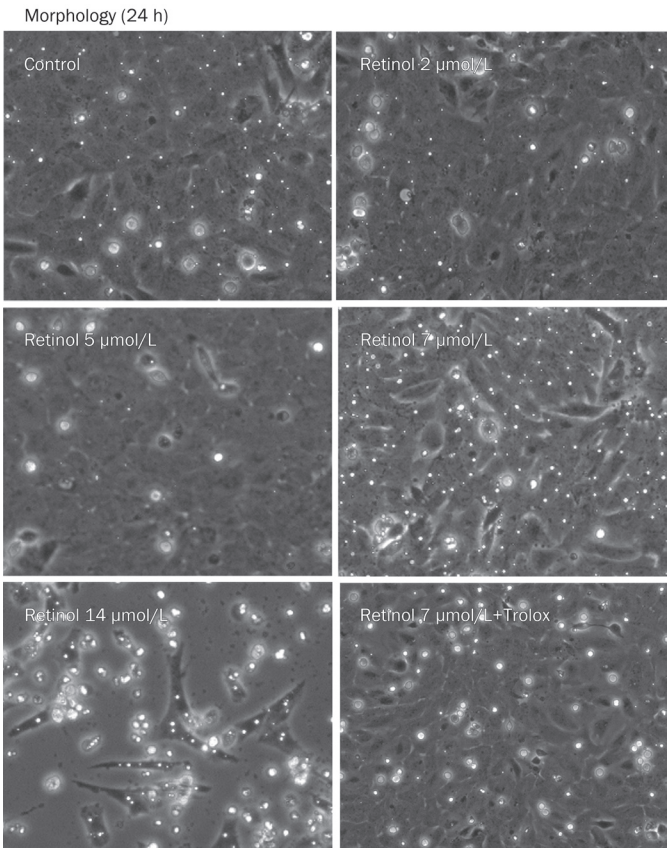

Figure 2. Cell morphology was examined by phase-contrast microscopy (Nikon Eclipse TE 300, ×100). Sertoli cells were treated with retinol at 2, 5, 7, and 14 μmol/L for 24 h. Retinol 7 μmol/L induced mild body cell shrinkage and retinol 14 μmol/L caused extensive cell detachment. Trolox (100 μmol/L) inhibited the effect of retinol 7 μmol/L.

most cells were detached. Co-incubation with the antioxidant Trolox (0.1 mmol/L) prevented the changes in morphology induced by retinol, indicating the involvement of oxidative stress in this effect. Based on these results and on the results presented at Figure 1 we used the concentration of 7 μmol/L to test the pro-oxidant effects of retinol on morphological and proliferation parameters of Sertoli cells throughout this work.

In previous works, we demonstrated that retinol led to the activation of different signaling pathways in an oxidant-dependent fashion, and that the antioxidant Trolox inhibited this effect[15, 18]. Here, we wanted to establish the possible involvement of different signaling pathways in the induction of morphological and proliferative changes in Sertoli cells by analyzing parameters related to pre-neoplasic transformation. With this aim, we performed assays using pharmacological inhibitors of different MAPKs involved in cell cycle activation and transformation, such as p38, ERK1/2, and JNK, as well as inhibitors of PKA, PKC, and Akt. Sertoli cells were incubated with retinol and protein kinase inhibitors for 24 h, and the cell morphology was examined by phase-contrast microscopy (Figure 3A).

We observed here that the JNK inhibitor SP600125 (10 μmol/L) blocked the morphological alterations induced by retinol (Figure 3A). The other protein kinase inhibitors had no effect or caused new patterns of morphology modification in retinol-treated cells, such as observed for the p38 inhibitor SB203580 (10 μmol/L) and the Akt inhibitor LY294002 (10 μmol/L). To better understand how these morphological modifications were associated to malignant deformation, we calculated the deformation coefficient *D* (Figure 3B), a morphological relationship among spreading and confluent cells, related to cell malignancy, invasiveness and contact inhibition applied to cancer cell lines[24]. The coefficient *D* for cells treated with retinol for 24 h (D=2.812±0.229) was significantly lower than in control cells (D=5.258±0.538), indicating loss of substrate adhesion and contact inhibition[24]. Besides Trolox, the p38 inhibitor SB203580 and the ERK1/2 inhibitor U0126 (10 μmol/L) also inhibited this effect, while other protein kinase inhibitors did not. Cells co-treated with retinol and the PKA inhibitor H89 presented a negative value for the coefficient *D*, which is probably related to a loss of cell integrity resulting in cell detachment observed at later time periods (data not shown). These results suggest that p38 and ERK1/2 are involved in the activation of signaling pathways leading to morphological changes related to loss of contact inhibition and modulation of cell adhesion.

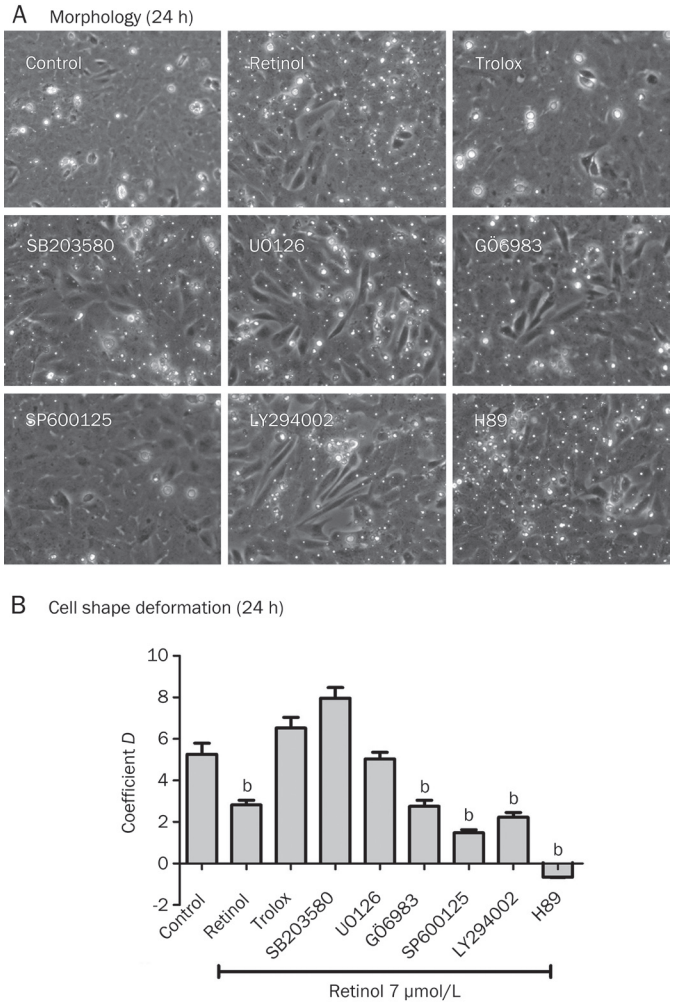

Figure 3. Effect of different protein kinase inhibitors on cell morphology modification by retinol. (A) Sertoli cells were treated with retinol 7 μmol/L in the presence or absence of the antioxidant Trolox (100 μmol/L), the p38 inhibitor SB203580 (10 μmol/L), the JNK inhibitor SP600125 (10 μmol/L), the Akt inhibitor LY294002 (10 μmol/L), the ERK inhibitor U0126 (10 μmol/L) the pan-PKC inhibitor GÖ6983 (10 μmol/L) and the PKA inhibitor H89 (1 μmol/L) for 24 h, and the cell morphology was examined by phase-contrast microscopy (Nikon Eclipse TE 300, ×100). (B) Cell deformation after 24 h was also analyzed by calculation of the coefficient *D*, an index of cell transformation-related deformation, obtained by morphometrical measurement of scanned phase-contrast photomicrographs of cells plated at dispersed and confluent densities. Bars represent mean±SEM from 22 individual cells analyzed per each group; data were analyzed by one-way ANOVA with Duncan's *post hoc* test. $^{b}P<0.05$ in relation to control.

In previous works, we found that Sertoli cell cultures treated with retinol for 24 h developed spots of proliferative focus when subjected to a 14 d-treatment with 10% Fetal Bovine Serum (FBS)-supplemented culture medium[18, 20]. Here, we studied the inhibition of different kinases on this effect. With this aim, Sertoli cells were incubated for 24 h with retinol in the presence or absence of the different protein kinase inhibitors; after this treatment, the medium in all groups was replaced for fresh 10% FBS medium (without retinol and protein kinase inhibitors), and cells were cultured in these conditions for 14 d with medium replacement every 3 d. In cells treated with retinol we observed a significant increase in proliferative focus formation, which was blocked by Trolox (Figure 4 and 5A). The ERK1/2 inhibitor U0126 also blocked retinol-induced proliferative focus formation, and p38 inhibition significantly decreased the number of proliferative focus in the plate well. PKC, Akt, and JNK inhibition had no effect on retinol-induced proliferative focus formation. Cells treated with retinol plus the PKA inhibitor H89 (1 μmol/L) for 24 detached from culture dishes within 1 week of 10% FBS-medium incubation.

Previously, we observed that retinol induced an increase in [^{3}H]dT incorporation that was associated to activation of cell division[18]. Here, we investigated the effect of the different protein kinases on this parameter. As previously observed, Sertoli cells incubated with retinol for 24 h had increased [^{3}H]dT (Figure 5B), and this effect was prevented by the antioxidant Trolox. The p38 inhibitor SB203580, the JNK inhibitor SP600125, the Akt inhibitor LY294002 and the ERK inhibitor U0126 decreased [^{3}H]dT incorporation to control levels when co-incubated with retinol. The pan-PKC inhibitor GÖ6983 (10 μmol/L) did not affect [^{3}H]dT incorporation, while the PKA inhibitor H89 decreased [^{3}H]dT incorporation in retinol-treated cells.

Altogether, our results suggest that the protein kinases p38, Akt, JNK, and ERK1/2 are associated to morphological changes, proliferative focus formation and activation of cell division induced by pro-oxidant concentrations of retinol. We then evaluated the activation states of these protein kinases by the immunodetection of their phosphorylated (i.e., active) isoforms by western blot (Figure 6). We observed an increase in the phosphorylation of p38, Akt, JNK, and ERK1/2 within 60 min of incubation with retinol 7 μmol/L (Figure 6A); phosphorylation levels of all kinases peaked around 15–30 min. We evaluated the effect of Trolox on the phosphorylation state of each protein kinase in Sertoli cells treated with retinol by 15 min, and compared with the effect of each specific protein kinase inhibitor. Trolox was able to completely or partially inhibit the effect of retinol on the phosphorylation of all kinases; besides, our results confirm that the protein kinase inhibitors SB203580, LY294002, SP600125, and U0126 were all effective in inhibiting, respectively, p38, Akt, JNK, and ERK1/2 phosphorylation.

Discussion

Retinol and retinoic acid are widely recognized as potent morphogens[1]. Retinoids regulate gene transcription through nuclear receptors belonging to the superfamily of steroid/thyroid/vitamin D-related hormone receptors known as retinoid receptors[3]. Such nuclear action is considered a key point in brain development and establishment of morphological patterns during embryonic and fetal development[2]. The observation of antioxidant properties of vitamin A *in vitro* and *in vivo* also led to the hypothesis that retinol and derivatives could act in cancer prevention/treatment, due to combined

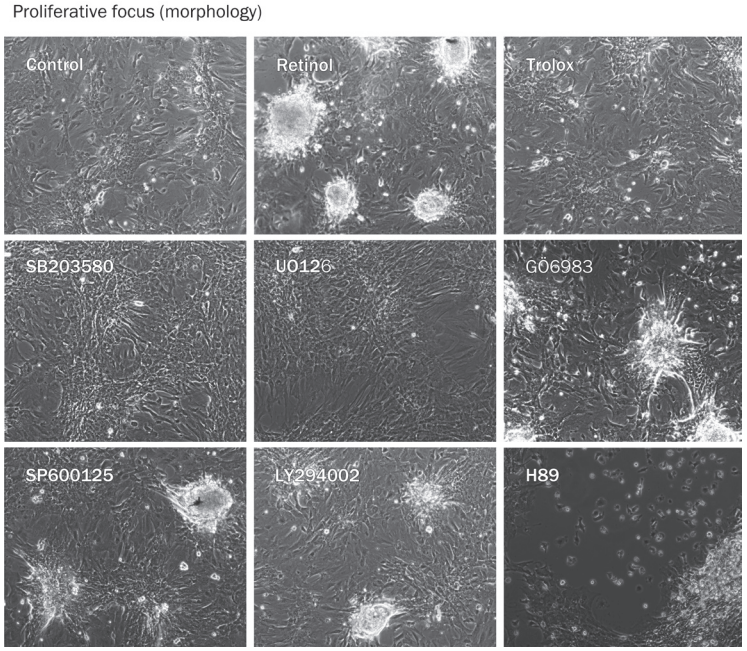

Figure 4. Proliferative focus morphology. Sertoli cells were treated for 24 h with retinol in the presence or absence of the antioxidant Trolox (100 μmol/L), the p38 inhibitor SB203580 (10 μmol/L), the JNK inhibitor SP600125 (10 μmol/L), the Akt inhibitor LY294002 (10 μmol/L), the ERK inhibitor U0126 (10 μmol/L) the pan-PKC inhibitor GÖ6983 (10 μmol/L) and the PKA inhibitor H89 (1 μmol/L); medium was then replaced in all groups for 10% FBS-supplemented 199 medium without any other compound for 14 d, with exchange for fresh medium every 3 d. At the end of the 14 d period, morphology was examined in a phase-contrast microscope (representative micrographs at ×40 are depicted) and proliferative foci were counted in each well (see Figure 5A for scores).

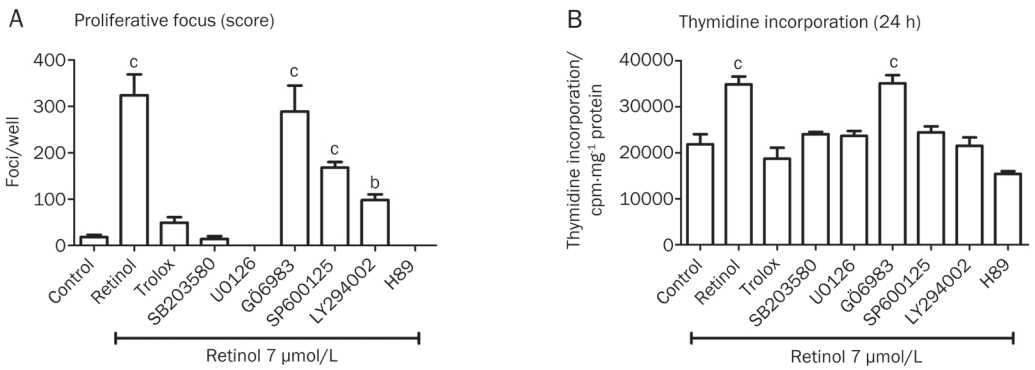

Figure 5. Proliferative focus scores and [^{3}H]dT incorporation in Sertoli cells. (A) Sertoli cells were treated for 24 h with retinol in the presence or absence of the antioxidant Trolox (100 μmol/L), the p38 inhibitor SB203580 (10 μmol/L), the JNK inhibitor SP600125 (10 μmol/L), the Akt inhibitor LY294002 (10 μmol/L), the ERK inhibitor U0126 (10 μmol/L) the pan-PKC inhibitor GÖ6983 (10 μmol/L) and the PKA inhibitor H89 (1 μmol/L); medium was then replaced in all groups for 10% FBS-supplemented 199 medium without any other compound for 14 d, with exchange for fresh medium every 3 d. At the end of the 14 d period, proliferative foci were counted in each well. (B) Sertoli cells were previously incubated with medium containing [^{3}H]dT, and then treated for 24 h in the same medium with retinol 7 μmol/L in the presence or absence of the above-mentioned compounds. Nuclei were isolated and incorporation of [^{3}H]dT was counted. Bars represent mean±SEM from three independent experiments (triplicate); data were analyzed by one-way ANOVA with Duncan's *post hoc* test. $^bP<0.05$, $^cP<0.01$ *vs* control.

free radical scavenging and control of cell cycle by retinoid receptor activity modulation[4].

More recently, extensive clinical trials and experimental works evidenced a pro-neoplasic effect of retinol and derivatives[28–31]. Retinoids have been more properly considered "redox-active" molecules rather than solely antioxidants; its redox actions in biological systems are certainly dependent on a variety of factors, such as its intracellular concentration and interaction with other redox-active molecules[32]. Although a role for retinoid receptors may not be completely discharged in such malignant effect, there is strong evidence pointing to a more prominent role of free radicals and other nuclear receptor-independent pathways in the mechanism of neoplasic transformation by retinoids. Free radicals and related species have been extensively recognized as potential inducers of different types of cancer[33], and MAPK-controlled signaling pathways and related proteins have been increasingly implicated in the control of cell cycle and triggering of oncogenic processes[34]. Retinoids have been described to evoke both types of responses in Sertoli cells, a well-recognized physiological target of retinol and RA[35, 36].

We have previously demonstrated that concentrations above 5 μmol/L are able to induce deleterious effects on cells due to enhanced free radical production and oxidative dam-

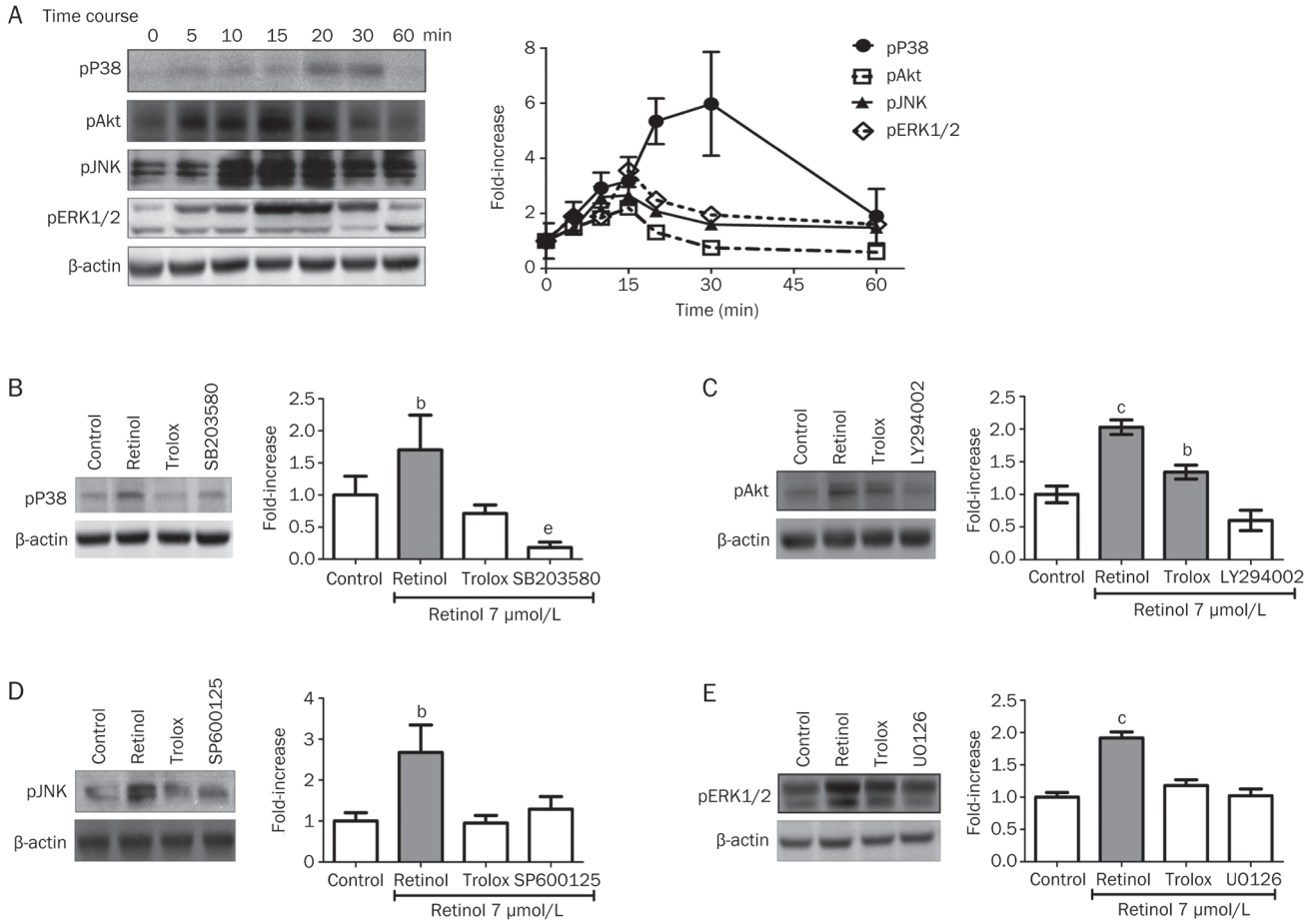

Figure 6. Representative immunoblots and quantification of levels of phosphorylated p38, Akt, JNK, and ERK1/2 in retinol-treated Sertoli cells. (A) Sertoli cells were treated with retinol 7 μmol/L and the time course of p38, Akt, JNK, and ERK1/2 during 60 min was evaluated by western blot using antibodies against phosphorylated forms of these protein kinases. Beta-actin was used as internal control. (B) The effect of the antioxidant Trolox (100 μmol/L) on p38 phosphorylation at 15 min of incubation with retinol was compared with the effect of the p38 inhibitor SB203580 (10 μmol/L). The effect of Trolox on Akt (C), JNK (D), and ERK1/2 (E) phosphorylation was also compared, respectively, with the effect of the inhibitors LY294002 (10 μmol/L), SP600125 (10 μmol/L), and U0126 (10 μmol/L). Bars represent mean±SEM from three independent experiments (triplicate); data were analyzed by one-way ANOVA with Duncan's *post hoc* test; asterisks denote significantly higher than control. $^{b}P<0.05$, $^{c}P<0.01$ *vs* control. $^{e}P<0.05$ *vs* Trolox.

age to biomolecules[17, 19, 21, 31, 37]. We also observed that retinol induces the rapid activation of phosphorylation-controlled signal pathways involving ERK1/2, JNK, and Src in a redox-dependent fashion, indicating the involvement of reactive species in the so-called non-genomic signaling by vitamin A[18, 38]. Since kinase activation by retinol displays a peak of phosphorylation followed by a return to control levels within the period of 60 minutes, it seems that free radical production during the initial moments of retinol incubation are important for this effect. Normally, retinoid receptor activation in Sertoli cells is part of the paracrine signaling involved in the support and control of spermatogenesis, along with testosterone and Follicle-stimulating hormone (FSH).

Sertoli cells cease mitosis after birth and remain as fully differentiated and non-proliferative supportive cells. Physiological concentrations of retinoids do not affect the Sertoli cell cycle homeostasis in normal conditions[36]. However, pro-oxidant concentrations of retinol may induce proliferative effects related or not to malignancy, as free radicals are recognized to be involved in the regulation of cell cycle, especially in cell division and cell death[39]. Here, we observed that specific concentrations of retinol increase free radical production and parameters related to cell division and deformation. Cell cycle activation induced by pro-oxidant concentrations of retinol is probably related to cell transformation, since [^{3}H]dT incorporation was accompanied by proliferative focus formation and cell shape deformation, and these effects were reversed by antioxidant treatment. MAPK and Akt activation is also involved in the redox-dependent promotion of cell division by retinol, but not all these kinases are necessarily involved in cell transformation. Although the involvement of MAPKs in cell division control and transformation is well recognized, as mentioned earlier, different members of the MAPK family and related kinases may regulate different path-

ways associated to activation of normal mitosis and malignant transformation in a given cell type, and this may vary under different conditions.

Many of the cell cycle regulatory effects promoted by different members of the MAPK family have also been observed to be evoked or strongly influenced by free radicals and related species. ERK was demonstrated to be involved in the free radical-mediated promotion of transformation or in the increase to transformation susceptibility[40, 41]. The p38 MAPK was observed to be a key contributor for the redox signaling involved in UVA-mediated transformation[42] and was postulated to exert a selective role in promoting free radical-mediated tumorigenesis[43].

The extent of the role of cell phenotype in modulation of cell growth is a central question in the biomedical sciences[44]. In human non-small cell lung carcinoma cell lines, two- and three-dimensional growth patterns were described to follow a common growth dynamic associated to malignancy, such as in the case of the association with the Gompertz model for growing[45, 46]. It has been suggested that cell-shape compression control the inhibitory feedback as a geometrical arrest of mitosis, reflecting the influence of the cytoskeletal network organization[47]. As cells become rounded, DNA synthesis gradually stops[48]; inversely, most cells require spreading on extracellular matrix substrate for proper growth and normal function[49]. Such relationships among growth and shape have been studied by regression analysis and resulted in a cell deformation parameter — the deformation coefficient *D*, which describes the amplitude of cell shape variation, showing positive correlation with kinetic parameters of growth described by the Gompertz model[24].

Decrease in coefficient *D* value is related to decreased cell-to-cell recognition, adhesion and contact inhibition, and retinol treatment led to a decrease in this parameter. ERK1/2 and p38 inhibition reversed this effect, indicating that pathways controlled by these kinases are involved in the modulation of morphological parameters related to malignant transformation in these cells. Other kinase-controlled pathways such as the JNK and Akt seem to be involved in other effects promoted in a redox-dependent fashion by retinol in these cells; JNK inhibition blocked proliferative focus formation, while Akt inhibition hindered [^{3}H]dT incorporation, indicating a role in DNA synthesis. While inhibition of some kinases blocked or partially inhibited specific parameters related to proliferation or morphology change, our results indicate that ERK1/2 are involved in all aspects related to redox-dependent modifications on such parameters. ERK1/2 are highly sensitive to regulation by reactive species[50], and previous works from our group indicated that these kinases are involved in the activation of matrix metalloproteinase-2 by retinol in a redox-dependent fashion[51].

It has been increasingly clear that the concentration of retinoids influences their actions on biological systems, and this seems to be related to changes in their redox profile. As a redox active molecule, retinol may take part in different oxidation-reduction cycles of several biomolecules and micronutrients that change their oxidation states according the redox conditions of their microenvironment[5]. It was observed both in cell cultures and animal models[10, 52] that retinol-induced oxidative stress is caused by the administration of concentrations above the reported physiological limit, which would increase the availability of this molecule to take part in oxidation-reduction cycles inside cells. On the other hand, it was recently reported that retinol is able to induce the mitochondrial activity by enhancing pyruvate dehydrogenase activity through a nongenomic mechanism of PKC activation, thus resulting in increased free radical formation[53]. This would explain why increased concentrations of retinol induce reactive species production in both cell cultures and animal models.

Concluding, reactive oxygen species production induced by retinol activates different protein kinase pathways, which we found to be related to different morphologic and proliferative alterations in Sertoli cells. Inhibition of p38, JNK, ERK1/2, Akt, and PKA decreased retinol-induced [^{3}H]dT incorporation; p38, ERK1/2, JNK, and Akt are also involved in retinol-induced proliferative focus formation. ERK1/2 and p38 inhibition reversed transformation-associated deformation, while other treatments did not show any effect. Co-treatment with the antioxidant Trolox inhibited phosphorylation of p38, ERK1/2, JNK, and Akt, indicating the activation of these kinases during retinol treatment is dependent on oxidative stress. These results indicate that consumption of vitamin A at high levels must be better evaluated at clinical and epidemiological levels, as concentrations of retinol slightly above cellular physiological levels induces the activation of several pathways associated to cell deformation and pre-neoplasic transformation, as observed here. Experimental therapies or supplementation protocols using vitamin A should be more extensively studied in regard to their safety, possible toxicological effects and long-term side-effects.

Acknowledgements

This work was financed by the Brazilian agencies CNPq (IBN-Net #01.06.0842-00 and 470234/2008), FAPERGS (PqG 6/2010-1008860 and 11/1893-7) and PROPESQ-UFRGS. The authors have no conflict of interest.

Author contribution

Daniel Pens GELAIN performed research, analyzed data and wrote the manuscript. José Claudio Fonseca MOREIRA supervised research and designed experiments. Matheus Augusto de Bittencourt PASQUALI, Fernanda Freitas CAREGNATO, and Mauro Antonio Alves CASTRO performed research.

References

1 Marletaz F, Holland LZ, Laudet V, Schubert M. Retinoic acid signaling and the evolution of chordates. Int J Biol Sci 2006; 2: 38–47.

2 Malaspina A, Turkheimer F. A review of the functional role and of the expression profile of retinoid signaling and of nuclear receptors in human spinal cord. Brain Res Bull 2007; 71: 437–46.

3 Mongan NP, Gudas LJ. Diverse actions of retinoid receptors in cancer prevention and treatment. Differentiation 2007; 75: 853–70.
4 Fields AL, Soprano DR, Soprano KJ. Retinoids in biological control and cancer. J Cell Biochem 2007; 102: 886–98.
5 Halliwell B, Gutteridge JMC. Free radicals in biology and medicine. 4th ed. Oxford Oxford University Press; 2007.
6 Omenn GS, Goodman GE, Thornquist MD, Rosenstock L, Barnhart S, Gylys-Colwell I, *et al.* The Carotene and Retinol Efficacy Trial (CARET) to prevent lung cancer in high-risk populations: pilot study with asbestos-exposed workers. Cancer Epidemiol Biomarkers Prev 1993; 2: 381–7.
7 Omenn GS, Goodman GE, Thornquist MD, Balmes J, Cullen MR, Glass A, *et al.* Effects of a combination of beta carotene and vitamin A on lung cancer and cardiovascular disease. N Engl J Med 1996; 334: 1150–5.
8 Murata M, Kawanishi S. Oxidative DNA damage by vitamin A and its derivative via superoxide generation. J Biol Chem 2000; 275: 2003–8.
9 Pasquali MA, Schnorr CE, Feistauer LB, Gelain DP, Moreira JC. Vitamin A supplementation to pregnant and breast feeding female rats induces oxidative stress in the neonatal lung. Reprod Toxicol 2010; 30: 452–6.
10 Pasquali MA, Gelain DP, de Oliveira MR, Behr GA, da Motta LL, da Rocha RF, *et al.* Vitamin A supplementation for different periods alters oxidative parameters in lungs of rats. J Med Food 2009; 12: 1375–80.
11 Masia S, Alvarez S, de Lera AR, Barettino D. Rapid, nongenomic actions of retinoic acid on phosphatidylinositol-3-kinase signaling pathway mediated by the retinoic acid receptor. Mol Endocrinol 2007; 21: 2391–402.
12 Canon E, Cosgaya JM, Scsucova S, Aranda A. Rapid effects of retinoic acid on CREB and ERK phosphorylation in neuronal cells. Mol Biol Cell 2004; 15: 5583–92.
13 Liou JC, Ho SY, Shen MR, Liao YP, Chiu WT, Kang KH. A rapid, nongenomic pathway facilitates the synaptic transmission induced by retinoic acid at the developing synapse. J Cell Sci 2005; 118: 4721–30.
14 Liao YP, Ho SY, Liou JC. Non-genomic regulation of transmitter release by retinoic acid at developing motoneurons in *Xenopus* cell culture. J Cell Sci 2004; 117: 2917–24.
15 Gelain DP, Moreira JC, Bevilaqua LR, Dickson PW, Dunkley PR. Retinol activates tyrosine hydroxylase acutely by increasing the phosphorylation of serine40 and then serine31 in bovine adrenal chromaffin cells. J Neurochem 2007; 103: 2369–79.
16 Gelain DP, de Bittencourt Pasquali MA, Zanotto-Filho A, de Souza LF, de Oliveira RB, Klamt F, *et al.* Retinol increases catalase activity and protein content by a reactive species-dependent mechanism in Sertoli cells. Chem Biol Interact 2008; 174: 38–43.
17 Gelain DP, de Bittencourt Pasquali MA, Caregnato FF, Zanotto-Filho A, Moreira JC. Retinol up-regulates the receptor for advanced glycation end products (RAGE) by increasing intracellular reactive species. Toxicol In Vitro 2008; 22: 1123–7.
18 Gelain DP, Cammarota M, Zanotto-Filho A, de Oliveira RB, Dal-Pizzol F, Izquierdo I, *et al.* Retinol induces the ERK1/2-dependent phosphorylation of CREB through a pathway involving the generation of reactive oxygen species in cultured Sertoli cells. Cell Signal 2006; 18: 1685–94.
19 Dal-Pizzol F, Klamt F, Frota ML Jr, Moraes LF, Moreira JC, Benfato MS. Retinol supplementation induces DNA damage and modulates iron turnover in rat Sertoli cells. Free Radic Res 2000; 33: 677–87.
20 Dal-Pizzol F, Klamt F, Dalmolin RJ, Bernard EA, Moreira JC. Mitogenic signaling mediated by oxidants in retinol treated Sertoli cells. Free Radic Res 2001; 35: 749–55.
21 Dal-Pizzol F, Klamt F, Benfato MS, Bernard EA, Moreira JC. Retinol supplementation induces oxidative stress and modulates antioxidant enzyme activities in rat sertoli cells. Free Radic Res 2001; 34: 395–404.
22 Draper HH, Hadley M. Malondialdehyde determination as index of lipid peroxidation. Methods Enzymol 1990; 186: 421–31.
23 Levine RL, Garland D, Oliver CN, Amici A, Climent I, Lenz AG, *et al.* Determination of carbonyl content in oxidatively modified proteins. Methods Enzymol 1990; 186: 464–78.
24 Castro MA, Klamt F, Grieneisen VA, Grivicich I, Moreira JC. Gompertzian growth pattern correlated with phenotypic organization of colon carcinoma, malignant glioma and non-small cell lung carcinoma cell lines. Cell Prolif 2003; 36: 65–73.
25 Ross AC, Zolfaghari R, Weisz J. Vitamin A: recent advances in the biotransformation, transport, and metabolism of retinoids. Curr Opin Gastroenterol 2001; 17: 184–92.
26 de Oliveira RB, Klamt F, Castro MA, Polydoro M, Zanotto Filho A, Gelain DP, *et al.* Morphological and oxidative alterations on Sertoli cells cytoskeleton due to retinol-induced reactive oxygen species. Mol Cell Biochem 2005; 271: 189–96.
27 Gelain DP, de Bittencourt Pasquali MA, Caregnato FF, Moreira JC. Vitamin A (retinol) up-regulates the receptor for advanced glycation end products (RAGE) through p38 and Akt oxidant-dependent activation. Toxicology 2011; 289: 38–44.
28 Kim J, Kim MK, Lee JK, Kim JH, Son SK, Song ES, *et al.* Intakes of vitamin A, C, and E, and beta-carotene are associated with risk of cervical cancer: a case-control study in Korea. Nutr Cancer 2010; 62: 181–9.
29 The ABC-Cancer Prevention Study Group. The effect of vitamin E and beta carotene on the incidence of lung cancer and other cancers in male smokers. The Alpha-Tocopherol, Beta Carotene Cancer Prevention Study Group. N Engl J Med 1994; 330: 1029–35.
30 Omenn GS, Goodman G, Thornquist M, Grizzle J, Rosenstock L, Barnhart S, *et al.* The beta-carotene and retinol efficacy trial (CARET) for chemoprevention of lung cancer in high risk populations: smokers and asbestos-exposed workers. Cancer Res 1994; 54: 2038s–43s.
31 Klamt F, Dal-Pizzol F, Roehrs R, de Oliveira RB, Dalmolin R, Henriques JA, *et al.* Genotoxicity, recombinogenicity and cellular preneoplasic transformation induced by vitamin A supplementation. Mutat Res 2003; 539: 117–25.
32 Krinsky NI, Johnson EJ. Carotenoid actions and their relation to health and disease. Mol Aspects Med 2005; 26: 459–516.
33 Oyagbemi AA, Azeez OI, Saba AB. Interactions between reactive oxygen species and cancer: the roles of natural dietary antioxidants and their molecular mechanisms of action. Asian Pac J Cancer Prev 2009; 10: 535–44.
34 Haagenson KK, Wu GS. The role of MAP kinases and MAP kinase phosphatase-1 in resistance to breast cancer treatment. Cancer Metastasis Rev 2010; 29: 143–9.
35 Silva FR, Leite LD, Wassermann GF. Rapid signal transduction in Sertoli cells. Eur J Endocrinol 2002; 147: 425–33.
36 Hogarth CA, Griswold MD. The key role of vitamin A in spermatogenesis. J Clin Invest 2010; 120: 956–62.
37 de Oliveira RB, de Bittencourt Pasquali MA, Filho AZ, Dalmolin RJ, Gelain DP, Gottfried C, *et al.* Can electrons travel through actin microfilaments and generate oxidative stress in retinol treated Sertoli cell? Mol Cell Biochem 2007; 301: 33–45.
38 Zanotto-Filho A, Gelain DP, Schroder R, Souza LF, Pasquali MA, Klamt F, *et al.* The NF kappa B-mediated control of RS and JNK signaling in

vitamin A-treated cells: duration of JNK-AP-1 pathway activation may determine cell death or proliferation. Biochem Pharmacol 2009; 77: 1291–301.

39 Burhans WC, Heintz NH. The cell cycle is a redox cycle: linking phase-specific targets to cell fate. Free Radic Biol Med 2009; 47: 1282–93.

40 Hsu TC, Young MR, Cmarik J, Colburn NH. Activator protein 1 (AP-1)- and nuclear factor kappaB (NF-kappaB)-dependent transcriptional events in carcinogenesis. Free Radic Biol Med 2000; 28: 1338–48.

41 Yang S, Misner B, Chiu R, Meyskens FL Jr. Common and distinct mechanisms of different redox-active carcinogens involved in the transformation of mouse JB6P+ cells. Mol Carcinog 2008; 47: 485–91.

42 Cooper KL, Liu KJ, Hudson LG. Enhanced ROS production and redox signaling with combined arsenite and UVA exposure: contribution of NADPH oxidase. Free Radic Biol Med 2009; 47: 381–8.

43 Kennedy NJ, Cellurale C, Davis RJ. A radical role for p38 MAPK in tumor initiation. Cancer Cell 2007; 11: 101–3.

44 Chen Z, Smith CW, Kiel D, Van Waes C. Metastatic variants derived following *in vivo* tumor progression of an *in vitro* transformed squamous cell carcinoma line acquire a differential growth advantage requiring tumor-host interaction. Clin Exp Metastasis 1997; 15: 527–37.

45 Castro MA, Schwartsmann G, Bernard EA, Moreira JC. Phenotype modulation of cellular UV-sensitivity. Cancer Lett 1999; 145: 65–72.

46 Castro MA, Schwartsmann G, Moreira JC. Intercellular contact-dependent survival of human A549, NCI-H596 and NCI-H520 non-small cell lung carcinoma cell lines. Braz J Med Biol Res 2001; 34: 1007–13.

47 Olive PL, Durand RE. Drug and radiation resistance in spheroids: cell contact and kinetics. Cancer Metastasis Rev 1994; 13: 121–38.

48 Chen CS, Mrksich M, Huang S, Whitesides GM, Ingber DE. Geometric control of cell life and death. Science 1997; 276: 1425–8.

49 Ruoslahti E, Vaheri A. Cell-to-cell contact and extracellular matrix. Curr Opin Cell Biol 1997; 9: 605–7.

50 McCubrey JA, Lahair MM, Franklin RA. Reactive oxygen species-induced activation of the MAP kinase signaling pathways. Antioxid Redox Signal 2006; 8: 1775–89.

51 Dalmolin RJ, Zanotto-Filho A, De Oliveira RB, Duarte RF, Pasquali MA, Moreira JC. Retinol and retinoic acid increase MMP-2 activity by different pathways in cultured Sertoli cells. Free Radic Res 2007; 41: 1338–47.

52 Pasquali MA, Gelain DP, Oliveira MR, Behr GA, Motta LL, Rocha RF, *et al.* Vitamin A supplementation induces oxidative stress and decreases the immunocontent of catalase and superoxide dismutase in rat lungs. Exp Lung Res 2009; 35: 427–38.

53 Acin-Perez R, Hoyos B, Zhao F, Vinogradov V, Fischman DA, Harris RA, *et al.* Control of oxidative phosphorylation by vitamin A illuminates a fundamental role in mitochondrial energy homoeostasis. FASEB J 2010; 24: 627–36.

Acta Pharmacologica Sinica (2012) 33: 568–576
 1671-4083/12 $32.00
www.nature.com/aps

Original Article

Covalent protein binding and tissue distribution of houttuynin in rats after intravenous administration of sodium houttuyfonate

Zhi-peng DENG, Da-fang ZHONG, Jian MENG, Xiao-yan CHEN*

Shanghai Institute of Materia Medica, Chinese Academy of Sciences, Shanghai 201203, China

Aim: To investigate the potential of houttuynin to covalently bind to proteins *in vitro* and *in vivo* and to identify the adduct structures.
Methods: Male Sprague-Dawley rats were intravenously injected with sodium houttuyfonate (10 mg/kg). The concentrations of houttuynin in blood, plasma and five tissues tested were determined using an LC/MS/MS method. The covalent binding values of houttuynin with hemoglobin, plasma and tissue proteins were measured in rats after intravenous injection of [1-^{14}C]sodium houttuyfonate (10 mg/kg, 150 mCi/kg). Human serum albumin was used as model protein to identify the modification site(s) and structure(s) through enzymatic digestion and LC/MS^n analysis.
Results: The drug was widely distributed 10 min after intravenous injection. The lungs were the preferred site for disposition, followed by the heart and kidneys with significantly higher concentrations than that in the plasma. The extent of covalent binding was correlated with the respective concentrations in the tissues, ranging from 1137 nmol/g protein in lung to 266 nmol/g protein in liver. Houttuynin reacted primarily with arginine residues in human serum albumin to form a pyrimidine adduct at 1:1 molar ratio. The same adduct was detected in rat lungs digested by pronase E.
Conclusion: This study showed that the β-keto aldehyde moiety in houttuynin is strongly electrophilic and readily confers covalent binding to tissue proteins, especially lung proteins, by a Schiff's base mechanism. The findings explain partially the idiosyncratic reactions of houttuyniae injection in clinical use.

Keywords: sodium houttuyfonate; houttuynin; arginine-specific modification; pyrimidine adduct; LC/MS^n analysis; tissue distribution; houttuyniae preparations

Acta Pharmacologica Sinica (2012) 33: 568–576; doi: 10.1038/aps.2011.174; published online 5 Mar 2011

Introduction

Idiosyncratic drug reactions are a major source of concern because they can cause drug treatment limitations and even drug withdrawals from the market. The toxic mechanisms remain largely undefined, but accumulating data suggests that the covalent binding of drugs or their reactive metabolites/intermediates to cellular proteins is associated with idiosyncratic toxicity[1–4].

Drug-induced idiosyncratic reactions cannot be predicted from the pharmacological mechanism(s) of drugs, as they usually have a low occurrence rate of 1 in 1000 or even 1 in 100 000 patients[5]. To date, no available animal models can accurately predict the toxic interactions of drugs with the human immune system. Several experimental methods have been used to understand this toxic phenomenon[2]. Using radiolabeled drugs is the most common approach to assess their potential for covalent binding with biological macromolecules and to evaluate the idiosyncratic risk.

Houttuyniae injection (or sodium new houttuyfonate injection) was once widely used in clinical practice for the treatment of chronic bronchitis, pneumonia, upper respiratory infection, and other infectious diseases in China[6, 7]. Despite its clinical efficacy, occasionally serious and even fatal allergic reactions have been reported during an intravenous (iv) drop infusion of these injections[8–10]. As a result, the intravenous injection has been suspended since 2006 (although its oral preparations are still used in the clinic), and its safety has drawn great public attention.

The major active ingredients in houttuyniae preparations are a class of β-keto aldehyde compounds[11], including houttuynin (decanoyl acetaldehyde). It has been reported that some aldehyde compounds, such as formaldehyde[12, 13], acetaldehyde[14, 15], acrolein[16, 17], 2-nonenal[18, 19], and aldehyde intermediates formed by metabolism[20–22] might react with protein

* To whom correspondence should be addressed.
E-mail xychen@mail.shcnc.ac.cn
Received 2011-10-24 Accepted 2011-11-17

nucleophiles to form aldehyde-protein adducts, which are capable of specifically interfering with costimulatory signals on T cells and of inducing immunotoxic effects[23]. Therefore, we hypothesized that the acute or idiosyncratic toxicities of houttuyniae injection might be caused by the covalent binding of β-keto aldehyde compounds to cellular proteins.

In this study, houttuynin is used as a representative compound to investigate the *in vivo* distribution of the β-keto aldehyde-type structural moieties existing in houttuyniae injection and oral preparations, and their potential to covalently bind to proteins *in vivo*. To improve the water solubility of houttuynin, an adduct with sodium bisulfite (sodium houttuyfonate, see Figure 1) was used, which could liberate houttuynin under physiological conditions. Human serum albumin (HSA) was used as a model protein to investigate the covalent binding chemical mechanism of houttuynin to target proteins through enzymatic digestion and LC/MS^n analysis.

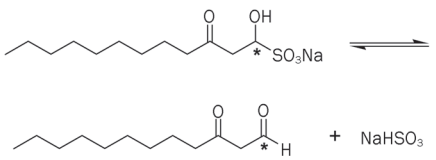

Figure 1. Reversible balance of sodium houttuyfonate and houttuynin in aqueous solution. (*) denotes the radiolabeled carbon.

Materials and methods

Chemicals and reagents

Sodium houttuyfonate (98.9% purity) was obtained from Qingping Pharmaceutical Co Ltd (Shanghai, China). [1-^{14}C] Sodium houttuyfonate (specific activity, 4.98 Ci/mol) was synthesized in our laboratory. HSA (Fraction V) was purchased from Sigma-Aldrich (St Louis, MO, USA). Pronase E was obtained from Roche Diagnostics GmbH (Mannheim, Germany). HPLC-grade methanol and acetonitrile were purchased from Sigma-Aldrich (St Louis, MO, USA) and HPLC-grade formic acid from Tedia (Fairfield, OH, USA). Other chemicals that were used were all of analytical reagent grade and commercially available.

Animals and treatment

The experiments were performed according to procedures approved by the Animal Care and Use Committee of the Shanghai Institute of Materia Medica (Shanghai, China). Fifteen male Sprague-Dawley rats (200±20 g) were divided randomly into five groups (three rats per group). In group 1, the rats received an iv administration of [1-^{14}C]sodium houttuyfonate at a target dose of 10 mg/kg (radioactivity: 150 μCi/kg) dissolved in normal saline solution at 2 mg/mL, and the animals were euthanized at 10 min after the injection; in groups 2–5, the rats were given non-radiolabeled sodium houttuyfonate at the same chemical dose and administration route, and the animals were euthanized at 10 min, 1 h, 5 h, and 24 h after dosing, respectively. For each group, blood was collected into heparinized tubes via exsanguinations. A portion of blood was centrifuged at 2000×*g* for 10 min to isolate plasma. The obtained plasma and the remaining blood were removed for the covalent binding and liquid chromatography tandem mass spectrometry (LC/MS/MS) analyses. Heart, liver, spleen, lung and kidney tissues were collected and stored at -80 °C until analysis.

Quantification of houttuynin in rat blood, plasma, and tissues

Houttuynin concentrations in rat blood, plasma, and the five tested tissues were determined by LC/MS/MS employing pre-column derivatization, which was reported previously by our laboratory[24]. Briefly, tissue samples of approximately 250 mg were homogenized with 1 mL of methanol. After centrifugation at 16 000×*g* for 5 min, the supernatants were used to determine houttuynin concentrations in tissues. To 100 μL of blood, plasma and tissue homogenate samples in glass tube, 50 μL of benzophenone (2.0 μg/mL, internal standard, IS) and 100 μL of 2,4-dinitrophenylhydrazone solution were added. Houttuynin and IS were derivatized and subjected to LC/MS/MS analysis. Standard curves were fitted to the equations by a linearly weighed ($1/x^2$) least squares regression method in the concentration range of 10.0–20 000 ng/mL for blood and plasma samples and 40.0–80 000 ng/g for tissues.

In vivo covalent protein binding assay

Aliquots of samples (150 μL of blood, 150 μL of plasma, and 500 μL of tissue homogenates) were placed in test tubes, and 1.5 mL of acetonitrile was added to each tube to precipitate protein. The mixtures were sonicated, vortexed for 10 min and were then placed at -20 °C for 30 min. Samples were centrifuged at 2000×*g* for 10 min, and the precipitate was washed several times with 1.5 mL of acetonitrile to remove any unbound radioactivity. Aliquots of the supernatant were checked for radioactivity, and no more washing was performed until the radioactivity level was within two-fold of that of the control samples. The resultant protein pellets were then dissolved in 4 mL of 100 mmol/L sodium hydroxide. Subsequently, 50 μL of the sample was transferred to a 1.5-mL Eppendorf tube, and 500 μL scintillation fluid (AIM Research Co, Hockessin, DE, USA) was added. The sample was vortexed for 1 min. The radioactivity was measured by a PE 1450 liquid scintillation analyzer (Perkin-Elmer, Waltham, MA, USA), and the protein concentration was determined by Bradford assay using a standard kit (Bio-Rad)[25]. Covalent binding to proteins was expressed as micromole equivalents per gram of protein.

In vitro covalent binding of [1-^{14}C]houttuynin with HSA

HSA (0.05 μmol, 0.50 mmol/L) was dissolved in 100 μL of 100 mmol/L phosphate-buffered saline (PBS, pH 7.4) at 37 °C. The reaction was started by adding [1-^{14}C]sodium houttuyfonate aqueous solution (684 nCi/μmol, 1.0 mmol/L) in a total incubation volume of 0.2 mL. Reactions were terminated at the pre-determined time points (0 min, 1 min, 10 min, 1 h, 3 h, 8 h,

and 24 h) by adding 600 μL of acetonitrile. The reaction samples were treated as described above. The total radioactivity and protein concentration of the incubation samples at each time point were measured as described above.

To further evaluate the covalent adduction of HSA by houttuynin, the washed protein from the 1 min to 24 h incubation periods was dissolved in 100 mmol/L PBS (100 μL, pH 7.4), and the protein concentrations were determined by the Bradford assay. The sample was treated with SDS-loading buffer and boiled for 5 min to denature HSA. The resulting HSA sample was then loaded on 8% SDS-polyacrylamide gels[26]. After the first electrophoresis, the target protein band was stained with Coomassie and was cut and transferred into dialysis tubing. The band was electrophoresed for 1 h in 150 V to recovery the protein[27]. After the second electrophoresis, 50 μL of running buffer solution containing [1-^{14}C]houttuynin-modified HSA in dialysis tubing was dissolved in 500 μL scintillation fluid, and the radioactivity was compared with the control sample by liquid scintillation counting.

Pronase E digestion

The washed protein pellets from rat blood, plasma, tissue homogenates and houttuynin-modified HSA were resuspended in 400 μL of water. Pronase E was dissolved in 100 mmol/L Tris buffer (pH 7.5) and 0.5% SDS solution[28], giving a final concentration of 1.0 mg/mL. This solution was added to the protein suspensions (1:10, *w/w*). The mixture was incubated for 72 h at 37 °C, then loaded onto a Waters Oasis® HLB C_{18} cartridge (30 mg, 1 mL; Milford, MA, USA). The cartridge was pretreated sequentially with 2×1 mL methanol and 2×1 mL water. After loading the sample, the cartridge was washed with 1 mL water. The modified amino acids were eluted with 1 mL methanol. The eluate was evaporated to dryness at 30 °C under a gentle stream of nitrogen. The residue was reconstituted in 200 μL acetonitrile/water (50:50, *v/v*). An aliquot of 20 μL was injected into the LC/MS^n system.

Instrumentation and analytical methods

An API 4000 triple quadrupole mass spectrometer (Applied Biosystems, Concord, Ontario, Canada) equipped with a Turbo Ionspray (ESI) source and an Agilent 1100 HPLC system consisting of a G1322A vacuum degasser, a G1311A quaternary pump, and a G1316A column oven (Agilent Technologies, Waldbronn, Germany) was employed to determine houttuynin in blood, plasma and tissue samples. The chromatographic separation and MS conditions were the same as in the reference[24].

LC/MS^n experiments for identifying the modification sites and structures of adducts were carried out on an Agilent 1200 HPLC system coupled with a 6330 MSD Trap XCT Ultra (Agilent Technologies, Waldbronn, Germany). The mass spectrometer was equipped with an ESI source. The ionization mode was positive. The interface and MS parameters were as follows: nebulizer pressure, 40 psi (N_2); dry gas, 12 L/min (N_2); dry gas temperature, 350 °C; spray capillary voltage, 3500 V; skimmer voltage, 40 V; ion transfer capillary exit, 124 V; scan range, *m/z* 200–2000; spectra average, 3; and target 200 000. For MS^n spectra, the fragmentation amplitude varied between 0.8 and 1.0 V. Data acquisition was performed in full-scan MS and MS^n modes (n=2 or 3). All data acquired were processed through Agilent Chemstation Rev B 01.03 software (Agilent, Palo Alto, CA, USA). Chromatographic separation was performed with a Capcell Pak C_{18} UG 120 column (100×4.6 mm id, 5 μm; Shiseido, Tokyo, Japan) protected by a Security-Guard C_{18} column (4.0×3.0 mm id, 5 μm; Phenomenex, Torrance, CA, USA). The mobile phase consisted of acetonitrile with 0.1% formic acid (solvent A) and 0.1% aqueous formic acid (solvent B) running at a constant flow rate of 0.6 mL/min. The solvent gradient was initially held at 10% A for 2 min and then increased linearly to 60% A over another 13 min. It was kept at 60% A for an additional 1 min, then increased to 90% A in 0.5 min. Afterwards, it was kept at 90% A for 8.5 min and was finally immediately decreased to 10% A in 0.5 min, where it was held constant at 10% A for 4.5 min before the next sample injection.

High-resolution mass spectral analysis was performed using a quadrupole time-of-flight hybrid mass spectrometer (Synapt Q-TOF MS, Waters, Manchester, UK) operated in (+)ESI mode. The mass resolution was adjusted to 10 000 (FWHM). A leucine enkephalin solution (*m/z* 556.2771, Waters) was used as the internal calibration standard. The capillary and cone voltages were set at 2.7 kV and 20 V, respectively. The nebulization gas (N_2) was set to 700 L/h at a desolvation temperature of 300 °C and a source temperature of 120 °C.

Statistical analysis

The ORIGIN 6.1 software package (OriginLab, Northampton, MA, USA) was used for statistical analysis and data display. The data were expressed as the mean±standard deviation.

Results

Tissue distribution of houttuynin in rats

Houttuynin was rapidly distributed into tissues after an iv dose of 10 mg/kg, achieving peak concentrations within 10 min postdose. In the assayed rat tissues, houttuynin concentrations were highest in lung tissue, ranging from 68 878±2839 ng/g to 625±229 ng/g from 10 min to 24 h, followed by heart, kidney, blood, spleen and plasma; they were lowest in liver tissue (Table 1). The ratios of tissue to the plasma concentration of houttuynin at 10 min were greater than the reference value of 1.0 except for liver tissue (ratio 0.38), demonstrating that houttuynin was distributed into tissues preferentially to plasma. Moreover, high ratios of blood to plasma (>1.0) at each sampling time from 10 min to 24 h suggested that houttuynin was not only distributed into plasma but also into erythrocytes, which might lead it to conjugate with hemoglobin in the erythrocytes. The concentrations of houttuynin in the blood, plasma and liver at 24 h were higher 6% of the peak concentrations.

The covalent binding levels of houttuynin to hemoglobin, plasma and tissue proteins at 10 min were high, ranging from 254 to 1137 nmol equivalents/g protein. Among them, the

Table 1. Tissue distribution of houttuynin in Sprague-Dawley rats following a 10 mg/kg iv dose of sodium houttuyfonate (n=3). Mean±SD.

	Concentration (μg/L; ng/g)			
	10 min	1 h	5 h	24 h
Blood	11 794±86.2	7 309±2819	2 693±504	803±254
Plasma	4 148±708	3 054±155	1 756±88.8	511±28.3
Heart	19 500±3962	8 315±1911	698±55.6	310±85.9
Liver	1 573±244	1 397±192	237±37.2	155±80.8
Spleen	5 259±758	2 207±211	317±41.1	311±142
Lung	68 878±2839	21 141±8364	1 430±298	625±229
Kidney	14 004±5188	9 816±4697	1 084±407	324±155

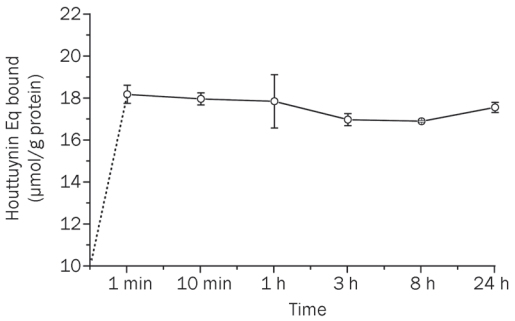

Figure 3. Covalent binding assay of [1-^{14}C]sodium houttuyfonate (1.0 mmol/L) with HSA (0.25 mmol/L) following incubation.

highest radioactivity existed in lung tissue, and the lowest radioactivity was found in plasma and liver (Figure 2).

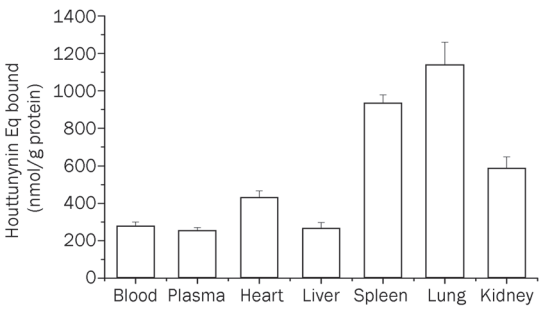

Figure 2. Covalent binding assay of houttuynin with proteins of plasma, blood and five tissues after a 10 mg/kg iv dose of [1-^{14}C]sodium houttuyfonate to rats (n=3).

In vitro protein covalent binding assay

When [1-^{14}C]sodium houttuyfonate (1.0 mmol/L) was incubated with HSA, covalent adducts with HSA rapidly formed, reaching 18.2±0.4 μmol equivalents/g protein after only 1 min of incubation and maintaining the binding level after 60 min of incubation (Figure 3). This yield was not statistically significant from that measured at the 24-h time point. The covalent binding of houttuynin to HSA was high and rapid, and multiple molecules of houttuynin were adducted to HSA.

SDS-PAGE analysis of the washed protein pellets obtained from the [1-^{14}C] sodium houttuyfonate and HSA incubation experiment also revealed the presence of one radiolabeled protein band with a molecular mass of 66.5 kDa. By liquid scintillation counting, the radioactivity of protein-bound [1-^{14}C]houttuynin was found to be 10 times higher than that of the control sample in the 1 min to 24 h incubation samples, which further established that houttuynin could readily covalently bind with HSA.

In vitro identification of pronase E-digested houttuynin-HSA adducts

To break down the modified HSA into individual amino acids, native and houttuynin-treated HSA that had been washed were digested with pronase E and then analyzed by LC/MS^n. In Figure 4, peaks for five adducted amino acid residues designated as P1–P5 were observed at 14.0, 15.0, 17.7, 18.5, and 19.6 min, respectively.

High-resolution MS analysis revealed that the pronase E enzymatic product P1 contained four nitrogen atoms ($C_{18}H_{32}N_4O_2$), indicating that P1 corresponded to an arginine adduct. The protonated P1 molecule at m/z 337 was 162 Da higher than that of the arginine standard, indicating that the adduct was formed by a condensation reaction (1:1) of houttuynin with an arginine residue accompanied by the loss of two water molecules (Figure 5A). Taken this possible reaction pathway into account[29], a reasonable mechanism for this condensation reaction is proposed in Figure 6. The initial reaction of the primary N$^{\omega}$-amino group of arginine occurred with the carbonyl carbon of houttuynin and resulted in the formation of a carbinolamine intermediate; next, one water molecule was eliminated in the reaction to form a Schiff's base. Subsequently, an intramolecular nucleophilic addition of an N$^{\omega-1}$ amine to the remaining carbonyl carbon of the original houttuynin occurred. This resulted in the formation of a cyclic carbinolamine intermediate. Further rearrangement and dehydration of the exocyclic imine to a conjugated system formed a stable pyrimidine derivative. In the MS/MS spectrum (Figure 5A), P1 showed typical losses of 18 Da (H_2O), 35 Da (H_2O and NH_3), and 63 Da (NH_3 and HCOOH) from the $[M+H]^+$ ion. Collectively, the data suggested that the structure of P1 was a pyrimidine-type adduct in houttuynin and arginine residues[30].

P2 exhibited the protonated molecule $[M+H]^+$ at m/z 327, which was 180 Da higher than that of the lysine standard. This indicated that the addition of one molecule of houttuynin to lysine residues was accompanied by the loss of one water molecule. In the MS/MS spectrum of P2 (Figure 5B), major fragment ions at m/z 310 and 264 were also 180 Da higher than those in the MS/MS of lysine, corresponding to a neutral loss of ammonia (NH_3, loss of 17 Da) as well as formic acid (NH_3 and HCOOH, loss of 63 Da). The adduct could be easily reduced by $NaBH_4$, resulting in a novel and stable adduct with an expected mass increment of 4 Da produced by the

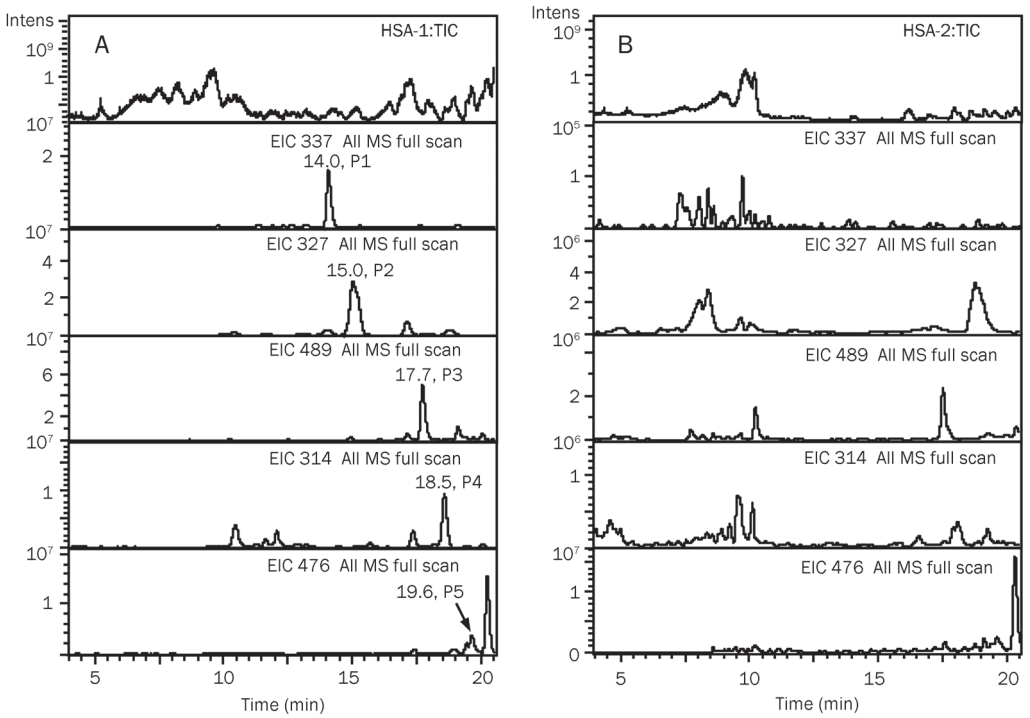

Figure 4. LC/MS^n analysis of the pronase E digest of HSA with houttuynin (A) and without houttuynin (B).

elimination of hydrogen. Based on the data, the P2 structure was proposed as a houttuynin-lysine Schiff's base. Theoretically, by a nucleophilic addition reaction, both aldehyde and ketone groups of houttuynin can react with the primary amine of lysine to form imine derivatives.

A reduction product of the Schiff's base adduct of houttuynin and N$^{\alpha}$-t-BOC-L-lysine was synthesized and purified. The obtained authentic compound was characterized by MS and NMR. Compared with the NMR data of N$^{\alpha}$-t-BOC-L-lysine, the synthesized adduct displayed an oxygenated methine proton at δ 3.68 (1H, m, H-3), corresponding to a carbon signal at δ 71.1 in the DEPT spectrum. This implied that the C-1 of the aldehyde group in houttuynin reacted with the primary amino group of BOC-lysine to form a Schiff's base adduct.

Data from multi-stage and high-resolution MS analyses also showed that the corresponding structure of P2 was a Schiff's base adduct of lysine and the aldehyde group, not lysine and the ketone group of houttuynin. In the MS/MS spectrum of P2, the elemental compositions of two fragment ions at *m/z* 173 and 156 were assigned as $C_8H_{17}N_2O_2$ and $C_8H_{14}NO_2$, respectively, by accurate mass measurement indicating that lysine structure existed. They were formed by C_{α}-C_{β} bond cleavage in houttuynin. Their mass fragment patterns are presented in Figure 5B. If the two ions were derived from the ketone adduct of houttuynin and lysine, their formation should be involved in the cleavage of two chemical bonds: one is via C_{α}–C_{β} bond cleavage, and another is via C–C cleavage in the houttuynin aliphatic chain, which requires high collision energies. This is difficult under an atmospheric pressure ionization mode. If a ketone adduct was formed, a fragment ion produced by acetaldehyde loss (-44 Da) should be observed in its MS/MS spectrum. Based on the foregoing analysis, P2 was finally assigned as the reaction product of the aldehyde group of houttuynin with lysine. The result indicated that the aldehyde group of houttuynin was much more reactive than its ketone group under the conditions used in the present study (pH 7.4, 37 °C) due to steric and electronic reasons.

LC/MS^n analysis of P3 displayed a molecular ion M$^+$ at *m/z* 489, 342 Da higher than that of the lysine standard, indicating the addition of two molecules of houttuynin to lysine residues with the loss of three water molecules. The MS/MS spectrum of P3 gave only one fragment ion at *m/z* 360 (Figure 5C). P3 was confirmed to be a houttuynin-lysine pyridinium adduct by comparing its chromatographic behavior, MS^n and NMR data with the prepared standard.

P4 showed the protonated molecule [M+H]$^+$ at *m/z* 314, 180 Da higher than that of the aspartate standard. This indicated the addition of one houttuynin molecule to an N-terminal aspartate residue accompanied by the loss of one water molecule. In the MS/MS spectrum (Figure 5D), a similar mass fragment pattern to that of P2 was displayed. The major fragment ions at *m/z* 160 and 142 were derived from C_{α}–C_{β} bond cleavage in houttuynin. Other fragment ions formed by the neutral loss of water (-18 Da), formic acid (-46 Da), and acetic acid (-60 Da) were also observed. As a result, P4 was tentatively identified as the Schiff's base adduct of houttuynin and N-terminal aspartate formed by aldehyde carbonyl addition reaction.

P5 exhibited similar MS behavior with P3. LC/MS^n analysis of P5 gave a molecular ion at *m/z* 476, which was 342 Da higher than that of aspartate, and a major fragment ion at *m/z* 360 (Figure 5E). This allowed us to assign P5 as the pyridinium derivative of houttuynin with N-terminal aspartate formed by the addition of two molecules of houttuynin to

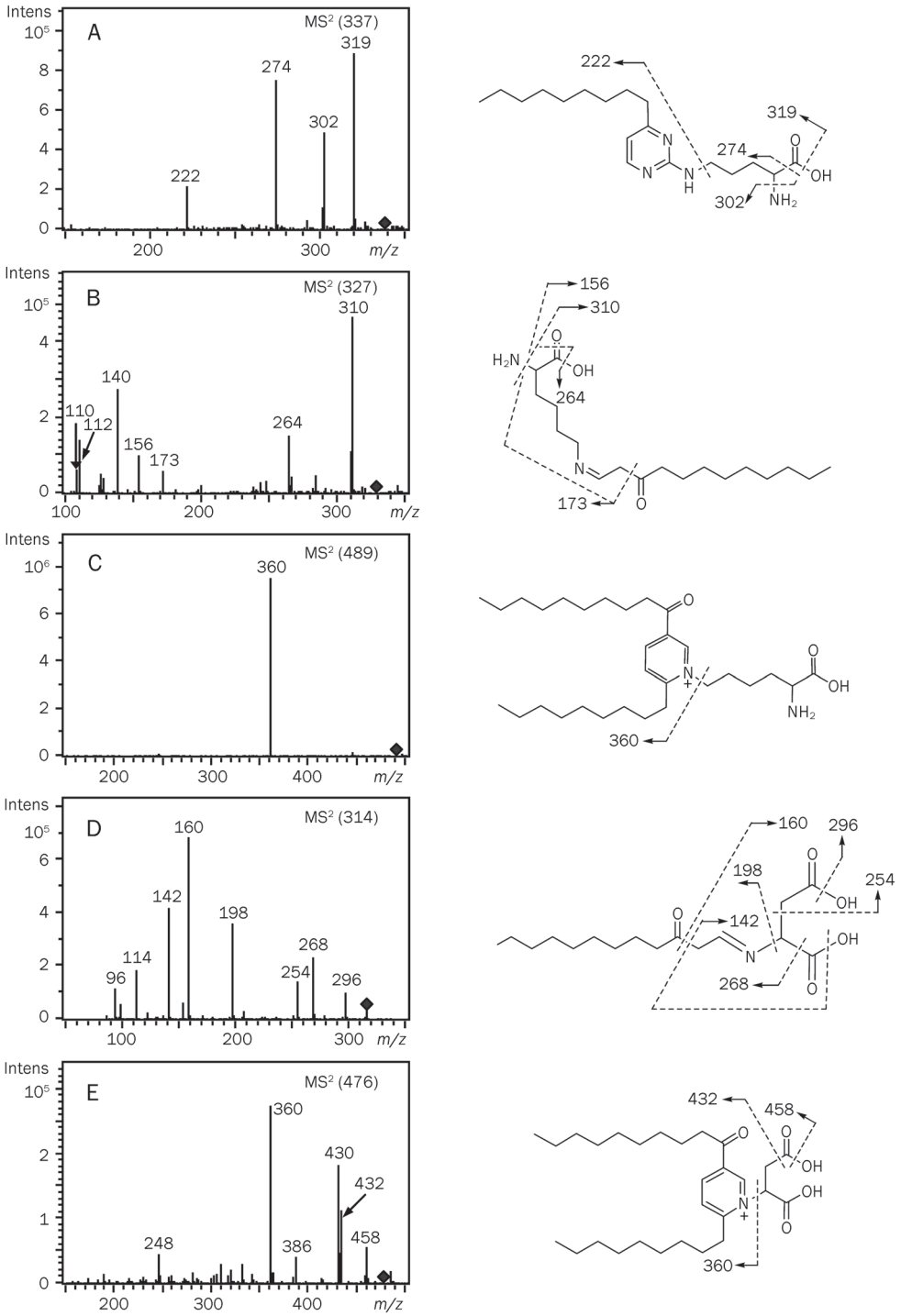

Figure 5. MS/MS spectra of the pronase E digest of HSA with houttuynin. (A) $[M+H]^+$ at *m/z* 337 (P1, arginine adduct); (B) $[M+H]^+$ at *m/z* 327 (P2, lysine adduct); (C) M^+ at *m/z* 489 (P3, lysine adduct); (D) $[M+H]^+$ at *m/z* 314 (P4, aspartate adduct); (E) M^+ at *m/z* 476 (P5, aspartate adduct).

aspartate residues with the loss of three water molecules.

Identification of adducts of houttuynin with *in vivo* proteins

The blood, plasma and tissues collected at 10 min after an iv administration of [1-^{14}C]sodium houttuyfonate were digested by pronase E and analyzed by LC/MS^n method. Compared with the blank samples, only one houttuynin-related adduct was detected in lung tissue (Figure 7). The adduct was assigned as an arginine-derived pyrimidine adduct by comparing its chromatographic behavior and MS^n spectra with the product P1 from the pronase E-digested houttuynin-HSA adducts.

Discussion

Accumulating evidence suggests that the covalent binding and formation of drug-protein adducts are related to drug organ toxicities of the liver, kidneys and lungs as well as to hypersensitivity reactions and carcinogenesis[2, 31]. Several pharma-

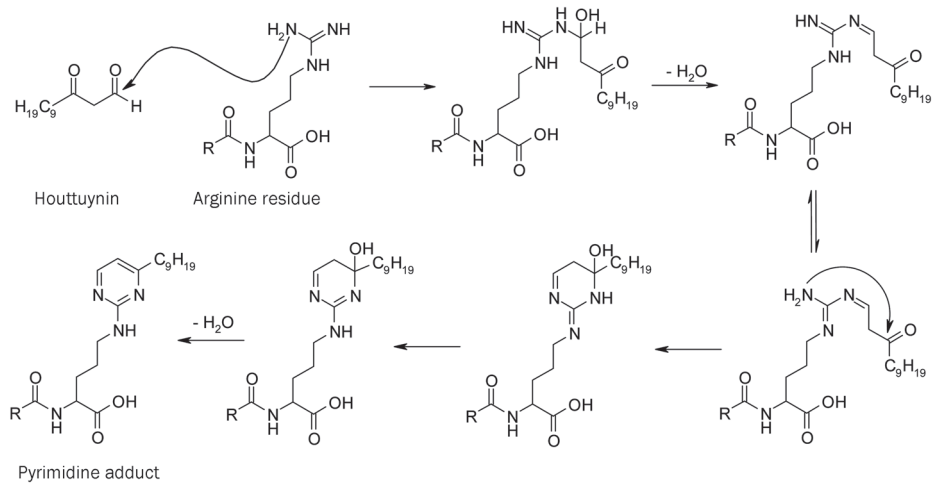

Figure 6. Proposed mechanism for the formation of the houttuynin-arginine adduct.

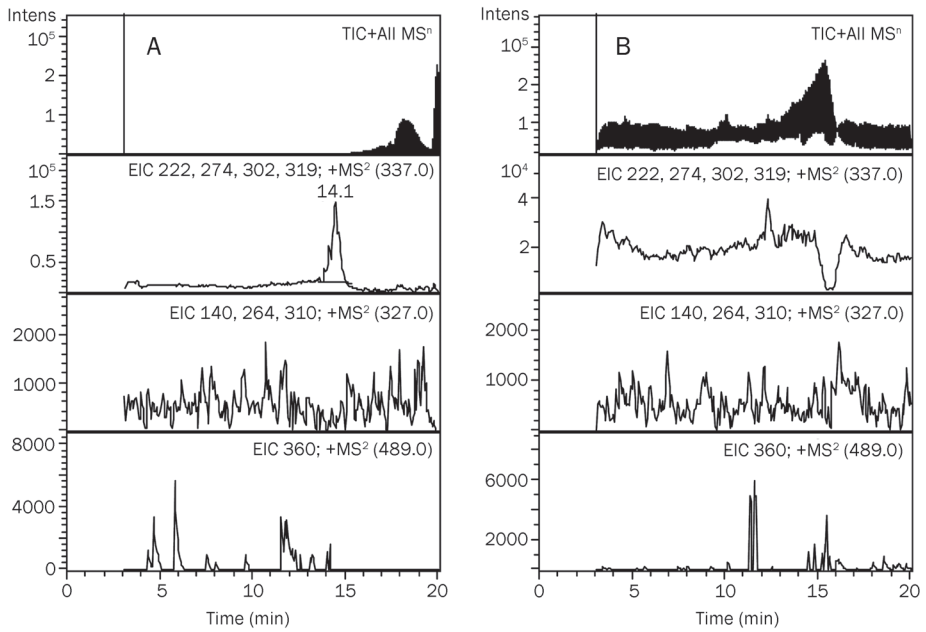

Figure 7. LC/MS^n analysis of the pronase E digest of lung tissue collected at 10 min after a 10 mg/kg iv dose of [1-^{14}C]sodium houttuyfonate (A) and blank lung tissue (B).

ceutical companies, such as Merck and Pfizer, recommend that levels of covalent protein binding *in vivo* for a drug candidate should be <50 nmol drug equivalents/g protein, although they emphasized that other factors should also be considered on a case-by-case basis.

In the present work, the tissue distribution of houttuynin in rats was investigated. After an injection, houttuynin was distributed rapidly into different tissues and was eliminated slowly from the body. The drug concentrations in the lung were higher than those in any other tissues. The lung was identified as the target organ of houttuynin, which was consistent with its therapeutic efficacy for pneumonia. The total plasma radioactivity was compared with the houttuynin concentration measured by the LC/MS/MS method. It was found that the major drug-related component in plasma was unchanged houttuynin, not its metabolites. The low distribution level in the liver indicated that hepatic metabolism may not be a significant pathway of houttuynin elimination. The covalent binding levels of houttuynin to the blood, plasma and tissue proteins were high, ranging from 254 to 1137 nmol equivalents/g protein, and were approximately 5 to 22 times higher than the acceptance criteria value of 50 nmol equivalents/g protein[2]. The covalent binding level was closely correlated with houttuynin concentrations in rats.

HSA contains numerous nucleophilic residues that react with electrophiles. In addition, HSA is a common target of reactive species of drugs. In this experiment, HSA was used as a model protein to identify the structures of houttuynin-related adducts. The covalent binding of houttuynin with HSA was high and rapid, and the adducts formed mainly through a Schiff's base mechanism. Houttuynin selectively adducted with arginine guanidinium, lysine amines and the N-terminal amine of HSA under physiological conditions, and the resulting adducts contained a Schiff's base and pyridinium

formed by condensation reactions of houttuynin with lysine or N-terminal residues (1:1 or 2:1), as well as a pyrimidine adduct formed by a 1:1 houttuynin-arginine reaction. *In vivo*, only the houttuynin-arginine pyrimidine adduct was detected; the other adducts were not observed at a measurable concentration.

This study showed that β-keto aldehyde compounds are capable of covalently binding to cellular proteins. The major adduct in the study was houttuynin-arginine pyrimidine, mainly due to the alkalinity and nucleophilicity of arginine guanidinium. Similar pyrimidine adducts derived from methylglyoxal and arginine-containing proteins have been reported previously[30]; however, little is known about their behaviors.

In conclusion, this study provided clear evidence that houttuynin is widely distributed into tissues after iv administration of sodium houttuyfonate, especially in lungs, and the β-keto aldehyde in houttuynin readily conferred covalent binding to tissue proteins. These findings may partially explain the idiosyncratic reactions to houttuyniae injection. We should draw great attention to the safety of preparations containing houttuynin.

Acknowledgements

This work was supported by the grants from the National Natural Science Foundation of China (No 90709036 and No 81173117). We would like to thank Prof Jiang ZHENG at the University of Washington (Seattle, WA, USA) for helpful discussions about radioactivity research and Ms Cen XIE of our laboratory for assistance in the *in vivo* covalent binding assay.

Author contribution

Zhi-peng DENG and Xiao-yan CHEN were responsible for the study design, data analysis and paper writing. Zhi-peng DENG and Jian MENG conducted the experiments. Da-fang ZHONG was a senior advisor and provided valuable advice for this study and for writing the manuscript.

References

1 Uetrecht J. Immune-mediated adverse drug reactions. Chem Res Toxicol 2009; 22: 24–34.
2 Baillie TA. Metabolism and toxicity of drugs. Two decades of progress in industrial drug metabolism. Chem Res Toxicol 2008; 21: 129–37.
3 Li AP. Overview: Evaluation of metabolism-based drug toxicity in drug development. Chem Biol Interact 2009; 179: 1–3.
4 Stepan AF, Walker DP, Bauman J, Price DA, Baillie TA, Kalgutkar AS, *et al*. Structural alert/reactive metabolite concept as applied in medicinal chemistry to mitigate the risk of idiosyncratic drug toxicity: A perspective based on the critical examination of trends in the top 200 drugs marketed in the United States. Chem Res Toxicol 2011; 24: 1345–410.
5 Kalgutkar AS, Soglia JR. Minimising the potential for metabolic activation in drug discovery. Expert Opin Drug Metab Toxicol 2005; 1: 91–142.
6 Zheng ZH. Clinical study on children respiratory tract infection treated by herba houttuyniae injection combination with antibiotics. Xibei Yao Xue Za Zhi 2006; 21: 33–4.
7 Sun GZ, Ju CD, Zhang XW, Yu RX. Investigation on clinical effect of herba houttuyniae injection by aerosol inhalation for respiratory tract infection on 107 cases. Chin Trad Pat Med 2001; 23: 421–3.
8 Wang XX. Twenty cases of adverse reaction caused by intravenous drop infusion of herba houttuyniae injection. Zhongguo Zhong Yao Za Zhi 2002; 27: 392–3.
9 Gao R, Wen WL, Tang XD. Adverse reaction and countermeasures of herba houttuyniae injection. Trad Chin Drug Res Clin Pharmacol 2006; 17: 383–5.
10 Du X, Shang J, Sun DF. Two cases with allergy induced by new sodium houttuyfonate. Chin J Pharmacoepidemiol 2004; 13: 349–50.
11 Liu JB, Cao RH, Wu QF, Ma CM, Wang ZH, Peng WL, *et al*. Synthesis and antibacterial evaluation of novel 4-alkyl substituted phenyl β-aldehyde ketone derivatives. Eur J Med Chem 2009; 44: 1737–44.
12 Kita T, Fujimura M, Myou S, Ishiura Y, Abo M, Katayama N, *et al*. Potentiation of allergic bronchoconstriction by repeated exposure to formaldehyde in guinea-pigs *in vivo*. Clin Exp Allergy 2003; 33: 1747–53.
13 Arican RY, Sahin Z, Ustunel I, Sarikcioglu L, Ozdem S, Oguz N. Effects of formaldehyde inhalation on the junctional proteins of nasal respiratory mucosa of rats. Exp Toxicol Pathol 2009; 61: 297–305.
14 Israel Y, MacDonald A, Niemelä O, Zamel D, Shami E, Zywulko M, *et al*. Hypersensitivity to acetaldehyde-protein adducts. Mol Pharmacol 1992; 42: 711–7.
15 Linneberg A, Gonzalez-Quintela A, Vidal C, Jørgensen T, Fenger M, Hansen T, *et al*. Genetic determinants of both ethanol and acetaldehyde metabolism influence alcohol hypersensitivity and drinking behaviour among Scandinavians. Clin Exp Allergy 2009; 40: 123–30.
16 Furuhata A, Ishii T, Kumazawa S, Yamada T, Nakayama T, Uchida K. N^{ε}-(3-methylpyridinium) lysine, a major antigenic adduct generated in acrolein-modified protein. J Biol Chem 2003; 278: 48658–65.
17 Uchida K, Kanematsu M, Sakai K, Matsuda T, Hattori N, Mizuno Y, *et al*. Protein-bound acrolein: Potential markers for oxidative stress. Proc Natl Acad Sci U S A 1998; 95: 4882–7.
18 Lee SH, Blair IA. Characterization of 4-oxo-2-nonenal as a novel product of lipid peroxidation. Chem Res Toxicol 2000; 13: 698–702.
19 Aldini G, Gamberoni L, Orioli M, Beretta G, Regazzoni L, Facino RM, *et al*. Mass spectrometric characterization of covalent modification of human serum albumin by 4-hydroxy-trans-2-nonenal. J Mass Spectrom 2006; 41: 1149–61.
20 Roller SG, Dieckhaus CM, Santos WL, Sofia RD, Macdonald TL. Interaction between human serum albumin and the felbamame metabolites 4-hydroxy-5-phenyl-[1,3]oxazinan-2-one and 2-phenylpropenal. Chem Res Toxicol 2002; 15: 815–24.
21 Waldon DJ, Teffera Y, Colletti AE, Liu J, Zurcher D, Copeland KW, *et al*. Identification of quinone imine containing glutathione conjugates of diclofenac in rat bile. Chem Res Toxicol 2010; 23: 1947–53.
22 Baba A, Yoshioka T. Structure-activity relationships for degradation reaction of 1-β-O-acyl glucuronides: kinetic description and prediction of intrinsic electrophilic reactivity under physiological conditions. Chem Res Toxicol 2009; 22: 158–72.
23 Sanderson JP, Naisbitt DJ, Park BK. Role of bioactivation in drug-induced hypersensitivity reactions. AAPS J 2006; 8: 55–61.
24 Duan XT, Zhong DF, Chen XY. Derivatization of β-dicarbonyl compound with 2,4-dinitrophenylhydrazine to enhance mass spectrometric detection: Application in quantitative analysis of houttuynin in human plasma. J Mass Spectrom 2008; 43: 814–24.
25 Bradford M. A rapid and sensitive method for the quantitation of microgram quantities of protein utilizing the principle of protein-dye binding. Anal Biochem 1976; 72: 248–54.
26 Laemmli UK. Cleavage of structural proteins during the assembly of the head of bacteriophage T4. Nature 1970; 227: 680–5.

27 Kang B, Tong Z. A fast staining-destaining method for SDS-PAGE which favours the recovery of protein. Prog Biochem Biophys 2000; 27: 210–1.
28 Kapteyn JC, Montijn RC, Dijkgraaf GJP, Ende HVD, Klis FM. Covalent association of β-1,3-glucan with β-1,6-glucosylated mannoproteins in cell walls of Candida albicans. J Bacteriol 1995; 177: 3788–92.
29 Oe T, Lee SH, Elipe MVS, Arison BH, Blair IA. A novel lipid hydroperoxide-derived modification to arginine. Chem Res Toxicol 2003; 16: 1598–605.
30 Oya T, Hattori N, Mizuno Y, Miyata S, Maeda S, Osawa T, *et al*. Methylglyoxal modification of protein. Chemical and immunochemical characterization of methylglyoxal-arginine adducts. J Biol Chem 1999; 274: 18492–502.
31 Stepan AF, Walker DP, Bauman J, Price DA, Baillie TA, Kalgutkar AS, *et al*. Structural alert/reactive metabolite concept as applied in medicinal chemistry to mitigate the risk of idiosyncratic drug toxicity: A perspective based on the critical examination of trends in the top 200 drugs marketed in the United States. Chem Res Toxicol 2011; 24: 1345–410.